Application of remote sensing and geographical information system for the study of mass movements in Lebanon

Chadi Abdallah

ACADÉMIE DE PARIS

UNIVERSITÉ PIERRE ET MARIE CURIE
PARIS 6

Mémoire des Sciences de la Terre

Présenté par

M Chadi ABDALLAH

Pour obtenir le grade de

DOCTEUR DE L'UNIVERSITÉ PARIS 6

Sujet de la thèse :

Application de la télédétection et des systèmes d'informations géographiques à l'étude des mouvements de terrain au Liban

UFR Des Sciences de la Terre
4, place jussieu – 75252 Paris cedex 05

THESE DE DOCTORAT DE L'UNIVERSITÉ PARIS 6

Spécialité

Géosciences et Ressources Naturelles

Présenté par

M Chadi ABDALLAH

Pour obtenir le grade de

DOCTEUR DE L'UNIVERSITÉ PARIS 6

Sujet de la thèse :

Application de la télédétection et des systèmes d'informations géographiques à l'étude des mouvements de terrain au Liban

11 Juillet 2007

Devant le jury de : (préciser la qualité de chacun des membres)

M	Jean CHOROWICZ	Directeur de thèse
M^{me}	Christine KING	Rapporteur
M	Jean Paul DEROIN	Rapporteur
M	Alain TABBAG	Examinateur
M	Mohamad KHAWLIE	Co directeur de thèse
M	Damien DHONT	Co directeur de thèse

ACKNOWLEGMENTS

My sincere thanks to the Authorities of the Lebanese National Council for Scientific Research ***(LCNRS),*** who have supported my scholarship.

Thanks extend to the Secretary General of the LCNRS ***Dr. Mouin Hamzé*** for his aid and support.

Special thanks to ***Prof. Jean Chorowicz*** who gave me the honor to be his student, supported, supervised and guided this work.

To the man who could not pass a day without learning something new from him, deep thanks to ***Dr. Mohamad Khawlie*** for his continuous encouragement, support and valuable guidance through my dissertation and all other work.

Deep thanks also to my friend and colleague ***Dr. Rania Boukheir*** for her enormous help and participation in this work.

Thanks also for ***Dr. Damien Dhont*** for his help and being a co-advisor of this thesis.

Many thanks to ***Dr. Christine King*** and ***Dr. Jean Paul Deroin*** for accepting reviewing this work.

Special thanks for ***Mr. Souhail Kanaan*** from the LCNRS for his support and encouragement.

Also Thanks extend to ***Dr. Francisco Gomez (Paco)*** for hosting me during my visit to The United States and making his Lab at Missouri University and the GPS equipment available and at my disposal.

Thanks also to ***Rani Jaafar*** and ***Samer El Hashem*** for their help in the GPS campaigns.

Also special thanks to ***Dr. Gebran Karam*** for giving the access to the GPS equipment.

Finally, I would like to thank all my colleagues at the ***Remote Sensing Center*** for their aid and for being supportive.

Dedication

To my Family;

Mom,

Tarek & Ali,

with deep

&

sincere love

Abstract

Among the various natural hazards, mass movements (MM) are probably the most damaging to the natural and human environment in the Mediterranean countries, including Lebanon which represents a good case study of mountainous landscape. Although affecting vast areas in the country, the phenomenon was not studied at regional scale, and related maps are still lacking. Therefore, this research deals with the use of remote sensing and geographic information system (GIS) techniques in studying MM in Lebanon.

In this context, the first part reviews existing knowledge on the topics of mass movements (MM) specifically in the Mediterranean region, and defines research gaps. It exposes the diverse types of MM, their magnitudes, the causative agents and their bad consequences. It clarifies confusions related to MM-terms (hazard, susceptibility, risk, etc.), and compares the efficiencies of the most used methods for MM susceptibility/hazard zonation. It includes also a statement on remote sensing and GIS benefits and constraints in mass movement studies, pointing out possible ways of research.

The second part is dedicated to the detailed description of the study area *"the Mediteranean slopes of central to north Lebanon"* within Lebanon. Physical/morphodynamic and socio-economic characteristics of the area are exposed, as well as the natural hazards, MM events, their socio-economic impacts and mitigation measures. All previous studies about MM hazard in Lebanon are reviewed. The studied area, extending from the Mediterranean coast to around 3000 m elevation, covers ~36% of the total area of Lebanon. It represents the geoenvironmental diversity of this country in terms of geology, soil, hydrography, land cover and climate. It is characterized by problematic human activities (e.g., chaotic urban expansion, artificial recharge of groundwater, overgrazing, forest fire) enhancing environmental decline and inducing MM, with minimal government control.

The third part compares the applicability of different satellite sensors (Landsat TM, IRS, SPOT4) and preferred image processing techniques (False Color Composite "FCC", Pan-sharpen, Principal component analysis "PCA", Anaglyph) for the mapping of MM recognized as landslides, rock/debris falls and earth flows. Results from the imagery have been validated by field surveys and analysis of IKONOS imagery (1 m) acquired in some locations witnessing major MM during long periods. Then, levels of accuracies of detected MM from satellite imageries were plotted. This study has demonstrated that the anaglyph produced from the two panchromatic stereo-pairs SPOT4 images remains the most effective tool setting the needed 3-D properties for visual interpretation and showing maximum accuracy of 69%. The PCA pan-sharpen Landsat TM-IRS image gave better results in detecting MM, among other processing techniques, with maximum accuracy level of 62%. The errors in interpretation fluctuate not only according to the processing technique, but also due to the difference in MM type. They are minimal once 3D anaglyph SPOT4 is considered, varying between 31% (landslides), 36% (rock and debris falls) and reaching 46% in the case of earth and debris flows.

The fourth part explores relationships between MM occurrence and different factor terrain parameters. Parameters expressed by: 1- preconditioning factors, like: elevation, slope gradient, slope aspect, slope curvature, lithology, proximity to fault line, karst type, distance to quarries, soil type, distance to drainage line, distance to water sources, land cover/use, and proximity to roads, and 2- triggering MM factors, like: rainfall quantity, seismic events,

floods and forest fires, were correlated with MM using GIS-approaches. This study indicates, depending on bivariate remote sensing and GIS statistical correlations (Kendall Tau-b correlation), that lithology is the most influencing on MM occurrence, having the highest correlation with other parameters (i.e. 7 times correlated at 1% level of significance and 3 times at 5%). It also shows that statistical correlations to mass movements exist best between parameters at the following decreasing order of importance: soil type/distance to water sources (acting similarly on MM occurrence), karst/distance to quarries/land cover-use, proximity to faults, slope gradient/proximity to roads/floods, seismic events, elevation/slope aspect/forest fires. These correlations were verified and checked through field observations and explained using univariate statistical correlations. Therefore, they could be extrapolated to other Mediterranean countries having similar geoenvironmental conditions.

The fifth part proposes a mathematical decision making method – Valuing Analytical Bi-Univariate (VABU) that considers two-level weights for mapping MM susceptibility/hazard (1:50,000 cartographic scale) within the study area. The reliability of this method is examined through field surveys and depending on a GIS comparison with other statistical methods – Valuing accumulation Area (VAA) (depending on one weight level) and Information Value (InfoVal) (requiring detailed measurements of MM areas). Three susceptibility maps were derived using preconditioning parameters, while hazard maps were produced from triggering ones. The coincidence values of overlapping susceptibility maps were found to be equal to 47.5% (VABU/VAA), 54% (VABU/InfoVal) and 38% (VAA/InfoVal). The agreement between hazard maps showed closer values than susceptibility ones, oscillating between 36.5% (VAA/InfoVal), 39% (VABU/VAA), and 44 % (VABU/InfoVal). Field verification indicates that the total precision of the produced susceptibility maps ranges from 52.5% (VAA method), 67.5% (InfoVal method) and 77.5% (VABU method). This demonstrates the efficiency of our method, which consequently can be adopted for predictive mapping of MM susceptibility/hazard in other areas in Lebanon and may be easily extrapolated using the functional capacities of GIS.

The sixth part predicts the geographic distribution and volume of block falls (m^3) across the study area using GIS decision-tree modelling. Such mapping was unavailable in Lebanon, but also in many other countries putting effort on landslide research rather than other types of MM. Several decision-tree models were developed using (1) all terrain parameters, (2) topographic parameters only, (3) geologic parameters only, and adopting various processing techniques (pruned and unpruned trees). The best regression tree model combined all parameters and explained 80% of the variability in field blocks falls' measurements. The unpruned model built using four geological parameters (lithology, soil type, proximity to fault line, and karst type) seems also interesting, classifying 68% of block falls and referring to a small amount of input data (4 parameters). The produced predictive quantitative block falls' map at 1:50,000 appears extremely useful for decision-making, helping adoption of mitigation measures to reduce the occurrence of harmful block falls.

The seventh part focuses on monitoring MM activity through integrating space borne radar data and Global Positioning System (GPS) techniques. ERS radar imageries were processed using InSAR and permanent scatters techniques. The analysis showed difficulties in detecting ground deformations due to MM. Nevertheless, the analysis is still in its preliminary stage and future planned work will take into consideration other manipulating procedures for detecting the displacements. On the other hand, a GPS installation in Hammana area; one of the Lebanese villages lying in a major landslide, was conducted. Two campaigns were raised, but results are still lacking since there is not enough data accumulation. More observations are

still needed to build up a comprehensive picture on the direction and velocity of the movement.

Keywords: mass movements (MM), satellite images, visual interpretation, geographic information systems (GIS), statistical correlations, regression models, susceptibilities/hazard maps.

Résumé

Parmi les aléas naturels, les mouvements de terrain (MT) sont probablement les plus nuisibles à l'environnement naturel et humain, notamment dans les pays méditerranéens, incluant le Liban qui représente un bon cas d'étude de région montagneuse. Ce phénomène n'a pas été étudié à l'échelle régionale bien qu'il affecte de vastes zones dans ce pays, et les cartes d'aléa manquent encore. La recherche présentée ici est consacrée à l'utilisation des techniques de télédétection et des systèmes d'informations géographiques (SIG), pour l'étude des MT au Liban.

La première partie passe en revue les connaissances existantes sur le thème des mouvements de terrain (MT), plus spécifiquement dans la région méditerranéenne, et définit les lacunes de recherche. Elle expose les divers types existants de MT, leurs magnitudes, les agents causatifs, et leurs effets. Elle clarifie la terminologie utilisée pour les MT (aléa, susceptibilité, risque, etc.), et compare les méthodes les plus utilisées pour la cartographie de l'aléa/susceptibilité aux MT. Elle présente aussi un état des avantages et problèmes de la télédétection et du SIG dans les études de mouvements de terrain, en insistant sur les voies possibles de recherche.

La deuxième partie est consacrée à la description détaillée de la région d'étude qui couvre *les versants méditerranéens du nord du Liban central*. Les caractéristiques physiques/morpho-dynamiques et socio-économiques de cette région sont exposées, ainsi que les aléas naturels, les événements de MT, les impacts socio-économiques et les mesures de conservation. Toutes les études sur l'aléa MT au Liban sont revisitées. La région d'étude, s'étendant de la côte méditerranéenne jusqu'à 3000 m d'altitude, couvre à peu près 36 % de la superficie totale du Liban. Elle est représentative de la diversité géo-environnementale de ce pays en termes de géologie, sol, hydrographie, occupation du sol et climat. Elle se caractérise par des activités humaines problématiques (par exemple une expansion urbaine chaotique, la recharge artificielle des eaux souterraines, un surpâturage, des incendies de forêt), accroissant la dégradation de l'environnement et induisant les MT, avec un contrôle gouvernemental minime.

La troisième partie compare l'efficacité de différents capteurs satellitaires à résolutions variées (Landsat TM, IRS, SPOT4) et diverses techniques de traitement d'image (composition colorée, fusion, analyse en composantes principales ACP, vision stéréoscopique) pour la détection visuelle des mouvements de terrain classés en glissements, éboulements de blocs rocheux et de débris, et coulées de boue. Les résultats ont été validés sur le terrain et en analysant des images IKONOS (1 m) acquises en certaines localités menacées par des MT sur de longues périodes. Ensuite, les niveaux de précision de la détection des MT à partir des images satellitaires ont été calculés. Cette étude a montré que l'anaglyphe produit à partir des images panchromatiques stéréo SPOT4 reste l'outil le plus efficace grâce aux caractéristiques 3D jouant un rôle essentiel dans l'interprétation visuelle et montrant un niveau de précision (pourcentage des MT détectés et vérifiés sur le terrain) maximal de 69 %. De plus, l'image de fusion Landsat TM-IRS, calculée par ACP, fournit des résultats de détection des MT meilleurs que les autres techniques, avec un niveau de précision de 62 %. Les erreurs d'interprétation fluctuent non seulement en fonction de la technique de traitement utilisée, mais aussi en fonction des types de MT. Elles sont minimes quand l'anaglyphe (3D) SPOT4 est pris en considération, variant de 31 % (glissements), 36 % (éboulements de blocs rocheux et de débris) à 46 % dans le cas des coulées de boue.

La quatrième partie explore les relations entre l'occurrence de MT et les paramètres du terrain. Ces paramètres sont: 1- les facteurs de prédisposition, comme l'altitude, la pente en gradient, l'aspect de pente, la courbure de pente, la lithologie, la proximité aux failles, le type de karst, la distance aux carrières, le type de sol, la distance aux réseaux de drainage, la distance aux sources, l'occupation/utilisation du sol et la proximité aux routes, et 2- les facteurs déclenchants, comme la quantité de pluies, les événements sismiques, les inondations et les incendies de forêt, qui ont été corrélés avec les MT en utilisant les approches SIG. Cette étude montre, en se basant sur les corrélations statistiques bi-variées satellitaires et SIG (corrélation Kendal Tau-b), que la lithologie est ce qui influence le plus l'occurrence des MT, puisqu'elle a la corrélation la plus élevée avec les autres paramètres (7 fois corrélée à un niveau de signification de 1 %, et 3 fois à 5 %). Elle montre aussi que les corrélations statistiques entre ces paramètres et les mouvements de terrain existent suivant l'ordre d'importance décroissant suivant : type de sol/distance aux sources (agissant de manière similaire sur l'occurrence des MT), karst/distance aux carrières/occupation/utilisation du sol, proximité aux failles, gradient de pente/proximité aux routes/inondations, événements sismiques, altitude/aspect de pente/incendies de forêt. Ces corrélations sont vérifiées sur le terrain et expliquées en utilisant des corrélations statistiques uni-variées. Par conséquent, elles peuvent être extrapolées à d'autres pays méditerranéens caractérisés par des conditions géo-environnementales similaires.

La cinquième partie propose une méthode mathématique décisionnelle (méthode analytique bi-univariée d'évaluation ou «*Valuing Analytical Bi-Univariate (VABU)*») qui considère deux niveaux de pondération pour la cartographie de l'aléa/susceptibilité des MT (échelle 1/50000) dans la région d'étude. La fiabilité de cette méthode est examinée sur le terrain et en la comparant avec d'autres méthodes statistiques - *Valuing accumulation Area (VAA)* (un seul niveau d'évaluation) and Information Value (InfoVal) (nécessitant des mesures détaillées des MT). Trois cartes de susceptibilité sont dérivées en utilisant les facteurs conditionnant l'occurrence des MT, tandis que les cartes d'aléa sont produites à partir des facteurs déclenchants. Les valeurs de coïncidence de superposition des cartes de susceptibilité sont de 47,5 % (VABU/VAA), 54 % (VABU/InfoVal) et 38% (VAA/InfoVal), respectivement. L'accord entre les cartes d'aléas montre des valeurs proches de celles des cartes de susceptibilité, variant entre 36,5 % (VAA/InfoVal), 39 % (VABU/VAA), et 44 % (VABU/InfoVal). La validation sur le terrain indique que la précision totale des cartes de susceptibilité produites varie entre 52,5% (méthode VAA), 67,5% (méthode InfoVal) et 77,5% (méthode VABU). Cela démontre l'efficacité de notre méthode qui peut être adoptée pour une cartographie prédictive de l'aléa et de la susceptibilité des MT dans d'autres régions au Liban, et peut être aussi aisément extrapolée en utilisant les capacités fonctionnelles du SIG.

La sixième partie prédit la distribution géographique et le volume des blocs rocheux (m^3) dans la région d'étude en utilisant la modélisation suivant un arbre décisionnel. Une telle cartographie est indisponible au Liban, mais aussi dans d'autres pays qui portent plutôt leur effort sur la recherche des glissements plutôt que les autres types de MT. Plusieurs modèles d'arbres décisionnels ont été développés en utilisant, (1) tous les paramètres de terrain, (2) les paramètres topographiques uniquement, (3) les paramètres géologiques, et en adoptant plusieurs techniques de traitement. Le meilleur arbre de régression combine tous les paramètres et explique 80 % de la variabilité dans les mesures des blocs rocheux sur le terrain. Le modèle construit en utilisant les quatre paramètres géologiques (lithologie, type de sol, proximité aux failles et type de karst) parait aussi intéressant car il classe 68 % des blocs rocheux tout en se référant à un petit nombre de données d'entrée (4 paramètres). La carte

produite de ‘prédiction quantitative des blocs rocheux’ à l’échelle du 1/50 000 apparait extrêmement utile pour la décision, aidant à l’adoption des mesures de conservation afin de réduire l’occurrence de movements nuisibles de blocs rocheux.

La septième partie s’intéresse à la surveillance de l’activité des MT à travers l’intégration des données spatiales radar et des techniques GPS (Système de positionnement global). Les données radar ERS sont traitées en utilisant les techniques InSAR et *des réflecteurs permanents*. Cette analyse montre des difficultés pour la détection des MT. Cependant, elle est jusqu’à présent préliminaire, et un plan de travail futur prendra en considération d’autres traitements pour la détection des déplacements. D’un autre côté, une installation GPS a été effectuée dans la région de Hammana, un village libanais menacé par un grand glissement. Deux campagnes ont été rassemblées, mais les résultats manquent encore puisqu’il n’y a pas des données accumulées suffisantes. Plus d’observations sont nécessaires afin de construire une représentation compréhensive de la direction et de la vitesse du mouvement.

Mots-clés: mouvements de terrain (MT), images satellitaires, interprétation visuelle, système d’informations géographiques (SIG), corrélations statistiques, modèles de régression, cartes d’aléas/susceptibilités.

TABLE OF CONTENTS

LIST OF FIGURES

CHAPTER VII

LIST OF TABLES

CHAPTER VII

LIST OF ANNEXES

GENERAL INTRODUCTION

Mass movements (MM) constitute a hazard that is among the most widespread on the earth's surface. They are considered a significant aspect of surficial instability contributing to losses in land and socio-economics through their damaging of the natural and human environments. They occur frequently in areas where morphotectonic events (uplift, faulting and earthquakes) prevail. The latter are important throughout the Eastern Mediterranean basin (Almeida-Teixera *et al.*, 1991), but seem to play a subordinate role in the triggering or activation of earth movements by comparison with anthropic and climatic causes (Cascale *et al.*, 1994; Wu and Sidle, 1995; Gostelow *et al.*, 1996; Poesen and Hooke, 1997; Atkinson and Massari, 1998). The most common human activities in the Eastern Mediterranean basin that can induce MM are mainly represented by artificial recharge of groundwater, mining subsidence, civil engineering practices (reservoir, dam and road construction), chaotic housing encroachment, industrial developments, service pipes, loading and unloading of slopes and disposal of fluid and/or solid waste on, and within, the ground. Climatic causes in the basin are mostly influenced by global changes especially the last three decades, enhancing extreme rainfall events with torrential and episodic character, triggering MM.

Until recently, earth observation and mass movement investigations have relied on the interpretation of aerial photographs. For a long time, satellite imagery has lacked the spatial resolution to provide detailed mapping at the scale of an individual mass movement. However, the development of modern earth observation techniques in diverse aspects, like different active and passive platforms, high and very high spatial resolutions, multitemporal, multispectral, extraction from digital elevation models (DEMs) and multiple image processing techniques, improved the mapping and monitoring possibilities. Similarly, GIS *(Geographic Information Systems)* technology remains a powerful and flexible tool facilitating the integration of multiple data layers and spatial simulation to explore cause-effect MM relationships and improving hazard assessment.

Such issues are addressed in this research from different perspectives, focusing on mass movements (MM) in Lebanon. The country represents a good case study for several reasons:

(1) Lebanon is a part of the Eastern Mediterranean region, having a combination of unconsolidated rock type, erodible soils, steep slopes, heavy rainfall, active tectonic movement, rapid land use change and intense human interference;

(2) It offers an abundant and complex set of MM that can be taken as a basis for assessment;

(3) The impact of mass movements problem has not yet been treated in detail although it affects vast areas, threatens natural resources and human life. Previous studies in such domain are scarce, being mostly descriptive of the grave situation of MM occurrence or giving some indications of the engineering/geotechnical properties for the unstable lithological formations (Searle, 1972; Khawlie and Hassanain, 1979, 1984a, b; Khawlie, 1985). And mapping MM at a regional scale (e.g., 1:50,000) has not been performed yet;

(4) The “detailed measurements” of MM are difficult to implement in Lebanon, as is the case with several other developing countries with limited amounts of resources – i.e. financial and human expertise.

(5) Appropriate management plans are still lacking, protective measures are not efficient and unstable from an engineering point of view.

(6) The need to apply and test the use of satellite imageries of very high resolution needed for coverage of MM with the rough often inaccessible Lebanese topography.

Therefore, there is a need for investigation mapping and the MM phenomenon and its evolution, followed by efforts to establish measures for its management. This will assure sustainable management of natural resources. In this context, the research was conducted with significant use of remote sensing and GIS, on a variety of aspects, including MM hazard mapping and modeling, the synergy obtained from merging different kinds of remote sensing data, the integration of satellite imageries and GIS data and monitoring approaches.

This work (Doctoral Thesis) is carried out as a part of the project entitled *"Développement de la méthodologie spatiale pour la cartographie des zones à risque d'érosion hydrique et des mouvements de masse. Apports de l'exemple du Liban"* held at international level in collaboration between the "Université Pierre et Marie Curie - Paris 6 – Laboratoire de tectonique" (France) and the National Council for Scientific Research/Remote Sensing Center (Lebanon) (2003-2007). It was partially financed by Cèdre Franco-libanais program, and supported by a scholarship dedicated from the National Council for Scientific Research (CNRS – Lebanon).

The thesis is organized in seven chapters (**Figure i**). **The first chapter gives an overview of existing studies on mass movements in the Mediterranean region at various spatial and temporal scales**. It shows also the general geographic distribution of MM through the Mediterranean basin, and their bad consequences. It assesses and compares the relative efficiencies of diverse adopted methodologies used in MM hazard/susceptibility zonation, and defining major constraints and relevant improvements. It clarifies MM-related terms (hazard, vulnerability, risk, etc.), explains the adopted classifications of diverse types of MM (slides, falls and flows), and shows the corresponding magnitudes of MM and their causative agents. It includes also a statement on remote sensing and GIS benefits in MM studies, pointing out possible ways of research.

The second chapter corresponds to a description of the study area in Lebanon used for implementing the adopted approach. It comprises pictorial explanations of the physical/morphodynamic (dominant geomorphology and geology, soil distribution and characteristics, land cover/use modes, hydrology and climate) and socio-economic characteristics of the area. It exposes also other occurring natural hazards (soil erosion, flooding, and forest fires) in the area, due to their close relation to MM events. At the same time, it shows some concrete examples of MM throughout Lebanon, their socio-economic impacts, as well as the mitigation measures that are taken. It reviews existing knowledge and previous studies on the topic of MM in Lebanon.

The third chapter compares statistically the applicability of different satellite data sensors (Landsat TM, IRS and SPOT4)**, and preferred image processing techniques** (False Color Compoiste, pan-sharpen, principal component analysis and anaglyph) **for the mapping of diverse types of MM.**

Figure i. Simplified flow diagram of the logical approach used in this work.

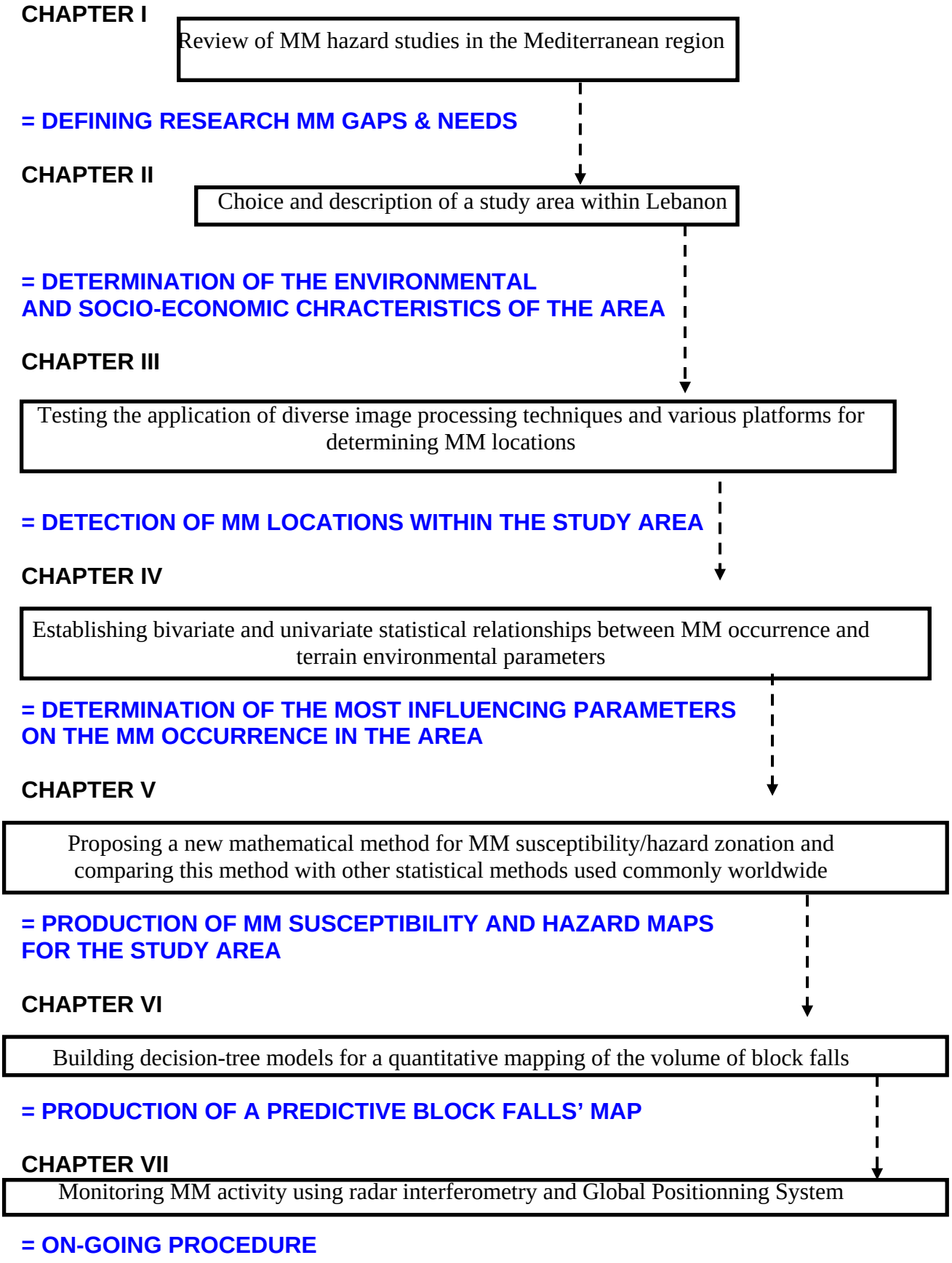

The comparative results obtained from medium and high resolution remote sensing data are validated by field surveys and visual analysis of other satellite images enabling detailed investigations (IKONOS).

The fourth chapter tests the influence of diverse terrain parameters, either triggering MM (e.g., rainfall, earthquakes) or preconditioning MM (e.g., rock type, high groundwater level, morphology). The considered parameters are extracted from remote sensing or GIS data, and statistical correlations (univariate and bivariate) between them and MM detected in Chapter III from satellite imageries and verified in the field are built and explained (with drawing charts).

In the fifth chapter, a newly adapted mathematical decision making method (i.e. valuing analytical bi-univariate method) is proposed for performing MM susceptibility/hazard mapping. This method is compared, using a spatial, attribute and correspondence analysis, with other statistical methods commonly used worldwide (i.e. valuation area accumulation and information value methods). Its reliability is checked in the field and levels of accuracies are plotted. The advantages and problems of the new method are also explored.

The sixth chapter focuses on building simple, realistic, practical and informative decision tree - regression models for a quantitative mapping of the volume of block falls (m^3) using the prepared terrain parameters in chapter IV. This chapter highlights the reasons behind using the concept of decision-tree modeling, and describes in detail the steps needed for building diverse tree models depending on different terrain parameters, and diverse processing techniques. It evaluates the performance of the built models by measuring the proportion of variance explained and comparing the deduced results. It indicates also the relative importance of the terrain parameters in building the trees.

The seventh and last chapter is dedicated for presenting the on-going studies for MM monitoring using radar interferometery data and Global Positioning System (GPS). The interferometry procedure was performed during a research visit to the University of Missouri in the United States. While the GPS procedure was tested on the major well-known landslide of Hammana (Mount Lebanon).

– I –

A review of mass movement hazard analysis in the Mediterranean region

CHAPTER I
A review of mass movement hazard analysis in the Mediterranean region

The first part of this work reviews existing knowledge in the Mediterranean region on mass movement hazard at various spatial and temporal scales, and defines research gaps. It exposes diverse types of mass movements (MM), their negative consequences, their causative agents, and the most commonly used models for hazard zonation. It further reflects on the benefits of using remote sensing and GIS in mass movement studies, existing problems and possible ways that can overcome these problems.

1. Distribution and consequences of mass movements

Mass movements are natural hazards that could result in severe damages and are difficult to control. They are quite important in the Mediterranean region as they are widespread, occurring in all its countries (**Figure 1.1**). They inflict economic losses and cause numerous fatalities and injuries. Annual economic losses from MM are estimated at 10-15 millions $ in a small country like Lebanon (Khawlie, 2000), or much more attaining for example 1 billion $ in Italy (Schuster and Fleming, 1986). The 996 MM that occurred in Italy from 1410 to 1999 were estimated to cause 12,421 casualties (Guzzetti, 2000). They can occur on a frequent basis in many areas, such as in the rugged mountainous chains, i.e. Alps, Pyrenees, and the Apennines (Poesen and Hooke, 1997). Most losses occur in settlements developed on gently sloping hillsides (Creath, 1996). Too often, their occurrence in areas where other natural disasters take place, such as earthquakes, floods, or volcanic eruptions, tends to mask their true impact and leads to un-credited losses.

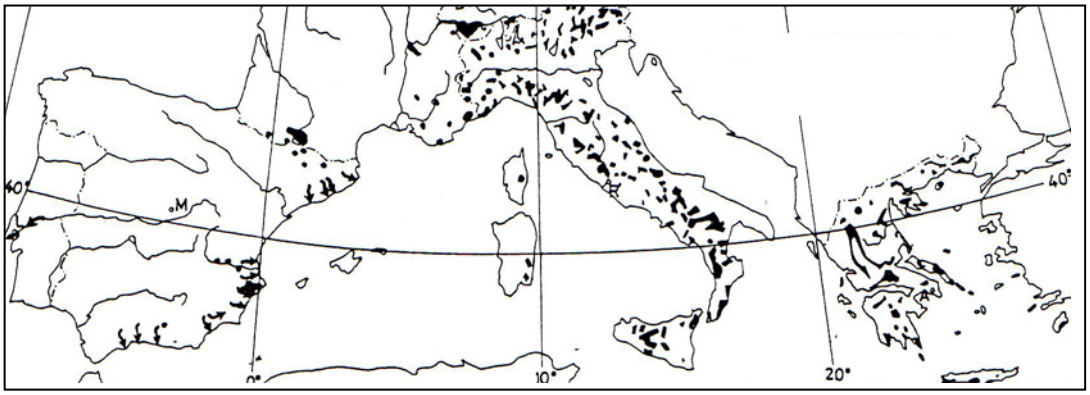

Figure 1.1. Areas affected by mass movements in the European northern Mediterranean region (Poesen and Hooke, 1997).

MM can occur as rapid sudden, short-lived events, as a slow moving slide mass, or as imperceptibly slow moving soil creep. They pose serious direct and/or indirect hazards of short or long term. The most obvious direct effects are the destruction of structures that support transportation, parks and recreational areas, residential and commercial buildings, sewers and dams. In Italy, it has been estimated that over 1,000 urban centers are threatened

by landslide activity (Pellegrini and Surian, 1996). The indirect effects of MM can also be very destructive, burying facilities, impairing their use and leading consequently to reduce property value. For instance, once MM occur in narrow valley floors, they create temporary dams that quickly impound water, resulting later in catastrophic flooding. If their deposits accumulate on flood plains, they lead to a drastic decrease in agricultural production. The most important indirect long-term effect of MM in mountainous terrain is represented through landscape evolution.

2. Concepts

2.1. Definitions

The terminology concerning MM is a major problem (Flageollet, 1994) because it varies according to various points of view from the numerous disciplines that are concerned (geomorphology, geology, geography, soil science, civil engineering, etc.). According to Varnes (1978), standardization of the terminology is an objective that cannot be obtained.

Mougin (1973) and Filliat (1981) restricted the concept of mass movement to displacements of rock bodies under effects of gravity as the major factor. Crozier (1986) claimed that water is the major agent that helps rock materials move downwards. Foucault and Raoult (1992) referred to more or less fast movements of ground or mass rock, in the context of slopes. For us, mass movement represents down slope movement of earth materials such as rock or soil. The terms “mass movement”, “slope movement”, and “slope failure” when used in a generic sense, are generally equivalent in meaning. Most specific studies in the Mediterranean region use the general term of “sliding” referring to all types of mass movements **(Table 1.1)**. This is because landslides are widespread and constitute the most frequent type of movement. They are considered as part of everyday vocabulary.

2.2. Classification of mass movements (MM)

Several classifications of mass movements exist (Coates, 1977; Varnes, 1984; Kehew, 1995; Cruden and Varnes, 1996). These classifications are based on forms of motion and mechanisms, but mass movements in reality involve a more complex combination of processes. Yatzut (1967) argued that too much complex a classification would be ineffective. Three principal types of movement are widely recognized in the Mediterranean region – slide, fall and flow, and are classified depending on several criteria: 1) type of movement, 2) type of material being displaced, 3) moisture content, 4) type of strain and failure and 5) rate of movement (**Figure 1.2, Table 1.1**).

Detailed and precise MM records in the whole Mediterranean region, however, are still lacking due to several limitations, such as the complexity of the Mediterranean terrains, the different levels of awareness and investigation of the impact of MM on the territory, and the limited resources available for inventory and maintenance. Nevertheless, in some specific locations, the information on historical and recent MM is available from bibliography and archives. As an example, a large database has been constructed in Italy showing 31,000 landslide events at 21,400 sites (equivalent to a density of 1 landslide per 15 km^2) (Guzzetti, 2000). This information was obtained from about 100,000 newspaper articles and 2,000 scientific and technical reports.

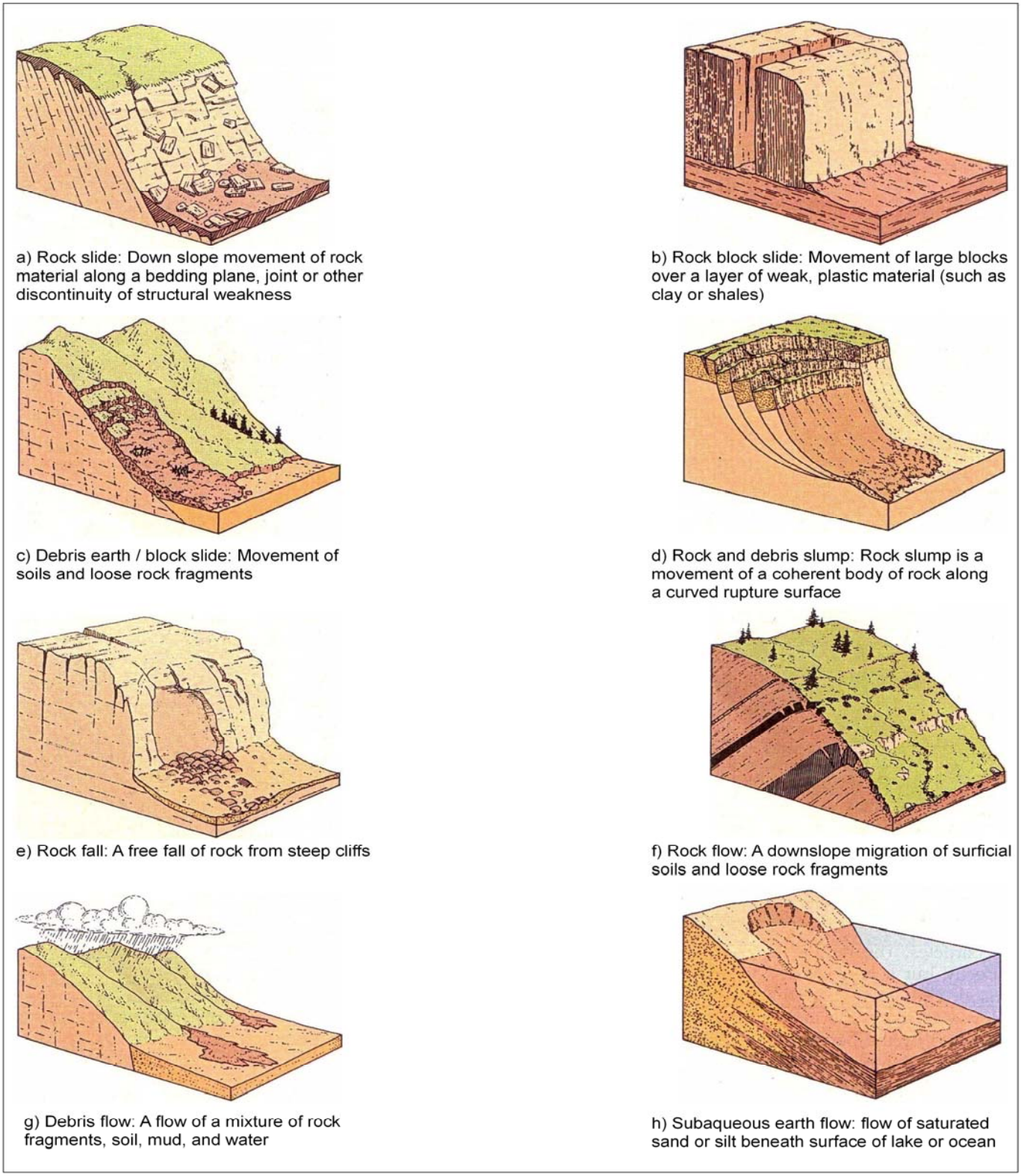

Figure 1.2. Diagram illustrating various types of mass movements (adapted from Hamblin, 1992).

Table 1.1. Classification of most common mass movements in the Mediterranean environments [adopted from Varnes (1978), Marshak (2001), and Gary and Aurora (2006)].

	Type of movement		Materials in motion	Moisture content	Nature of movement	Rate of movement
Slide	Translational	Rock slide	Unfractured rock mass	Low	Shallow slide approximately parallel to ground surface of coherent rock mass along single fracture	Very slow to extremely rapid
		Rock block slide	Fractured rock		Shallow slide approximately parallel to ground surface of fractured rock	Moderate
		Debris/earth slide	Rock or soil debris	Low to moderate	Shallow slide of deformed masses of soil	Very slow to rapid
		Debris/earth block slide			Shallow slide of largely undeformed masses of soil	Slow
	Rotational	Rock slump	Rock	Low	Rotational movement along concave failure plane	Extremely slow to moderate
		Debris/earth slump	Rock or soil debris	Moderate		Slow
Fall	Rock fall		Detached rock joint blocks	Low	Fall of individual blocks from vertical faces	Extremely rapid
	Debris/earth fall		Detached cohesive units of soil		Toppling of cohesive units of soil from near-vertical faces such as river banks	Very rapid
Flow	Rock flow		Rock (especially readily deformable types such as shales and clays)	Low	Slow plastic deformation of rock, or soil	Very slow to extremely slow
	Debris flow		Mixture of fine and coarse debris (20-80% of particles coarser than sand-size)	High	Flow usually focused into pre-existing drainage lines	Very rapid
	Earth flow	Slow	> 80% sand-size	Low	Confined elongated flow	Slow
		Rapid	Soil containing sensitive clays	Very high	Rapid collapse and lateral spreading of soil following disturbance, often by an initial slide	Very rapid

In addition, the exact distribution of each type of MM (slide, fall and flow) is often restricted to particular studied zones in a given country **(Table 1.2**). The MM density varies between 0.29 and 0.54 per km^2 according to the studied region. It is highest in the case of slides reaching 0.29 per km^2 in Southeast Spain.

2.2.1. Slides

The great majority of slides in the Mediterranean environments are small and shallow, with lengths of a few tens of meters and depths of 2-3 m. Slides in deeper bedrock are less common, but may attain enormous dimensions and involve the movement of millions of

cubic meters of material, such as those due to escape tectonics in Turkey or in the Alps (Chorowicz *et al.*, 1999; Dhont *et al.*, 2005).

Table 1.2. Type and quantity of mass movements (MM) occurring in selected regions of the Mediterranean area.

Studied region	Area (km^2)	Corresponding number of MM		
		Slides	Falls	Flows
Scisti dei Laghi-Southern Alps (Piccio, 1988)	227	42	22	3
Umbria region-Italy (Cardinali *et al.*, 2001)	8456	2243	1608	381
Rio Aguas-Southeast Spain (Griffiths *et al.*, 2002)	550	160	90	50

Very large slides usually break up to form debris avalanches, but in some cases the materials travel a significant distance as a coherent mass. This is most likely to occur where competent beds slide over incompetent strata (often clay or mudstone) dipping steeply roughly parallel to the natural slope.

Some slides took place during ancient times and are still continuing their activity until today. An example is the Fadalto landslide located in Italy, which goes back to the late glacial period, and includes a large scarp with debris accumulation that occupies a belt of about 280 m (Eisbacher and Clague, 1984; Pelligrini and Surian, 1996). Slides can be subdivided into translational slides, which have predominantly planar shear surfaces, and rotational slides in which the shear plane is concave-up (**Table 1.1, Figures 1.2a, b, c, d**). Translational movement is common in cliff forming units, particularly where there are interbedded competent and incompetent rocks. It is increased by the presence of marls, and invariably marly or argillaceous limestones. Rotational movement commonly occurs in relatively unconsolidated poorly cemented sandstones, weathered basalts and the surficial cover. The rotational movement may result in the upper part of the slumped mass being back-tilted towards the failure surface. The material may move as a single block due to the en-echelon nature of the joints or the intercalating weak surfaces. But usually it is broken into several discrete segments separated by transverse fissures. Micro-slides, due to their high frequency, finally result in more important denudation processes than large ones. The most common slide type in the Mediterranean environments is a composite type because the successive, different lithologies do not respond the same to a given set of triggering mechanisms (Khawlie and Hassanain, 1979; Piccio, 1988; Cardinali *et al.*, 2001; Griffiths *et al.*, 2002). In fact, the movement may start as translational along a joint parallel to the cliff face and either continues downward, thus becoming prone to rotational mode, or may induce rock/debris fall.

The slipped material deposits on the slope in either a hummocky or a lobate form depending on the water content. This type of slope movement creates a great deal of property damage. A good example is the landslide disaster which affected the city of Ancona, central Italy, in 1982 (Alexander, 1991).

2.2.2. Falls

Falls occur when masses of rock or other material detach from a steep slope or cliff and descend by free fall, rolling or bouncing. In the Mediterranean environments, falls are less frequent than slides and are restricted mostly to scarp-rock outcrops with vertical to very steeply dipping and dense joints (**Figure 1.2e**). Falls generally occur quite suddenly with very high velocities. Large rock falls originating from a considerable height above the ground spread their debris over an extensive area unless the dispersal of material is confined by topography. Anyway, they are a common threat in mountainous areas (Carere *et al.*, 2001; Fard, 2001; Bathurst *et al.*, 2003). The highest rockfall hazard exists when joints and bedding planes are inclined at a steep angle, as is the case in the highly folded sedimentary rocks that are common in alpine mountain belts.

2.2.3. Flows

Debris and viscous flows are less related to structural discontinuity (joints, bedding planes) (**Figure 1.2f, g, h**). High water content induces the material to move faster and farther from the source. A good example is a huge earth flow in Aaqoura area (Lebanon), where artificial lakes facilitate this flow (**Figure 1.3**). Although the course of debris flows is guided by channels, and to that extent is predictable, the speed and range of movement of these events mean that they tend to claim more lives than landslides.

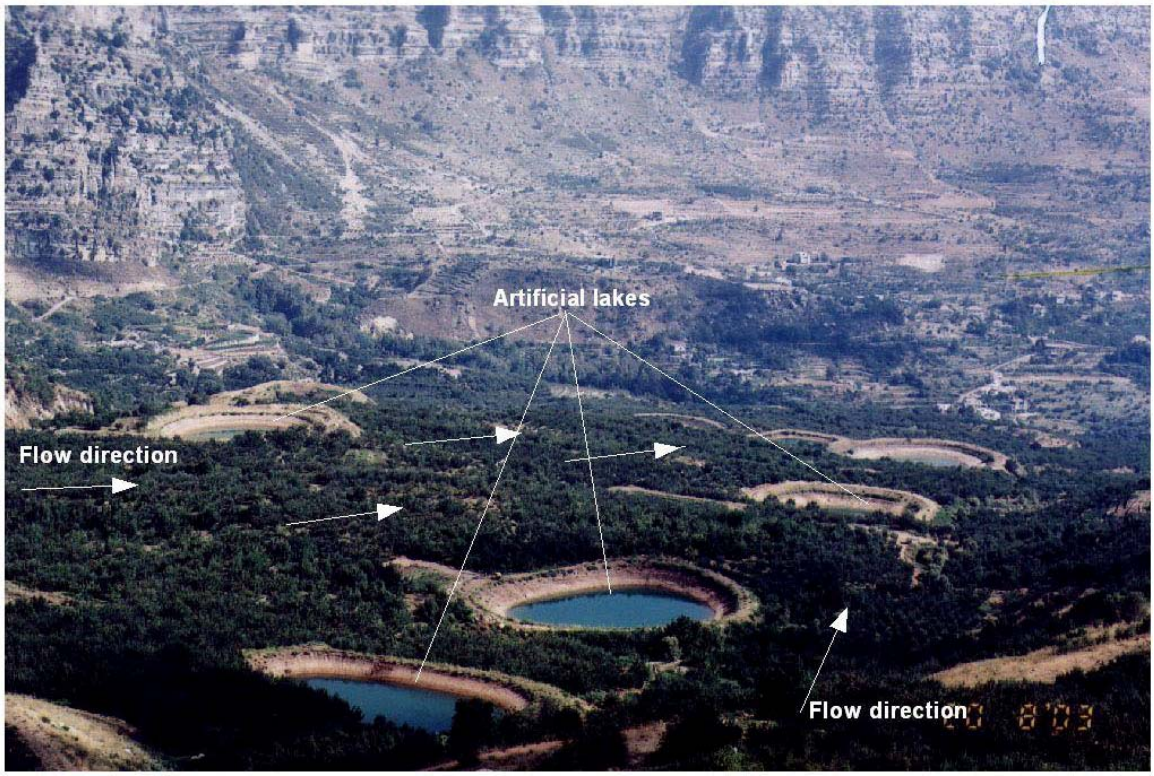

Figure 1.3. The huge earth flow of Aaqoura area (Lebanon) facilitated by artificial lakes.

2.3. Magnitudes of mass movements (MM)

There is no agreeing upon a precise definition yet for the term *"magnitude of MM"*. If one borrows the terminology, for instance, from the term magnitude used for earthquakes, it is the amount of energy released based on direct measurements of the size (amplitude) of seismic waves. The magnitude of MM, on the other hand, is generally referred to as the description of the amount of transported materials, the amount of destruction, and/or the number of losses in lives caused by such events.

Thereof, MM varies widely in magnitude; generally, public interest in MM is aroused only when there is a clear demonstration of imminent disasters. Such interest is directly proportional to whether money, property, or life will be taxed, lost or jeopardized. In the following, some examples of international events reflecting on their magnitudes are given **(Table 1.3)**. It is unfortunate that relevant similar data on Mediterranean region is still scarce and difficult to find.

In spring of 1983, Utah was revisited by a spate of MM and sustained direct damages from landslides, debris flow, mudflows and flooding costing millions of dollars, accompanying an El Niño event. Mass movements were so widespread and extensive that 22 out of 28 counties in the state were declared national disaster areas.

Additionally, the debris flow associated with the Verny earthquake (Kazakhstan) of June 1887 is believed to have involved 70 millions m^3 regolith (Yadav and Kulieshius, 1992). Seven other large mudflows, ranging between 0.5 and 50 millions m^3 occurred at Almaty (Kazakhstan) during the period 1921-1988. Since 1991, millions of m^3 of volcanic debris have been carried off the flanks of Mount Pinatubo (Philippine) by lahars (lahars refer to flow incorporating volcanic debris).

By 1996, lahar processes affected an area approaching 1,000 km^2 and the volume was estimated at 2 billion m^3, the magnitude and rates of affected lahar processes surprised many experienced researchers, but one reason might be the fact that intense rains from Typhoon Yanya began the eruption period itself. At about 8 pm in the evening of Sunday 9 April 2000, a huge landslide occurred in the Yi Gong district, Tibet, China. A gigantic volume of soil and rock slipped from the upper hillside. It traveled about 8 km and lasted about 10 minutes. The landslides were composed of snow, glacial ice, trees, soil and rock. It destroyed a 2.5 km long section of the highway connecting Qinghai province to Tibet, blocked the Yi Gong River at the toe of the slope, and resulted in flooding several villages. The estimated volume of this landslide was 300,000,000 m^3 and is thus considered one of the largest landslides recorded in the world (Zhou *et al.*, 2001).

3. Factors causing mass movements

The study of MM involves an understanding of the factors that affect their occurrence. They are difficult to assess with confidence. They can be divided into preconditioning and triggering factors. Some of them are quasi-static, while others are dynamic.

Mass movements often are triggered by other natural hazards, also of high frequency in the Mediterranean environments. For example, landsliding and flooding are closely related because both may occur due to heavy precipitation, runoff, and ground saturation. Debris flows usually occur in small, steep channels and are often mistaken for floods. Landslides and lateral spreads often result from seismic activity. Consequently, the simultaneous or sequential occurrence of different hazards may produce cumulative effects

that differ significantly from those expected from a single event. This is of crucial importance in defining factors related to the occurrence of a given type of mass movements.

Table 1.3. Magnitude of mass movements (MM) occurring in various countries.

Locality	Date	People deceased	Remarks
Brenno Valley, Switzerland	1512	600	Rockslide dammed valley; dam broke causing destruction
Mount Conto, Switzerland	1618	2,430	Rockslide
Lake Zug, Switzerland	1887	11	180 m long section of the shore collapsed destroying several houses and making 650 persons homeless
Trondheim, Norway	1893	111	Flow in marine clays due to liquefactions
Frank, Canada	1903	70	Rock avalanches destroyed most of the town
Kure, Japan	1945	1,154	Rocky mud flow
Vainto, Italy	1963	2,000	Rockslide into reservoir created wave that flooded below dam
Aberfan, Wales	1966	144	Man-made mining spoiled hill; landslide buried mostly children
Brazil	1966-67	2,700	Combined toll from debris avalanches and floods
Huascaran area, Peru	1970	21,000	Combined rock avalanche and debris flow buried two cities
St. Jean Vianney, Canada	1971	31	Slab flows buried people and houses
Faraya, Lebanon	1975	5	Landslide caused damage to the electrical and telephone network. Estimated financial loss 5 million dollars (M$)
Ancona, Italy	Dec 1982	269	Landslide caused damage to two hospitals, a university building, 2 highways, 280 private buildings, more than 3,000 people homeless and 269 deaths
Chaouen, Morocco	1983	27	Landsilde caused damage to the road network, infrastructure and houses
Several areas in Lebanon (Cedars, Broumana, Dahr El baidar, Bcharri, Ainata	1984	90	Landslides and snow avalanches caused damage to bridges, canals, roads houses, agricultural areas, 3000 cattle heads deceased. Estimated financial loss 68 M$
Hezerta, Lebanon	March 1992	20	A huge avalanche buried and destroyed several houses
Iceland	1995	34	Avalanches
Sarno, Italy	May 1998	153	Debris flow caused damages on the infrastructures and hundreds of people were homeless
Valle Caudina, Italy	1999	23	Several slides causing death, serious damages for the buildings and infrastructure in Cervinar town
Wulong County, China	May 2001	79	Landslide destroyed more than 100 houses in Chongqing city
Philippines	Dec 2003	200	Devastating mudslide

Sources - Close and McComick (1922), Zaruba and Mencl (1969), Blank (1971), Browing (1973), Nakona (1974), Schindler and Gyger (1988), Khawlie (1994), Fiorillo *et al.* (2001), Canutti *et al.* (2004), Glade (2004) & Wang *et al.* (2002).

3.1. Climate

The Mediterranean climate is characterized by episodic winter rainfall, and dry summers, with a distinctive regime of soil or rock moisture. Intense rains exhibit an erratic temporal and spatial distribution, and can be very localized, particularly in the driest parts of the Mediterranean (Alonso-Sarria and Lopez-Bermudez, 1994; Garcia-Ruiz *et al.*, 1996; Wainwright, 1996). Although very intense rains also occurred in historical times, there are indications that intense rainstorms have increased over the last 15 years due to the global climate changes (De Ploey *et al.*, 1991; Joftic *et al.*, 1992). For instance, the highest rainfall intensities have been recorded in mountainous areas (orographic effect) within about 100 km from coasts. They vary in 24 hours from 130 mm in Lebanon (Tayara, 1998), 298 mm in Greece (Groove, 1996), 400 mm in Italy (Giordano, 1986), 790 mm in Spain (Lopez-Bermudez and Romero-Diaz, 1993) and even exceptionally 1000 mm in France (Benech, 1994). Climate change and its impacts have been analyzed in Lebanon (MoE, 1999), reflecting a marked potential towards environmental and climatic effects. The impact on the precipitation regime (Safi, 1999) and on water (Khawlie, 2003) reveals a closer shift to semi-arid or arid conditions, which imply more flash floods.

These scarce showers can initiate mass movements through lubricating inherently weak zones of rock and soil, and assisting in removing support along the toe (bottom) of a slope, such as running water in stream acting on the base of its banks. In few particular cases, extreme rainfall events do not produce visible effects in the scarp due to the presence of karst, which absorbs a large part of the surface waters of the surrounding areas (Khawlie and Hassanain, 1984a; Pellegrini and Surian, 1996).

In the context of global environmental changes occurring in the Mediterranean environments, i.e. the effects of warmer climates, glaciated areas can be considered as potential or detrimental causes of large gravity phenomena (Bruckner, 1909; Panizza, 1973). These have been predisposed by the strain exerted by the glaciers along the structural discontinuity (joints, bedding planes) and by the alternate action of expansion and contraction, due to the increase and reduction of the glacial mass. The progressive thinning and the retreat of the glaciers can also be seen as a determining cause of the gravity phenomena.

3.2. Neotectonic movements

Mass movements also occur frequently in areas where minor and major morphotectonic events (uplift, subsidence, faulting, jointing and earthquakes) occur (recent or past), the latter being important throughout the Mediterranean basin (Piloni, 1607; Shorn, 1902; Almeida-Teixera *et al.*, 1991; Pelligrini and Surian, 1996; Aeillo *et al.*, 2004; Del Gaudio and Wasowski, 2004). Besides the immediate effects of failure of already precariously stable material, earthquakes may aggravate other situations of instability by decreasing the shear resistance of rocks. Some examples showing the strong relations between seismic events and mass movements were described in the historic literature. The major earthquake that hit Lebanon in 551 A.D. depicts the huge slides occurring at Chekka, and in fact was responsible for constructing its current coastal configuration (Khawlie, 1992). In 1927, a destructive earthquake affected the west bank of Jordan river triggering major landslides stopping the river flow for 21 days (Ambraseys and Barazangi, 1989). Mediterranean rocks include numerous discontinuities, which greatly influence material behavior, especially structural discontinuity (joints, bedding planes) which may release or

concentrate stresses. Volcanic eruptions play also a subordinate role in the triggering or activation of earth movements by comparison with anthropic and climate causes (Eisbacher and Clague, 1984).

3.3. Geology and soils

Mass movements are quite important where clayey rocks (clay-stones, marls, shales, muds, flysch) or morainic materials outcrop. The presence of these rock types in the Mediterranean region favors various types of mass movements, including landsliding (Demmak, 1984; Roose, 1994; Chebbani *et al.*, 1999). The clayey, shaly, or marly horizons are potential shear planes as they retain water. Once saturated, they behave like a liquid resulting in occurrence of rapidly moving mudflows. The soluble carbonate rocks also pose problems; they may include expanding clays which interact with and weaken the carbonate cement, hence weakening the rock itself.

Many soils in the Mediterranean exhibit a high susceptibility to mass movement because of their loamy to loamy-sand texture (Poesen, 1983). The high temperatures and the low rainfall amounts in the summer cause relatively low organic matter contents in these soils. Many of the Mediterranean soils are therefore very susceptible to movement (FAO, 1983; Ozden and Sonmez, 1998). Changing the type of vegetation covering a slope may increase soil moisture. Within a year, this higher soil moisture content may produce a 300% increase in visible landslide activity (Cruden and Varnes, 1996). Dispersive soils, cracking soils and rocky outcrops are some of the features which are influential in the production of overland flow in the Mediterranean. On the other hand, more than 60% of the land area in the Mediterranean consists of soils containing significant amounts of rock fragments in the top layer (Childs and Flint, 1990; Poesen and Lavee, 1994). These rock fragments should be considered as natural soil-surface stabilizers, which often favor infiltration and reduce runoff and soil movement by rain and runoff.

3.4. Topography

Steep slopes are common throughout the Mediterranean region, particularly in mountains. The steeper the slope, the more likely it is to fail and the easier it is to upset equilibrium. Most MM occur along slopes that are 20° or 25° and steeper (La Roca Cervignon and Calvo-Cases, 1988; Keefer, 1993; Cardinali *et al.*, 2002). In addition, slope aspect is strongly affected by the microclimate and vegetation cover, thus impacting soil development and mass movement intensity. Southern and western-exposed slopes are warmer, have higher evaporation rates and lower water storage capacity than northern and eastern exposed slopes in the Mediterranean environments. Runoff may also be affected by slope aspect depending on the direction of winds during rainfall. However, the north aspect, considered a high potential hazard for mass movement occurrence, can lose its effect in some cases once coupled with human activities (land use change and road construction). The southern aspect has thus the most effect on landslide occurrence (Sefidgari, 2002). Slope length is less important in MM mechanisms than its gradient and aspect in the Mediterranean environments (FAO, 1983; Roose, 1994), however, under similar precipitation, longer slopes accumulate a larger volume of water (Mutcher and Greer, 1980; Lal, 1982). Recent work has demonstrated that both form (curvature) and position represent first-order controls on landslide initiation (Montgomery and Dietrich, 1994; Dietrich *et al.*,

1995; Brunsden, 1999). High roughness slopes are more prone to landsliding because gradient changes favor rainfall infiltration into the soil.

River proximity to slopes is an important factor in enhancing the mass movement occurrence, although landslide susceptibility is greatest along the ridge, slides can occur along the banks of rivers and ditches (improved drainages).

3.5. Vegetation

Vegetation limits the movement of the debris present along slopes in two folds, i.e. hydrological (capacity of infiltration into the soils, soil moisture, groundwater level, etc.), and mechanical (root length). Where the vegetation cover is sparse, the slow movement inside the debris will not be ceased. Dry Mediterranean environments under natural conditions are biologically marginal, and they can be expected to be highly susceptible to mass movement (Roose *et al.*, 1993; Thornes, 1995; Garcia-Ruiz *et al.*, 1996).

3.6. Human activities

Land-use activities affect the intensity of mass movement significantly. Clearance of forest or erecting terraces for agriculture, tillage of the top soil, rock fragment removal from top soil, abandonment and regeneration of land, uncontrolled burning, and overgrazing are among the main human activities in Mediterranean landscapes. These activities are constantly reshaping the contours of the land (topography) and thus altering the natural slope. In some instances, they can be considered as the primary cause of mass movements. As an example, unregulated mining operations have turned stable terrain (limestone) into landslide-prone terrain. Residential development not only adds weight to the slope but may also lubricate fractures due to garden watering, and the seepage of water from swimming pools and sewage effluent systems. In addition, vibration of trucks, machinery, blasting, fluctuating groundwater level (well drilling and overpumping), and loss of root binding can constitute important transitory stresses that may lead to failure.

4. Definitions and clarifications of MM-related terms

Several works related to the mapping of mass movement hazard exist worldwide, but until 1984, the used terminology was diversified and confusing. Many terms were referring to the same types of MM maps, i.e. risk, danger, susceptibility, potential, density, etc. For example, in France, the term “risk” is used in the mapping of MM (Antoine and Pachoud, 1976; Godefroy and Humbert, 1983). It has the same meaning as hazard in several dictionaries (Oxford, Larousse, Petit Robert). Varnes (1984) clarifies the differences between the used terms through defining risk, hazard and vulnerability. These definitions are the most widely used during the last years (Einstein, 1988; Carrara *et al.*, 1992), and are given as follows.

4.1. MM hazard term

MM **Hazard (H)** (*aléa en français*) can be defined as the occurrence probability **(P)** of a dangerous event for a given duration and location (Varnes, 1984). The temporal component is accessible with difficulty; hence, hazard is mostly restricted to its spatial component. Practically, hazard is expressed for a return fictive period, non quantified, but

supposed to cover mainly the life duration of goods and infrastructures related to human activity. Fell (1994) pointed out some that confusion derives from the hazard assessment concept, and proposed that hazard is the product of magnitude **M** (or volume in m^3) and probability of occurrence of MM; in a broad sense, **H** will be derived using the following formula **H = M * P.** The introduction by Fell (1994) of the concept of probability **(P)** to avoid the use of hazard as meaning chance or probability, and reserve the term hazard (H) in its sense of danger (H = M * P), is very useful because it clarifies the term and avoids problems with the translations of the English terms ‘‘hazard’’ and ‘‘risk’’ into other languages**.**

In a given duration and return period, hazard probability (%) is not calculated, but its intensity is assessed as the importance of potential disorders. Hazard nature is relative to the type of mass movements (MM) in question. It describes the prevailing conditions among which MM are occurring. Spieker and Gori (2000, 2003a, b) would consider an “ideal MM hazard map” to have zonations showing not only the chances that a MM may form at a particular place, but also the chances that a MM from farther upslope may strike that place.

4.2. MM vulnerability term

Vulnerability (V) represents the potential of losses which can result from the occurrence of a mass movement, and distinguishes the human vulnerability (potential number of deaths, injuries, etc…), the socio-economic vulnerability (direct damages to infrastructures, perturbations of economical activity) and the vulnerability of public or functional interests (perturbation of some social functions – circulation, health, education, etc….). It can be expressed on a scale of 0 (no damage) to 1 (total loss). Morgan *et al.* (1992) and Fell (1994) introduce the vulnerability equation as follows:

$$\mathbf{V = V(S) + V(T) + V(L)}$$

Where

V(S) is the spatial vulnerability which means that an element will be affected by the landslide given that the landslide occurs, and therefore it represents the vulnerability derived from the spatial position of the element at risk.

V(T) is the temporal vulnerability which expresses a likelihood of temporal impact, taking into account temporal changes of the element at risk. A house, for instance, may or may not be occupied, depending on the time of impact.

V(L) is the life vulnerability which expresses the likelihood of loss of life of an individual occupant in the impacted element, or the proportion of the value of the impacted element which is lost.

Mejía-Navarro *et al.* (1994) defined the vulnerability in a different way by considering it as ‘‘the intrinsic predisposition of any element to be at risk of a mental or economic loss upon the occurrence of a hazardous event of **intensity i**’’. It included ecosystem sensitivity, economic vulnerability and social structure vulnerability. Prina *et al.* (2004) took account of four factors for defining the vulnerability – physical, social, environmental and economical. **Figure 1.4** shows the values of these factors (Leone *et al.*, 1996), each of them varying between 0 (no impact) and 100% (total destruction).

Subjective probability is an expression of the degree of belief in an event occurring based on a person’s experience, prejudices, optimism, etc. (Malczewski, 1999). Conditional probability is the knowledge about the likelihood of the hypothesis being true, given a piece of evidence (Favre *et al.*, 2000; De Araujo *et al.*, 2004). For example, one can not be certain

whether landslides always occur in areas of topographic convergence. The knowledge might be expressed as the user being 90% certain (i.e. probability = 0.9) that landslides will occur in areas of topographic convergence (Gorsevski *et al.*, 2003).

According to Leone *et al.* (1996) and Prina *et al.* (2004), as far as physical damage is concerned, it must be assessed in terms of structural failure, but also in terms of operational failure, for instance when the tilting of a house or a road exceeds an acceptable value, even though no cracks are reported. It also depends on the building material used and the maintenance of the structures. Social vulnerability can also be conditioned by the capacity of the population to anticipate the threatening phenomenon and its ability to prevent any excessive exposure (spontaneous evacuation, preventive measures carried out). Two main aspects of the environmental vulnerability depend on one hand on the presence of protective forest against rockfall which may induce major damage if they are affected by the movement of the slide and on the other hand on the possibility of damming a stream which may then induce flooding upstream and downstream, if the natural dam caused by the slide breaks. This last situation may also be called secondary vulnerability, and requires to be extended the investigated zone much further than the zone strictly exposed to the original landslide.

Bell and Glade (2004) considered the vulnerability of people, buildings and people in buildings, in terms of specific processes of given magnitudes. They assessed vulnerability with values from 0.1 for debris fall and rockfall affecting people up to a highest value of 0.5 for people and buildings under threat from debris flows and rockfall.

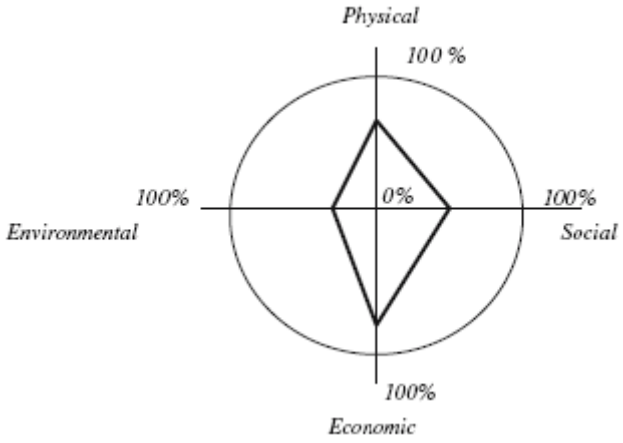

Figure 1.4. Projection of values of vulnerability factors (Leone *et al.*, 1996; Prina *et al.*, 2004).

4.3. MM risk term

The **specific risk (Rs)** is the product of the hazard (H) by vulnerability (V) according to Varnes (1984) and the product of the probability (P) by vulnerability (V) referring to Fell (1994). It shows the expected annual cost of MM damage throughout the affected area and combines the probability information from a MM hazard map with an analysis of all possible consequences (property damage, casualties and loss of service'' (Spieker and Gori 2000). **Elements at risk (E)** combine all the elements of the territory which are the

population, properties, economic activities, including public services, etc. The **total risk (Rt)** is the product of specific risk (Rs) times the element at risk (E) so **Rt = S (E · P · V).**

Mejía-Navarro *et al.* (1994) defines the risk as the probability that a loss affecting an **element ‘‘e’’** would occur as a consequence of an event of intensity equal to or greater than **‘‘i’’.** Risk was thus a function of geological hazard and vulnerability.

Fell and Hartford (1997) proposed a quantitative assessment of risk (R(DI)) to an individual, as the annual probability of loss of life, based on Morgan *et al.* (1992), and expressed by the equation:

$$\mathbf{R(DI) = P(H) \; X \; P(S/H) \; X \; P(T/S) \; X \; V(L/T)}$$

where P(H) is the annual probability of the landslide, P(S/H) is the probability of spatial impact or probability of the landslide impacting a building, P(T/S) is the probability of temporal impact or probability of the building being occupied and V(L/T) is the vulnerability of the individual (probability of loss of life of the individual given impact).

Xie and Xia (2004) proposed a systems theory for risk evaluation of landslide hazard reminiscent of Varnes’ (1984) concepts. They defined risk as ‘‘probability of landslide of different intensity and probable loss caused by landslide’’ and divided this into ‘‘pure risk’’, when there is only ‘‘loss without returns’’ and ‘‘speculative risk’’ when chances of loss and return stand side by side. As the returns of the landslide hazard are negligible compared with the loss, the landslide hazard risk is pure risk. In order to evaluate the risk of landslide hazard, the occurrence possibility and following loss need to be analysed. The assessment system of landslide hazard risk includes three elements: the hazard evaluation of landslide, the evaluation of vulnerability and the evaluation of loss caused by landslide.

Belle and Glade (2004) defined the landslide risk **(R)** as a function of the probability of the hazardous event or natural hazard **(H)** and its consequences **(C)** on the elements at risk **(E)**:

$$\mathbf{R = H \; x \; C \; x \; E}$$

with a new parameter of consequences (C) defined as the potential outcomes arising from the occurrence of a natural phenomena (including vulnerability and the probability of temporal and spatial impact, as well as the probability of seasonal occurrence):

$$\mathbf{C = Ps \; x \; Pt \; x \; Vp \; x \; Vpe \; x \; Pso}$$

where P is probability and refers to space **(s)** or time **(t)** values and V is vulnerability of buildings **(p)** and people **(pe)**, while **Pso** is the probability of seasonal occurrence, for instance snow avalanches only happen in winter. From these equations, the individual risk to people Ripe was derived from **Ripe = H x C x Eipe**, and the object risk to people in buildings Rpe was obtained from **Rpe = H x C x Epe**, with vulnerabilities referring to people and people in buildings, respectively.

Hollenstein (2005), based on natural hazards in Switzerland, proposed a simple definition of risk: **R = F x N**, where **F** is frequency of an event and **N** the damage. For natural hazards, he extended the risk definition to **R = P · I · E · V**, where **P** is the probability (reciprocal of the return period), **I** is the intensity, **E** is the exposure or spatio-temporal distribution of the target objects and **V** is the vulnerability.

4.4. MM mapping/zoning, susceptibility and assessment

The term **"mapping"** or **"zoning"** of a hazard designs the partition of a given territory into elementary surfaces, which are classified into degrees or hazard levels. Those can be indicated quantitatively or qualitatively (low, medium, high, etc.) and express the intensity of the hazard. Microzoning covers the same definition applied to studies with large scales (superior to 1:25,000). Different approaches to hazard-risk mapping or analysis are found in Baldelli *et al.* (1996), Chowdhury and Flentje (1996), Leroi (1996), Borga *et al.* (1997), Chung and Fabbri, (1999), Codebo *et al.* (2000), Parise (2001), Vaunat and Leroueil (2002), Zerger (2002), Babu and Mukesh (2003), Fernandez *et al.* (2003), Ferrier and Emdad Haque (2003), Remondo *et al.* (2003), Chau and Lo (2004), Rocha (2004), Spizzichino *et al.* (2004), Ayenew and Barbieri (2005).

The **sensitivity** or **susceptibility** of a MM hazard is a constant of proportionality between causes of MM and their effect. It measures the maximal local intensity possible for a conjunction of causes. The degree of sensitivity is known if the reaction is already produced (traces, proofs). In this case, there is certainty of danger and the magnitude can be derived. If traces are not shown, one should focus interest on causes and factors [state (permanent) factors and triggering (occasional) factors]; once existing, the reaction will be proportional to the combination of factors. The recurrence of triggering factors allows assessing the occurrence probability of hazard. While susceptibility maps provide zonations of areas with similar instability or similar conditions that generate landslides, a true landslide hazard map should offer a zonation of areas with similar probabilities of landslides in a given period of time, based on quantitative analysis of data.

Assessment of a hazard is to determine the importance or size, or amount of danger of MM, which may include the mapping, but also the set of procedures needed to understand the hazard.

5. Evaluation of mass movements' hazard

Evaluating the hazard of mass movements can be conducted at various scales, approaching it either as a detailed site study or a regional appraisal.

5.1. Individual sites

On-site hazard monitoring of mass movements is conducted in the Mediterranean countries mainly for engineering purposes. It is based on the deterministic limit equilibrium methods of soil mechanics to quantify the forces responsible for the mass movements, or to ascertain the existing forces acting on a slope or soil mass. These methods allow ensuring the stability of engineered embankments where the moisture content, material characteristics and slopes vary within narrow, defined limits. But the study of local site conditions and material properties is costly and time consuming. Also evaluating sites covers hazard for major well-known mass movements only, and neglect the minor ones that are more widespread. As an example, in Lebanon, the most common studied site at field scale is that of Hammana, where major mass movements occurred in 1860, 1914, 1948, 1954, 1956, 1960 and 1963 (Aker, 1980; Khawlie and Hassanain, 1984b). In addition, the complexity of formation and evolution hampers deterministic modeling of MM. For that,

the simple graphical correlation between consistence and moisture profiles can be used as a basis for designing rhexistatic models.

5.2. Regional appraisal modeling

Recently, an increasing trend towards the use of regional appraisal modeling in the Mediterranean environments is noted. This is due to the recognition and importance of accounting for spatial heterogeneity, newly developed tools and technology, especially Geographic Information System (GIS), remotely sensed (RS) imagery, and digital terrain analysis, which make it possible to consider small-scale heterogeneity in these environments, and analyze a variety of spatial and non spatial data about the causative factors responsible for the MM activity in a region.

Regional appraisals typically range from simply allocating the mass movements to the more complex zonation of MM hazard based on causative interacting factors. This zonation leads to the mapping of areas with an equal probability of occurrence within a specified period of time. In some cases, these appraisals deal with mass movement potential for specific types of projects. Such maps are called Landslide Hazard Zonation (LHZ) or Landslide Susceptibility Zonation (LSZ) maps.

6. Zonation of mass movements (MM)

6.1. Methods of MM hazard/susceptibility zonation

A number of methodologies for landslide hazard/susceptibility zonation over large areas are proposed which are belonging to qualitative, semi-quantitative and quantitative GIS-assisted approaches. Each of these approaches has its value for certain applications and disadvantages for other objectives, given the specific conditions of the Mediterranean environments. In this context, the GIS technology has been applied to examine landslide hazard in several Mediterranean countries, such as Jordan (Al-Homoud and Masanat, 1998; Husein *et al.*, 2000); northern Spain (Duarte and Marquinez, 2000); Tuscany, Italy (Luzi *et al.*, 2000), central Italy (Carrara *et al.*, 1991), Southern Italy (Budetta *et al.*, 1994; Refice and Capolongo, 2002), and Fabriano, Italy (Luzi and Pergalani, 1996). Despite the methodological and technical differences, most proposed methods consider that geological and geomorphological conditions of future MM should be similar to those conditions that led to past and present slope instability. Therefore, mapping past and recent slope movements, together with the identification and mapping of the inducing or preparatory factors of slope instability, are the keys in predicting future landslides (Carrara *et al.*, 1999).

Very few methods tackle rockfalls on a regional scale. Studies of rockfalls are often based on field surveys, and hazard is estimated either by an empirical assessment of the susceptibility to failure, or by the calculation of a safety factor derived from models of rock mechanics (Carere *et al.*, 2001; Crosta *et al.*, 2001). Several methods for the evaluating landslide hazard can be distinguished.

6.1.1. Qualitative methods

Qualitative MM susceptibility maps have been made in different countries of the world, depending on expert opinions (Radbruch, 1970; Scott, 1972; Davies, 1974; Pomeroy, 1974; Meneroud and Calvino, 1976; Antoine, 1977; Humbert, 1977; Hinojosa and Leon, 1978;

Kienholtz, 1978; Mahr and Malgot, 1978; Méneroud, 1978; Rodrìguez Ortiz *et al.*, 1978; Landry, 1979; Aniya, 1985; Atkinson and Massari, 1998; Irigaray *et al.*, 1996; Agili *et al.*, 2004; Amaral and Furtado, 2004; Coe *et al.*, 2004).

a. Distribution analysis

This is the simplest of all methods, the distribution analysis only depicts direct mapping of MM locations from field observations and use of remote sensing data, and thus do not provide information on predictive behavior of future MM activity. This inventory of existing MM commonly forms the basis for hazard zonation. The MM distribution can be mapped based on field observations that provide only point-based information, but they are costly and time-consuming. Moreover, they do not secure information on areas with difficult access, especially the rugged mountainous karstic landscapes frequently present in the Mediterranean region. Remotely sensed data are shown to be of considerable potential use for MM investigations using two distinct approaches. The first approach is to determine the number, distribution, type, and character of MM. The second approach complements the first one by measuring MM dimensions (e.g., length, width, thickness, local slope). In addition, remotely sensed data can provide terrain information pertaining to mass movements (physiography, geomorphology, geological structures, land cover/use, etc.)

a.1. Aerial photographs (stereoscopic and stereo-oblique)

Until recently, remote sensing technologies, relying upon the interpretation of aerial photographs, were applied widely for regional MM investigations (McDonald and Grubbs, 1975). These photographs are obtained from aircrafts, with sufficient overlap between successive ones enabling stereoscopic pairs to be produced. The conventional stereopairs, even those of black and white mode, are still convenient for the identification of MM due to their high spatial resolution, but are costly and also time consuming. Using parallax equations, measurements of the heights of MM surface structures can be made from stereo aerial photographs providing information on flow emplacement parameters (such as emplacement rate, and velocity).

Stereo Oblique Aerial Photography (SOAP) consists of acquiring photographs from a low flying helicopter with the doors removed to facilitate a clear uninterrupted view of the slopes. When compared to a walk-over field surveys, this technique provides a relatively rapid, cost-effective means of assessing large areas of ground, which may be otherwise with inaccessible, dangerous and high slopes.

a.2. Optical satellite imagery

Optical (visible, infrared) space remote sensing (RS) offers promising possibilities for identification and monitoring of mass movements, but their effective use in mountainous areas of the Mediterranean environments is hampered by cloud cover. Satellite imagery has been used in the analysis of MM occurrence primarily through the analysis of color composites (Sauchyn and Trench, 1978; Greenbaum *et al.*, 1996). But, the primary restriction in most cases has proven to be the low spatial resolution preventing the extraction of small MM. Mixed success can be achieved with the use of more complex analyses techniques such as linear spectral un-mixing (*principal component analysis*) helping removing spectral confusion caused by the presence of contracting surface features

in single pixels (Girard and Girard, 2003), digital image processing (minimum distance classification, parallelepiped or Bayesian classifier) (Health and Dowling, 1980; Stephens, 1988), and/or integration of multi-source data (merging or fusion) (Huang and Chen, 1991).

However, operational remote sensors with high spatial [e.g., IKONOS (1 m), Quickbird (0.67 m), etc.] and spectral [e.g., TERRA-ASTER (with 6 channels in the SWIR and 5 channels in the TIR), AVIRIS data (224 spectral bands), etc.] resolutions can improve MM investigations (Mulders, 2001). The high spatial resolution enables detecting very small MM and the high spectral one allows mapping of geological units in areas of poor exposure and the estimation of soil thickness prone to landsliding.

a.3. Microwave (Synthetic Aperture Radar Interferometry, InSAR)

Radar imageries, at different wavelengths and polarisation, can be obtained from both satellites and aircrafts. Radar data can be acquired either night or day and effectively "sees" through clouds. Currently available SAR (synthetic aperture radar) data including ERS (25 m spatial resolution), RADARSAT with 10-15 m spatial resolution and stereo capability, JERS (18 m) and others have proved efficient for mass movement evaluation in gentle sloping areas (Chorowicz *et al.*, 1998). The analysis of the SAR time series with the permanent scatterer technique (Ferretti *et al.*, 2000, 2001; Kimura and Yamaguchi, 2000; Rizzo and Tesauro, 2000; Refice *et al.*, 2001; Colesanti *et al.*, 2003, Schiavon *et al.*, 2003; Singhroy and Molch, 2004) enables the detection of very small movements. With the advent of repeat-pass interferometry, it has become possible to detect subtle changes (at mm scales) in the landscape such as seismic displacement (Singhroy, 1995; Massonnet *et al.*, 1996) and monitoring of large structures, i.e. hydrological sites at risk (Pieraccini *et al.*, 2001; Leva *et al.*, 2003).

Differential synthetic aperture radar (SAR) interferometry from spaceborne platforms has been shown capable of measuring landslide displacement fields of centimetric order over relatively large areas (Fruneau *et al.*, 1996; Massonnet and Feigl, 1998; Rott *et al.*, 1999; Vietmeier *et al.*, 2000). Nevertheless, its application is restricted in the rugged mountainous Mediterranean areas (Buchroithner, 1995; Fruneau *et al.*, 1996) because it can experience ground deformations in excess of the phase gradient limit (Carnec *et al.*, 1996), which eliminate interferometric correlation (Massonnet and Feigl, 1998; Luzi *et al.*, 2005). Attempts are being made to better integrate radar interferograms, field measurements, and ancillary remote sensing of MM to obtain calibrated interferograms which will provide useful geologic and geophysical information to the MM monitoring community (Bulmer and Wilson, 1999; Catani *et al.*, 2005). However, even such improved technologies are rarely utilized to their full potential in hazard assessment.

a.4. Airborne thermal and lidar data

Airborne multispectral thermal data seem useful also for mapping landslides in coal measures, particularly if they are underlain by abandoned mine workings, or entrapped moisture due to groundwater springs (Donnelly and McCann, 2000). Airborne laser scanners enable elevation models to be derived for the ground surface and identify changes in topography such as subsidence and precursory ground movements as slopes (Gordon *et al.*, 2003). They can be used to measure features of landslides such as ridge wavelengths and amplitudes, thickness variations in debris as well as local, regional and underlying slope.

a.5. Multispectral video and hyperspectral scanners

Multispectral video cameras operate at the visible to near infrared portion of the spectrum and can be mounted on low-flying aircraft. They generate pixels of less than 1 m, and therefore suitable for mapping of landslide groundwater systems (Hansen, 1984). Airborne hyperspectral scanners are much more complicated and expensive instruments that the multispectral video and can be conveniently mounted onto a helicopter or fixed wings aircraft. They are able to record complete reflectance spectrum from blue wavelengths (450 nm), through the visible and near-infrared regions, to the short-wave infrared (2500 nm). Therefore, the system is able to resolve individual vegetation or mineral species which may be particularly useful for the identification of stream deposits which emerge from the toe of landslides, and for the mapping of lithological units (Gibson *et al.*, 2000; Ramlin *et al.*, 2000).

b. Heuristic methods

Heuristic or predictive GIS models (parameter models) are based on rules and expert knowledge (Gupta *et al.*, 1999; Meisina *et al.*, 2001; Saha *et al.*, 2002). They are considered as direct or semi-direct methods in which the geomorphological maps are renumbered to hazard/susceptibility maps, or built on the results of exploratory subjective analysis, which identifies cause-effect relationships from the spatial coincidence between observed erosion features and landscape factors. Such models lack deterministic capability, because they neither simulate nor explain the mechanisms involved in mass movement. They are not able to take into consideration, for the purpose of prediction, the role played by the activating factors. This lack must be overcast especially when in instances certain triggering factors like earthquakes are the main causes of MM occurrence in the Mediterranean environments. However, the scarcity of seismic and rainfall intensities records in many Mediterranean countries can be one of the principal problems towards the integration of earthquake and rainfall activity in the GIS predictive models.

6.1.2. Semi-quantitative methods

Also, semi-qualitative susceptibility, hazard or slope instability maps based firstly on analysis of slope angles, lithology and relative amounts of landslip material have been published (Blanc and Cleveland, 1968; Bowman, 1972; Radbruch and Crowther, 1973; Nilsen and Brabb, 1977; Nilsen and Wrigth, 1979). But according to Varnes (1978), these maps are considered closer to MM inventories than to MM hazard maps. In addition, the use of the term ‘‘susceptible’’ to indicate the degree of instability relates these maps to susceptibility maps in the sense developed by Brabb *et al.* (1972). The latter introduced a semi-quantitative method consisting of a bivariate analysis of MM area percentages in slope angle intervals, expressed by relative susceptibility numbers, from which a susceptibility zonation was obtained. The susceptibility classes were I (0–1%), II (2–8%), III (9–25%); IV (26–42%); V (43–53%) and VI (54–70%) and L (landslide deposits, 100%). The logical analytical method proposed by Bughi *et al.* (1996) is a variation of the qualitative methods, where the field survey data on slope deformation helps to decide the numerical weights. Remote sensing and GIS techniques may be utilized here for thematic map preparation and overlay analysis. Another approach to mapping landslides involves landslide density or isopleth maps. The landslide isopleth or density contour technique was adopted to

generalise and quantify the areal distribution of landslide deposits in a form that would combine more easily with other data when preparing derived maps (Schmidt and MacCannel, 1955; Varnes, 1978).

6.1.3. Quantitative methods

To remove subjectivity in qualitative analysis, various quantitative methods have been employed for MM hazard/susceptibility zonation. These methods can broadly be classified into six types: factor overlay, statistical methods, physically-based indexes, distribution-free methods, geotechnical/deterministic methods and landslide frequency analysis.

a. Factor overlay

The simple overlay of a MM distribution on maps representing geo-environmental factors, i.e. lithology, soils, proximity to fault line, rainfall intensity, slope gradient, slope curvature, etc. highlights the degree of spatial coincidence between MM occurrence and specific factors. By sequentially overlaying all the layers, homogeneous domains are singled out whose number, size and nature are strictly dependent on the criteria used in classifying the input factors. This overlay is particularly suited to raster GIS where factors are mapped either as discrete or continuous data. Owing to the matrix format of the data, computer processing and manipulation is fast and algorithmically simple. But since grid-cell limits do not bear any relation to the geological, geomorphological or other environmental boundaries, many investigators argued that the approach was relatively inaccurate and aesthetically unacceptable (Seshgiri *et al.*, 1982; Choubey and Litoria, 1990; Pachauri and Pant, 1992; Dikau *et al.*, 1996; Carrara *et al.*, 1999; Guzzetti *et al.*, 1999).

b. Statistical techniques

Mass movement hazard zonation can also be done using statistical computerized approaches, determining the weight of different classes of each causative factor, under a GIS environment. They analyze MM factors in order to obtain what is called MM-prone areas, but they are lacking temporal forecasting. Among these, the most commonly used are: 1) Information Value (InfoVal) method (Yin and Yan, 1988; van Westen, 1997); 2) Landslide Nominal Risk Factor (LNRF) method (Gupta and Joshi, 1989); 3) valuing area accumulation method (Carrara and Guzzetti, 1995; Kelarestaghi, 2003); 4) statistical index method (van Westen, 2000; Rautela and Lakhera, 2000); 5) analytical Hierarchy Process (AHP) (Saaty, 1980; Barredol *et al.*, 2000); 6) Weighted linear combination (WLC) (Lee *et al.*, 2002; Ayalew *et al.*, 2004); 7) multiple regression method (Chung *et al.*, 1995; Ercanoglu *et al.*, 2004); 8) logistic regression method (Mark and Ellen, 1995; Wieczorek *et al.*, 1996; Atkinson and Massari, 1998; Guzzetti *et al.*, 1999; Gorsevski *et al.*, 2000; Lee and Min, 2001; Ohlmacher and Davis, 2003; Lee, 2004); 9) discriminant analysis (Simons *et al.*, 1978; Carrara, 1983; Baeza and Corominas, 2001; Carrara *et al.*, 1991, 1995, 2003); 10) contingency-table analysis (Santacana *et al.*, 2003); and 11) frequency ratio method (Lee and Talib, 2005). It should be noted that the corresponding formulae of these methods are not the same (natural algorithm, difference, mean, etc.); they all relate one or more predictor variables to some measure of MM occurrence **(Table 1.4).**

The first two methods (Information Value and Landslide Nominal Risk Factor) are bivariate statistical analyses used to prepare landslide susceptibility maps. They consider

each individual thematic map in terms of landslide distribution and can be easily implemented in GIS. Valuing area accumulation method and statistical index (Wi) method simply define the weight value of factors through considering the MM density in each class factor divided by the MM density in the entire map. In the AHP method, the weighting of selected parameters is done in a logical way where the parameters could be arranged with their priorities. It is based on three principles: decomposition, comparative judgment and synthesis of priorities (Malczewski, 1999). Also valuing of classes is very easy, that could repeat its stages several times until it gives a better result. WLC is a concept to combine maps of MM-controlling parameters by applying a standardized score (primary-level weight) to each class of a certain parameter and a factor weight (secondary-level weight) to the parameters themselves. To use multiple regression, MM occurrence must be expressed as a continuous variable. But because regression estimates are unconstrained, they may be negative or greater than 100% and, hence, can not be directly interpreted as probabilities. General logistic regression, one of a family of generalized linear models, seems to be interesting in mapping MM susceptibility because it can use categorized predictor variables (Jager and Wieczorek, 1994), continuous variables, and mixtures of the two (Bernknopf *et al.*, 1988; Gorsevski *et al.*, 2000). Using discriminant analysis, observations are classified into two mutually exclusive groups: they are a location or area where a MM (1) has occurred or (2) has not occurred. Each vector consists of a vector of independent variables. The differences between the MM group and the non-MM group are expressed by coefficients that project every observation onto a line connecting the centroids of the two groups; an observation is classed as a MM if its score is close to the MM centroid than to the non-MM centroid. Unfortunately, no way exists to express discriminant scores as probabilities of occurrence of MM, except by categorizing the scores and computing proportions of misclassifications. In effect, discriminant analysis simply converts a multivariate problem into a univariate contingency-table analysis. This latter is the simplest prediction method in which a cross-tabulation is made between two outcome states (MM and non-MM) versus the discrete categories of a predictor variable. The frequency ratio method is the ratio of the area where MM occurred in the total study area, and also, is the ratio of the probabilities of a MM occurrence to a non-occurrence for a given attribute.

The probabilistic prediction models (Chung *et al.*, 1995) provide quantitative estimates of future landslide activity based on prediction from past events. The “weight of evidence” approach is also a kind of bivariate analysis utilizing Bayesian probability model (Lee *et al.*, 2002; Cevik and Topal, 2003). The weighting factor values may be selected either arbitrarily, mainly on the basis of expert opinion (Anbalagan, 1992; Turrini and Visintainer, 1998) or through some intermediate processes (Dai *et al.*, 2000; Lee and Min, 2001).

Another method of mass movement modeling is source and pathway characterization. In this method, the source of the potentially hazardous process is generated at random, either throughout the model, or within different components of the terrain weighted items based on past occurrence. The distributive path of the phenomenon is calculated by mathematical modeling of the process. This is based on deterministic models in which an appropriate mathematical simulation of the process is used. Except for simple equations, this simulation is best performed outside the GIS or in a closely linked system where the

Table 1.4. Statistical techniques commonly used worldwide for MM hazard/susceptibility zonation.

Statistical method	Formula	Terms defined
Information Value (InfoVal) method or Statistical index method	$Wi = \ln\left(\frac{Densclass}{Densmap}\right) = \ln \frac{Npix(Si)/Npix(Ni)}{\sum_{i=1}^{n} Npix(Si) / \sum_{i=1}^{n} Npix(Ni)}$	***Wi:*** is the weight given in the ith class of particular thematic layer ***Denclass:*** is the landslide density within the thematic class ***Densmap:*** is the landslide density within the entire thematic layer ***Npix(Si):*** is the number of landslide pixel in a certain thematic class ***Npix(Ni:)*** is the total number of landslide pixel in a certain thematic class ***n:*** is the number of classes in a thematic map
Landslide Nominal Risk Factor (LNRF)	$LNRF_i = \frac{Npix(Si)}{\left(\sum_{i=1}^{n} Npix(Si)\right)/n}$	***Npix(Si):*** is the number of landslide pixels containing landslides in i^{th} thematic class **n:** is the number of classes present in the particular thematic map
Valuing area accumulation method	$Wa = 1000\left(\frac{A}{B}\right) - 1000\left(\frac{C}{D}\right)$	***A:*** the number of landslides in each class of factor ***B:*** The area of each class factor ***C:*** the total number of landslide in the study area ***D:*** The total area that is studied
Analytical Hierarchy Process (AHP)	$M = w_1X_1 + w_2X_2 + w_3X_3 + w_4X_4 + w_5X_5 \ldots\ldots\ldots + w_nX_n$	***M:*** susceptibility coefficient ***X1….Xn:*** are MM influencing factors ***W1….Wn:*** are weights of these factors
Weighted linear combination (WLC)	$P\{D\} = N\{D\}/N\{T\}$	For a given, number of a unit cell, **N{D},** containing an occurrence, **D** **T:** total area
Multiple regression method	$P(Yi = 1) = [1 + \exp(\boldsymbol{X_i b})]^{-1}$ $\boldsymbol{X_i b} = \log\left[\frac{P(Yi=1)}{P(Yi=0)}\right]$	$\boldsymbol{Y_i}$ is the state of cell i $\mathbf{X_i}$ is a vector of coefficients to be estimated **b** is a vector of coefficients to be estimated
Logistic regression method	$Y = Logit(p) = \ln(p/(1-p)) = C_0 + C_1X_1 + C_2X_2 + \ldots + C_nX_n$	***p*** is the probability that dependent variable ***(Y)*** is 1, ***P/(1-p)*** is the so-called odds or likelihood ratio, C_0 is the intercept, and $\boldsymbol{C_1, C_2, \ldots C_n}$ are coefficients, which measure the contribution of independent factors $\boldsymbol{(X_1, X_2 \ldots\ldots X_n)}$
Frequency ratio method	$LSI = \sum Fr$	***Fr:*** rating of each factor or range

GIS functions as a spatial database, pre-processor of parameters (e.g., overlay and quantification of map layers) and as a post-processor for visualization of the simulated outcomes (Brimicombe and Bartlett, 1993).

c. Physically-based indexes

Distributed, physically based slope stability indexes are also proposed for shallow landsliding. Lan *et al.* (2004) mapped MM hazard using a certainty factor model (CFM), with a positive CF value means an increasing probability of MM occurrence, while a 0 value indicates difficulty of assessing MM occurrence with any certainty. This model is a probability index function originally developed by Shortliffe and Buchanan (1975) and modified by Heckerman (1986), and introduced in GIS MM research by various authors (Chung and Fabbri, 1993, 1998; Binaghi *et al.*, 1998; Luzi and Pergalani, 1999).

Spatial prediction, performed using SINMAP (Stability Index MAPping) after Pack *et al.* (1998), was based on limit equilibrium failure analysis using an infinite slope stability model and a steady-state hydrological model (TOPMODEL) as described by Beven and Kirkby (1979) and Connell *et al.* (2001).The stability index (SI) was defined as probability of slope stability [SI = Prob(Fs>1)] over the distribution of uncertain parameters (cohesion C, friction angle, effective rainfall q, and soil transmissivity T). The stability index was employed to define six hazard classes from high stability (SI > 1.5) to low stability (SI=0). The parameters were obtained from a DEM and geotechnical field investigations.

The quasi-dynamic wetness index is another example, defined by a simple algebraic expression of the coupled subsurface flow and slope stability model for a better understanding of the relationships between topography and rainfall variability (Gritzner *et al.*, 2001; Borga *et al.*, 2002; Bou Kheir *et al.*, 2007a). Its influence on shallow landsliding offered significant improvements over steady-state models.

d. Distribution-free methods

During the last 7 years, distribution-free methods such as neural network (Lee *et al.*, 2003, 2004a, b; Arora *et al.*, 2004) and neuro-fuzzy-analysis (Elias and Bandis, 2000; Ercanoglu and Gokceoglu, 2002) have been also implemented for MM hazard zonation. These methods do not depend on distribution assumptions of the data. Here, the weights are computed in an objective manner.

e. Geotechnical/deterministic methods

Geotechnical/deterministic approaches are based on slope stability analyses which rate soil and rock mechanics parameters such as cohesion, friction angle or rock massif discontinuities (Vecchia, 1978; Okimura and Kawatani, 1986; Miles *et al.*, 2000; Romeo, 2000; Zhou *et al.*, 2001; Refice and Capolongo, 2002; Carro *et al.*, 2003; Shou and Wang, 2003; Moon and Blackstock, 2004). Some of these investigation and interpretation methods include the use of survey markers, extensometers, inclinometers. These methods have allowed substantial improvements in the understanding MM patterns. A significant limitation of these approaches is the need of material data (mechanical properties, water saturation, etc.) that are difficult to obtain over large areas (Terlian *et al.*, 2005). They are applicable only when the ground conditions are fairly uniform across the study area, and the mass movement types are relatively easy to analyze (Terlian *et al.*, 1995; Petley *et al*, 2005). The advantage of the

geotechnical models is that they permit quantitative factors of safety to be calculated, while the main problem is the high degree of simplification that is necessary for the use of such approaches.

f. Frequency analysis

In addition to the previous methods, landslide frequency analysis methods have also been reported for site specific studies on landslides. These are indirect methods in which earthquakes and/or rainfall records or hydrological models are used for correlation with known landslide dates to obtain threshold values with a certain frequency (Capecchi and Forcardi, 1988; Jibson *et al.*, 1998).

The final result of zonation process is the production of MM hazard zonation maps. The spectrum of MM hazard zonation maps produced in the Mediterranean region through modeling can be characterized by several criteria.

6.2. MM risk assessment and mapping

Widespread interest in landslide risk assessment and mapping is reflected in a number of excellent reviews and general papers published during the last 20 years (Brabb, 1984; Einstein, 1988; Chacon *et al.*, 1996; Chowdhury, 1996; Leone *et al.*, 1996; Leroi, 1996, 1997; Fell and Hartford, 1997; Highland, 1997; Baynes and Lee, 1998; Leroueil and Locat, 1998; Guzzetti, 2000; Dai *et al.*, 2002; Sorriso-Valvo, 2002; Spiker and Gori, 2003a; Castelli *et al.*, 2004; van Westen, 2004).

Several methods of risk assessment are available in the literature. An early attempt was a quantitative land-capability analysis by Laird *et al.* (1979) with examples from the San Francisco Bay region, California. The aim was to make earth science information more useful to planners by making it easier to incorporate into the planning process. This measured the ability of land to support different types of development with a given level of geological and hydrological costs. Total social costs (level 1) were chosen to rank the relative importance of various geological and hydrological conditions. The land costs (level 2) and all the expenses derived from the correction or control of the different natural hazards (level 3) affecting the lot including hazards, constraints and resources (in US dollars) were totalled. The study cost was assessed from the contribution of geotechnical investigations, engineering and construction practices necessary to prevent damage from slope failure. Thirteen geotechnical firms were interviewed and the building cost and cost of mitigation measures estimated. The final formula to estimate landslide costs was as follows:

Cost in dollar/acre = (costs of levels 1; 2 and 3 of investigation per acre) + (cost of special engineering measures in dollar per acre)

Probabilistic methods were also developed by Carrara *et al.* (1992) and Rezig *et al.* (1996). Chowdhury and Flentje (2003) approached slope reliability analysis to landslide risk, and Remondo *et al.* (2004) assessed landslide hazard and risk mapping on the basis of past damage using historical data. Also Bernknopf *et al.* (1988) derived an economic evaluation from a probabilistic landslide hazard map in Cincinnati (Ohio, USA).

6.3. MM hazard/susceptibility zonation maps

6.3.1. Hazard zonation map types

At present, most of the existing mass movement hazard zonation maps at regional scale in the Mediterranean countries are rated qualitatively, with subjective ordinal categories of probability (high, moderate or low). However, an ability to assess quantitatively the probability of mass movement hazard at each site would be of considerable significance for implementing mitigation processes. But it is difficult to represent mass movement hazard in quantitative terms related to probability over large areas. This is because mass movements do not have a clear magnitude/frequency relation, as is the case for floods or earthquakes. However, slope maps can be a helpful tool for estimating the probable areas where a mass movement might occur.

Most inventory maps determine the number and geographic distribution of MM, without differentiating their types. Most of them are dedicated to landslide hazard, without being able to produce maps related to rock falls. Small-scale maps show only MM locations, whereas large-scale maps may distinguish MM sources from deposits, classify different kinds of MM and show other pertinent data (Spieker and Gori, 2000; 2003a, b). In addition, very few maps complement the information about distribution by measuring dimensions, i.e. length, width, thickness, sediment delivery to streams, etc., and determining the approximate age of MM and the approximate stand age at time of failure. This approach would allow deriving quantitative parameters on mass movements that are necessary for an improved understanding of landslide processes, including the computation of landslide rates (number/area/time) or material transfer rates (volume/area/time).

Hazard maps are often produced in the Mediterranean environments without a vulnerability analysis. This is not useful for effective decision making because a small hazard in a densely populated area or strategic location may cause a disaster many times greater than a larger hazard in a sparsely populated area. In addition, losses resulting from the occurrence of a mass movement can be confused with those produced by other natural hazards.

6.3.2. Spatial scale

Current mass movement inventory and hazard maps are not standardized around the Mediterranean environments. They are published at different scales with various levels of details. Mass movements are often local scale features, even though they can occur in great numbers over a wide area (especially when triggered by a large earthquake or very intense rain). This and the limited areal extent of many damaging mass movements with significant socio-economic effects (often as little as few tens of square meters or less), imply that satellite observation and monitoring will require much greater spatial and vertical resolution with respect to that used in the study of other natural disasters such as floods, earthquakes and volcanic eruptions. For the evaluation of the suitability of RS images for landslide inventory mapping, the size of individual slope failures in relation to the ground resolution cell is of crucial importance. Although sizes of landslides vary enormously according to their types, some useful information can be found in the literature. It is believed that 1:25,000 should be considered as the smallest scale to analyze slope instability phenomena on aerial photographs (Carrara *et al.*, 1995).

However, the working scale must be determined by the requirements of the users for whom the survey is executed. Regional scales (1:100,000-1:500,000) can be used in the early phases of regional development projects to evaluate possible constraints, due to instability, in the development of large engineering projects and regional development plans. Medium

scales (1:25,000-1:50,000) are used for the determination of hazard zones in areas affected by large engineering structures, roads and urbanization plans. Large scales (1:5000-1:15,000) are used at the level of site investigations prior to the design phase of engineering works. More detailed scales (1:5000 or larger) are also required during site investigations aimed at providing reliable information for designing engineering control works needed to prevent or repair slope failures (Turner and Schuster, 1996).

6.3.3. Time scale

The most common available mass movement hazard maps in the Mediterranean countries usually include information on the classification of the mass movement type and their location. However, in most cases, active and dormant mass movements are not distinguished. Mass movements events may occur on a return interval of one or two years, decades, centuries, or even millennia. Some mass movements are inactive during dry periods and move only during or following extended periods of infiltration from rain or melting snow. Others move slowly and can occur in isolated events separated by one hundred years or more. Others also can transform suddenly to collapse catastrophically. As an example, man-made cuttings may last for more than 50 years showing no sign of trouble, and then suddenly collapse. Once multi-temporal satellite image analysis is included in the inventory maps, the character of mass movement activity can be determined. Monitoring this activity can be aided by detecting ground vibrations associated with movement or measuring moisture conditions that could destabilize a hill slope. Even though old mass movement areas may be prone to move and likely to pose a threat, active ones are more hazardous. Moreover, more frequent events may cause the fresh scars often seen on the landscape, where the larger, infrequent events are probably the real shapers of the landscape.

7. Major constraints in evaluating MM hazard zonation and relevant improvements

A number of problems may limit the effectiveness of previously mentioned models notably on spatial relationships.

7.1. Uncertainties in the collected MM hazard factors

Owing to the inherent complexity of MM processes, effective hazard assessment and zoning generally require a great quantity and quality of input data compared to other environmental applications. Unfortunately, in many Mediterranean countries, data needed for the assessment are generally inadequate in terms of accuracy, consistency and confidence. In recent years, GIS technology has provided valuable tools for acquiring some of these data, especially on morphological factors and basin or sub-basin characteristics as derived from DTMs, or storing and manipulating most of them in more efficient and innovative ways. However, GIS has not significantly influenced the acquisition of geological information on such factors as rock composition, texture, structure, degree of weathering, the density and orientation of fractures, the attitude of bedding or foliation, and stratigraphic setting, similarly this applies to soil information such as soil cohesion, soil angle of friction, pore water pressure, unsaturated hydraulic activity and soil moisture. In most cases, these data are not

integrated on regional MM hazard models, because the most common way to collect them follows difficult, traditional and costly ways. They are based on field surveys, and there is as yet no sound practice to extend the site measurement of rock properties to mappable units. Therefore, neglecting these useful data, model results can not be as satisfactory as expected.

Moreover, even when financial problems are overcome, some types of relevant data will never be entirely forthcoming. This is the case for historical records of the past spatial and temporal occurrence of landslides over a region, that are largely unknown and difficult to obtain, even though these are essential in order to predict extreme events in the future.

The spatial resolution of data is a further constraint. Different resolution data, or even data at the same resolution but derived from source data at different scales, will require different models. In many circumstances, high spatial resolution raw data are not available or more costly to be suitable for an acceptable hazard assessment. In addition, some specific geotechnical data or seismic wave parameters can not be acquired systematically over wide regions.

Models use a map of past or active mass movements and map representation but recognition and interpretation of mass movement forms can vary, even when made by experienced professionals (Fookes *et al.*, 1991; Carrara *et al.*, 1995), and frequently only provide a snapshot of a continuously changing pattern. A significant level of uncertainty also arises in any application where parameters, which vary naturally across a spectrum, are mapped into discrete classes (Burrough, 1993). It is unfortunate that researchers are now investing more time and resources to tune-up MM hazard models founded upon existing, often unreliable data than in initiating long-term projects for the acquisition of new data on the causes of MM occurrence.

7.2. Uncertainty in the models

Many of the existing parameter models are based on assumptions regarding the nature and influence of causal factors, and many of the interrelationships between the various components of the slope stability system are not always thoroughly understood. In fact, the significance and choice of factors in explaining stability differ according to the authors' background (hydrologist, geologist, seismologist, engineer or meteorologist). Each discipline emphasizes his factors as more important, giving them more weight. While rainfall may be the main triggering factor in some cases (Atkinson and Massari, 1998; Irigaray *et al.*, 2000; Dai *et al.*, 2003), under other climatic regimes local topography has been found to have more influence on the specific location of landsliding than rainfall pattern or geology (Esmali and Ahmadi, 2003). In some cases, the occurrence of landslides is believed to be controlled only by the lithology (Baeza, 1994). Kelarestaghi (2003) indicates that slope aspect and distance from main drainage have little effect on landslide occurrence. Santacana *et al.* (2003) considered that slope geometry (slope angle, watershed size, degree of concavity), lithology and land-use are the most predominant factors affecting the amount of rainfall that infiltrates into the soil and the groundwater flow path. Some authors integrate, in addition to the factors described previously, elevation as an effective parameter in landslide occurrence, because the number of slope failures increases with altitude (Gallart and Clotet-Perarnau, 1988). For all the above, the important factors must be determined and prioritized to consider the dominant type of mass movement that occurs. The overlapping of MM distribution and conditions enable the dangerous zones to be defined, but not the return period or the probability of occurrence of the instability processes. In fact, most regional landslide hazard assessments provide a ranking of terrain units in terms of susceptibility, not including the temporal

component of the hazard. Hence, the susceptibility expresses the likelihood that a MM will occur in an area based on the local terrain conditions (Soeters and van Westen, 1996).

Another additional problem in MM susceptibility evaluation is the different spatial incidence of different types of mass movements, normally related to distinct threshold conditions concerning preparatory factors. This may lead to poor correlations between inducing factors and MM distribution when different types of MM are considered as a whole. This constraint may be solved by defining types of MM prior to the susceptibility assessment, not only because different movements may occur under different terrain conditions (Yan, 1988; Carrara *et al.*, 1992; Irigaray *et al.*, 1996; Leroi, 1996), but also because the impact of slope failures on the environment has to be evaluated according to type of failure (Soeters and van Westen, 1996).

As for heuristic models, the use of GIS-based approaches in the domain of MM hazard has several constraints. GIS remains in this domain a pioneering activity, used more to display data than as a technique that can thoroughly manipulate data and extract new and different information (Ottens, 1992). This is due to several reasons, i.e. hazard evaluation is an intrinsically complex operation; standard procedures for hazard assessment are still lacking; experts in natural hazards find it difficult to make valid use of GIS; and hazard models are frequently developed by GIS experts who have little experience of natural hazards. Two major deterrents to GIS statistical MM hazard techniques undoubtedly are: 1) the logistics of collecting and calculating quantitative data, and 2) the probability values computed from such techniques can often fall outside their range, which makes it difficult to relate the output to a systematic probability surface. For these inherent constraints, GIS is a powerful and a flexible tool for assessing and improving the models on which the hazard assessment is based. For example, rapid updating of data layers and the ease of model re-runs allow assessment of the effects of various mitigatory measures through time. GIS can also improve confidence in hazard zoning through the application of generalization techniques (Carrara *et al.*, 1992), sensitivity analysis of both individual parameters and model specifications (Lodwick *et al.*, 1990) and improved methods of recording and propagating data uncertainty (Brimicombe, 1993).

Source and pathway characterization is rarely well developed for landslides as it requires high resolution data. Considerable uncertainty remains in estimating the timing and frequency with which events occur. Therefore, there is a great potential to supplement zoning based on spatial distributions of landslides and controlling factors with simulation of typical mass movement pathways (again with sensitivity analysis) in support of decisions on mitigatory measures. There is actually a significant lack in objective measurement of the weight of each factor type in MM events. This type of research should be encouraged and developed when new MM occurs.

7.3. Inherent complexity and validation of MM hazard evaluation

Most MM hazard maps in the Mediterranean areas attempt to identify where MM deposits occur on the basis of their relevance to the surrounding geo-environmental conditions. Therefore, there is a need to provide information on potentially unstable slopes under the assumption that slope failures are more likely to occur in the future under the conditions which led them to happen in the past and recently. The MM models do not directly incorporate the magnitude of the event, i.e. its speed, size, kinetic energy, etc. nor its temporal pattern of recurrence. Hence, they can not be classified as “true” hazard models. In addition, it is of paramount importance also to build specific models for each slope-failure type.

The relative efficiency of the various geo-environmental models used in corroborating or zoning MM in the Mediterranean is still lacking. Therefore, data verification is an important part in any hazard study dealing with mass movement hazard zonation, and requires considerable manpower resources to carry out independent checks of the input data with the original data source. In addition to checking of input data accuracy, the output map should also be verified carefully.

8. Conclusion

This chapter constitutes a base allowing an overview of some major MM hazard studies done in the Mediterranean area including modelling approaches. Developments of MM-oriented GIS are needed, and some approaches are described in this thesis such as the comparative analysis of MM detection from satellite imageries, the identification and visualization of new relationships linking landscape characteristics and MM process, the quantitative mapping of MM occurrence, etc. All these were conducted in Lebanon as it experiences different types of MM, and it lies along the eastern Mediterranean region, witnessing tectonic events (uplift, faulting and earthquakes), climatic and anthropic changes, which play a crucial role in triggering and activating the MM.

– II –
Description of the Mediterranean Slopes of Central to northern Lebanon (Study area)

CHAPTER II
Description of the Mediterranean Slopes of Central to northern Lebanon (Study area)

This chapter displays the geographic context as well as diverse geoenvironmental aspects (geology, soil, hydrology, climate, morphology, etc.), socio-economic characteristics and hazards of the study area within Lebanon. It exposes the MM occurrence, concrete examples of MM prevailing in the area, their negative impacts and the applied mitigation measures. It also highlights the MM studies being conducted in the country.

1. Geographic location

The study area is located between latitudes 33° 37' 49'' and 34° 26' 46'' N and longitudes 35° 22' 26'' and 36° 20' 42''E, which correspond in the Lambert conformal conic projection (commonly used in Lebanon), (x, y), upper left coordinates (127500 and 286500) and lower right coordinates (205000 and 187000). This area spreads over the central and northern parts of the Lebanese territory overlooking the Mediterranean (**Figure 2.1**). It is bounded by the Mediterranean Sea to the West, El abde, north of Tripoli, to the north and Damour (south of Beirut) to the south. The eastern boundary of the area touches the piedmonts of Mount-Lebanon facing Bekaa valley in the east. The total area sums up to 3750 km^2, hence 36% of the total area of Lebanon (10452 km^2). It extends 103 km from north to south and spans 42 km from east to west at its widest point.

The study area is classically known to include local sites that have experienced major mass movements, and reflects well the lithological, morphological, pedological, hydrological and climatic diversity of Lebanon (Abdallah, 2001). In addition, its selection depended on other criteria: (1) Chaotic urban expansion with highest population density enhancing environmental decline in the area; (2) Absence of any government control; and (3) The area provides a valuable example on the regional scale, namely the Eastern Mediterranean.

2. Physical and morphodynamic characteristics

2.1. Geomorphology

2.1.1. Physiographic surfaces

Many authors described the topography of occidental Lebanon through showing a west-east profile of the region, thus revealing major topographic features of the study area. Abu El-Ainein (1973) divided the region into coastal plain, deeply incised valleys and highlands. Sanlaville (1977) described the surfaces as segments constituted by the coastal plain, the plateaus at the coast, highly elevated region not exceeding 1500 m altitude, and high mountains. Hakim (1985) classified it as lower mountains (altitudes between 300-900 m), moderate mountains (altitudes between 900-1600 m) and elevated mountains (altitudes more than 1600 m). In this study, geopmorphological units are distinguished from west to east depending on different altitudes and topo mass distribution as follows **(Figure 2.1)**:

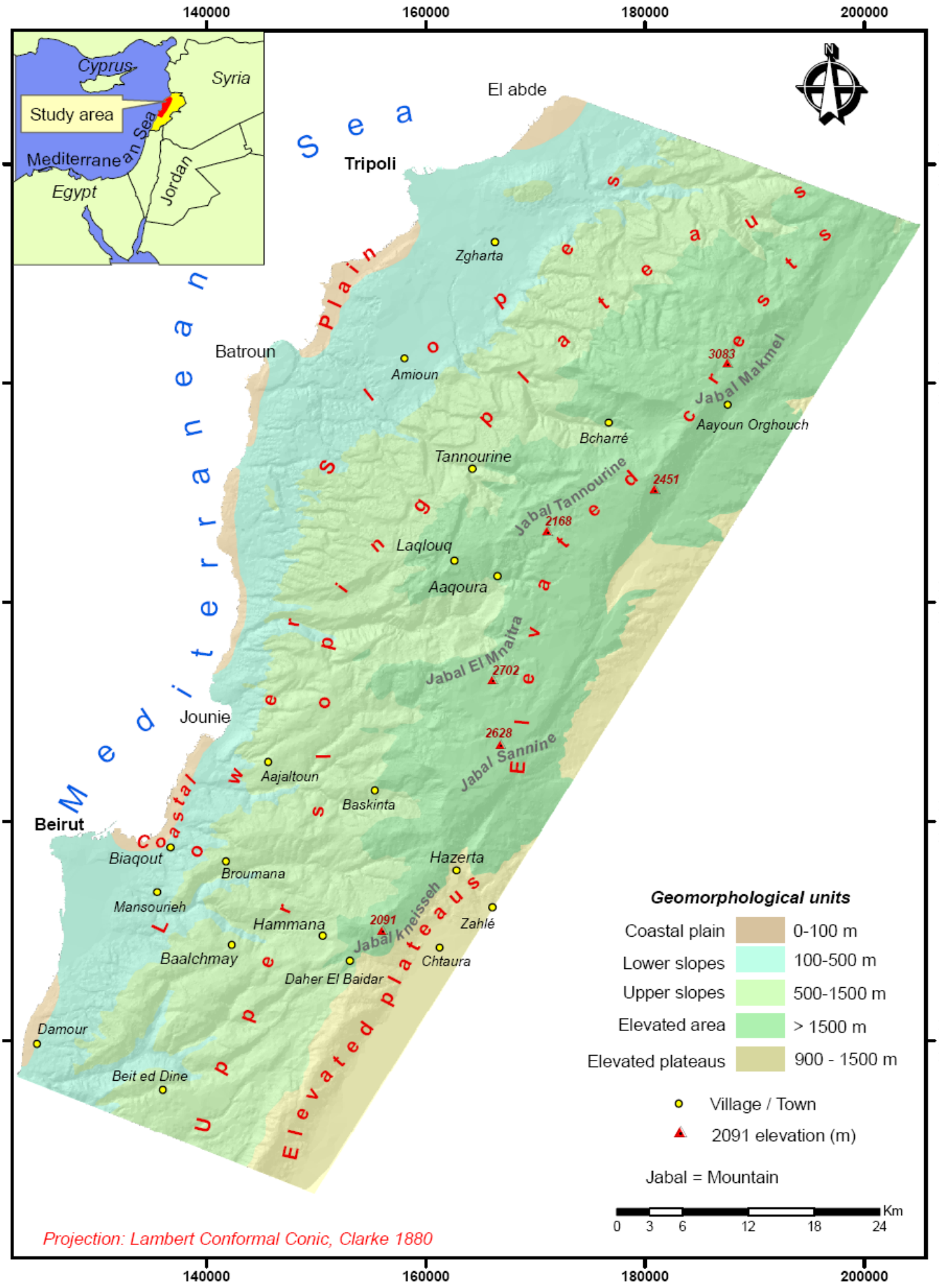

Figure 2.1. Study area location and its geomorphological units.

*The *coastal plain*, occupying around 2%, is narrow, less than 5 km in width and less than 100 m in altitude, and covered by dense clusters of urban congregations. It is dominated by carbonate rocks of the Middle Cretaceous and overlain by alluvial and beach Quaternary deposits.

*The uplifted faulted and folded *Mount Lebanon***,** parallel to the shoreline, running the entire length of the area with a SSW-NNE trend with elevations ranging between 100 m and more than 3000 m. It dips steeply seaward, with an east-west gradient of 75-100 m/km. Mount Lebanon can be further divided into four major parts:

-The lower slopes (850 km^2 or 23%) cover almost all the rock units existing in the study area. They lie parallel to the coastline with an elevation between 100-500 m. The width averages about 10 km, although in some areas like Tripoli, Batroun and Chekka, the slopes juxtapose the sea. Several villages occur on these slopes.

-The upper sloping plateaus (1290 km^2 or 34%) range from 500 to 1500 m in elevation. They are dominantly of the Jurassic, Lower Cretaceous and Cenomanian age. Valleys are deeply incised with scattered villages.

-The elevated plateaus, facing the Bekaa valley to the east (900-1500 m), assure the passage from the coastal area into the Bekaa valley. They are mainly constituted of the Cenomanian and some Quaternary deposits, and occupy 8% of the study area. The monocline is less sharp than the western flank of Mount Lebanon with a gradient of 25-50 m/km.

-The elevated crests exceed 1500 m altitude and are made up of the Cenomanian limestone and dolomitic limestone. These crests correspond to the highest peaks in Lebanon and are represented from north to south by Jabal Makmel (Jabal = mountain) with Kornet es-Souda peak being 3083 m, Jabal Tannourine 2168 m, Jabal El Mnaitra 2702 m, Jabal Sannine 2628 m, and Jabal Kneisseh 2091 m. In this zone, villages are sparse and human action is limited to quarrying leading to massive landscape degradation and occasionally to slope instability. The elevated crests are considered to be a major topographic unit in the study area, occupying 33%.

2.1.2. Karst

Karstic exposures are notably widespread in Mount Lebanon where massive limestone outcrops are exposed. Hakim (1985) estimated that approximately 65% of the Lebanese terrain is karstified on various scales resulting in different local landforms. Some 2250 km^2 (60%) of the study area are characterized by large surface karstic landforms that dominate the carbonate rocks. Four major types can be recognized according to Bou Kheir *et al.* (2003) as follows **(Figure 2.2)**: (1) areas with distinct depressions (6%), (2) areas with distinct lapies (15%), (3) areas with developed karsts (28%) such as karren and other surface dissolution features with relatively small exposures, and (4) areas with non-apparent karst (11%), which are covered by thick soil accumulations. These landforms reflect a remarkable implication in terms of water infiltration, therefore, reducing in some localities possibilities of sliding and increasing other types of MM such as mass and block falls **(Figure 2.3)**.

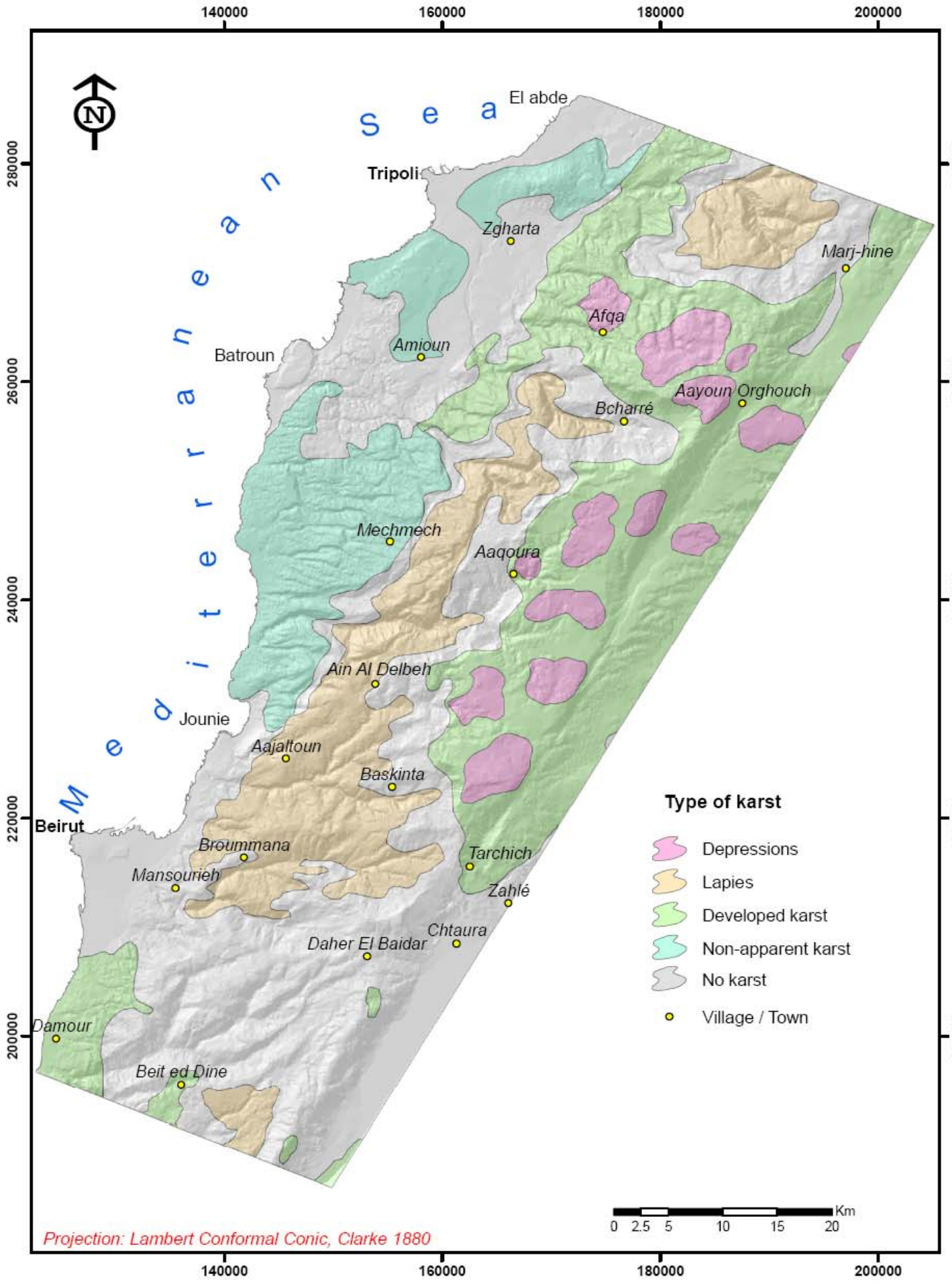

Figure 2.2. General distribution reflecting dominance of karstic type in the study area.

Figure 2.3. Huge block fall due to karstification processes in Tarchich area (Mount Lebanon).

2.2. Geology

The geology of the study area is well documented in Dubertret (1953, 1955, 1966), El-Qareh (1967), Ghattas (1975), Tuglaman (1975), Beydoun (1972, 1977, 1988) and Hakim (1985).

2.2.1. Stratigraphy-lithology

The outcropping stratigraphic sequence in the study area exposes rock formations from the Middle Jurassic to the Quaternary **(Figure 2.4)**. Studying the 1:50,000 geological maps (Dubertret, 1945) reveals 39 rock units. They comprise sediments of the Mesozoic (Jurassic and Cretaceous) and Cenozoic and eruptive rocks (basalts) **(Figure 2.5, Table 2.1).**

▪Mesozoic

***Jurassic**

The oldest rocks observed in the area are Middle Jurassic in age. They are thick, possibly greater than 2 km but poorly known largely due to the cliff forming and monotonous character (Beydoun, 1988). For most of the Jurassic time (210-144 million years ago), the region appears to have been a stable area upon which marine carbonates were deposited.

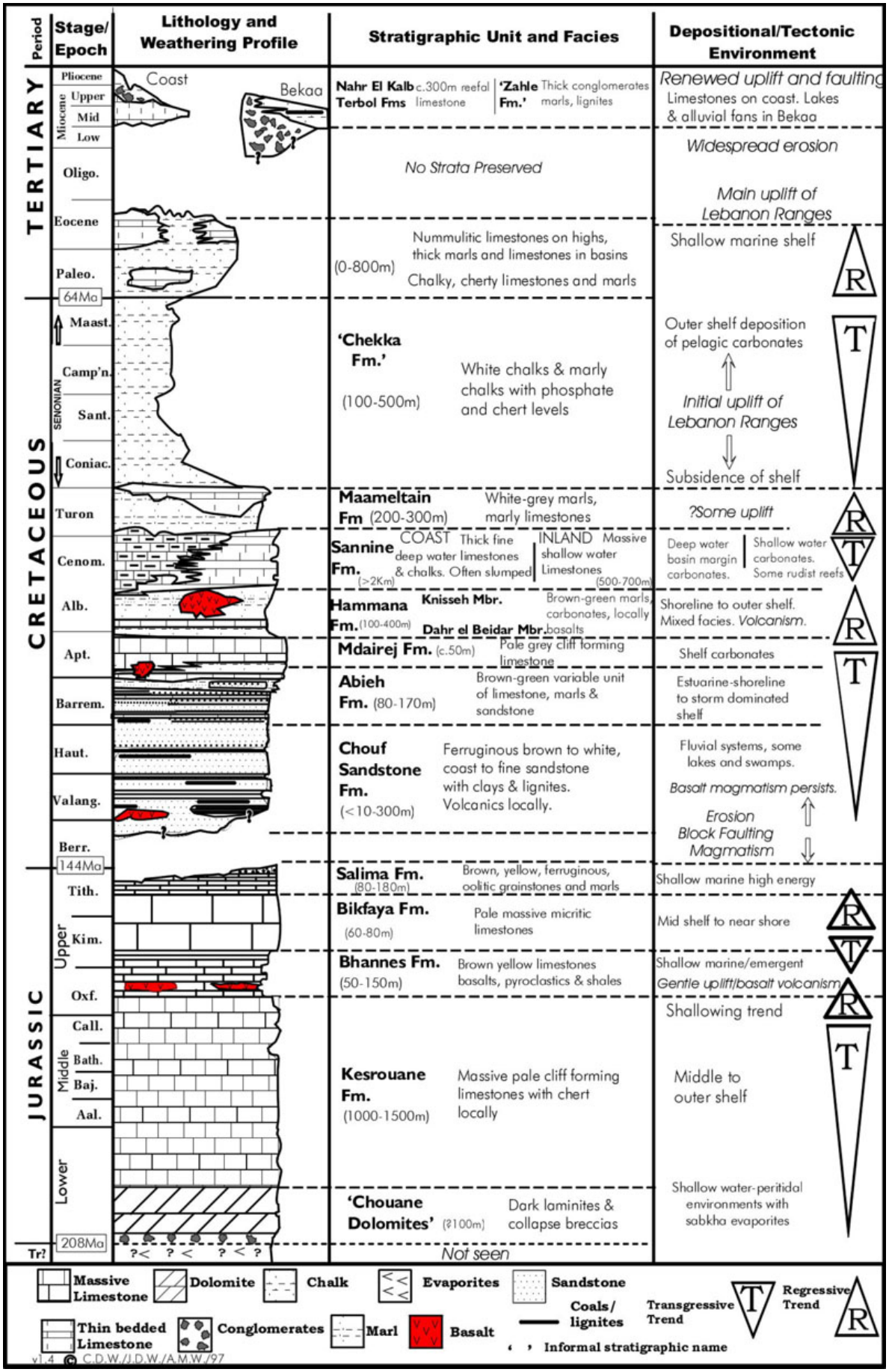

Figure 2.4. Stratigraphic column of Lebanon [adopted from Dubertret (1966), Beydoun (1977) and Walley (1998)].

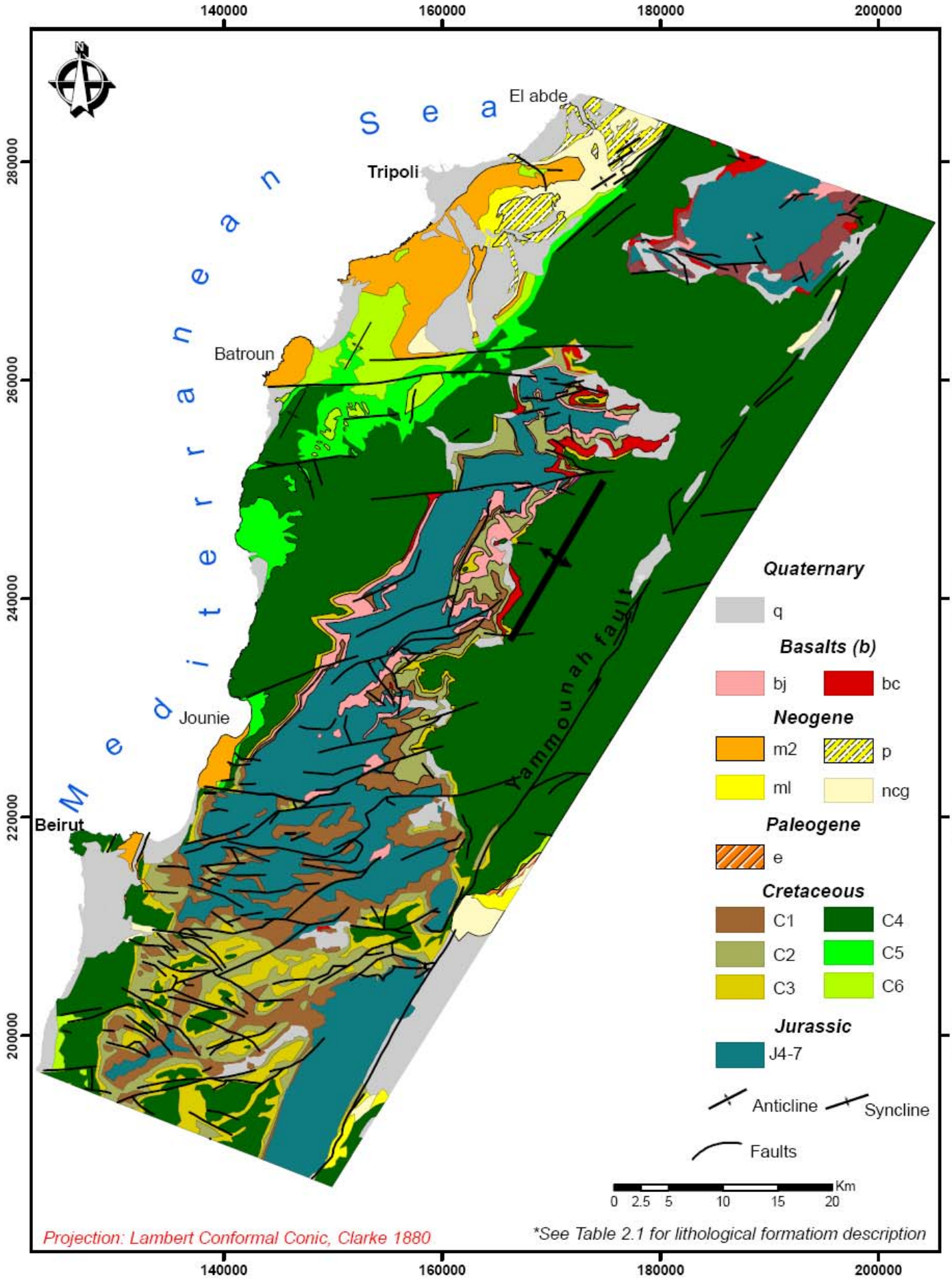

Figure 2.5. Simplified geological map of the study area at 1:200,000 cartographic scale (Dubertret, 1955).

Table 2.1. Stratigraphic succession of the study area (adapted from Dubertet, 1945; Hakim, 1985; Beydoun, 1988).

Era	Period	Epoch		Lithology	Maximal thickness (m)	Local nomenclature	Area coverage (km^2)	Percentage of total area (%)
Cenozoic	Quaternary	Holocene q		Marine deposits, river terraces	Variable	-	336.03	8.909
		Pleistocene q		Dunes, alluvial, fluvial deposits	Variable	-	79.45	2.12
	Neogene	Pliocene	Plaisancian p	Lenticular conglomerates, marly limestone, volcanic materials	360	-	37	1
		Mio-Pliocene ml		Marl limestone	Variable	-	20.6	0.55
		Mio-Pliocene ml1		Pudding stone			63	1.68
		Miocene: -Vindobonian ncg		Conglomeratic limestone, marl	320	-	6.9	0.18
		-Burdigalian m2		Marls	285	-	11.46	0.3
		-Burdigalian m2b		Marly limestone	80	Jabal Terbol limestone	98	2.6
	Paleogene	Eocene: -Lower Lutetian e2b		Limestone, marly limestone	370	-	1.5	0.04
		e2a					1.2	0.03
Mesozoic	Cretaceous	Upper	Senonian C6	Chalky marl, marly limestone	400	Chekka marl	78.68	2.1
			Turonian C5	Marly limestone, limestone	200	Maameltein limestone	111.5	2.97
			Cenomanian C4	Limestone, dolomitic limestone	700	Sannine limestone	1550.8	41.4
		Lower	Albian C3	Shaly limestone, marl, limestone	200	Hammana marl	126	3.37
			bC2b	Basalt	-	-	37.8	1
			Upper Aptian C2b	Limestone, dolomitic limestone	50	Falaise de Blanche/Mdairej limestone	135	3.6
			Lower Aptian C2a	Clastic limestone, sandy limestone, marly limestone	50	Abeih formation	100.8	2.69
			bC1	-	-	-	2.2	0.05
			Neocomian-Barremian C1	Quartzic-calcareous sandstone, intercalation of siltstone & clays	Variable	Grès de base/Chouf sandstone	233	6.22
	Jurassic	Upper	Portlandian J7	Oolithic limestone, marly limestone	180	Salima limestone	23.22	0.62
			bJ6	Basalt	-	-	41.2	1.1
			Kimmeridjian J6	Dolomite, gray limestones, dolomitic limestone	200	Bikfaya limestone	550.8	14.7
			bJ5	Basalt	-	-	0.06	0.001
		Middle	Callovian J4	Dolomite, dolomitic limestone	650	Kesrouane limestone	103.8	2.77

The Jurassic rocks comprise around 19% of the study area and are subdivided into Middle and Upper Jurassic.

•Middle Jurassic

-Callovian (J4): massive, thick bedded, fractured and karstified dolomites and dolomitic limestones with marl intervals.

•Upper Jurassic

-Kimmeridjian (J6): massive, thick bedded, highly fissured (or fractured), jointed and well karstified dolomite, limestone and dolomitic limestone, including frequent horizons of chert nodules. Some basaltic extrusions appear in small patches in Mount Lebanon.

-Portlandian (J7): oolitic limestone with marly limestone intercalations. This unit is an unconformity and is thus absent in many localities indicating a non-depositional or at the level of differential erosional period during the late Jurassic uplift.

***Cretaceous**

At the end of the Jurassic, further tectonism continued to occur in the region. There was a widespread eruption of basalt lava and ashes from a number of vents. The tectonic phase and volcanism were temporary and the area underwent block faulting with emergence and erosion that lasted for ten million years or so, resulting in the deposition of the sandy Lower Cretaceous. During that Early Cretaceous, Lebanon was covered by a series of swamps, rivers and deltas which gave a widespread sequence of sands and shales. During the latter part of the Early Cretaceous, sea level began to rise and marine incursions became increasingly dominant. The Late Cretaceous witnessed a high sea level transgression which contributed to thick sequences of limestones. The Cretaceous rocks comprise the major rock body in the area, occupying 2373.78 km^2, i.e. 63.4%.

•Lower Cretaceous

-Neocomian-Barremian (C1) is composed of fractured, quartzitic and calcareous continental sandstone, with intercalations of siltstones and clays, with locally interbedded lignite, to near-shore shales and sandy limestone. The porosity of the sandstones is reduced due to the presence of the impermeable clay beds.

-Lower Aptian (C2a) is a moderately thick-bedded, clastic limestone, interbedded with marly argillaceous sandy limestones and shales.

-Upper Aptian (C2b) (*muraille blanche*) is a massive, thick bedded, jointed, stylolitic, partially karstified limestone and dolomitic limestone. The volcanism that began in the Upper Jurassic persisted throughout the Lower Cretaceous (bC2b) covering 1% of the total study area.

-Albian (C3) is made of thin-bedded, marly limestone and shales, upgrading into moderately thick-bedded limestone, interbedded with marl. Its distribution is patchy in Mount Lebanon.

•Late Cretaceous

-Cenomanian (C4) is the most dominant formation in the study area. It is formed of chert-bearing, massive to thinly bedded, highly fractured and jointed outcrops. It is a well karstified limestone and dolomitic limestone.

-Turonian (C5) is moderately thick, with marl interbeds, to thinly bedded limestone and occasionally with chert nodules, marl and marly limestone. It is distributed along the coastal plain, in the elevated areas and in the Bekaa valley.

-Senonian (C6) made up of marl and marly limestone, altering from massive to jointed, fractured to soft, and friable in some localities.

▪**Cenozoic**

The Cenozoic (i.e., last 60 million years) witnessed an enormous change in the area from the Mid Eocene time, when the area was covered by shallow seas, in which carbonates were being deposited, to the present state of an emergent and eroding land mass. The Tertiary (Paleogene and Neogene) rocks occupy an area of 239 km^2, or approximately 6% of the total area. They are found largely along the coastal stretch as patches, especially in the Chekka-Tripoli area. The Quaternary deposits occupy an area of about 415.48 km^2, i.e. around 11%.

***Paleogene,** in the Bekaa valley:

-Lower Lutetian (e2a) and (e2b): moderately thick to thinly bedded, partially karstified beds of Nummulitic limestone, with chert nodules, interbedded with marly limestone.

***Neogene,** made up of the Miocene that outcrops along the coast and in Mount Lebanon near the Yammounah Fault, Pliocene marine facies that form small islands along the coast and Mio-Pliocene continental facies that are well represented in the Bekaa valley and in Mount Lebanon.

-Miocene is formed by: 1) massive, friable, marly limestone, and marl, with silty marl in many instances attributed to **Burdigalian (m2) & (m2b)** and 2) thick deposits of conglomeratic limestone and marl ascribed to **Vindobonian (ncg)**.

-Mio-Pliocene made up of marl and marly limestones (ml and ml_1).

-Pliocene constituted by massive deposits of marly limestones and conglomerates with basaltic rocks of the **Plaisancian (p)**.

***Quaternary:** The major Quaternary deposits are shown in **Table 2.2**, mainly:

-Pleistocene (q): dunes and alluvial deposits, covering 8.909% of the region, from which scree (eboulis) are dominant (3.134%) and well distributed (106 polygons) in the upper slopes and elevated crests of the area.They are followed by siltstones (1.43% of the area) indicating a big water retention, inducing MM.

-Holocene (q): marine deposits and river terraces, occupying 2.12% of the area. They are constituted by fluvial terraces (1.8%), beach terraces (0.01%) and tuffs (0.01%) in the lower slopes, while alluvial terraces are prevailing in the coastal plain. Fluvial and alluvial terraces are nearly equally distributed in the area, with a higher distribution dominance than beach terraces and tuffs.

2.2.2. Structural geology

Lebanon is part of the unstable shelf of the Eastern Mediterranean along the active transform border between the Levantine and Arabian plates, known as the Dead Sea Fault Zone (DSFZ). Mount Lebanon and Anti-Lebanon can be considered as belts related with the restraining bend of the DSFZ. The Bekaa depression, on the other hand, is neither strictly a

graben nor an elongated syncline, but possesses structural features of both (Sabagh, 1966; Beydoun, 1972). These main features started during the Late Cretaceous where the collision zone was offshore and far to the NNW of Lebanon **(Figure 2.6)**, which gave rise to the first gentle uplifting of Mount Lebanon and Anti-Lebanon area. Substantial uplift occurred in the Late Eocene and Oligocene resulting in emergence and the marking out of the three fold NNE-SSW trending pattern of modern Lebanon. During the uplift time, the sea drained from the interior of the Bekaa depression and restricted to shallow marine incursions along the line of the present day coast. Since then, there has been continued uplift and local tilting over the last five million years and various block slides due to the strike-slip faulting. From these three main structural features, the anticline of Mount Lebanon constitutes the major part of the study area which also reveals local folds distributed in its northern and eastern parts **(see Figure 2.5)**.

Table 2.2. Distribution of the Quaternary deposits in the study area.

Epoch	Geographical distribution*	Lithology	Number of polygons	% of the area
Pleistocene	LS + P	Alluvials (qa)	16	0.82
	CP	Ramleh and fixed dunes (qd)	55	0.41
	LS	Red decalcified soil of ramleh (qdd)	12	0.74
	CP + LS	Dunes (qdm)	27	0.5
	EC	Colluvial deposits (qc)	24	0.51
	US + EC	Scree (eboulis) (qe)	106	3.134
	US + EC	Mass movements (qed)	5	0.175
	US + EC	Alluvial fans (qj)	6	0.28
	EC	Aaqoura earth flow (qm)	2	0.03
	EC	Siliceous colluvium (qs)	1	0.03
	LS + P	Cultivated terrain (qt)	25	0.81
	CP	Brown alluvial terrain (qab)	1	0.04
	P	Siltstones (ql)	5	1.43
Holocene	LS	Fluvial terraces (qaf)	21	1.8
	CP	Alluvial terraces (qat)	27	0.3
	LS	Beach terraces (qds)	4	0.01
	LS	Tuffs (qT)	1	0.01

Coastal Plain = CP; Lower Slopes = LS; Upper Slopes =US; Elevated Plateaus = P; Elevated Crests = EC

Figure 2.6. Schematic east-west cross section across Lebanon (Walley, 1998).

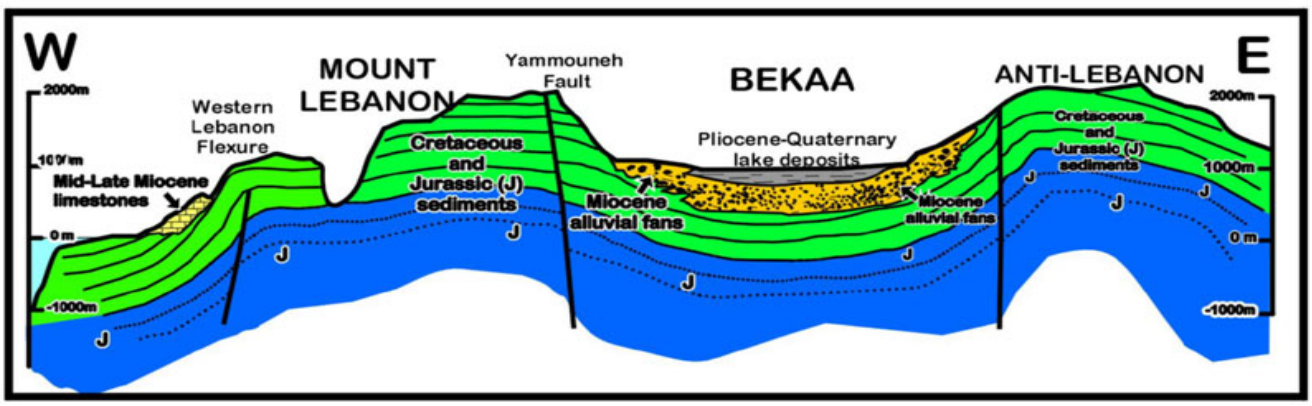

In addition to the major fault (Yammounah fault, central segment of DSFZ) that runs along the western margin of the Bekaa with a NNE-SSW strike and links the major fault of the Jordan valley to the Ghab valley fault of northern Syria, other faults are recognized being almost vertical, with around 10-15 km length, and main strikes being NNE-SSW and NNW-SSE, with a less frequent E-W trend (Khawlie, 1995).
Moreover, different faults of the study area are well developed locally in the following rock formations: J4, J6, C2b and C4; many of them characterized by relative small displacements (< 1 m) and showing dense spacing.

2.3. Soils

The soils of Lebanon have been well studied by many researchers: Reinfenberg (1935, 1952), Gèze (1956), Lamouroux (1978), Sayegh and Saliba (1969), Verheye and Osman (1974), Tarzi and Paeth (1975) and Darwish and Zurayk (1987).
The dominant types of soils in the study area are shown by the soil map of Lebanon established by Gèze (1956) at a scale of 1:200,000 (**Figure 2.7**). The characteristics of the different soils covering the study area are detailed in **Table 2.3**.

Thirty-eight different soil units were identified of which twenty-five are pure soil types and thirteen are soil associations. Among these soil associations, twelve represent association of two “soil types” and one is formed with association of three “soil types” (Gèze, 1956).
These soils are typically Mediterranean in character. The most widely represented soils are terra rossa (red mountainous soils) occupying an area of 1421.62 km^2 (37.91%) developed on the Kimmeridjian (J_6), Cenomanian (C_4), Miocene (m2) and Mio-Pliocene (ml1) rock formations of Mount Lebanon. These soils reach a thickness ranging between 110 and 165 cm and have a well-developed profile. Generally, they are decarbonated, rich in iron oxides (e.g., hematite and goethite), with a neutral to a slightly acidic pH value (6.7-7.2) and high clay content (30 to 50%). These soils are of a strong surface structure, with medium gravel size (5-35%) and organic matter (2-2.5) contents, compacted in the subsoil, thus having a low to moderate infiltration rate (2.0-6.0 $cm.h^1$). Over saturation of these soils with water leads to loss of entire soil strength and hence soil movement (Darwish, 1988; Darwish and Zurayk, 1997).

2.4. Land cover/use

A recent land cover/use map at a scale of 1:20,000 was adopted from a project done by the Lebanese National Council for Scientific Research and the Lebanese Ministry of Agriculture (LNCSR-LMoA, 2002) based on CORINE (*Coordination des informations sur l’environnement*) Land Cover methodology (level 4).
This map was established using a visual interpretation of pan-sharpened Landsat TM (30 m) with IRS (5.8 m) images, both acquired in October 1998. Mainly five categories (or classes) were plotted: (1) natural vegetation cover, (2) agricultural lands, (3) bare lands, (4) water bodies and (5) human practices **(Figure 2.8)**. Each class in turn can be further subdivided into a number of sub-classes.

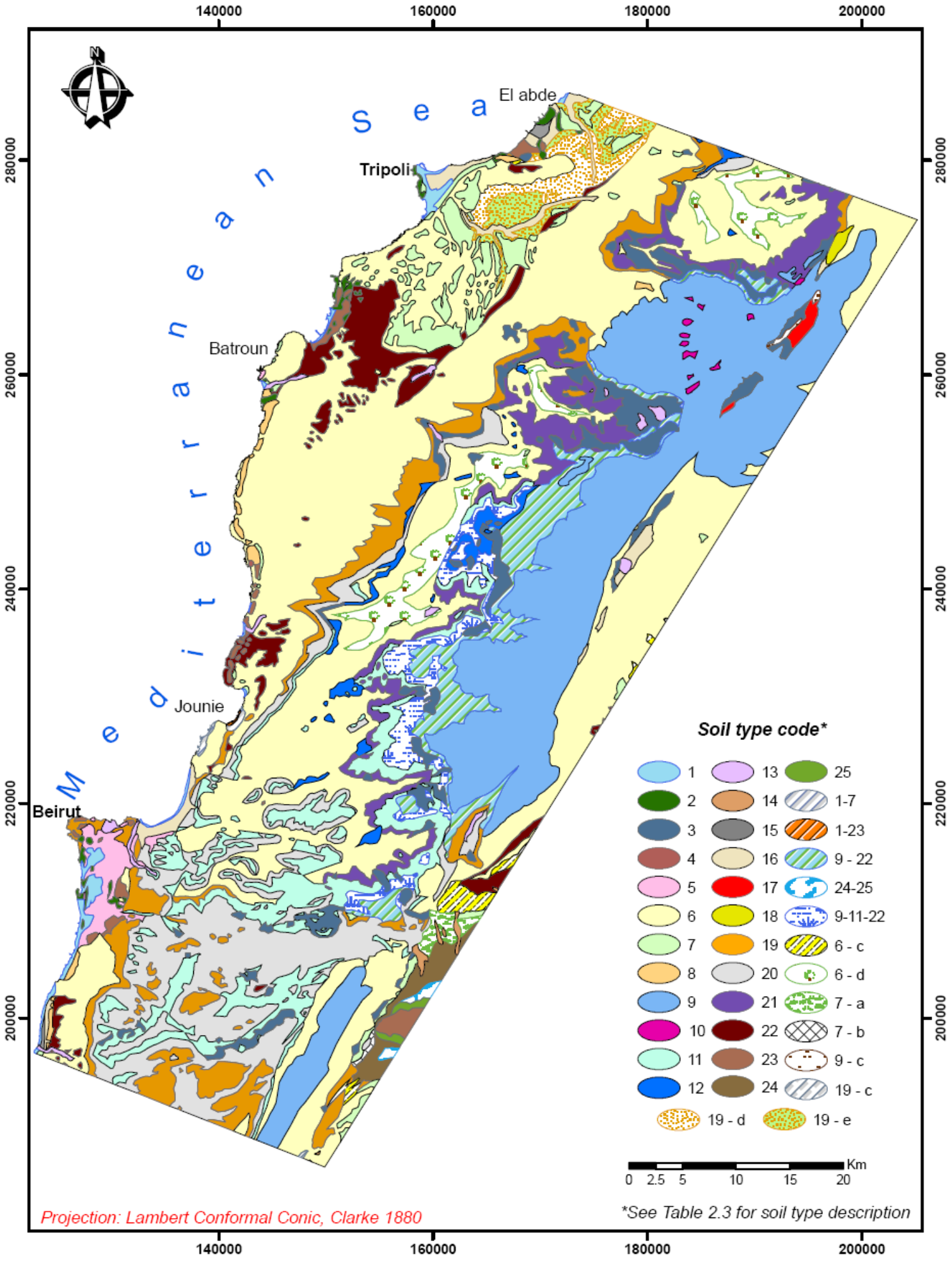

Figure 2.7. Soil map of the study area (Geze,1956).

Table 2.3. Characteristics of the different soil types in the study area (see Figure 2.7) (Gèze, 1956; Darwish, 1988).

Soil type (no.)	Predominant geology	Principal location*	Sand (%)	Clay (%)	Gravel content (%)	Organic matter (%)	Depth (cm)	Total $CaCO_3$ (%)	pH	% of the area
Pure soil units										
Coastal sand (1)	qdm	LS	70-80	5-10	35-65	0.5	100-150	5-10	6.2-6.4	0.50
dated dunes/Ramleh (2)	qaf, qs, p	CP + US	90-95	1-2	5-35	0	120-150	10-15	7.7	0.35
nd massive landslides (3)	C1, C4, C5, qc, qd	LS + US	40-50	30-40	35-65	1	100-150	15-20	7.4-7.6	3.70
age of human source artificial fills) (4)	qt	CP	-	-	-	-	-	-	-	0.005
alcified and rubified coastal sand (5)	qdd	LS	70-80	5-10	35-65	0.1	190-200	5-10	7.6	0.78
ious red mountainous soils (terra rossa) (6)	C4, m2	CP + LS	20-30	30-50	5-35	2-2.5	140-165	0	6.7-7	35.60
us red mountainous soils (terra rossa) (7)	qaf, qd, m2	CP + LS	20-30	30-50	5-35	2	110	4	7.2	2.31
Brown soils (8)	C4, C5, qat	CP	30-40	30-75	5-35	3	200	4-10	7-7.6	0.33
vish mountain soils (9)	J6, C4	US + ES	50-60	20-40	65-95	0.5	50-80	3-10	6.4-7	16.36
mountain soils with humus (10)	C4	EC	50-60	20-40	65-95	2	50-80	3-10	6.4-7	0.09
Sandy soils (11)	C1	LS + US	35-70	20-30	35-65	1	100-125	1.5-3	6.2-6.4	5.46
uous greyey soils (12)	bJ6	LS	30-40	40-50	35-65	0.5	200-250	1.5	6.8-7	0.87
t fluvial alluvium (13)	C4, C5, qat	CP + LS + P	30-40	40-50	65-95	1.5	150-180	35-40	8-8.5	0.37
ential fan deposit (14)	qat	P	40-50	30-40	65-95	0.5	150-170	10-15	7.5-8	0.11
uvium associated to coastal sand (15)	qat	CP + LS	40-50	30-40	35-65	0.5	150-200	10-15	6.2-6.4	0.06
associated with terra rossa (16)	qat	CP + LS + P	30-40	30-40	35-65	0.5	200	3	7.1	1.03
associated with yellowish ountain soils (17)	qat	P	40-50	30-40	35-65	0.5	100-120	30-40	6.4-7	0.16
m associated with black r greyey soil (18)	qat	P	30-40	30-40	35-65	1	125-150	45-60	6.2-6.4	0.09
oils on marl with bedded limestone (19)	C4	LS	20-30	30-40	5-65	1	130	40-45	7	5.29
oils on alternating marl, one and sandstone (20)	C2a, C3	LS + US	30-40	30-40	5-65	1.5	120	40-45	7	8.83
oils on alternating marl, , sandstone and basalt (21)	C2a, C1	US	30-40	40-50	0-35	2	170-200	40-45	7	3.59
White rendzina (22)	C6, C4, ml	LS + P	20-30	50-60	0-35	1.5	75-100	40-60	7.2-7.6	2.68
ck or grey soils (23)	qat,	CP + LS + P	20-30	30-55	5-35	2.5	190-200	50-87	7.5	0.65
eppic chestnut soils (24)	qat	P	30-40	16-30	5-65	0.5-1	130-150	15-30	7.4-7.6	0.63
k chestnut soils (25)	qat	P	30-40	16-30	5-65	0.5-1	130-150	15-30	7.4-7.6	0.10
sociated soil units										
1-7	qdm	CP + LS	70-80	5-10	35-65	0.5	100-150	5-10	6.2-6.4	0.06
1-23	qdm	LS	70-80	5-10	35-65	0.5	100-150	5-10	6.2-6.4	0.008
9-22	C4	US	40-50	40-50	35-65	1	60-90	30-40	6.7-7	3.21
24-25	qta	P	30-40	16-30	5-65	0.5-1	130-150	15-30	7.4-7.6	0.10
9-11-22	C1, C2	US	40-50	40-50	35-65	1	60-90	30-40	6.7-7	1.819
nes and bare rocks (c)	ncg	P	20-30	30-50	35-65	2-2.5	140-165	0	6.7-7	0.43
dolomitic sand (d)	J4 + J6	US	30-40	30-50	35-65	1	130-150	30-40	7.5	2.00
um associated with light chestnut soils (a)	ql	P	40-50	20-30	65-95	1.5	150-200	23-30	7.5	0.26
ious light steppic chestnut soils (b)	ql	P	50-60	20-30	35-65	1	130-150	30-40	7.5	0.04
nes and bare rocks (c)	ncg	P	50-60	20-40	65-95	0.5	50-80	3-10	6.4-7	0.04
nes and bare rocks (c)	ncg	P	20-30	30-40	65-95	1	130	40-45	7	0.008
9-poudingues (d)	ncg + ml	LS	20-30	30-40	5-65	1	130-150	40-45	7	1.07
and calcareous layer (e)	P	LS	30-50	20-30	5-65	1	130	40-45	7	1.01

Coastal Plain = CP; Lower Slopes = LS; Upper Slopes =US; Elevated Plateaus = P; Elevated Crests = EC

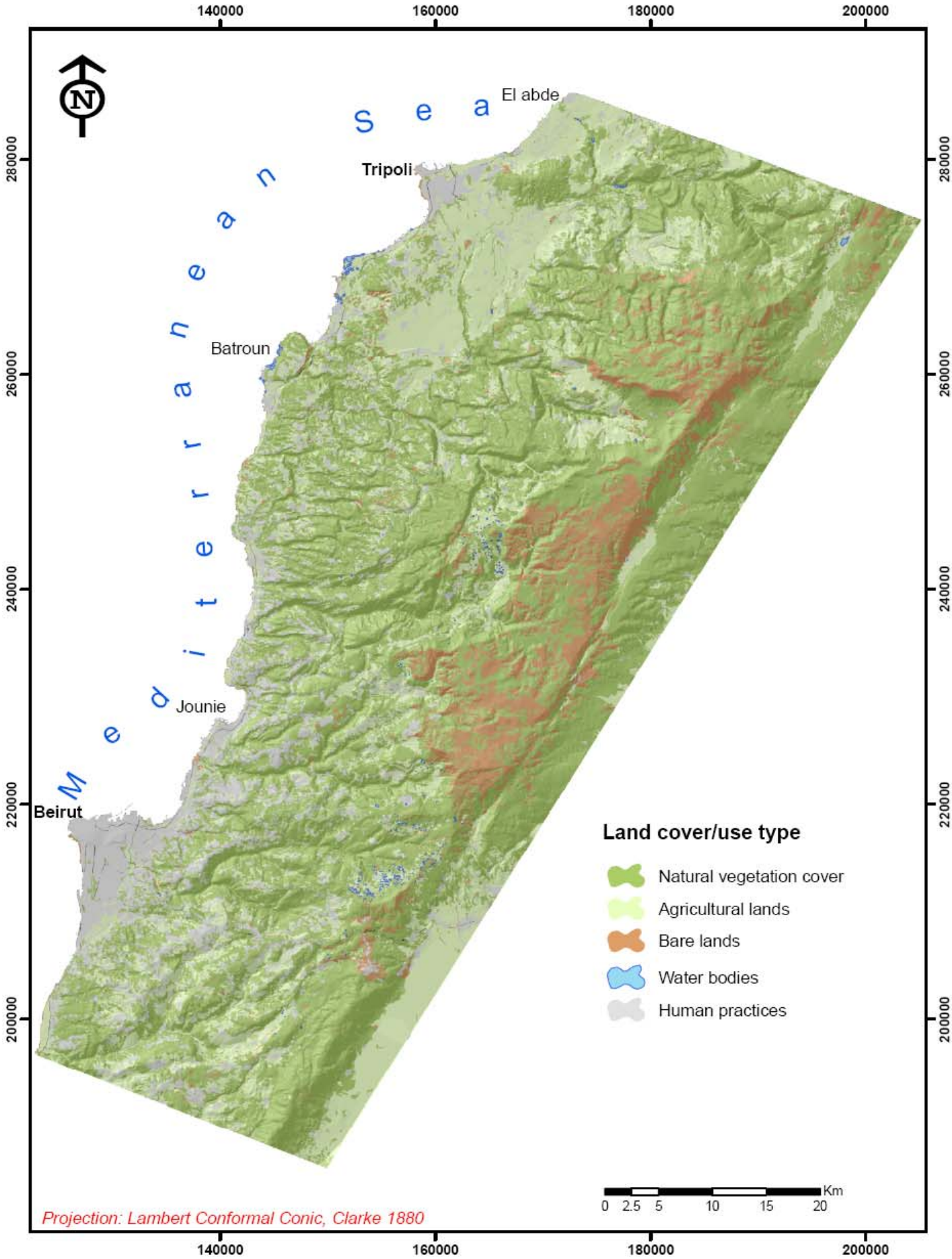

Figure 2.8. Simplified land use/cover map of the study area based on CORINE classification of level 1 description (LNCRS_LMOA, 2002)

1) Natural vegetation cover occupies the largest portion of the studied area (60.5%). It varies into dense and different open types of forests (22.17%) (*Pinus* species, *Cedrus* sp., *Juniperus* sp., *Cupressus* sp., *Quercus* sp., etc.), shrubs and herbaceous vegetation. The *Quercus* species are the most widespread forest trees in the study area (11.86%). They appear on the Jurassic (J_6) and Cenomanian (C_4) rocks and on the red, yellowish, sandy and mixed soils. Shrubs and grass are present with different proportions, 13.43% and 24.9%, respectively.

2) Agricultural lands make 21.926% of the study area. They include field crops (6.54%), orchards [deciduous fruit trees (5.76%), citrus (0.92%), bananas (0.11%), olives (6.67%) and grapevines (1.29%)], vegetables (0.386%) and greenhouses (0.25%). These lands can be either cultivated by one type of crop, such as olive trees, or by a combination of field crops or fruit trees. Bad irrigation practices and excess input of fertilizer application are common in the study area inducing the spread of secondary soil salinization which results in the destabilization of soil aggregates. This reduces soil water holding capacity, enhances runoff and increases sliding (NAP, 2003).

3) Bare lands are ascribed to the unexploited and unemployed terrains that are dominated by rocks, soils and beaches. These lands constitute 8.096% of the study area.

4) Water bodies include water surfaces such as lakes, reservoirs, marshes and rivers. They are very local patches occupying only 0.038% of the study area.

5) Human practices grouped into discontinuous and continuous urban areas, activity zones (industrial areas, airports, and seaports), artificial green zones, roads/highways, material extraction (quarries), embankments, etc. They occupy 9.44% of the study area with 2.36% for the discontinuous urban. The density of urban settlements is concentrated on the coastal stretch. Multi temporal image analysis (1985-1998) of Tripoli area and the surrounding revealed that the urban area increased about 35%, with a decrease of cultivated land of about 38% (Darwish *et al.*, 1999). This rapid urban chaotic growth is one of the principal causes of natural resources depletion that leads to induce natural hazards such as desertification, landslides, flash floods, etc. On the other hand, the numerous quarry excavations represent 0.46% of the study area. This figure was valid for the year 1998 (time of acquisition of the used satellite images), but recent studies indicate that quarries have increased to 387 covering 14.70 km^2 of the study area (MoE, 2006). Quarrying has resulted locally in an increased tendency to slope failure, landslides, and gully erosion. The problem will be aggravated since no attempt has been made to stabilize mountain slides and abandoned rock quarries in the perspectives of rehabilitation and restoration.

2.5. Hydrology

Seven perennial coastal rivers with a double number of intermittent streams dissect the study area. These coastal rivers have more or less the same lengths (< 50 km). From north to south, one can distinguish Naher (river) El Bared (37 km), Abou Ali (42 km), El-Jauz (33 km), Ibrahim (44 km), El Kalb (35 km), Beirut (48 km), and El Damour (45 km) rivers (**Figure 2.9**). They have a prevailing seaward flow direction with a general E-W orientation.

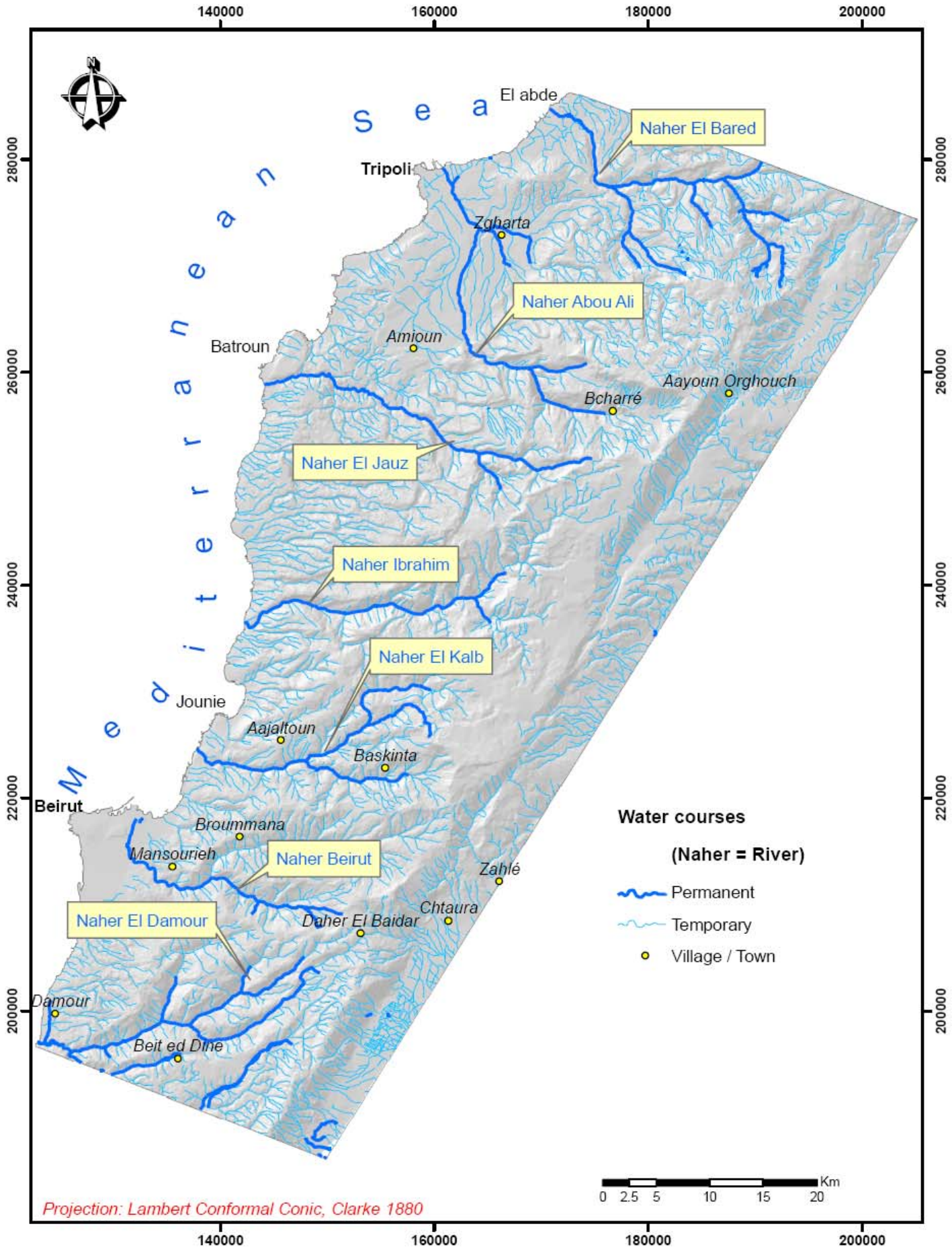

Figure 2.9. Drainage map and major rivers of the study area.

The distances between these rivers are approximately equal, i.e. 15-20 km, but with different discharge rates **(Table 2.4)** with Naher Ibrahim having the highest average discharge rate. Based on Way's classification (1978), the dendritic drainage pattern is the most dominant. Watersheds hosting these rivers are characterized by a funnel-like shape as a result of the influencing surface morphology and geologic-structure controls. According to Jaber (1993), METAP (1995), Khawlie (2000) and Khawlie *et al.* (2005), these watersheds share different physical and hydrological properties (**Table 2.4**).

A remarkable number of springs issue in the area, notably in the elevated region where the Cenomanian and Jurassic rocks are exposed. A total number of 789 different scale springs are shown on topographic maps at scale of 1:50,000 (though they are seventy years old, so some are not there anymore). Most of them are of the karstic type concentrated in the Jurassic and Cenomanian rocks, but the ordinary and fault springs are also found (Abdallah et al., 2002, 2006a) . Although the karstic springs are characterized by high water discharge, yet they reveal a clear seasonal fluctuation in their yield. Some of the major springs have an average discharge exceeding 1 m^3, and they feed the main rivers drained in the area. The Rachine spring (1.1 m^3), El-Jauz spring (2.2 m^3), Afqa spring (4.63 m^3) and Rouaiss spring (3.55 m^3) are some examples. Furthermore, a big number of springs are of a low discharge rate ranging between 10 and 25 l.

Table 2.4. Physical and hydrological properties of major watersheds in the study area.

Major hydrologic characteristics	**Major watersheds**						
	El Bared	**Abou Ali**	**El-Jauz**	**Ibrahim**	**El Kalb**	**Beirut**	**El Damour**
Average annual discharge (Mm^3/year)	170	370	82	480	251	252	250
Catchment area (km^2)	284	482	254	326	237	216	333
Average relief gradient (m/km)	25	46	42	47	57	57	51
Drainage density (km/km^2)	1.05	1.20	0.92	1.25	1.6	1.60	0.95

The Jurassic and Cenomanian rock formations are the dominant aquifers in the area, holding excellent hydrostratigraphic characteristics. The two aquifers are noted by the developed karstification. The karstic depressions or conduits span several kilometers long. Although affected by the overlying lithologies, the conduits often follow the prevailing slope direction of strata, which is normally seaward. In the study area, the depth to water in the Cenomanian formation ranges between 300-350 m, with an average yield per well of 25-35 l. While in the Jurassic, it is deeper and may reach some 450 m and yield of 25-50 l. Furthermore, there are several wells dug in the clastic and argillaceous formations. They often exhibit a relatively low and intermittent water discharge. Most of these wells are private and are used for local purposes, mainly irrigation.

2.6. Climate

A Mediterranean climate characterizes the study area with mild wet winters and dry hot summers. The number of climatic stations in the area is limited (5 stations). Beirut and Tripoli stations are situated at an altitude of 27 m in the coastal plain, Sir El Dennieh at 925 m and Cedar at 1524 m in Mount Lebanon, and Zahlé at 990 m altitude in the Bekaa area **(Figure 2.10)**. Due to civil war (1975-1990), long continuous period of pluviometric data records are not available.

According to the available pluviometric map at 1:200,000 scale (Plassard, 1971), the annual precipitation rate ranges between 600 mm on the coastal plain and more than 1400 mm over the crests, and decreases again to 700 mm in the elevated plateaus of Mount Lebanon facing the Bekaa valley **(Figure 2.10).** The huge mountain mass is an effective barrier to all moist-laden winds or cold fronts coming from the Mediterranean sea. Thus, there is an increase in the amount of rain from west to east (coast to inland), i.e. an altitude-related phenomenon. Significant portions (33%) of the area are under rainfall quantities ranging between 1100 and 1300 mm/year.

Most of the rainfall and snow takes place during the period extending from November to March (period responsible for 75-80% of precipitations with a climax in January which at some instances yields about 160-180 mm/month). Dryness takes over again from April to October. The 20-25% of remaining precipitation corresponds to thunderstorms of autumn and rain showers in spring (ACL, 1973, 1982). The number of rainy days varies between 60 and 80. The number of snowy days is equal to 10 at 1000 m altitude and can exceed 30 days higher than 1200 m, from which around 10 days are in January. Snow becomes more frequent at higher altitudes, where it represents 3/4 the quantity of precipitation at 2000 m. The snowmelt occurs progressively from April-May, but some plaques persist until autumn.

The variation in annual precipitation appears to be characteristic of the area. An example indicates that annual rainfall during the past ten years in Tripoli station was equal to 990 mm/year for the year 1999 with the highest precipitation rate, and during 2002 decreased to 378 mm (with the lowest precipitation rate), allowing evidence of dry areas and rainy areas **(Figure 2.11)**. Similarly, annual variations of monthly precipitations can be noticed in Zahlé climatic station, i.e. annual rainfall during 1999 equal to 303 mm, and during 2003 increased to 1027 mm.

A general characteristic of the precipitation is the torrential nature and high intensity. Although data on hourly basis is not available until now, the daily collected data give an idea on the intensity of precipitations. In some instances, 100 mm or more per 24 hours is observed. Some selected examples can demonstrate the high intensity rainfall occurring in the area. In November 1958, Beirut station received 52.6 mm during one hour (Blanchet, 1966). In 4 days, from 23 to 26 January 1963, 214 mm fell down. The examination of current data indicates also important thunderstorms and rain showers identical to those taking place during the past. During 24 hours, Beirut station recorded 78.7 mm on the third of January 1981, 83.3 mm on 7 December 1987, 105.3 mm on 18 November 1988 and 61.5 mm on 3 December 1991. Zahlé station also registered 190 mm on 20 January 2000 and 185 mm on 8 April 2000, indicating high rainfall intensity. These climatic characteristics (torrential and episodic rainfall) may enhance surficial cover instability inducing superficial movements and processes.

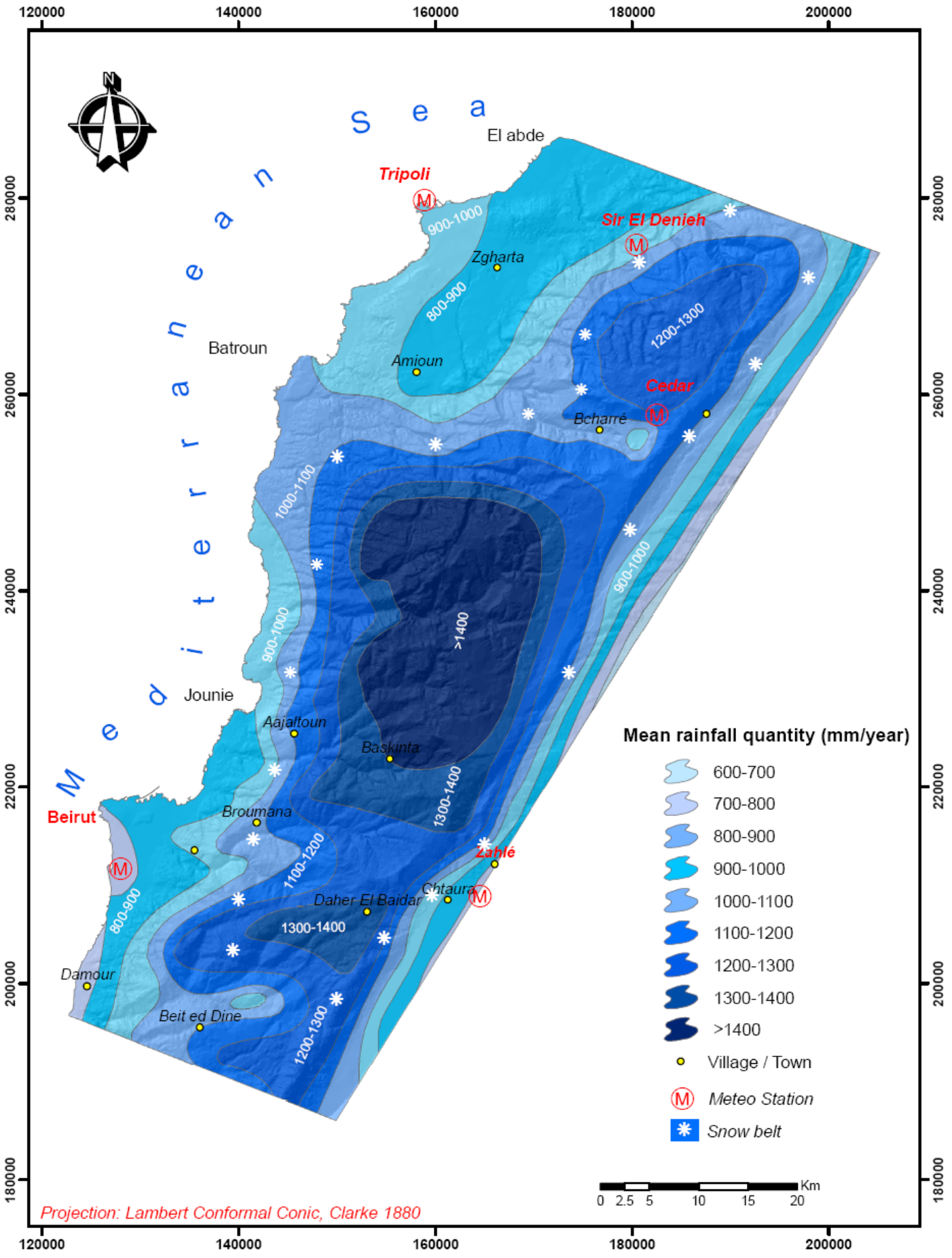

Figure 2.10. Rainfall map of the study area (Plassard, 1971).

Figure 2.11. Distribution of precipitation within the last ten years in Tripoli station - 1999 (lowest rainfall), 2002 (highest rainfall)

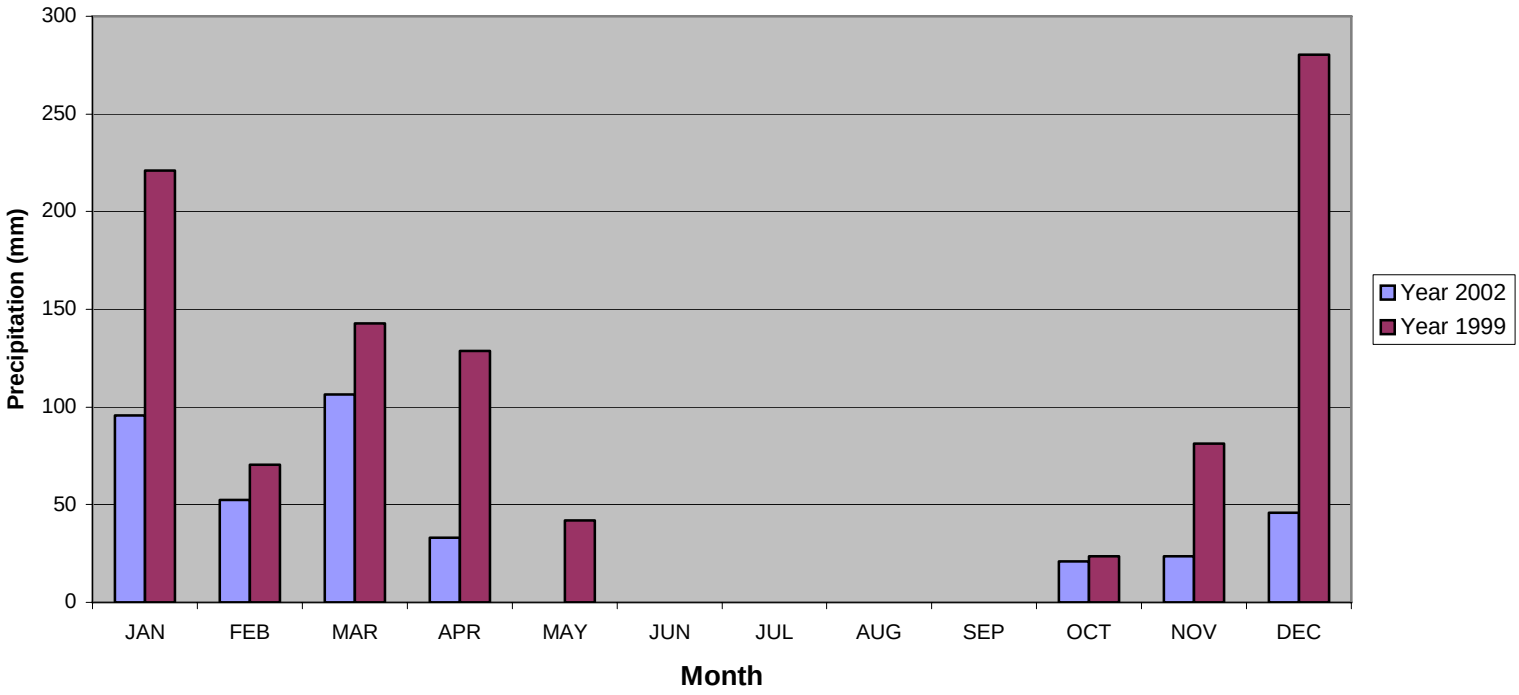

3. Socio-economic characteristics

The area comprises, in addition to Beirut and suburbs, 1094 villages that are part of the cazas (within larger governates divisions, i.e. the Mohafazats) of Tripoli (15 villages), Akkar (23 villages), Bcharré (26 villages), Koura (49 villages), Minié-Danniyé (65 villages), Zgharta (67 villages), and Batroun (91 villages) belonging to Mohafazat (or governorate) of North Lebanon, while cazas of Chouf (64 villages), Baabda (76 villages), Aley (98 villages), Kesrouane (145 villages), El Metn (156 villages) and Jbail (166 villages) are attributed to Mohafazat Mount Lebanon, and part of Hermel (1 village), West Bekaa (9 villages), Baalbeck (17 villages) and Zahlé (26 villages) ascribed to the Mohafazat El Bekaa **(Figure 2.12)**.

Rapid urban chaotic growth is one of the major factors affecting living conditions and the environment in Lebanon. This is particularly true because of the excesses of urbanization that took place during the war period. Along the coastal stretch, more than 24% of the terrain is urbanized (Huybrechts, 1997). The population in the study area increased by 32% between 1970 and 1980, but decreased later between 1980 and 1994 due to the civil war, and is expected to rise 59% by 2020 (**Table 2.5**). This increase will oblige construction of residential buildings in areas susceptible to MM taking into account the small stretch of the whole country. The major city is Beirut located directly on the coast, with a mean population density equal to 21228.3 person/km^2, compared to less populated cities of approximately 402 persons/km^2. In addition, roads are usually constructed in the study area on friable materials inducing instability processes (Khawlie and A'war, 1992).

Table 2.5. Projected population increase in the study area between 1970 and 2020.

Year	1970	1980	1994	2000	2005	2010	2015	2020
Population	758832	1123942	1035007	1182146	1320276	1474566	1647923	1842950

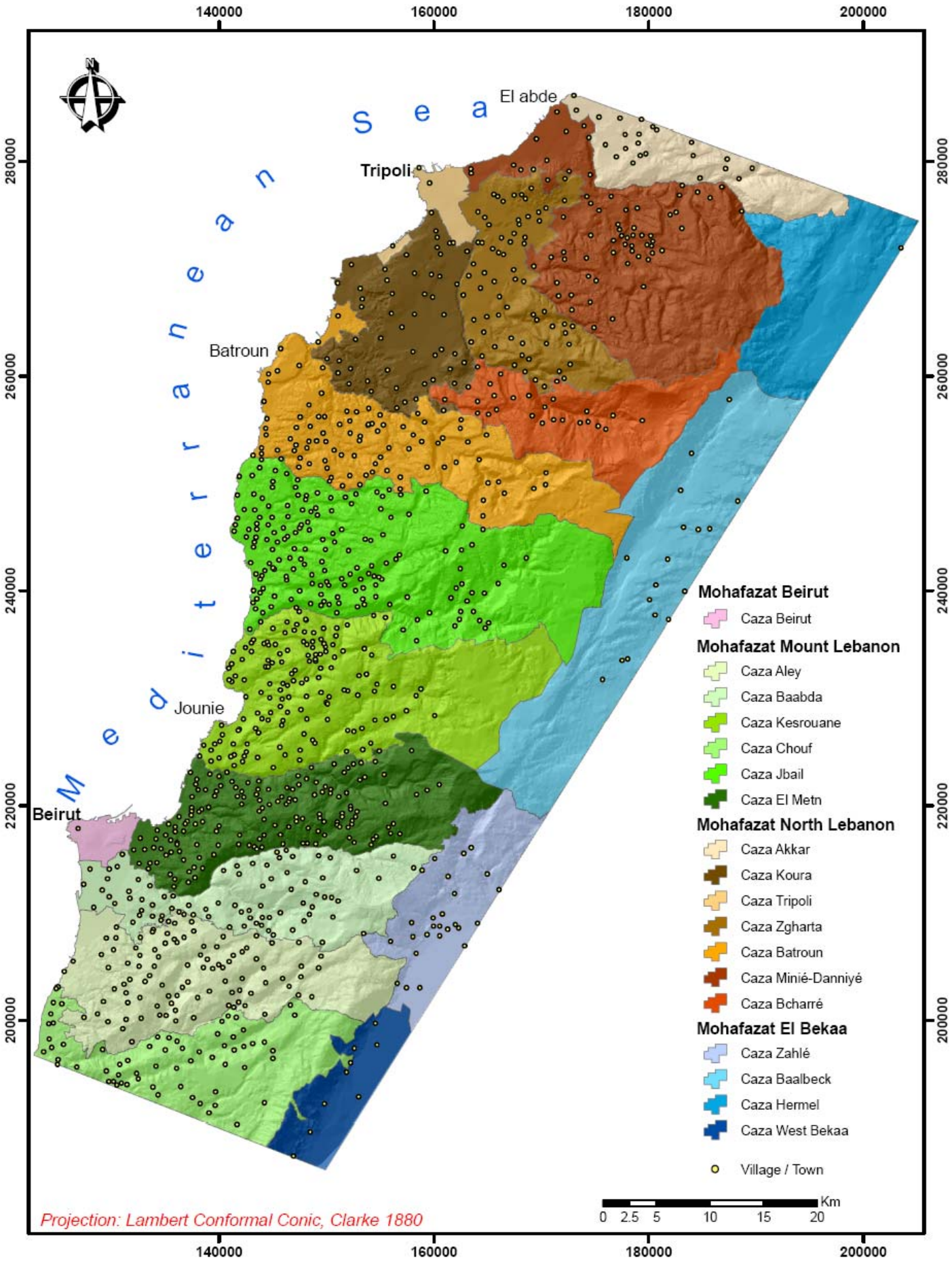

Figure 2.12. Villages locations and their administrative distribution in the study area.

4. Natural hazards in the study area

Certain hazards related to mass movement phenomena occur in the study area and can be described as follows.

4.1. Seismic activity

A main concern in the study region is the frequent and sometimes seriously damaging earthquakes. Historical records indicate that seismic events occurred at several intervals in the past ago **(Table 2.6)**. Beirut for instance, the major city in Lebanon and the study area, has been destroyed many times by earthquakes and tsunamis, most notably in 551 AD. This active seismicity may have direct or indirect impacts on mass movements.

4.2. Soil erosion

Soil erosion is a serious geo-environmental issue causing land degradation in Lebanon. Studies of erosion risk assessment using remote sensing and GIS in the central Lebanese karstic mountains (Qartaba-Jbeil area) showed the following categories of erosion classes: 6% very high, 88% moderate and 6% as low erosion (Bou Kheir *et al.*, 2001a). Around 36% of the Lebanese terrain located in the area of central Lebanon (starting from the coast at the capital Beirut going upward eastward through the mountains) is under high level of water-erosion and, moreover, about 52% of that erosion is observed on the rugged mountainous region (Bou kheir, 2002; Bou Kheir *et al.*, 2006). The high vulnerability of soil and rock cover to erode is due to the intensive run-off common with the sloping terrain, rendering the surface very unstable with various forms of mass movements. Erosion causes damages to vulnerable agricultural lands having shallow soils with low organic matter content, water pollution by soil particles and chemicals, mudflows which may affect urban areas, and of course, economic reverberations.

4.3. Flooding

The irregularity of rainfall, typical of the whole Mediterranean region, frequently leads to long spells of droughts interrupted by torrential downpours which give rise to catastrophic floods. In 1955, a huge flood occurred along Abou Ali river covering an area approximately 400 km^2. Direct damages started in the rural inner areas (Zghorta, Koura), destroying houses, bridges, killing 10-15 persons and over 2000 cattle head. In the Tripoli coastal area (the second largest city in the studied region as well as in Lebanon), where the influence of several branches of the river lie, damages covered about 100 km^2, more than 400 people died, 2000 families found themselves without houses, thousands of acres of citrus plantations were destroyed, 4 bridges of the city collapsed, as well as several events of failure of surficial cover (Khawlie, 1994). After the flood subsided, 1.5 m thick sediments and debris accumulated in many souks or in the houses, and a 200 000 m^3 of sediments were added at the river mouth building a delta (Beydoun, 1976).

Table 2.6. Major earthquake events occurrence (magnitude ≥ 6) and damages affecting the study area (adopted from Plassard and Kogos, 1981; Ambraseys and Barazangi, 1989; Khawlie, 1992; Beydoun, 1997).

Date	Location	Magnitude (equivalent)	Comments
1350 BC	Lebanon coast	6.5	Destruction of Byblos
349 AD	Off coast Beirut	7.0	Destruction at Beirut, Syrian Coast
6 July 551	Off coast Lebanon	7.0 +	Total destruction of Beirut, Chekka and a wide deformation of the landscape (slides) + tsunami
565	Ditto	6.7	Destruction at Baalbeck (Heliopolis)
5 April 991	Bekaa	6.7	Large destruction in Baalbeck and Damascus. Felt as far as Egypt
June-July 1201	Off coast Lebanon	6.0 +	Large seismic event with destruction. Felt in Syria
20 May 1202	Bekaa Valley	6.5	Large destruction at Baalbeck & temples collapsed. Mass failure and destruction in Damas, Tripoli, Tyr
Dec-Jan 1403	Off coast Lebanon	6.0	Sea receded and returned + tsunami
21 July 1752	Ditto	6.0	Destruction at Tripoli + tsunami
30 October 1759	West Bekaa	6.6	Destruction at Safad and Qunaitra. 2000 dead
25 Nov 1759	Bekaa valley	7.5	Destruction of Baalbeck temples. All the Lebanese coast was affected + tsunami + slides 4000 dead
12 May 1856	Off coast Lebanon	6.0 +	Sea receded and returned + tsunami + mass failure
16 March 1956	Roum (Jezzine)	6.0	Epicenter 50 Km from Beirut (at Roum Fault), Mass failure, 6000 houses (Total destruction), 17000 houses (partial destruction), 136 dead

An increasing frequency of flooding disasters is being witnessed in the last 25 years in Lebanon and the eastern Mediterranean basin. This is probably part of global climate change being felt around the world, indicating a trend towards more torrential episodes of rainfall (De Ploey *et al.*, 1991; Joftic *et al.*, 1992; Khawlie, 1999). The consequences of such events are tragic including annual financial losses (15 million dollars), casualties (5 persons dead per year), destruction of houses and agricultural lands, decease of cattles, tremendous damages to structures, utilities and public services (electricity, communications, etc.) and huge slides. A detailed scan of the newspapers between 1971 and 2003 indicate that around 41 major floods occurred in the study area **(Table 2.7)**. In March 2003, floods lasted for 10 days damaging large areas of the Lebanese territory with many slides and mass failure at various locations.

Last and not least in 2004 and 2005, slides occurred in the study area as a consequence of huge floods.

Table 2.7. A detailed scan of the floods and accompanying landslides between 1971 and 2003 as recorded in the Lebanese newspapers.

Month	1971-1981		1982-1992		1993-2003		Dates of occurring floods
	F*	L**	F*	L**	F*	L**	
November (N)	-	-	2	-	2	2	17N (1984), 21N (1986), **16N (1993)**, **7N (1994)**
December (D)	1	-	3	2	3	3	1D (1971), **18D (1984)**, **22D (1986)**, 25D (1987), **5D (1994)**, **10D (1997)**, **17D (1997)**
January (J)	4	1	2	1	2	2	2J (1972), 3J (1978), 9J (1979), **10J (1980)**, 19J (1986), **21J (1992)**, **1J (1994)**, **24J (1996)**
February (F)	3	-	5	-	3	2	3F (1975), 11F (1980), 13F (1982), 14F (1983), 20F (1986), 6F (1992), 12F (1992), **8F (1995)**, **9F (1998)**
March (M)	2	-	3	2	6	3	8M (1978), 12M (1981), **15M (1983)**, **23M (1987)**, 27M (1989), 28M (1996), 28M (1998), 2 M (2003), **5 M (2003)**, **15 M (2003)**, **22 M (2003)**

***F = number of occurring floods**

****L = number of occurring landslides**

Dates written in bold correspond to the occurrence of huge landslides accompanying floods

4.4. Forest fires

Forest fires and other wildfires represent a major threat and cause serious damages in Lebanon. More than 35% of the initial forest cover in Lebanon has deteriorated during the last 40 years leading to a forest cover reduction from 12% (1973) to less than 7% of the Lebanese territory nowadays (METAP, 1995; Talhouk *et al.*, 2001). Forestry service reports indicate that a high number of forest fire events take place each year (e.g., 1413 forest fires in 1997) with resultant large burnt areas (e.g., 3000 ha during 1998).

In most burnt areas, when the damage of vegetation cover is followed by violent rainstorms, the unprotected topsoil is subject to severe erosion and mass movement processes. If erosion is not stopped, further increase in runoff, and erosion on sloping ground may ultimately destroy the productive value of the land (Bou kheir *et al.*, 2001b, c). The increasing frequency and intensity of fires is a threat to the floristic species diversity in Lebanon, even those plant communities (e.g., maquis, garrigue, some pine communities) which have been adapted to naturally-occurring fires or depend on fires to maintain themselves **(Figure 2.13)**. These plant communities can play a major role in stabilizing the terrain via their roots or acting as a direct cover against the impact of rainfall. The potential loss of life and property is considered the most harmful negative consequences of widespread forest fires.

Figure 2.13. Forest fire influence in triggering landslides in Ramlieh area (Mount Lebanon).

(a) Photo taken in 1998 before fire occurrence

(b) Photo taken in 2003 showing sliding effect due to the forest cover destruction

5. Mass movements (MM) in Lebanon

Based on Varne's classification scheme (1958) accounting for types of materials and movements, and on the classification of typical mass movements (MM) in Lebanon (Khawlie and Hassanain, 1979, 1984a), five types of MM are common in the study area as follows: rock and debris falls (see Figure 2.1), earth creep **(Figure 2.14),** slides **(Figure 2.15)**, and earth flow **(see Figure 3.1)**.

Figure 2.14. Bending of the trees stem giving an indication of an earth creep movement in Zahle (Bekaa).

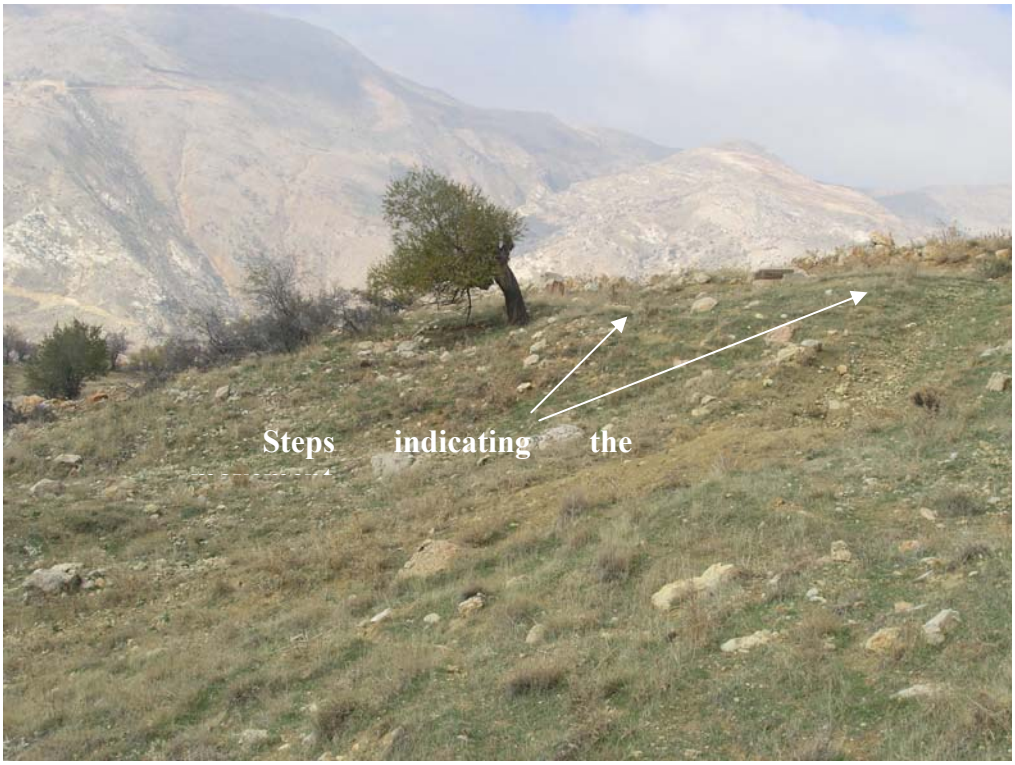

5.1. Examples of mass movements (MM) in Lebanon

One of the classical known spots in Lebanon seriously affected by mass movements is the Hammana area, situated in Mount Lebanon at 1170 m altitude **(Figure 2.15)**. It shows an amphitheatrical outline consisting of cliffs and their sloping perimeters (this is designed the erosional zone), and a central hummocky trough (the depositional zone) (Khawlie and Hassanain, 1979, 1984a). The climatic, human and engineering geological parameters are acting simultaneously towards enhancing mass movements.

Figure 2.15. Unstable Hammana area with several failure phenomena.

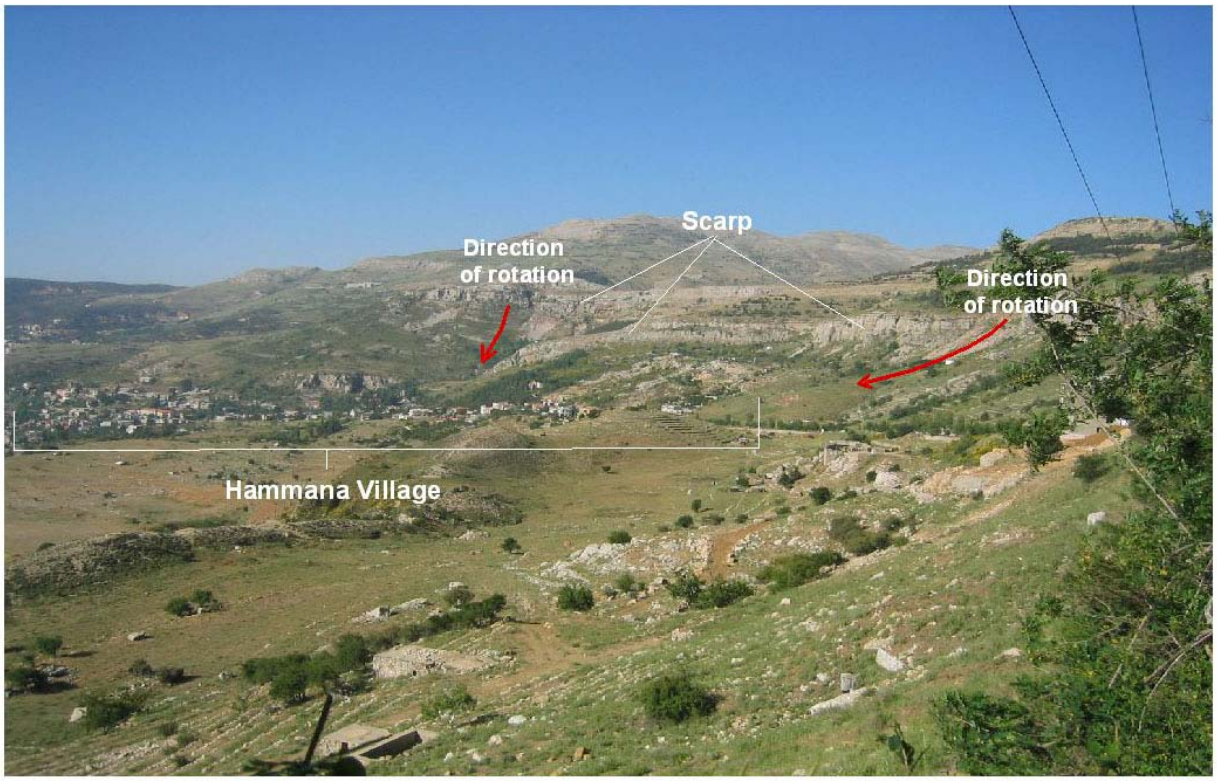

Three modes of failure are recognized in this area: large mass, single blocks and composite failures. Large mass failures involve toppling and translational slides related to the cliff-forming units, as well as rotational slides common in the relatively poorly cemented sandstones, weathered basalts and the surficial cover. Single mass failures involve wedge separation and are associated with some compact sandstone beds, the fresh basalts, and limestone units. The composite type applies to cases where more than one mode of failure develops simultaneously.

Previous studies and observations described movements in this area usually occurring at elevated spots with abundant water, mostly along inter-bedded competent and incompetent units. Cliffs develop debris falls and screes which eventually are dissected into small valleys. The materials making up the cover which develop on these features are prone to move. The movement starts gradually and is followed by a sudden rupture. This may recur several times in the same place before a slope becomes stabilized. Moving masses range in area between 2 x 2 m to 20 x 50 m and can be dangerous to the local community. Cracks in houses and roads,

destruction of agricultural terraces, and scarps of different sizes are very common in the area. Major movements occurred in 1860, 1914, 1924, 1948, 1954, 1956, 1960, and 1983. Minor movements occurred in other years. Some large movements are correlated with major earthquakes especially those of 1924 and 1956 (Khawlie and Hassanain, 1984a). Small seismic tremors that would traverse the Hammana area on almost daily basis could promote also mass movements to a wide extent. In addition, periods of heavy precipitation in the mid to late winter season, as well as man-induced activities including the alteration of landforms such as in road and residential construction, quarrying, or changing the water regime in irrigation and drainage diversion can be considered major causes inducing movements in the area.

Another distinguishable MM in the study area, which is well-known by geologists, is the earth flow of Aaqoura area situated in the northern part of Mount Lebanon. It is active and moves several mm/year (Tavitian, 1974) subjecting the agricultural and residential properties to high risk. For example, on 25th March 2000, several cultivated lands were totally destroyed.

Other mass movements are recognized without being the subject of particular studies. In the year 1978, An-Nahar and Al Diar daily newspapers noted that the region of Shila in Zahlé, situated in the Bekaa valley, witnessed a large landslide due to the presence of large amounts of water caused by some broken pipe lines, in the unconsolidated sand dunes and steep slopes (20 degrees). The location of Mazrait Bani Assaf, situated at 51 km east of Beirut, with a highly karstified limestone witnesses in the same year a debris flow moving down 40 m and the sediments covered an area of about 30000 m^2. The village of Baalchmay in the Chouf region (Mount Lebanon) witnessed also in 1978 a landslide having 600 m length and a maximum width of 250 m. Its movement started long back but was too slow until the heavy precipitation in the year 1978 triggered the disastrous event. Other recent mass movements can also be noticed. For example, on 9th January 1996, heavy precipitation triggered a large landslide threatening several houses cutting off completely the road between Laqlouq and Tannourine. On 16th February 2000, a landslide took place in Biaqout in Mount Lebanon destroying two buildings completely and one partially. The principal cause of this disaster was the presence of a quarry just beneath those residential units. The removal or weakening of the supportive rocks led to the instability which triggered the slides.

5.2. Socio-economic impacts of MM in Lebanon

Estimations over the last 40 years indicate that mass movements cost each year 10-15 millions of US dollars in this small country with numerous fatalities and injuries (Khawlie, 2000). In fact, some concrete examples can give an idea about the importance of mass movement occurrence damages. The slide of Mazrait Bani Assaf mentioned above caused tremendous damages, i.e. complete destruction of several farmlands, partial destruction of the irrigation system, and occurrence of some fractures in the earth next to some houses with huge resettlement of the ground at the main road access to the village. On 18 March 1992, a huge slide, due to an avalanche, occurred in Hazerta near Zahlé which destroyed several houses and 20 people died. On 25th March 2000, an avalanche destroyed 10 houses and several sky resorts in Aayoun Orghouch (Mount Lebanon) and a huge earth flow occurred in Aaqoura area destroying many cultivated lands.

5.3. Mitigation measures

In spite of the bad impacts of MM in the study area, appropriate management plans are still lacking. Neither a hazard/risk map exists, nor have strategies been designed yet in Lebanon or in the study area for this purpose. Moreover, lack of awareness of the community clearly reflects a misunderstanding of the risks they are facing, and uncaring of the contractors in implementing geotechnical site analysis which may raise the cost value; in addition to the lack of obligatory preventive measures by engineering firms and the legislation **(Figure 2.16).** Only minor and local mitigation measures are being applied at specific sites. Terraces are obvious at many localities with different support specifications, though some are not quite stable from an engineering point of view. The workability during terrace construction loosens soils compactness and serves in increasing the stoniness soil ratio, thus reducing their quality drastically and preparing them for displacement. In many cases, notably when soils are rich in clay, the constructed terraces are subject to collapse due to clay swelling. This means that the protection barriers (terraces) do not properly serve their purpose, and in many instances land degradation is at a level exceeding that if they were not worked out **(Figure 2.17).**

Figure 2.16. Bad construction on a high risk area (relatively unstable Albian C3) rendering the newly constructed buildings unstable.

(a) Toppling of rocks triggered by heavy precipitation blocked the Mansourieh main highway partially (Mount

(b) Residents had evacuated and the building is for sale.

Another type of protective practices is represented by human-made channels, parallel to road alignment (0.25 m^2) or through some agricultural lands (> 1 m^2) and retaining walls or embankments which serve to prevent mass movements on road cuts or unstable construction sites. But these latter measures do not show reliable results. Rarely a wet season goes by without a catastrophic event taking place of collapse of these measures due to inappropriate construction and lack of maintenance **(Figure 2.18)**.

In addition, other barrier systems are newly introduced, i.e. reducing the slope angle and covering it with a retaining net **(Figure 2.19a)**. Because of their high construction expense, they are only reserved for specific locations. Nevertheless, the lack of proper geotechnical studies reduced in some places the maximum benefit and reliability of these barriers against slope instabilities. An example is the international Beirut-Damascus highway in Hammana-

Mdairej area, where the barriers have been installed to prevent erosional processes **(Figure 2.19b)**.

Figure 2.17. Un-maintained old terraces leading to degradation and increased land instability.

Figure 2.18. Collapsed retaining walls on road cut of Bikfaya area (Mount Lebanon) as a result of inappropriate wall construction.

Figure 2.19. Mass failure control by reducing slope angle and protective nets along Beirut-Damascus international highway (Hammana – Mdairej area).

However, the type of used barriers, their bad structuring, the characteristic nature of the terrain (marls and marly limestone) and high precipitation, subject the rocks to volume change due to an increase in water pressure, which led to a rotational slide. Therefore, this inappropriate design was not able to cope with the problem, and guarantee optimal safety for people crossing the highway. Hence, the implementation of effective surface cover conservation measures has to be preceded by mass movement hazard assessment. The measures consist of avoiding areas with high risk, or making a non conflicting use of areas with moderate risk, or applying special engineering design and construction for correcting adverse conditions.

5.4. Existing studies on MM in Lebanon

From what has preceded, studies dealing with mass movements (MM) in Lebanon seem to be few and mostly descriptive. Few articles tackled the problem. Searle (1972) detailed the geotechnical properties of the unstable Cretaceous clay-shale formations in Lebanon. Tavitian (1974) studied the Aquoura earthflow giving the engineering properties of the materials and slope stability. Aker (1980) presented reports about the subject relating landslide occurrence to periods of severe precipitation and improper land utilization. Khawlie and Hassanain (1979, 1984a, b) studied the phenomenon over several areas in Lebanon giving the types and distinctive features of various occurrences. They related it to different natural and human causes, interpreting both its geological and engineering dimensions. Moreover, Khawlie (1985) presented a national plan for assessing mass movements in Lebanon. Other studies have dealt indirectly with the subject focusing on instability of surficial materials, e.g. the engineering geological evaluation of marls (Khawlie and Ghalayini, 1985), or the analysis of the terrain and materials in assessing stability of highways (Khawlie and A'war, 1992), or the inherent lithological and geotechnical variability of the basal Cretaceous sandstone (Khawlie and Touma, 1993). The majority of these studies treat the mass movement phenomenon depending on the purpose of field work. The application of remote sensing and GIS in general are recent entries in the country, and being used in assessing processes of land degradation like the assessment of soil-water erosion (Bou Kheir, 2002).

6. Conclusion

This chapter demonstrates the widespread of MM occurrence and their harmful impacts on the society and the environment, showing that government solutions and resource management plans are still lacking. The high vulnerability of the area is due to a combination of weak geology, movement-prone surface cover, steep slopes, heavy torrential rainfall, active tectonic movement, rapid land use change and unchecked human interference. In fact, the chaotic and rapid urban expansion over the last years in Lebanon has aggravated the MM impacts since a large portion of the population occupies areas with high MM hazard. Therefore, due to the few available studies on MM, elaborating precise MM hazard maps of the study area is crucial for preventing their bad impacts, and a necessary scientific contribution for sustainable management plans. These maps can be easily implemented using remote sensing and GIS techniques. In this concern, the following chapters will focus on the utilization of satellite imageries with different resolutions (spatial, temporal and spectral) and various processing techniques that help in MM delineation. Similarly, GIS techniques can facilitate the integration of multiple data layers and spatial simulation to explore MM cause-effect relationships and hazard zonation.

- III -

Comparative analysis of Satellite images in assessing mass movements in the Study area

CHAPTER III

Comparative analysis of Satellite images in assessing mass movements in the Study area

1. Introduction

Satellite images have been used worldwide to visually identify large landslides without differentiating other types of MM (Carrara *et al.*, 1995; Verstappen, 1995; Chowdhury and Flentje, 1996; Liener *et al.*, 1996; Manotvani *et al.*, 1996; Irigaray *et al.*, 1996; Astaras *et al.*, 1997; Eyers *et al.*, 1988; Yuan *et al.*, 1998; Duan and Grant, 2000; Wetzel *et al.*, 2000; Zhou and Li, 2000; De la ville *et al.*, 2002; Hervas *et al.*, 2003). The overall mapping errors of visual image interpretation may vary between 60 and 90% when different surveyors are making the interpretation and judgment, even of the same area (Fookes *et al.*, 1991; Carrara *et al.*, 1992; Guzzetti, 1993; van Westen, 1993). Moreover, the reliability in detecting mass movements can differ to a wide extent according to the processing technique used and the sensor chosen. The new generation of commercial satellites with very high ground resolution like IKONOS (1 m) and Quickbird (67 cm) permits the mapping of different types of MM with conditions quite similar to aerial photographs, but their high cost limits their use in frequent sequences and for wide areas, especially in the developing countries. The common high ground resolution satellite images, such as SPOT 1 to 4-HRV, Landsat TM and IRS1-2, are less expensive, but their efficiency needs to be comparatively assessed. In this context, the chapter aims to assess the choice of resolution satellite data-types and image processing techniques for investigating MM.

2. Methodology

2.1. Approach

Our approach consists in measuring the efficiency of various common satellite data types for identification of mass movements (MM), which are recognized through well defined and objective characteristics. The choice of the satellite data types is based on experience (expertise) and their frequent use in revealing the main characteristic features of MM.

The concept of satellite data type is used in this study. A satellite data type is issued from a given sensor (e.g., SPOT-HRV stereo-couple), to which a given suite of processing (e.g., anaglyph coloration) has been applied, to finally result in a given type of image. The processing applied to a given scene dataset is chosen according to the characteristics of the objects to be detected and the properties of the sensors. For instance, anaglyph images of SPOT-HRV stereo-couples were produced because stereoscopy is the most important issue for geomorphological analysis of MM that the SPOT system can offer.

The image characteristics of the MM features were studied. The observation of the image characteristics is visual, but the identification is logical, and based on associations of image characteristics forming the landscape units. A two steps process was used comprising, first a detection stage and then an interpretation stage. This is necessary because the MM features that are of interest for interpretation have first to be visible with sufficient contrast in

the images. The features, taken together, must logically lead to the conclusion that they are indicative of MM.

Analyzing a satellite data type for MM identification consists of: 1) considering the already known MM, define some of their characteristics and determine if they can be observed or not; then examine if the detected characters permit identification; 2) try to discover unknown MM, searching for some of their characteristics, examine if they permit MM identification, and then check the interpretation in the field and/or with very high resolution image.

A common difficulty in comparative studies of satellite images is to assess how much they are efficient for analysis in certain objects. In this work, it was decided to base our measurement on an assessment chart assembling all the MM known in the study area. This knowledge is the sum of the MM that were already mapped before our analyses, plus those that were discovered in this study from various satellite data types, and then checked in the field. The chart is taken as the reference for measuring the efficiency of MM identification through remote sensing. The measure of efficiency of a given image-type is the percentage of the accuracy of different types of MM that were detected (identified) on this data type and verified through field observations using a Global Positioning System with a precision of 2.5 m. A MM unit is counted as one, whatever is its size.

2.2. Image characteristics of MM features

2.2.1. Elements of visual interpretation

Various types of mass movements (landslides, rock and debris falls, and earth flows) were delineated in the study area. For each category, satellite image analysis is based on a systematic observation and identification of key elements, which refer to different image units that correspond to landscape units. These properties (**Table 3.1**) are miscellaneous and differ according to the sensor and the type of MM. Radar, an active system, has proved to be efficient for the evaluation of mass movements in gentle sloping areas (Chorowicz *et al.*, 1998). Nevertheless, this evaluation shows difficulties in our study area and it will be discussed later in this work (Chapter 7).

Visual interpretation of passive sensor imagery used in the case study depends not only on spectral signatures of image units, but also on other properties, i.e albedo, 2D morphology, 3D morphology, micro-texture (texture at pixel scale), macro-texture (texture at scale of large groups of pixels), and neighborhood context (Chorowicz and Deroin, 2003) (**Table 3.1**). Spectral signatures and albedo relate to the physico-chemical properties of the ground surfaces. 2D and 3D shapes, micro-texture, macro-texture and context relate to the well organized spatial distribution of the scanned ground pixels. 3D morphology is also expressed by variations in intensity according to slope angles against sun orientation. It plays an important role in differentiating properties, due to the distinct topographic changes along the boundary between different landforms.

a. Landslides' characteristics

Albedo and spectral signatures of the displaced rocks, in contrast with their basement, depend on the lithology. When the displaced rocks are clays, moving upon marls, they show darker tones in the VIS-NIR range once compared to the surrounding **(Figures 3.1f/g, 3.2f/g, 3.3f/g)**, because water and vegetation are more persistent in impermeable grounds.

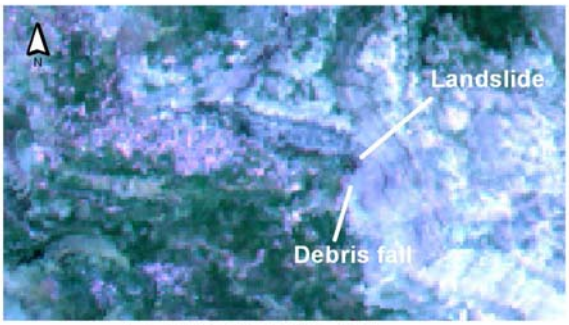

a) LANDSAT TM (3,5,7)

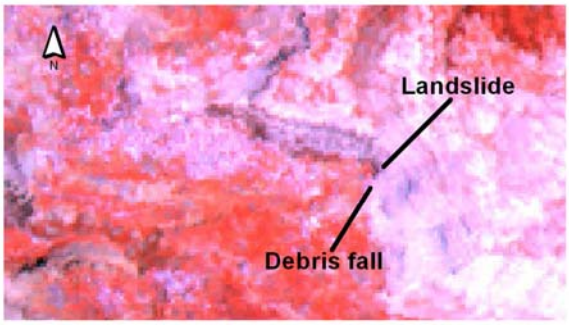

b) LANDSAT TM (4,5,7)

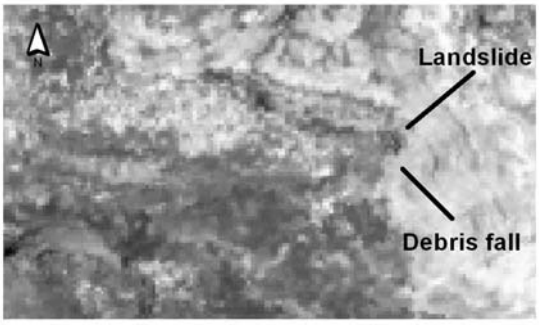

c) PCA of LANDSAT TM

d) Pan-sharpened IRS + LANDSAT

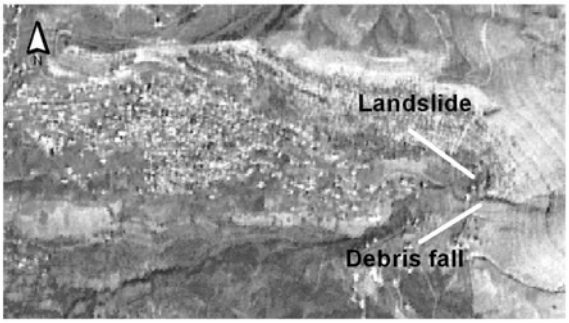

e) PCA (IRS + LANDSAT)

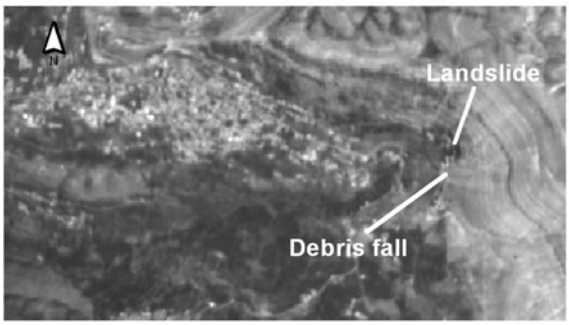

f) SPOT 4

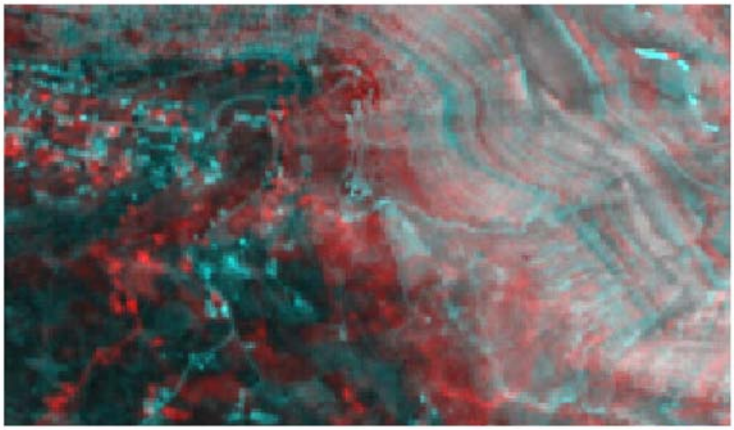

g) Anaglyph of SPOT4

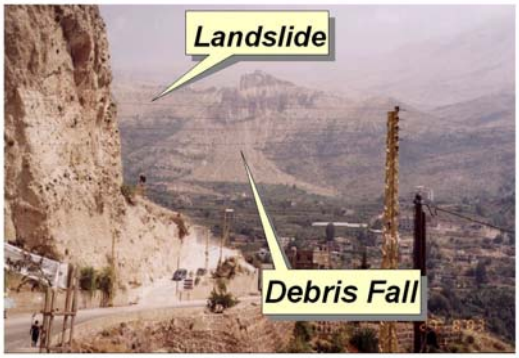

h) Photograph of Bcharee area

Figure 3.1. Landslide and debris fall of Bcharee area (North Lebanon).

Use special anaglyph lenses

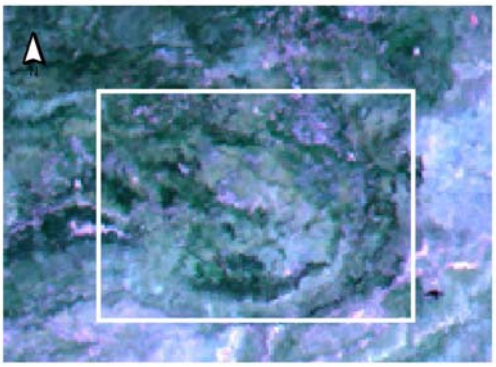

a) LANDSAT TM (3,5,7)

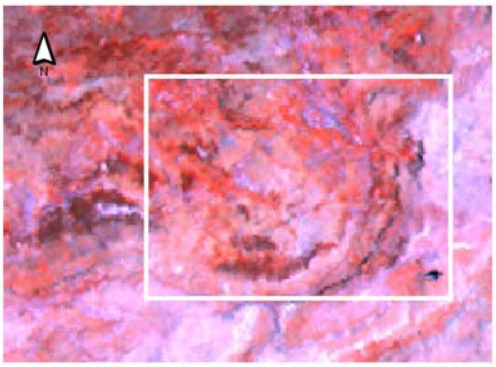

b) LANDSAT TM (4,5,7)

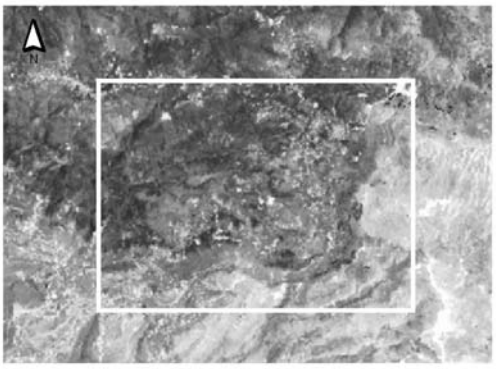

c) PCA of LANDSAT TM

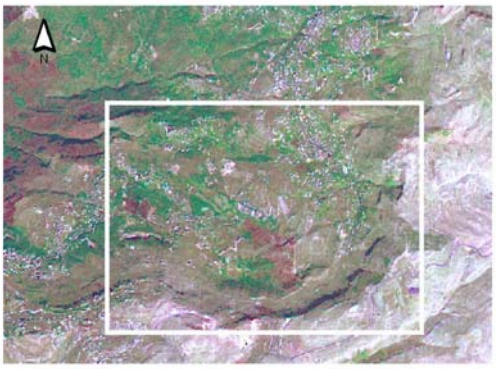

d) Pan-Sharpen IRS + LANDSAT

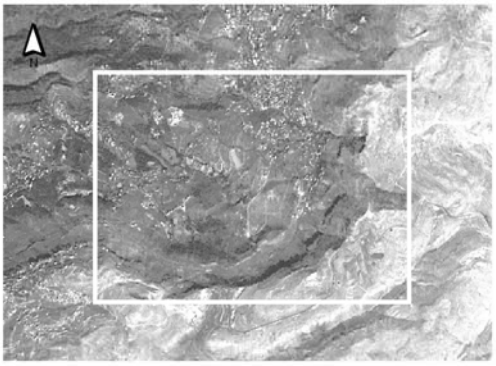

e) PCA (IRS + LANDSAT)

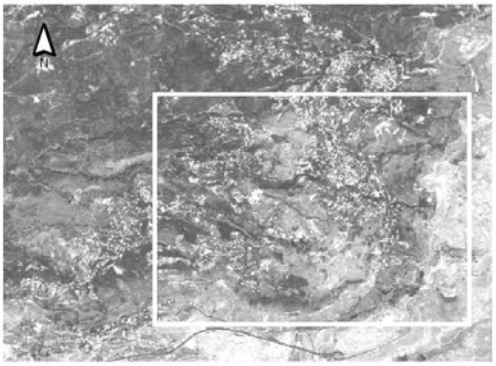

f) SPOT 4

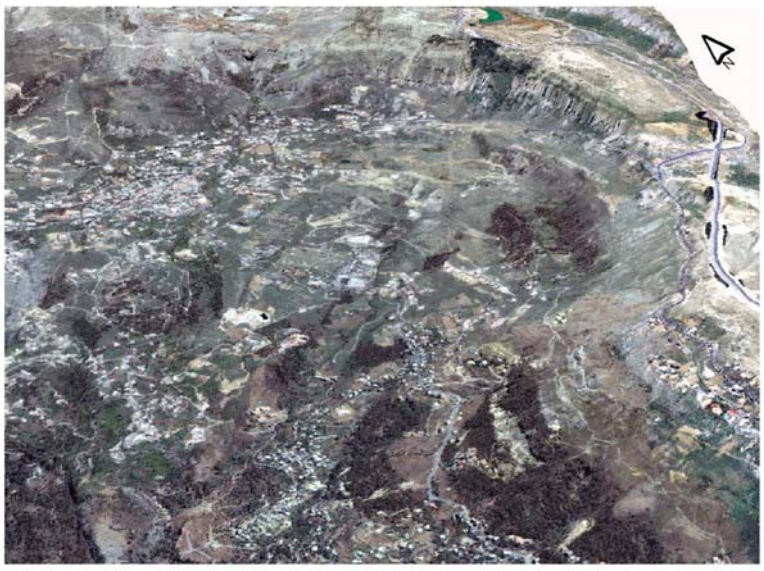

g) A 3D Pan-sharpened IKONOS

Figure 3.2. The large landslide of Hammana area (Mount Lebanon).

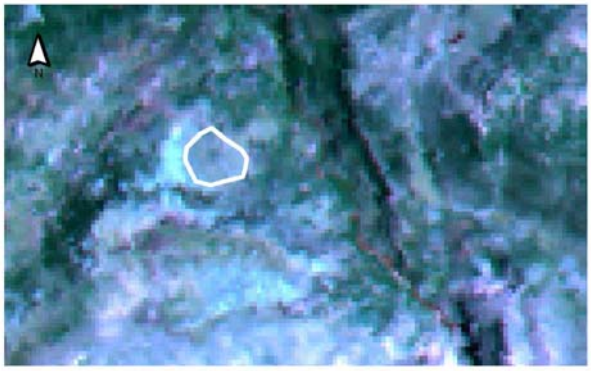

a) LANDSAT TM (3,5,7)

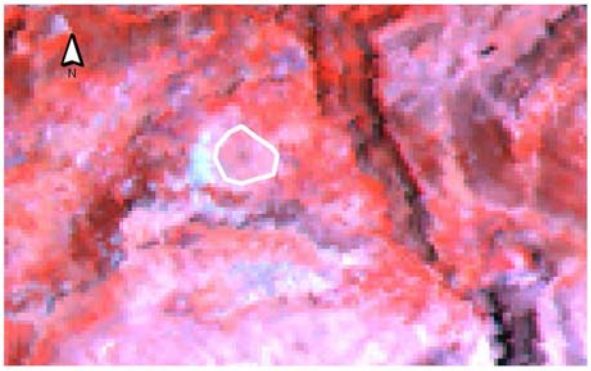

b) LANDSAT TM (4,5,7)

c) PCA of LANDSAT TM

d) Pan-sharpened IRS + LANDSAT

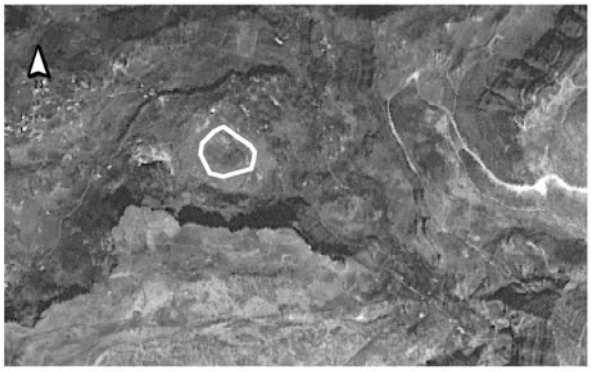

e) PCA (IRS + LANDSAT)

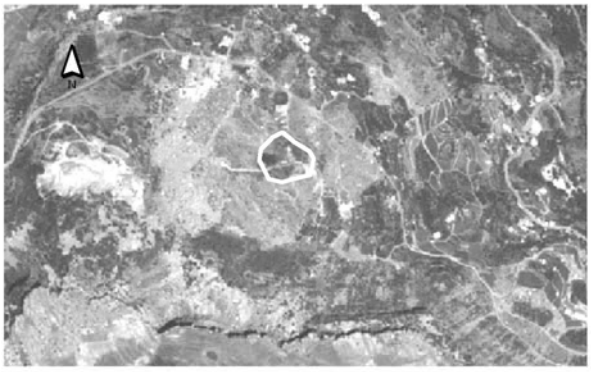

f) SPOT 4

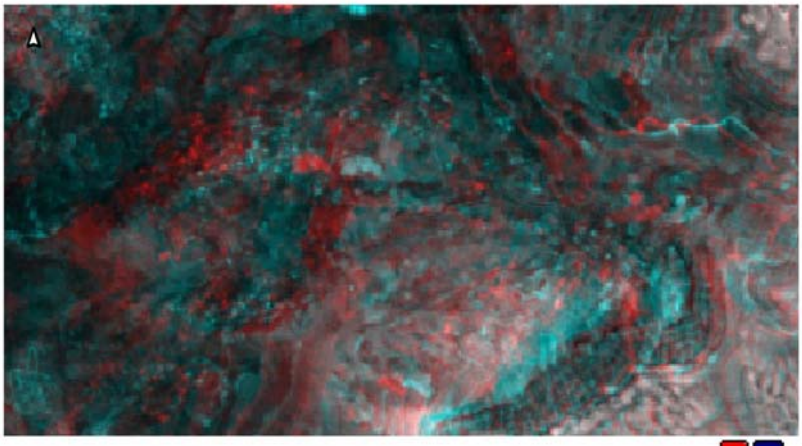

g) Anaglyph of SPOT4

Figure 3.3. Landslide of Ehmej area (North Lebanon).

When the displaced rocks like sandstones, limestone, or marls, are moving upon clay, soil moisture of MM will be low, and vegetation cover will be poor. Hence, light toned areas appearing in the VIS-NIR range can then give an idea about fresh landslides **(Figure 3.4)**.

Table 3.1. Relationships between image units' characteristics and the properties of landscape units in case of passive sensor.

Landscape units' properties	Image units' characteristics
	2D shape
	3D shape
Spatial distribution of ground pixels	Micro-texture
	Macro-texture
	Neighborhood context
Slope angle	3D shape
	Albedo
Physico-chemical properties	Albedo
	Spectral signature

The 2D morphology is that of sub-rounded or elongate image units. In 3D morphology, landslides have an arcuate back (upslope) scarp, a convex form in cross-section, and a lobed front **(Figures 3.1f/g, 3.2f/g, 3.3f/g)**. The micro-texture and the macro-texture are heterogeneous, because of the irregularities of the surface of the slid rocks. The neighborhood context is that of anomalies occurring in rather homogeneous talus at the scarp foot.

b. Rock and debris falls' characteristics

One of the main problems in identifying rock and debris falls by spectral signatures and albedo is the spectral similarity of the source bare rocks and fallen debris. The neighborhood context, however, is quite characteristic, debris originating from the weathering process and subsequent transport at the foot of the cliff-forming compact rock in mountainous areas. The neighborhood context can be determined by superimposing the available geological maps (Dubertret, 1945) and images on the digital terrain model DTM. The zones of detachment (wall forming hard rocks, generally well mapped) can then be differentiated from zones of accumulation (soft bedrock mapped).

In 2D morphology, sub-rounded shapes tend to characterize areas under the action of rock and debris falls **(Figures 3.1, 3.5)**. Rock falls also typically build up debris cones, usually of high albedo **(Figures 3.1, 3.5)**. In 3D morphology, zones of accumulation have convex and rough slopes **(Figure 3.5)**. These surface irregularities also show up by variable micro-texture and a spotty macro-texture.

c. Earth flows' characteristics

Earth flows are repeatedly initiated in a neighborhood context of contact zones between rock walls and, unstable overlying rocks on one side, and talus slopes on the other side. In 2D, they form large surfaces, but without clear 3D features. The micro- and macro-textures are variable due to the irregular surface at local scale.

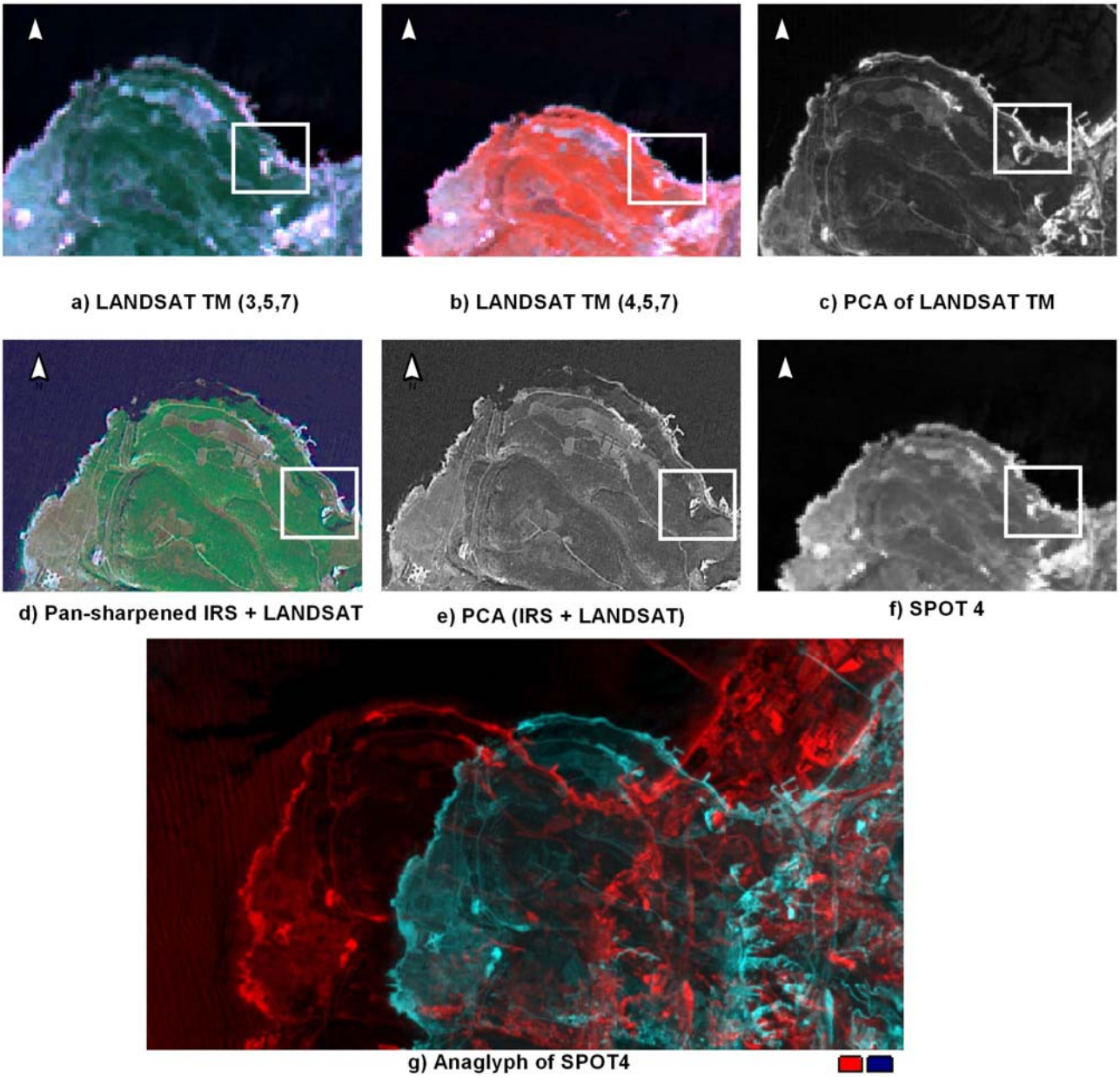

Figure 3.4. Ancient landslides triggered by a huge earthquake affecting the marls of the Senonian in Saidet El Nourieh (North Lebanon).

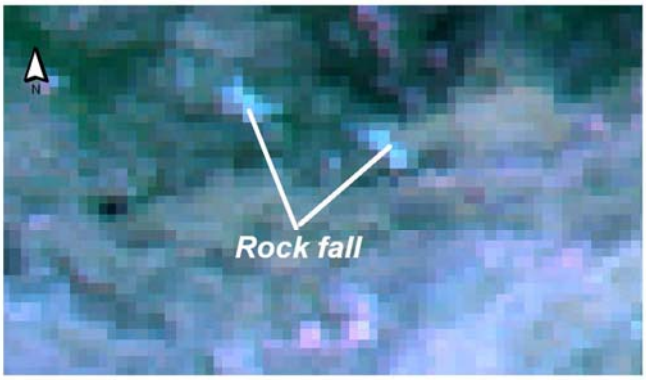

a) LANDSAT TM (3,5,7)

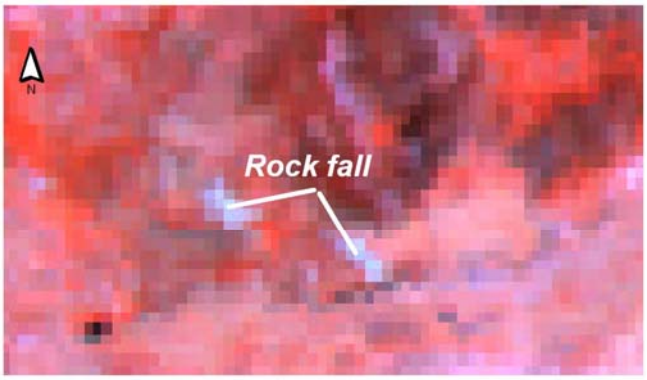

b) LANDSAT TM (4,5,7)

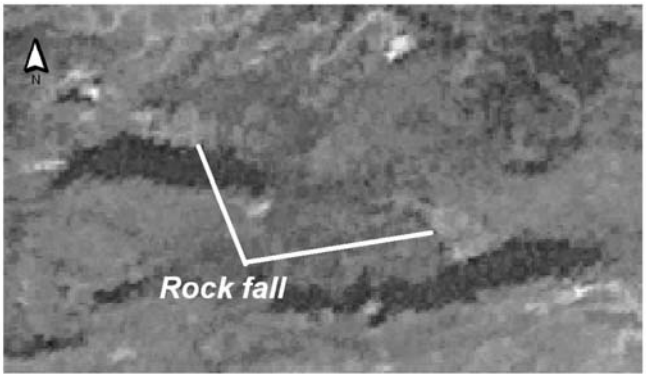

c) PCA of LANDSAT TM

d) Pan-sharpened IRS + LANDSAT

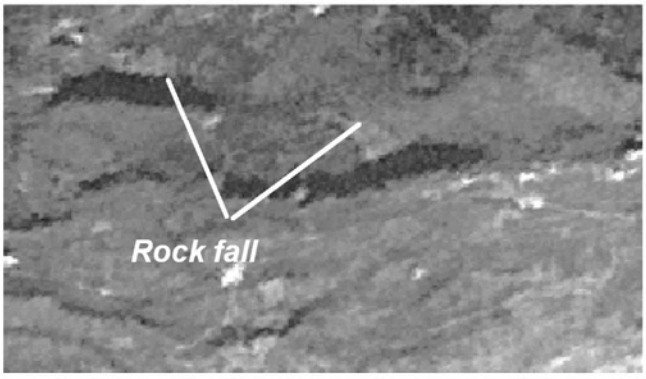

e) PCA (IRS + LANDSAT)

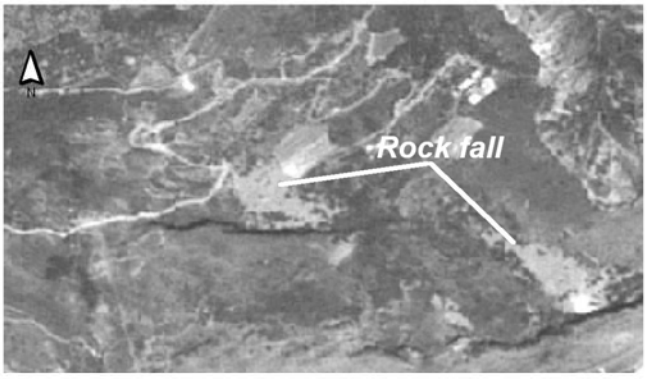

f) SPOT 4

g) A 3D Pan-Sharpened IKONOS

h) Potograph of the rock fall

Figure 3.5. Rockfall of the Ramlieh area (Mount Lebanon).

The displaced rocks are generally clayey, and consequently wet, with effects on the (low) values in VIS-NIR bands. The water content is high, and ponds may form **(Figure 3.6)**.

2.2.2. Ancillary data

Ancillary data (geology and DTM) were used in order to assist visual interpretation of satellite imageries. Lithologies were extracted from scanned and registered geological maps of Lebanon at 1:50,000 scale, specifically the sheets of Hamidieh, Halba, Batroun, Tripoli, Sir El Dannieh, Jbail, Qartaba, Baalbeck, Beirut, Zahle, Rayak, Saida, Jezzine and Rachaya (Dubertret, 1945). All the maps were digitized using heads up digitizing. Cleaning and building procedures were performed on existing polygons using ArcGIS 8.3.

A digital terrain model (DTM) was generated for the area from fourteen topographic sheet maps at scale 1:50,000 with contour intervals of 50 m (DGA, 1963). Contour lines of each topographic sheet were digitized separately and then the contour lines of all sheets were appended and joined together using ArcGIS software (version 8.3). Stream-lines and point elevation data were interpolated together with the contour lines in order to provide important structural information about the landscape. Interpolation based on triangulation methods was achieved (Abdallah *et al.*, 2006b).

2.2.3. Satellite data types

a. Choice

Considering the elements of visual interpretation that can be considered in the detection of mass movements, three optical sensors (Landsat TM, SPOT-4 P and IRS-1C Pan) that are commonly used in MM remote sensing were tested (Carper *et al.*, 1990; Guzzetti *et al.*, 1999; Mantovani *et al.*, 1996; Hervas *et al.*, 2003). Our choice is also based on the ease availability and relatively low cost of these data. For each of the satellite data types, the most common and evident image processing that can be applied using commercial software was applied.

All images have been registered and ortho-rectified using the generated DTM (ground pixel size, 50 m). Ortho-rectification is applied in order to minimize the geometric distortions caused by viewing geometry, platform instability, earth curvature and rotation, which are common in space borne remotely sensed data, especially in Lebanon mountainous areas where the high altitude variations within the frame of the image introduce additional distortions.

b. Sensors and processing

Landsat TM

The medium spatial resolution (30 m) Landsat TM image acquired on April 2003 comprises 7 spectral bands as usual. TM1 to TM5 and TM 7 are in the visible and near- to middle- infrared ranges. Band 6, in the thermal range, was not used. This left 6 bands to exploit for MM detection.

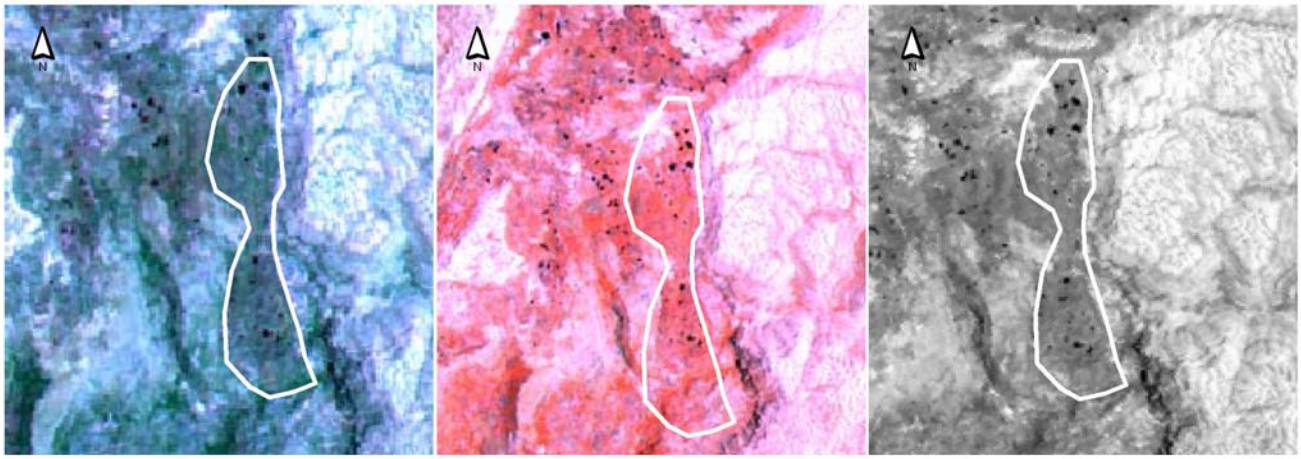

a) LANDSAT TM (3,5,7) b) LANDSAT TM (4,5,7) c) PCA of LANDSAT TM

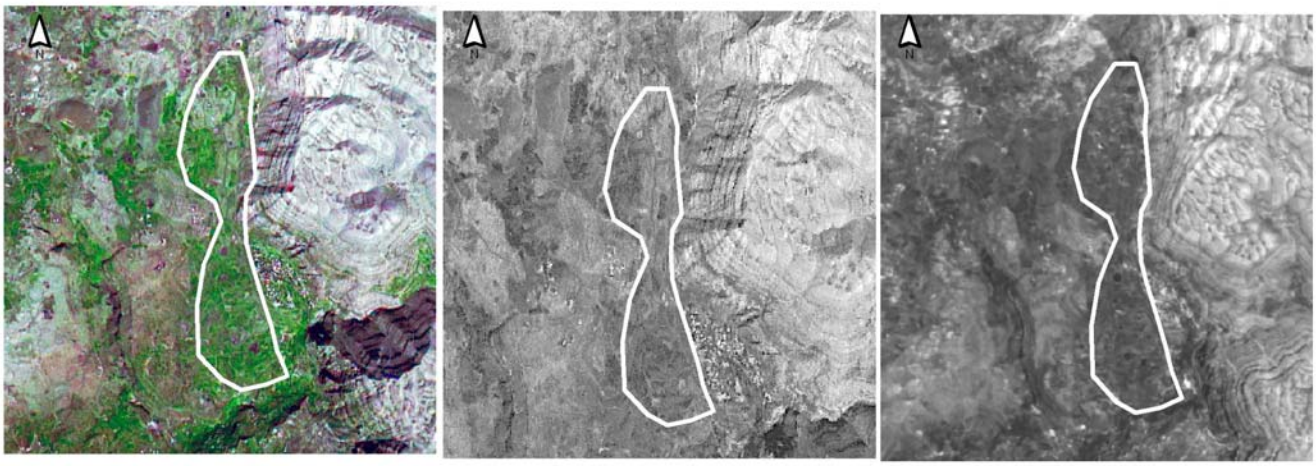

d) Pan-sharpened IRS + LANDSAT e) PCA (IRS + LANDSAT) f) SPOT 4

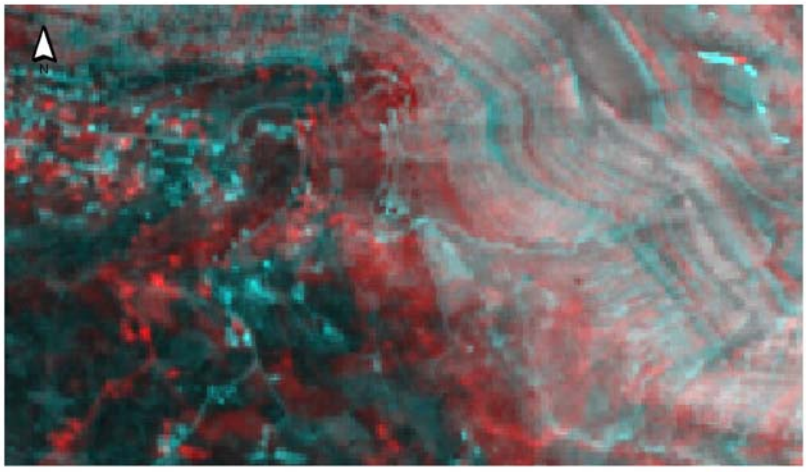

g) Anaglyph of SPOT4

h) Photograph of the Aaqoura flow showing the artificial water harvesting ponds

Figure 3.6. The huge (1.3 sq.Km) earth flow of Aaqoura area (delineated).

A radiometric correction was applied using Erdas imagine software (version 8.7) on Landsat TM images to achieve the means and variance equalization, i.e. the conformity. Red-green-blue false-color-composite (FCC) images were displayed for all possible band combinations.

Furthermore, a Principal Component Analysis (PCA) was applied on the six TM bands (visible, NIR, MIR, SWIR). This method enables to project all pixels of the multi-spectral image on axes that do not correlate (have the same information). The three first axes integrate almost 95% of the overall spectral information corresponding to the sum of all bands. Most of the information, which was distributed among 6 bands, can now be presented in a unique image made from the three first principal components files (PCA Landsat TM – see **Table 3.2**).

SPOT-4 Pan

The four scenes forming two panchromatic stereo-pair SPOT 4 images that were chosen are of high ground resolution (10 m). They were acquired with incident angles of 2.3 and 30.3 degrees, dated on 31/5/2002 and 1/6/2002, respectively. The close dates of image acquisition and the appropriate incident angles between the two SPOT-P scenes have been taken into account in the choice.

A Kernel 3 x 3-edge enhancement filter was applied on the SPOT panchromatic images. This process emphasizes the detailed high frequency image components and deemphasizes more general low frequency information. Thus, it helped to remove some undesired remnant changes, simply representing land use or vegetation growth changes in polygonal-shaped crop parcels, as well as those due to new houses and new easily identified road segments. Then, the two panchromatic stereo-pair SPOT 4-P images were processed using Geoimage software in order to obtain an anaglyph image setting the needed 3-D properties for visual interpretation.

IRS-1C Pan

The high-resolution (6 m) panchromatic band of the Indian Research Satellite image IRS-1C was acquired on April 2003. The good radiometric quality, snow free coverage, leaf-off state of forests of the most recent archive satellite data were behind the selection.

A dynamic stretching allowing achieving the means and variance equalization and a Kernel filter of 3 x 3-edge enhancement were applied. Landsat TM bands were co-registered with the IRS pan image making up the poor spatial resolution of Landsat TM image and increasing clarity. To allow better differentiation of vegetation and water content, a band combination of RGB 247 from Landsat TM image was selected to pan-fuse with the IRS-1C. The resulting image (Pan-sharpen Landsat TM-IRS of **Table 3.2**) is characterized by a ground resolution of 6 m. PCA was also applied to the 6 bands of pan-sharpen Landsat TM-IRS image (**Table 3.2**).

Ikonos

In addition, three pan-fused IKONOS (1 m) scene images were used to compare their usefulness for detecting mass movements with the previous images. They have been acquired also in April 2003 and cover 50 km^2 of the study area, shared into three zones (Hammana, Ramlieh and Saidet El Nourieh) that witnessed major mass movements for long periods. The

IKONOS images were draped on more precise 10 m contour interval DTM to assure better visual quality.

3. Results and discussion

3.1. Measurement of accuracy

Visual interpretation of the different satellite data types allowed delineating the various types of mass movements (landslides, rock and debris falls, earth flows). Nevertheless, it was difficult to detect and delineate earth creep through this type of technique. Field truthing campaigns were raised, with complementary use of the Ikonos imagery.

The resulting chart, comprising MM that were known before our study, plus those discovered using the various satellite data types, is the base for measuring the usefulness of different sensors of remote sensing in identifying MMs.

The number of MM types observed for each satellite data type was counted **(Table 3.2)**. Then, an accuracy level was retained as the percentage against total number of MM.

Table 3.2. Accuracy assessment for the detected mass movements from different treated images.

Used satellite images	Landslides (L)			Rock and debris falls (RDF)			Earth flows (Ef)		
	The few known-mapped + the detected number of L on the image (a)	Verified number of L in the field (b)	% of accuracy [(b/a) * 100]	The few known-mapped + the detected number of RDF on the image (a)	Verified number of RDF in the field (b)	% of accuracy [(b/a) * 100]	The few known-mapped + the detected number of Ef on the image (a)	Verified number of EF in the field (b)	% of accuracy [(b/a) * 100]
FCC 457 Landsat TM	96	55	57	43	22	51	1	1	100
FCC 357 Landsat TM	94	48	51	63	30	48	1	1	100
Pan-sharpen Landsat TM-IRS	109	61	56	83	47	57	1	1	100
PCA Landsat TM	107	57	53	82	42	51	1	1	100
PCA Pan-sharpen Landsat TM-IRS	123	74	60	111	69	62	1	1	100
SPOT4	138	86	62	119	75	63	1	1	100
Anaglyph from stereo-pairs panchromatic SPOT4	166	115	69	125	80	64	13	7	54

3.1.1. Landslide detection

The highest accuracy level (69%) for landslide identification was obtained on the SPOT 4-P stereo anaglyph image. This identification was effective due to the morphological characteristics provided in stereo SPOT. Panchromatic SPOT 4 images show close accuracies (62%) as a SPOT anaglyph image sharing almost similar landslides characteristics (2-D shape, albedo, size). Landslides appear as having a typical 3-D geometry **(Figures 3.1f/g, 3.2f/g, 3.3f/g)**. Additionally, they show darker tones once compared to the surrounding **(Figures 3.1f/g, 3.2f/g, 3.3f/g)**. In some cases, however, depending on the lithological characteristics of the rock units, especially marls of the Senonian (C6) **(Figure 3.4f/g)** or sandstone of the Neocomian-Barremian **(Figure 3.7e)**, light toned areas can give an idea about fresh landslides moving where vegetation cover is removed.

The overall accuracies for landslide detection of different approaches applied on Landsat TM and IRS images varied between 51 and 60%. Two FCC Landsat TM images show a good reliability in this detection. Nevertheless, all elements of visual interpretation (described above) contribute to clarify areas witnessing landslides. The most effective one is the combination RGB 457 (57%). In this combination, bare soils varied from light to dark cyan depending on light incidence and moisture content, while forests appear in deep red **(Figures 3.1b, 3.2b, 3.3b)**. Landslides were differentiated due to low spectral contrast between them and other bare soils areas **(Figure 3.4b)**. The second color composite RGB 357 revealed almost the same result (51%) in landslide detection as the previous FCC. Landslides appear in pale turquoise while bare soils have a light violet color and forests a dark green color **(Figures 3.1a, 3.2a, 3.3a)**. Nevertheless, the band TM 4 in the RGB 457 FCC provides a better contrast between the areas with and without vegetation cover, taking into account that landslide areas are non-vegetated or covered by disturbed materials. The use of the pan-sharpen Landsat TM-IRS image indicates some success in observing landslide features (56%). This color composite image highlights vegetation in bright/dark green colors, wet bare soils in light brown, and dry ones in dark brown **(Figures 3.1d, 3.2d, 3.3d, 3.4d, 3.7c)**. Landslides are distinguishable and clearer than the stable bare soils taking into account the increasing of clarity and the upgrading of the low resolution of Landsat TM.

Visual interpretation of the band constructed from the first PCA axis of Landsat TM image enhances in the detection of landslides, comparing to FCC combinations, even though the % of accuracies are close (PCA-53%, 457 RGB-57%, 357 RGB-51%). Landslides appear in dark color, while other land cover zones are in brighter colors **(Figures 3.1c, 3.2c, 3.3c)**. Nevertheless, in soft rock materials (sandstone, marls), a bright shining color characterizes landslides **(Figure 3.4c)**. Moreover, the PCA of the pan-sharpened Landsat TM-IRS image gives better results in detecting landslides and raises the level of accuracy to 60% compared to previous treatments applied on Landsat TM images **(Figures 3.1e, 3.2e, 3.3e, 3.7d)**.

3.1.2. Rock and debris falls detection

The differentiation of rock and debris falls was done with the aid of ancillary data (geology and DTM). Draping all the images on the DTM surface has clarified zones of detachment from zones of accumulation. Also, by superimposing the available geological maps (Dubertret, 1945) on the treated images, discrimination between features and facies that undergo rock and debris falls was possible.

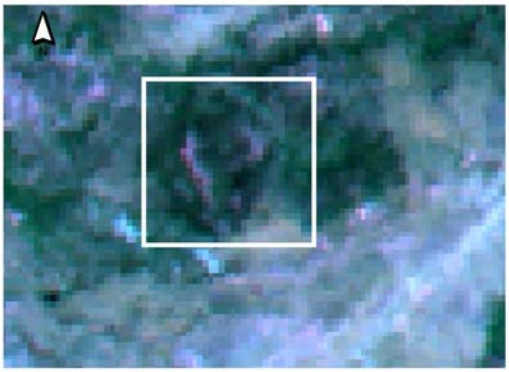

a) LANDSAT TM (3,5,7)

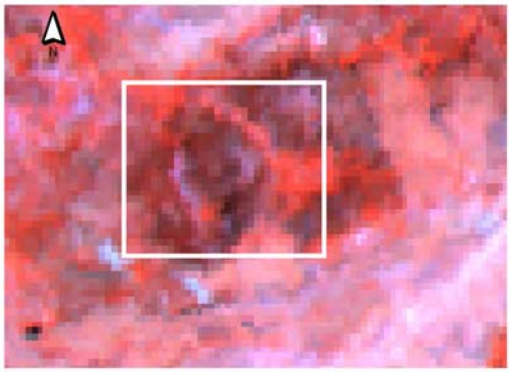

b) LANDSAT TM (4,5,7)

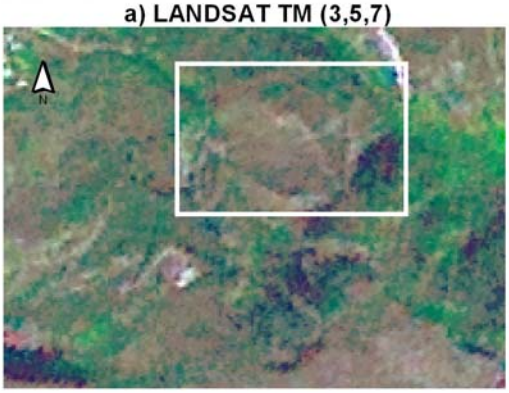

c) Pan-sharpened IRS + LANDSAT

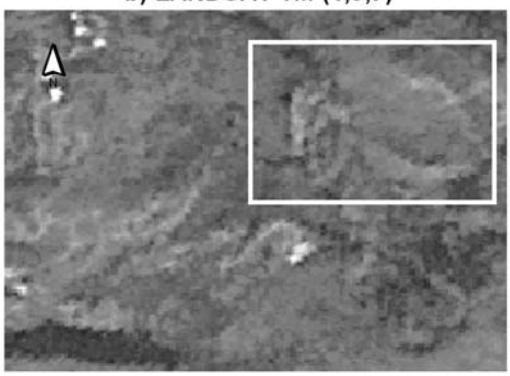

d) PCA (IRS + LANDSAT)

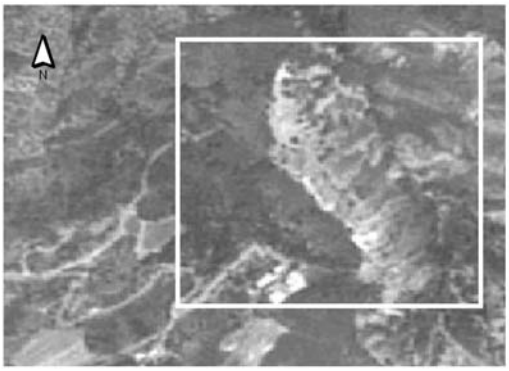

e) SPOT 4

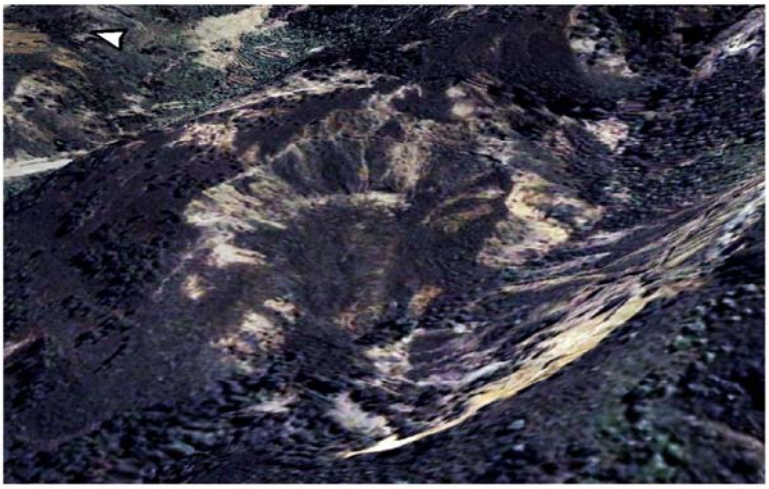

f) A 3D Pan-Sharpened IKONOS

g) Photograph of the slide

Figure 3.7. Landslide of the Ramlieh (Mount Lebanon).

Sub-rounded shapes tend to characterize areas under the action of rock and debris falls, which are correlated to the cliff-forming compact rock units **(Figures 3.1, 3.5)**. Related rock falls typically build up debris cones, usually of bright colors, whose slopes are limited by the stability of loose debris **(Figures 3.1, 3.5)**. Rock falls were found best represented by minimum threshold slope of 34 degrees (Heinimann *et al.*, 1998; Zemp, 2002). Zones of accumulation are dominated by convex and rough slopes **(Figure 3.5)**.

Rock and debris falls were best assessed from the anaglyph SPOT, the SPOT4 image and the PCA Pan-sharpen Landsat TM-IRS image with almost equal accuracy levels (63 - 64%). Both the stereoscopic vision (SPOT4) and the high resolution with the edge applied filter (SPOT panchromatic, pan-sharpen Landsat TM-IRS) are able to detect the structural uniformity of debris accumulations and to discriminate them from the irregular structure of bed rocks.

3.1.3. Earth flows detection

The only earth flow detected on all treated Landsat TM and IRS images was the huge one of Aaqoura area **(Figure 3.6)**. This mass movement is recognized easily through its coverage (~ 1.3 km^2) and its elongated shape. Nevertheless, the anaglyph of SPOT 4 has allowed the detection of some other earth flows. Such mass movements have repeatedly been initiated on contact zones between rock walls and unstable steep talus slopes over short distances. This matches some works conducted in the domain (Rickenmann and Zimmermann, 1993; Wilkerson and Schmid, 2003) and improved the usefulness of the stereo vision provided in SPOT4.

3.2. Comparative analysis between image treatments

A comparative analysis between detected and verified mass movements, using various image treatments was performed **(Figures 3.8a, b)**. Beside the anaglyph and SPOT 4 image, the enhancement processing applied on Landsat TM and IRS images (RGB, Pan-sharpen and PCA) was able to increase the number of detected landslides, without showing a proportional correlation with the corresponding levels of accuracy. This is shown when comparing the FCC 457 Landsat TM, the Pan-sharpen Landsat TM-IRS and the PCA Landsat TM images. It is obvious that the different treatments on the images (Pan-sharpen and PCA) have raised the number of the detected slides corresponding to a raise in the number of verified ones **(Figure 3.8a)**. The levels of accuracies have decreased, and errors in discriminating landslide features have increased. These confusions can be related to many causes. Since all geographic features, even the small ones, become apparent on the PCA image, a misinterpretation in detecting landslides exists. The morphometric characteristics of the terrain were integrating, revealing a similar appearance between small landslides, shadows and vegetated areas on steep slopes. In addition, man-made excavations also look almost similar to some landslides. Although the pan-fused image was draped on the DTM, erosion scars, looking linear, were confused with contact surfaces located between features and/or different lithologies. The anaglyph SPOT4 image showed both a high number of detected landslides and a good accuracy. However, some errors (31%) are related to patches presenting light tones indicating on-going erosion processes, especially on sloping areas.

Figure 3.8. Comparison between detected (RS) and verified (field) mass movements and the percentages of accuracies.

a) Landslide

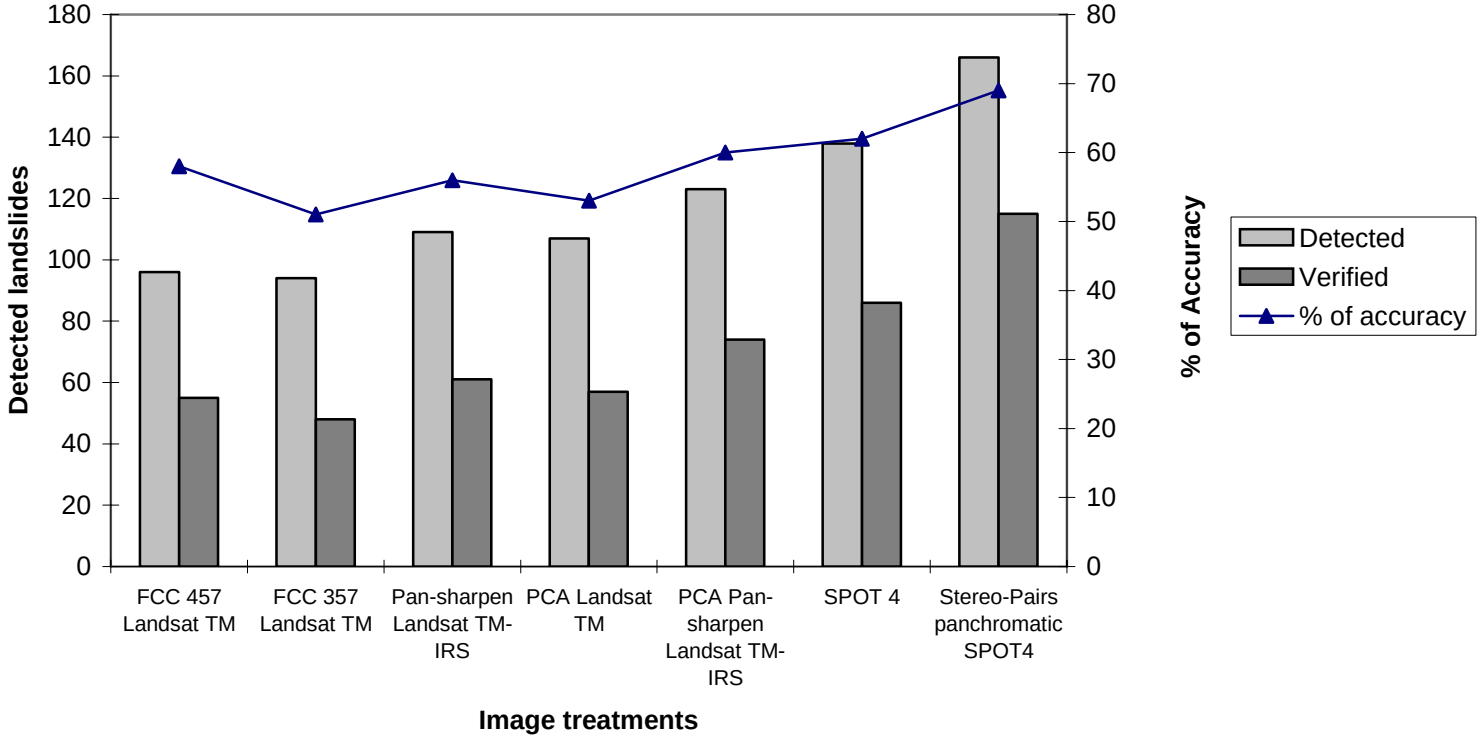

b) Rock and debris falls

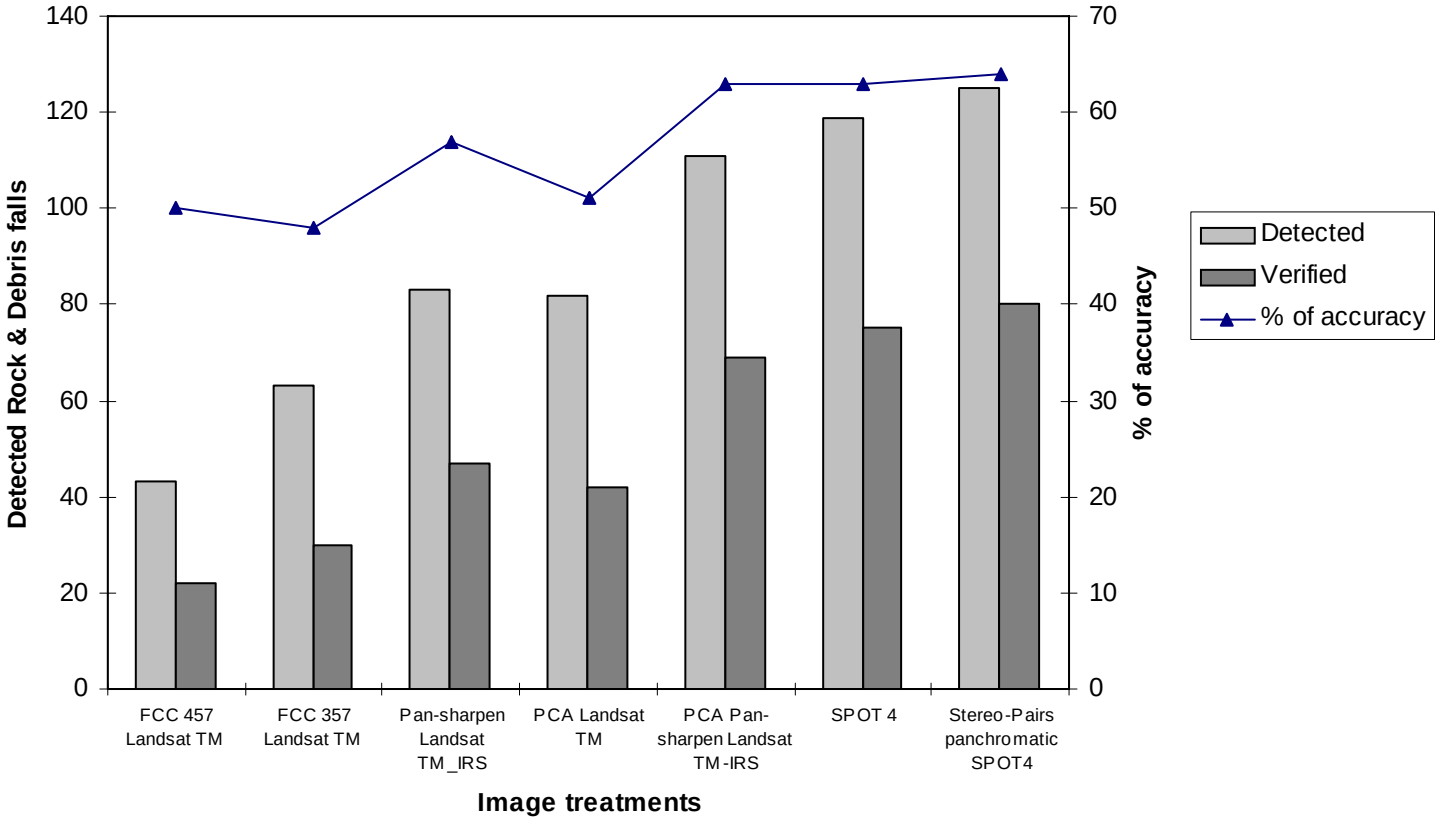

The applied enhancements (PCA, pan-sharpen, FCCs) on Landsat TM images plus the increase in spatial resolution have improved the distinction of rock and debris falls **(Figure 3.8b)**. Errors vary between 36 and 50%, which are due to the close similarity between bare rocks and debris, despite the utilization of ancillary data (geology and DTM) that were used for enhancing visual interpretation and decreasing errors.

The maximum accuracy levels (100%) **(Table 3.2)** in detecting earth and debris flows on treated Landsat TM and SPOT4 images can not be considered as a reliable indicator for visual evaluation, since the only detected flow was a big and well known feature. The SPOT4 anaglyph image, with a lower accuracy level (53%), allowed the detection of a more important number of flows.

3.3. Field analysis and IKONOS imagery

The ground truthing detected a total of 202 mass movements, comprising 115 landslides, 80 rock and debris falls and 7 earth flows. The majority of them occur in the upper sloping plateaus of Mount Lebanon (Figure 3.9), on cut slopes or on embankments along side roads and highways in mountainous areas. Some of these mass movements occurred near high-rise apartments in residential areas, causing great threat to many people. As noted, the most effective satellite imagery, the anaglyph of SPOT 4, allowed the detection of significant amounts of the total mass movement population (69% landslides, 64% rock and debris falls, 54% earth flows). Based upon the results of the study, the smallest MM size of 40 m (width and length) can be resolved confidently using this instrument. Although many small MM have a length in excess of 40 m, their width is very often less than this and such features, therefore, can not be delineated (Figure 3.10).

IKONOS imagery has been used for direct examination of mass movements in selected zones (5.3% of the study area). Draping this imagery on DTMs (Figures 3.2g, 3.4i, 3.5f, 3.6g) has improved MM detection, and can be considered in some cases an alternative for field campaigns, especially in remote areas. Nevertheless, the smallest MMs that could be mapped are in the order of 5 m in width and length. But, MM occurring in dense vegetated areas could not be easily recognized even on high resolution imagery (IKONOS) (Figure 3.11). In addition, the differentiation between man-made excavations like quarries, commonly distributed in the study area, and MM is difficult (Figure 3.12).

Conventional aerial photo stereo-pairs, even those of black and white mode, can be used due to their high spatial resolution. But because of their old date of acquisition (1962), they will be used for monitoring MM phenomena in selected areas in the future work.

4. Conclusion

This chapter shows that 3D anaglyph SPOT4 images have proven to be the best in sensing the types of mass movements (MM) of the study area, and gave a mean visual interpretation error (38%). However, the errors in interpretation differ according to the MM type, varying between 31% (landslides), 36% (rock and debris falls) and up to 46% in the case of earth flows. Additionally, and despite the distortion caused by applying fusion technique on the multispectral Landsat TM images, good results were also obtained once coupling these images with the principal component analysis. Accuracy of MM identification oscillates between 60% for landslides and 62% for rock and debris falls.

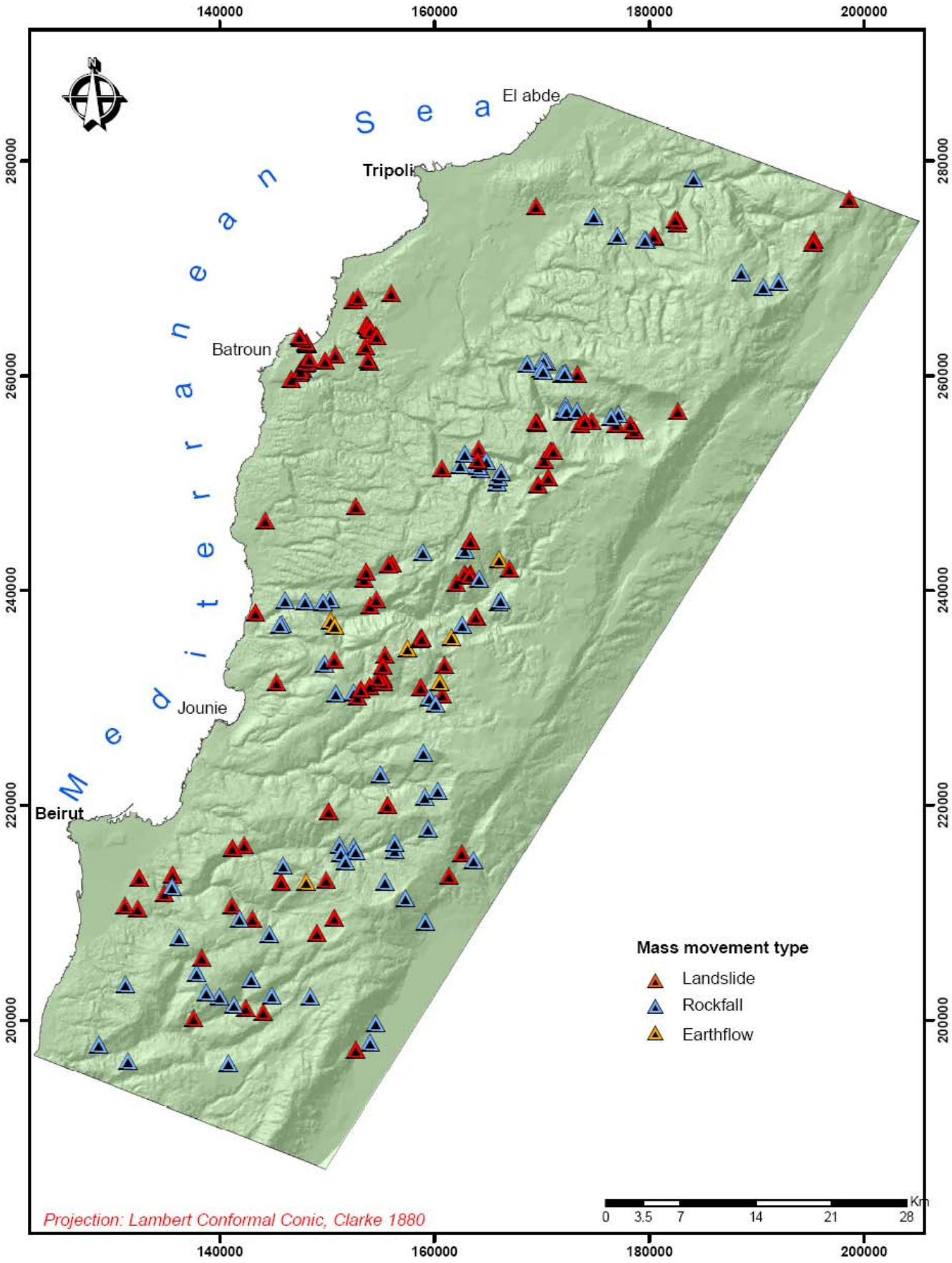

Figure 3.9. Location of mass movements detected by visual interpretation of satellite imageries and verified in the field.

It is obvious that visual interpretation of satellite imageries in detecting MM is a complex intuitive process of combining evidential information from different sources and subjecting such information to the knowledge, experience and heuristics at each level of processing, namely: detection, identification, analysis, and recognition. Nevertheless, the utilization of stereoscopic vision and enhancement applied on medium resolution imageries can improve the detection of MM and serve regional studies in many countries facing the hazards caused by mass movements, especially those located in the Mediterranean area. The detected MM and those verified in the field are examined in the next chapter according to their spatial environmental characteristics.

Figure 3.10. Example of small MM that can not be discriminated through visual image interpretations.

a) Small landslide on basaltic (tuff) formation. It resulted from human excavation nearby the area (building for

Slide

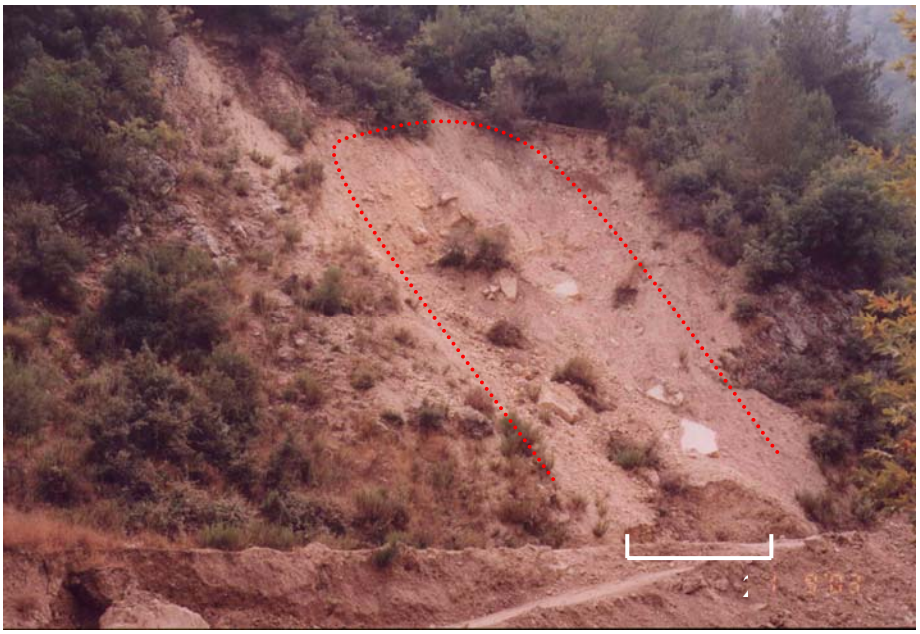

b) Photo showing a small landslide on the C_3 marly formation due to road excavation.

Slide

Figure 3.11. Ancient landslide among sandstone rocks, where the dense vegetation cover makes it difficult to delineate on the images.

Presumed slide Direction of the movement

Figure 3.12. Difficulty of image interpretation between man-made excavations (quarries) and MM.

- IV-

Sorting major parameters of mass movements' occurrence using GIS and Statistical Correlations

CHAPTER IV
Sorting Major Parameters Of Mass Movements' Occurrence Using GIS and Statistical Correlations

1. Introduction

This chapter aims to sort out parameters influencing the occurrence of mass movements (MM) in the study area and determining their relative weights at regional scale. This influence is crucial in building susceptibility and hazard MM maps. The susceptibility maps are related to the instability of the terrain itself while the hazard maps take into account also the triggering parameters (either natural or anthropic).

The sorting of the parameters that have a role in the occurrence of MM is not an easy task. There are neither universal criteria nor guidelines (Ayalew and Yamagishi, 2005). The general consensus of sorting the considered parameters must be operational, complete, non-uniform, measurable and non-redundant. However, it is possible to establish an *a priori* list of parameter categories that may intervene. In this present work, I have considered six major parameter categories, i.e. geomorphology, geology, soil, hydrology, climate, and anthropic influence responsible for instabilities and triggering conditions, depending on field observations and referring to several works conducted in this domain worldwide.

The diagnostic of the relative weights of these parameters can be done using statistical analysis to prevent the subjectivity of the different investigators in assuming the most significant ones depending on their own skill and experience. Up to now, many statistical methods have been used for this determination in many areas of the world (Yin and Yan, 1988; Gupta and Johsi, 1989; Carrara *et al.*, 1991; Siddle *et al.*, 1991; Wang and Unwin, 1992; Atkinson and Massari, 1998). Each method has its advantages and drawbacks. The univariate statistical method explores the relation between one parameter only and MM occurrence, and omits the effect of the whole parameters related together reflecting more the reality in the field.

The multivariate correspondence analysis (MCA) is a commonly used technique, appropriate for the analysis of environmental problems, allowing the use of parameters which are not measured in the same units (e.g., elevation, rainfall) and projects them on axes that do not correlate. However, this method has a major limitation related to the unique combination of axes taking only into account linear joint effects and defining therefore a unique condition of a given area. This unique condition is unrealistic due to the existence of several inducing and triggering situations that can interfere together and tend towards several conditions for the same area. This limitation is common also to linear regression that attempts to explain the relationships between MM and influencing parameters with a straight line fit of the data.

Other generalized linear models such as logistic regression were used to predict the influence of parameters on MM occurrence. Unlike linear regression, they consider categorical parameters, and do not assume linearity of relationship between the dependent (that needs to be explained or predicted) binary (dummy) variable representing the presence or absence of MM and the influencing independent (explicative) parameters. However, these models (e.g., logistic regression) require that the independent parameters be linearly related to the logit (a log of odds that are the function of P, the probability of a 1) of the dependent variable (MM occurrence).

To overcome all the limitations of the mentioned statistical methods (univariate, multivariate correspondence analysis, linear regression, logistic regression), I have used in

this study binary statistical approaches that explore dual relationships between terrain parameters according to their importance in causing mass movements. These approaches are used also to determine the most influencing parameters which can be used as weighted input data in prediction susceptibility and hazard MM maps. I have made use of Geographic Information System (GIS) for extracting the influencing parameters as maps needed for studying problems at regional scale, and for overlaying parameter maps and MM map locations obtained through visual interpretation of satellite imageries (refer to chapter III). This overlaying is essential for building tabular databases on which statistical analysis was run. In this context, I expose first the choice and preparation of the considered influencing parameters, their GIS manipulation and statistical running analysis, and then the obtained field, univariate and bivariate statistical correlations between parameters on one side, and between parameters and MM occurrence on the other side.

2. Choice and preparation of the influencing parameters

2.1. Approach

For each parameter category (geomorphology, geology, soil, hydrology, climate, anthropic influence), one or several parameters were considered as influencing the occurrence of MM within the study area according to our field observations and the consultation of several works done in similar or dissimilar environmental conditions **(Table 4.1)**. In this context, a field format (questionnaire) **(Table 4.2)** was established for each MM location, taking into account information relative to the lithological structure, soil, vegetation cover, type of land use around the mass movements, slope, elevation, the corresponding causes of MM (road construction, river and water ways, etc.) as well as human activities protecting against this phenomena. The chosen parameters were extracted from remote sensing or ancillary maps as stated below.

Table 4.1. Parameter categories and parameters considered in this study to investigate their relationships to mass movements' occurrence.

Parameter categories	Parameters
Geomorphology	Elevation
	Slope gradient
	Slope aspect
	Slope curvature
Geology	Lithology
	Proximity to fault line
	Karst type
	Seismic events
Soil	Soil type
Hydrology	Distance to drainage line
	Distance from water sources
	Floods
Climate	Rainfall quantity
Anthropic influence	Land cover/use
	Proximity to roads
	Distance to quarries
	Forest fires

Table 4.2. Simplified field format for mass movement evaluation.

Site No:	Photo No.:	Location:	Date:
Longitude:	Latitude:		Altitude:
Type of mass movement:			

Geology

-Litholog:				
-Thickness	Layered □	Bedded □	Massive □	
-Structures/forms	Faults □	Joints □	Fissures □	Folds □
	Cliffs □	Karst □	Ridges □	
-Weathering	Complete □	High □	Partly □	Fresh □
-Hardness	Extremely hard □	Very hard □	Hard □	Soft □ Very soft □
-Rock stability	Very low □	Low □	Medium □	High □ Very high □

Soil

-Texture	Sand:		Silt:		Clay:
-Compaction	Highly compacted □		Moderately compacted □		Friable □
-Organic matter (%)	< 1% □	1-2% □		2-3% □	> 3% □
-Soil moisture	Wet □	Moderately wet □			Dry □
-Stoniness	< 5% □	5-35% □	35-65% □	65-95% □	> 95% □
-Soil/rock contact	Sharp □	Gradational □			Mixed □
-Thickness (m)					

Water

-Location adjacent to the site	River □ Wadi □ Gully □ Others:		
-Drainage	Type:	Density:	
-Condition	Dry □	Running □	Stagnant □
-Groundwater	Seeps □	Springs □	Type of springs:
	Wells (artesian) □	Others:	
-Water velocity	Slow □	Rapid □	

Land cover/use

-Forests	Type:			
	Density: Dense □	Medium □	Dispersed □	
-Shrubs	Type:			
	Density: Dense □	Medium □	Dispersed □	
-Cultivated area	Type:	Irrigation: yes □	no □	
	Density: Dense □	Medium □	Dispersed □	
-Bare lands	yes □	no □		
-Urban	Dense □	Medium □	Dispersed □	

Slope

-Slope	Steep □	Moderate □	Gentle □	Flat □	
-Slope aspect	Non-oriented □	N □	NE □	E □	SE □
	S □	SW □	W □	NW □	

Causes of mass movements

Natural	Lithology □	Structure □	Soil □	Morphology □	Others:
Human-made	Deforestation □	Quarries □	Alteration of landforms □	Water diversion □	
	Non-maintenance □	Reclamation of badlands □		Others:	

Man-made protecting activities

Canals/pipes/reservoirs	yes □ no □	Retained walls	yes □ no □
Terraces	yes □	no □	
	Maintenance: yes □		no □

2.2. Field observations and causes of mass movements

It is obvious from our field observations and from the literature that there are a large number of causes interacting together inducing or enhancing mass movements. They can be divided into natural and human-made causes. The natural causes involve geomorphologic,

hydrological, and climatic aspects, as well as other natural hazards (e.g., seismic events, floods). Man-induced activities include the alteration of landforms such as in road and residential construction, quarrying, etc. I expose here the unstable Hammana area (Mount Lebanon) as an example trying to highlight the effect of these causes in determining the severity and the size of the MM processes in the whole study area.

Field investigations showed that Hammana area exhibits an irregular topography, and an amphitheatrical outline bounded by cliffs with steep gradients. The slopes are upstanding, convex, concave, or rectilinear. They have evolved such that they reflect a differential interaction between the materials constituting the slopes and the environmental conditions **(Figure 4.1a & 4.1b)**. The oldest geological formations are the Upper Jurassic limestones and the youngest is a recent unconsolidated cover. In between there are lower cretaceous sandstones followed by limestone, some being argillaceous and/or marly and some flow basalts. The area suffers a high density of faulting, jointing and fracturing. The major faults are vertical with main trends being NNE-SSW and NNW-SSE, with a less frequent E-W trend. The rocks and soils show wide variations in their geological and engineering parameters.

From our field observations, three modes of movements were recognized in Hammana area, and their inducing causes were observed. These modes can be summarized as follows: (1) large mass failures involving toppling and translational and rotational slides, (2) single mass failures and (3) composite failures. The toppling **(Figure 4.1c)** is exclusively related to the cliff-forming units. Conditions that promote toppling are competent rocks, medium to thick bedding, horizontal to gentle dips, steep slopes and vertical to very steeply dipping joints. The opening is increased by ice wedging, water pressure, fill material, and natural and man-induced vibrations. The climate, typified by cold wet winters and hot dry summers, helps to reduce the material strengths and promote deterioration. Water plays a major role by displacing air in pores, joints, fractures and bedding planes, causing a significant reduction in shear strength along the discontinuities, and inducing internal pressures which weaken the materials. Variations in the water table cause hydraulic gradients and effective stresses that obviously are acting on the porous sandstones, the weathered basalts, and the fractured limestones. Water action is also obvious in karstification, piping, gullying and undercutting. The natural causes, other than climatic and hydrologic, are earthquake seismic shocks. These shocks loosen bedrocks and soil materials, and cause the opening of numerous cracks in addition to inducing physical changes in sensitive sediments. It may be added than thin soil or vegetative cover in the area is another factor to consider as a thicker cover would afford better protection to what lies beneath.

Translational failure is common in the cliff forming units, particularly where there is interbedded competent and incompetent rock. It occurs on high-angle rock slopes with planar surfaces where large tensional joints paralleling the slopes enhance the sliding. Sliding potential is increased by the presence of marls, and invariably marly or argillaceous limestones **(Figure 4.1d)**. These beds may swell and shrink with successive wetting and drying, or they may act as surfaces with low sliding friction values. Rotational failure commonly occurs in the relatively unconsolidated poorly cemented sandstones, weathered basalts, and the surficial cover. Conditions promoting the rotational failure in Hammana area are the inherent weakness of the material, pore-water pressures, the numerous existing faults and abundant discontinuity planes.

Single mass failures involve wedge separation and are associated with some compact sandstone beds, the unweathered basalts, and ledge-making limestone units. The most important causative factor is the intersection of two joint sets. Usually single blocks move

and, due to the en-echelon nature of the joints, a zigzag cut characterizes the face of the rock slope.

Figure 4.1. Field observations showing the instability conditions of Hammana area.

a) Upstanding cliff slopes, and evolved slopes at their bases with various configurations

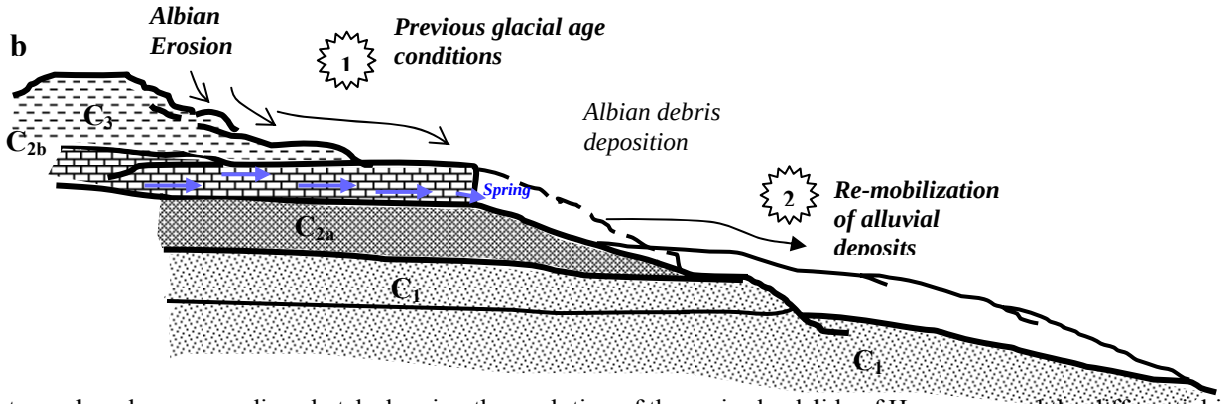

b) Photograph and corresponding sketch showing the evolution of the major landslide of Hammana and the differential interaction between slope materials and environmental conditions

c) Toppling as example of mass failure in cliff forming units affecting local community

d) Intercalation of marls and argillaceous limestone enhancing MM occurrence.

The movement may be facilitated by intercalating weak surfaces such as clayey or weathered horizons.

The composite type applies to cases where more than one mode of failure develops simultaneously. The movement may start as translational along a joint parallel to the cliff face and either continue deeper – thus becoming prone to rotational mode – or induce toppling of the newly exposed stress-released blocks. This type is common because the superimposed differing lithologies do not respond to the same triggering mechanisms in the same way. These field observations indicate that MM monitoring can be approached by geomorphologic, climatic, hydrologic and anthropogenic parameters.

2.3. Preparation of MM parameters

2.3.1. Geomorphological parameters

The main importance of topography is to permit the application of gravity to rock masses, moving along the main downslope gradient, or creating instable situations. Also, by controlling water flow sources, water flow direction and ground moisture, surface topography is an important factor that influences the density and spatial extent of mass movements (Maharaj, 1993; Pachauri *et al.*, 1998; Nagarajan *et al.*, 2000; Clerici *et al.*, 2002; Saha *et al.*, 2002). Therefore, I have tested the significance of four geomorphological parameters, i.e. slope gradient, aspect and curvature, and elevation, on the occurrence of MM.

First of all, I have derived the slope gradient (slope angle) from the constructed DTM (refer to chapter III) using specific ArcGIS software algorithms. In GIS, the slope can be calculated in percentage or degrees. The use of DTMs is common for slope derivation (Moore *et al.*, 1991) since the digital number DN for each pixel gives the elevation at particular location, and the pixel extent (*resolution = side x side*) corresponds to the horizontal distance; hence the slope gradient could be easily calculated. It was observed that the slope gradient calculated from the DTM had a range of 0-90° in the study area. Later on, I divided the obtained slope gradient into five classes as follows: 0-1°; 2-11°; 12-18°; 19-27°; and 28-90° **(Figure 4.2a).** These classes were determined using a clustering method based on the frequency distribution of slopes and the break-in-slope features that are influential on the existence of mass movements as observed in the field.

As for slope aspect**,** which is the orientation of the maximum slope direction, it can be extracted from the DTMs, eight major directions could be deduced as follows **(Figure 4.2b, 4.2c)**: north N, northeast NE, east E, southeast SE, south S, southwest SW, west W, northwest NW, adding to these directions the non-oriented areas (i.e. flat areas).

Curvature attributes are based on second derivatives: the rate of change of a first derivative such as slope gradient or slope aspect, usually in a particular direction. Curvature is negative for diverging flow (on ridges) and positive for converging flow in valleys, and 0 curvature indicates that the surface is flat. In a similar way, curvatures were derived through GIS from the constructed DTMs **(Figure 4.2d.)**.

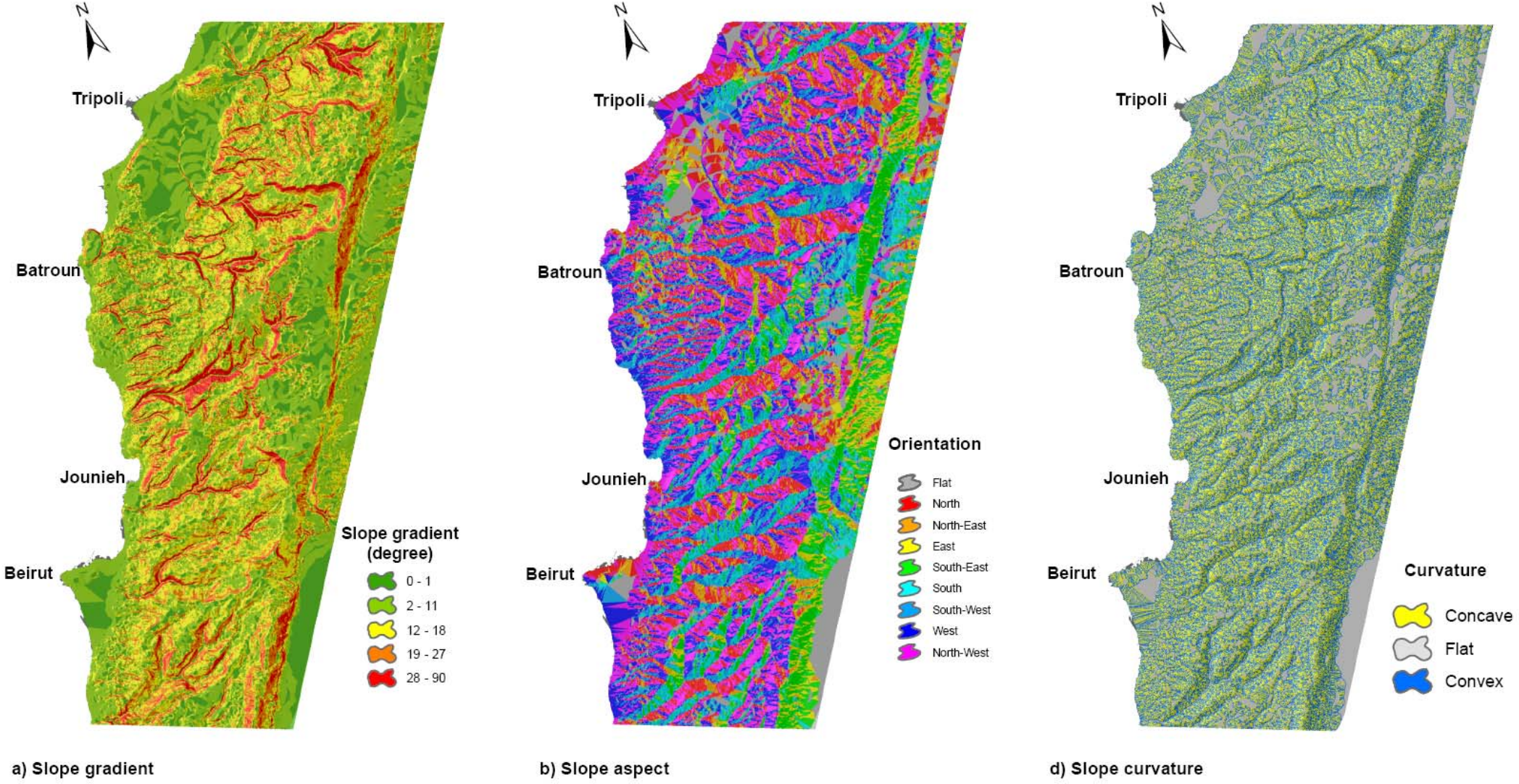

Figure 4.2. Geomorphological data extracted from the digital elevation model (50 m)

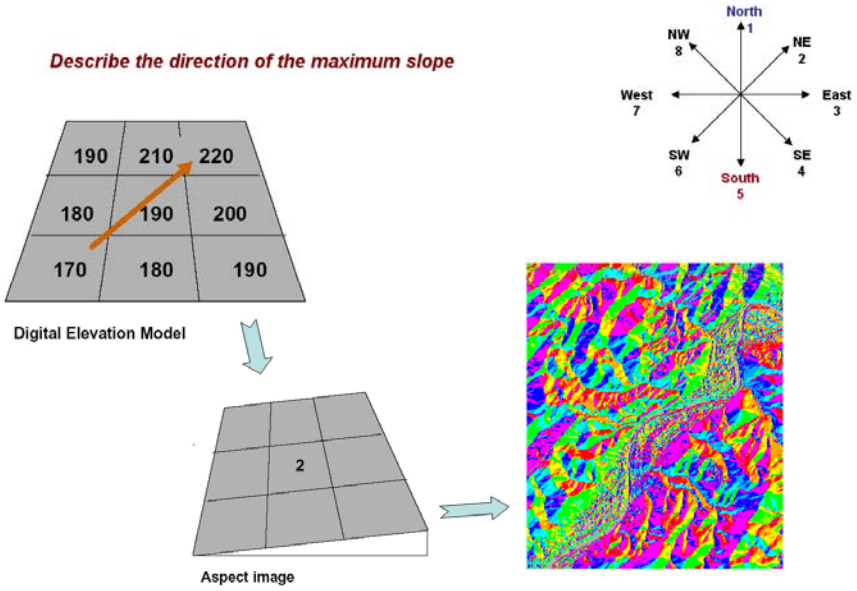

Figure 4.2c. Extraction of slope aspect from DEMs.

Elevation is useful for classifying the local relief and locate points of maximum and minimum heights. To calculate MM densities for different relief classes, I divided the relief map ranging from 0 to around 3000 m above mean sea level into 5 elevation classes. These classes are related to the geomorphic units composing the study area. They can be summarized as follows: coastal plain (< 100 m), lower slopes (100-500 m), higher sloping plateaus (500-1500 m), elevated plateaus (900-1500 m), and elevated crests (> 1500 m) (refer to chapter II, paragraph 2.1.1).

2.3.2. Geological and soil parameters

It is widely recognized that geology and pedology greatly influence the occurrence of landslides, because lithological and structural variations, and soil texture often lead to a difference in strength and permeability of rocks and soils (Carrara *et al.*, 1991; Anbalagan, 1992; Mejia-Navarro *et al.*, 1994; Pachauri *et al.*, 1998; Luzi and Pergalani, 1999; Dai and Lee, 2001). Therefore, I have evaluated lithology, faults, karst and soil types, and earthquake influences on MM occurrence.

In this context, I extracted lithology and faults from scanned and registered geological maps of Lebanon at 1:50,000 scale, specifically the sheets of Hamidieh, Halba, Batroun, Tripoli, Sir El Dannieh, Jbail, Qartaba, Baalbeck, Beirut, Zahle, Rayak, Saida, Jezzine and Rachaya (Dubertret, 1945). I digitized all the maps using heads up digitizing (on-screen digitizing). After cleaning and building procedures of the different feature types (lines and polygons), I created a buffer zone for the faults, and put it at 500 m as did many workers in the domain (Zaruba and Mencl, 1982; Guillande *et al.*, 1993; Dikau *et al.*, 1996; Saha *et al.*, 2002). This buffer value is an average threshold set based on a comprehensive assessment of how far slope failures extend from mountain scarps, topographic breaks and any other linear features. Then, I categorized the proximity to fault zones into five classes having an interval of 500 m as follows: < 500 m, 500-1000 m, 1000-1500 m, 1500-2000 m and 2000-2500 m **(Figure 4.3a)**. Karst and soil types were represented by a digital registered form of the available karst and soil maps of Lebanon established by Gèze (1956) and Bou Kheir *et al.* (2003), respectively at 1:200,000 scale.

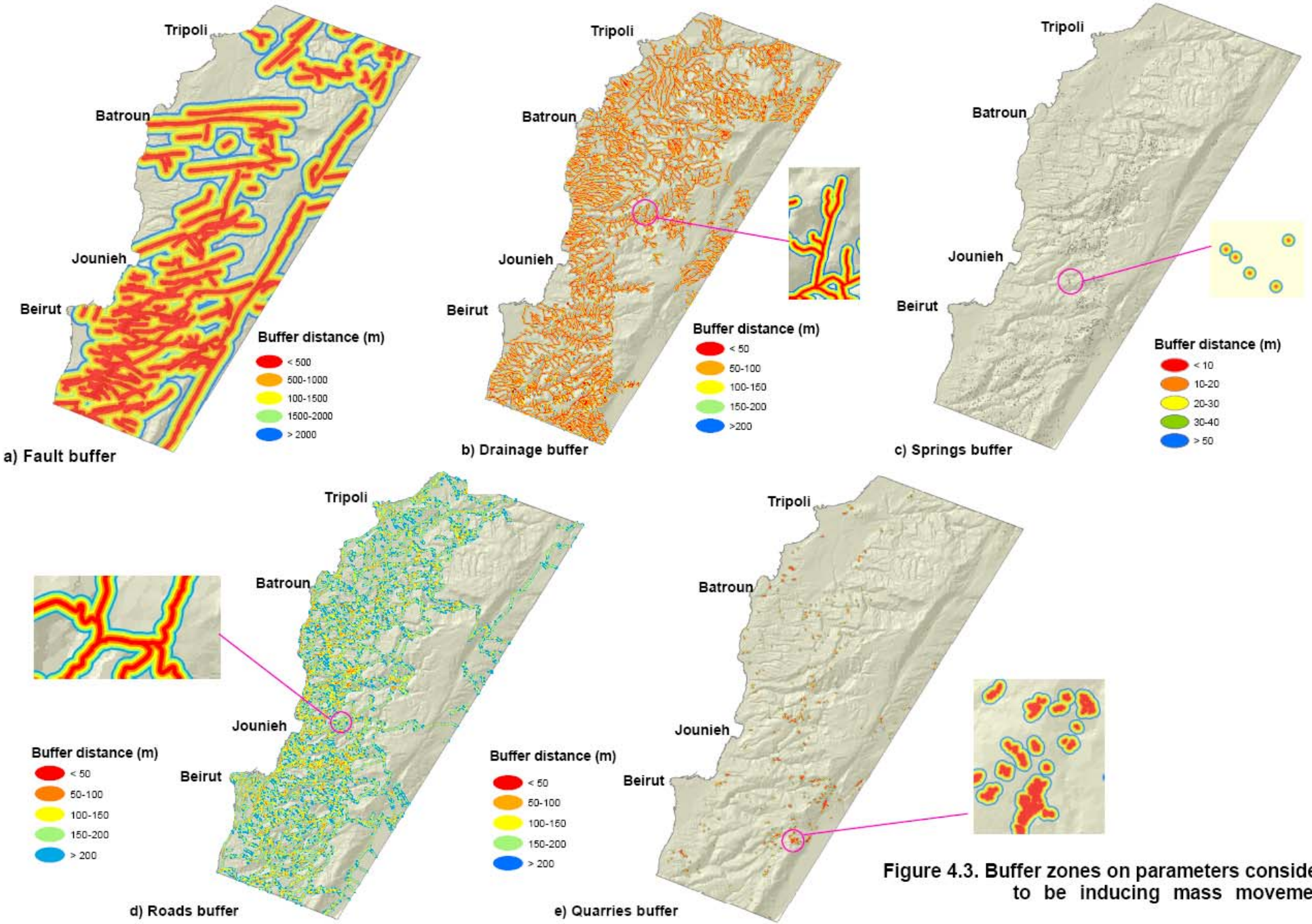

Figure 4.3. Buffer zones on parameters considered to be inducing mass movements.

I evaluated also in this study earthquake influences which is not the case of most preceding studies. Authors usually consider the seismic activity as relatively uniform throughout their studied areas (Cevik and Topal, 2003; Ayalew and Hamagishi, 2005). However, seismicity contributes to a wide extent to the instability of a given area, increasing indirectly the potential of mass wasting (Jibson *et al.*, 1998; Refice and Capolongo, 2002). For example, high content of ground water occurring in sandy soils may liquefy this soil during an earthquake. This can cause a landslide on a slope as gentle as 5 to 10%. Therefore, I have produced a seismic hazard map **(Figure 4.4a)** for the study area from the interpolation of all seismic events with magnitudes exceeding 2.5 on Richter scale during the last century. The inverse distance weighting interpolation of these magnitudes results into five seismic hazard classes **(Figure 4.4a).** This interpolation gives the weight for each point feature "epicenter", the effect of this feature will reduce as going apart from it. It should be noted that this sketch does not show all elements of seismic risk, e.g. along the Yammounah, or in Chekka area (north of Batroun), because only those elements of the last 100 years were taken into account.

2.3.3. Hydrological and climatic parameters

One of the controlling factors for the stability of slopes is the degree of water saturation. Streams may adversely affect stability by eroding the toe and/or saturating the slope (Gokceoglu and Aksoy, 1996; Dai *et al.*, 2002; Saha *et al.*, 2002). Therefore, I have extracted drainage networks from topographic maps at a scale of 1:50,000 (DGA, 1963).

For this extraction, I scanned and registered the topographic maps based on the affine transformation with a first polynomial order and using the Erdas imagine 8.7 software. The affine transformation scales, rotates, and shifts the registered maps from one coordinate system to another all in one equation. Afterwards, I delineated these networks on each digital topographic map using heads up digitizing.

I gave later on main streams (permanent ones) a different ID to be differentiated from the temporary water courses during digitizing procedures. All the digital drainage network maps were joint and appended by using *ArcGIS 8.3* software. Topology was built and maps were cleaned to ensure network connections and erase errors in the obtained coverage. The influence of drainage was given to the buffer zone up to a distance of 50 m from the closest drainage line, in accordance with comparable approach studies (Guillande *et al.*, 1993; Saha *et al.*, 2002). Thus, five classes were determined in the study area ranging between less than 50 m and 250 m **(Figure 4.3b)**.

The soil saturation is subjected to rapid variations following intense rainfalls and consequent increased flow from springs (Moore *et al.*, 1991). Natural instability in the ground is very much controlled by groundwater conditions. Therefore, I extracted springs from topographic maps of scale 1:50,000 and enclosed by 10 m buffer zones. Then, I differentiated five classes of the distance to water sources having an interval of 10 m between each class as follows: < 10 m, 10-20 m, 20-30 m, 30-40 m and 40-50 m **(Figure 4.3c)**.

Intense rain leads to soil saturation and a temporary rise in pore-water pressure, provoking destabilizing effects. For that, I reclassified the existing digital rainfall map at 1:200,000 scale (Plassard, 1971) into seven classes having an interval of 100 mm.

Flooding controls the activation of mass movements (MM), and therefore the relation between the affected areas by these hazards and the occurrence of MM has been studied. I extracted flooded areas **(Figure 4.4b)** from existing recent flood maps at 1:50,000 scale (STADL, 2002; Faour *et al.*, 2006).

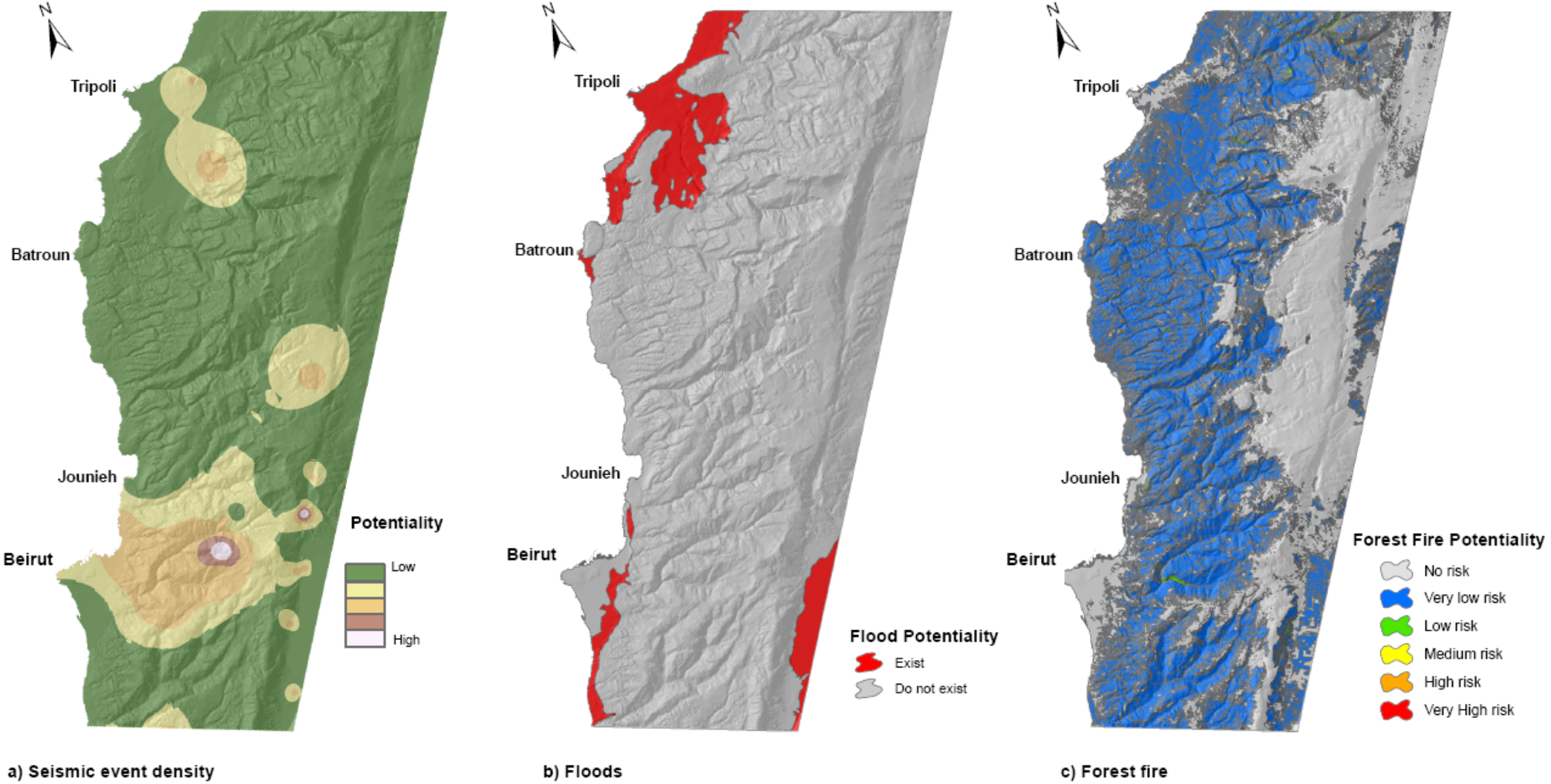

Figure 4.4. Natural hazard maps in the study area.

2.3.4. Anthropogenic parameters

Human activities can add, in addition to the above parameters, to the destabilization of the slope or overloading caused by the construction of buildings on the rims of landslide terraces. Land cover/use is an indirect indication of the stability of the slopes (Cevik and Topal, 2003). It has a twofold influence on the stability of superficial deposits: hydrological (capacity of infiltration into the soil, soil moisture, groundwater level, etc.) and mechanical (root strength) (Greenway, 1987). The land cover/use parameter was defined from a recent land cover/use map at 1:20,000 scale (LNCSR-LMoA, 2002).

Road-cuts are usually sites of anthropologically induced instability. A given road segment may act as a barrier, a net source, a net sink or a corridor for water flow, and depending on its location in the mountains, it usually serves as a source of landslides. Some slope failures start above roads but are often intercepted by them. For this reason, roads are included in GIS-based landslide susceptibility analyses (Larsen and Parks, 1997). The complete transportation network in the study area is about 3375 km in length, including tunnels, seaside highways and roads in the mountains. The traditional method in most GIS-based studies for considering the effect of roads on landslides is to construct buffers around them (Larsen and Parks, 1997). I choose a distance of 50 m above the road (maximum height of a talus cut created by the construction of a road). This parameter has been taken into account by other researchers (Chung *et al.*, 1995; Ayalew and Yamagishi, 2005). Then, I determined five classes of the proximity to roads oscillating between less than 50 m and 200 m **(Figure 4.3d).** Quarry locations were provided from the Lebanese Ministry of Environment. They also have been identified through visual interpretation of very high resolution pan-sharperned satellite imageries, i.e. IKONOS with 1 m pixel size acquired in 2002, and enclosed by buffer zones of 50 m. This buffer indicates their impact on the surrounding natural ecosystem by activating the MM occurrence (Abou Haidar, 1997; Mina, 2006). Then, I differentiated five classes of the distance to quarries as follows: < 50 m, 50-100 m, 100-150 m, 150-200 m and 200-250 m **(Figure 4.3e).**

Forest fires control also the activation of mass movements (MM). For that, I had referred to the available fire occurrence susceptibility map **(Figure 4.4c)** for establishing relationships between fires and MM. This map results from the combination of several factors related to the density of vegetation, fuel types, slope gradient and exposure and evapotranspiration, in addition to the probability of fires occurring during the past 25 years.

3. Parameters' manipulation in a GIS environment

All the mentioned parameters were handled at different levels of treatment with GIS software (*ArcGIS 8.3*). To obtain data homogeneity, I converted the obtained raster models (elevation, slope gradient, slope aspect, slope curvature and seismic events) from raster to vector using the Spatial Analyst extension of the ArcGIS software.

Mass movements were recognized through visual interpretation of remotely sensed data (chapter III). Their delineated areas were converted "*using ArcGIS appropriate extensions*" into centroides resulting in a point-theme-layer of the distribution of mass movements in the study area. This procedure was undertaken to reduce accuracy errors due to the shifting in overlapping layers and to easily differentiate the detachment areas from the zones of accumulation. Each mass movement point was given an ID number. Overlaying the "centroid" point-theme-layer with every thematic vector terrain parameter has permitted defining the parameter class in which each mass movement falls in each parametric layer. This overlaying is algorithmically simple, fast and easily computed. Thus, resulting attribute tables correlated the occurrence of the detected mass movements with

each category characterizing each terrain parameter. I exported then these tables to Microsoft Excel and gathered in a matrix sheet showing in the row fields the seventeen different terrain parameters and in the column fields the numbered mass movements.

4. Statistical analysis

I have produced first univariate statistical correlations, i.e. i.e. relations between mass movement frequency and the different categories of each parameter. On the other hand, I carried out bivariate correlations, and verified both correlations (univariate and bivariate) in the field. In order to determine the statistical correlations between the chosen parameters of different nature, homogenization of their categories is required. Some parameters are quantitative, like elevation, slope gradient, slope aspect, slope curvature, proximity to fault zone, distance to drainage line, distance to water sources, rainfall quantity, proximity to roads and seismic events, while others are qualitative like lithology, soil type, land cover/use, floods and forest fires. This is why the categories of those parameters were qualified by giving a random number for each category in each parameter. The idea is that the chaotic distribution of numbers will not be a weighting factor in the statistical correlations. For example, mass movement no. 4 falls on altitude between 100 and 500 m (i.e., category no. 2), slope gradient between 2° and 11° (no. 2), slope aspect towards the south (no. 6), slope curvature being concave (no. 2), lithology type C1 i.e. lithology no. 5, proximity to fault zone less than 500 m, i.e. no. 1, soil type no. 9-11-22 (yellowish mountain soils-sandy soils-white rendzina), distance to drainage line between 150 and 200 m (no. 4), distance to water sources between 10 and 20 m (no. 2), rainfall quantity exceeding 1400 mm/year (no. 3), land cover/use constituted by coniferous forest (no. 5), proximity to roads between 50 and 100 m (no. 2), seismic events of 5.5 magnitudes, falling on non-flooded area without being affected by fires during the past 25 years.

Non-parametric bivariate procedures of Kendall's tau-b rank correlation coefficients, with their significant levels were computed using the SPSS, a software package for manipulation and statistical analysis of data, in order to determine a correlation coefficient between more than two parameters having qualitative values. This is a measurement of the correlation between two ordinal level variables. For any sample of *n* observations, there are [n (*n*-1)/2] possible comparisons of points (X_i, Y_i) and (X_j, Y_j). If X_j -X_i and if Y_j - Y_i have the same sign, the pair of bivariate observations is *concordant*, if they have opposite signs, the pair is *discordant*. Simultaneously, if we consider C the number of pairs that are concordant and D the number of pairs that are discordant, then the strength of the relationship is given by the following equation:

$$Kendall's\ Tau = \frac{(C-D)}{(\frac{n}{2})}$$

If $X_i = X_j$, or $Y_i = Y_j$ or both, the comparison is called a 'tie'. Ties are not counted as concordant or discordant. On the other hand, *Kendall's Tau-b* is computed as the excess of concordant over discordant pairs (C - D), divided by a term representing the geometric mean between the number of pairs not tied on *X* (X_0) and the number not tied on *Y* (Y_0):

$$Tau\text{-}b = (C - D)/\ \mathrm{SQRT}\ [(C + D + Y_0)(C + D + Y_0)]$$

There is no easy intuitive meaning for *Tau-b*, which is the surplus of concordant over discordant pairs as a percentage of concordant, discordant, and approximately one-half of

tied pairs. The rationale for this is that if the direction of causation is unknown, then the surplus of concordant over discordant pairs should be compared with the total of all relevant pairs; Those relevant are the concordant pairs, the discordant pairs, plus either the X-ties or Y-ties but not both. And since direction is not known, the geometric mean is used as an estimate of relevant tied pairs. *Tau-b* requires binary or ordinal data. It reaches 1.0 (or -1.0 for negative relationships) only for square tables when all entries are on one diagonal. Although Kendall's tau correlation is not too easy to compute, it shows a wide range of advantages over other rank correlation methods like Spearman's correlation (Conover, 1980; Critchon, 1999). Those include a better statistical distribution of the considered parameter properties as well as a direct interpretation of the obtained values in terms of probabilities of observing concordant and discordant pairs, showing the strength of the relationships between variables.

5. Results and discussion

5.1. Univariate statistical obtained correlations

5.1.1. Usefulness of univariate correlations

In spite of the inherent interdependence of all the physical terrain parameters taken together, I plotted histograms in order to detect the univariate relations between mass movement frequency and the different categories of each parameter. These correlations, as well as field observations, will explain in detail the results obtained by the correlation matrix of the natural parameter weighting.

5.1.2. Relation between geomorphological parameters and MM

Examination of the distribution of mass movement frequency with the corresponding slope gradient categories shows a logical increase in the frequency of mass movements with an increase in slope gradient (**Figure 4.5a**). The maximum MM events are observed on slopes exceeding 27°. The higher the angle the greater is the shearing component of the forces acting at the potential surface of failure. Gentle slopes are expected to have a low frequency of mass movements because of lower shear stresses exerted on surficial materials associated with low gradients. At local scales, slope gradient affects the concentration of moisture and the level of pore pressure, and is often useful to resolve detailed patterns of instability, while at larger scales, it controls the hydraulic continuity.

The distribution of MM in various slope directions can be used to reflect on the influence of the general rock structure, exposure to sunlight, winds, rainfall (degree of saturation), discontinuities and physiography on MM distribution (**Figure 4.5b**). Mass movements are more frequent on slopes facing to the South, West and South-west, and decrease consequently to North and East. Slopes exposed to the south and west are warmer with higher evaporation rates and lower moisture storage capacity than those exposed to north and east. In addition, rainfall affects slope aspect depending on the direction of winds during rainfall, which commonly have a west and south-west trend in Lebanon. This shows that the regional physiography on the uplift has important influence on MM distributions and occurrences in the study area.

The slope curvatures indicate the capability of water run-off concentration or dispersion. Several studies suggest that shallow landslides mostly occur in topographic hollows where subsurface flow concentrates (Moore *et al., 1991*), with slope convexity favoring stable conditions. In our case, the more negative value (concave) **(Figure 4.5c)**,

the higher the probability of mass movement occurrence (68%). A flat area (rectilinear) has a very low value (3.5%). In particular, for negative values, the lower the value the higher the MM probability. The apparent reason is that following heavy rainfall an upwardly concave slope has more water and retains it longer.

Figure 4.5. Relation of mass movement frequency with geomorphological parameters.
a) Slope gradient

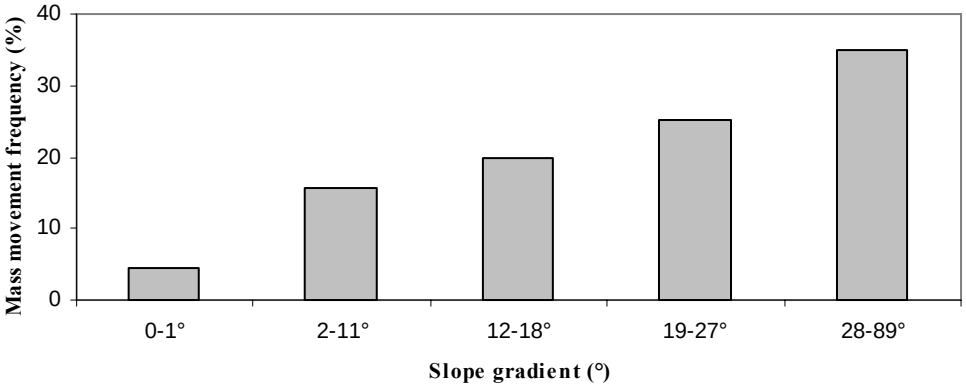

b) Slope aspect

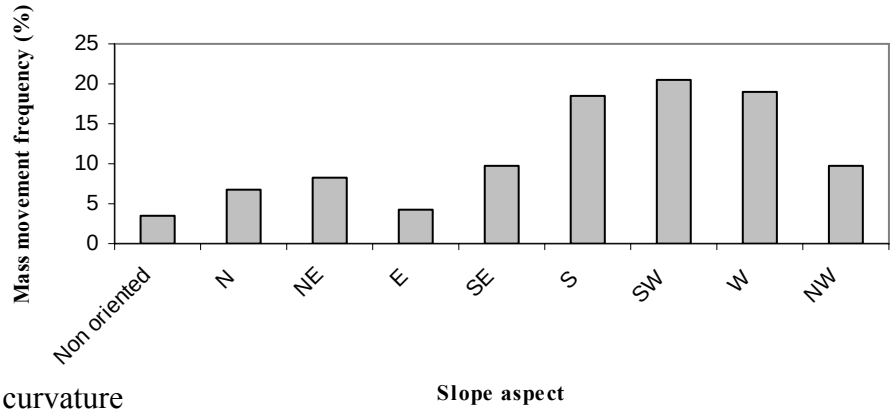

c) Slope curvature

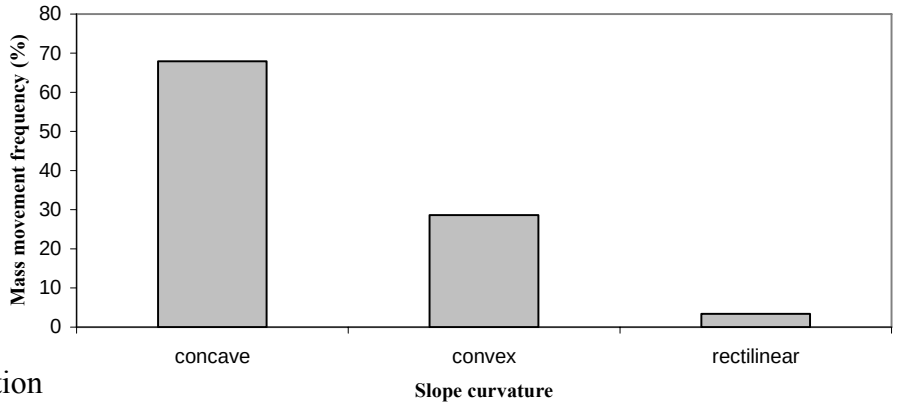

d) Elevation

The highest density of mass movements (MM) corresponds to the class with an elevation range of 500-1500 m, where many slope cuts are found in the western flank of Mount Lebanon **(Figure 4.5d)**. Density decreases both upward and downward from this elevation range in this flank. MM in the higher sloping plateaus (500-1500 m) are dominant (55%) due to the lithological character and structural control. While MM frequency decreases dramatically on the eastern flank of Mount Lebanon, having almost similar values like the coastal plain, affected by slope gradient.

5.1.3. Relation between geological/soil parameters and MM

The number of MM events in each of the 39 lithological types was counted in order to know the frequency of MM incidences in each rock type. Mass movement frequency relevant to lithological categories is shown in **Figure 4.6a.** Among the thirty-nine rock units, there are six with relatively high mass movement frequency (occurring at greater than 5%): Jurassic (J6) (21%), scree/eboulis (qe) (15%), Cretaceous (C1-14%, C6-12%, C4-10%), and basalts of the Jurassic (bj6) (6%). The Jurassic (J6, dolomite, limestone and dolomitic limestone) has a high frequency of movement for apparent reasons: 1) the fractured cliff-forming units which lead to the presence of rock falls, and 2) the failure of materials from the upper weaker successions (detachment area), mainly the (C1), leading to a predominance of debris falls. The scree, as their name indicates, are Quaternary deposits from weathered rocks. The Neocomian-Barremian unit (C1) is constituted in some localities by loosely cemented sandstones and in others by alternation of sand and clay. Sandstones are prone to the destabilizing action of water, due to poor cementation and open texture, allowing water to exert pressure on the sand particles weakening the sandstone. The Senonian (C6) shows a high frequency because it is dominated by impermeable, friable and chalky marls that dissociate and slide easily. These beds retain water, inducing weakening and lubricating effects plus undergoing volume change due to successive wetting and drying. Water also plays an important role in triggering the movement, especially when spring lines develop on valley slopes. In such cases, impermeable beds cause groundwater to migrate laterally and eventually induce water seeps at the surface, enhancing the instability factor (e.g. C2b “permeable layer” and C2a “semi-permeable”). The Cenomanian rocks (C4, limestone and dolomitic limestone) show characteristics such as bedding planes, jointing, veining and oriented microcomponents, which act as weak discontinuity planes. The basalts, which are volcanic extrusions, tend to be unstable at the surface, altering by water interaction and weathering into expansive clayey soil cover that is prone to movement.

The maximum occurrence of MM (37%) was observed also within a distance of approximately 0 to 500 m **(Figure 4.6b)** from a given fault, which agrees with other works in the domain (Zaruba and Mencl, 1982; Guillande *et al.*, 1993; Dikau *et al.*, 1996; Saha *et al.*, 2002). Farther away from the faults, MM occurrences gradually decrease. However, this is not necessarily the case in all areas of the world. An inverse relationship between the distance to the fault and the number of mass movements may exist (Uromeihy and Mahdavifar, 2000). In the study area, as the distance from the fault (buffer) increases, the likelihood of occurrence of mass movement decreases. It is significant to realize that a faulted terrain, reflecting high tectonic activity, would tend to induce a higher frequency of discontinuities in the rock mass in the vicinity of a fault, and perturbations in the circulation of water. This indicates the influence of fractures on the occurrence of mass movement and confirms previous works done in this regard.

The influence of karst on MM frequency is clearly shown in **Figure 4.6c**, with around 33% of MM occurring on karst terrains. MM frequency is higher on areas with distinct lapies than other areas with depressions, developed or non-apparent karsts, since lapies are reducing water infiltration, sliding while increasing mass and block falls. MM frequency is almost negligible with relation to quarries **(Figure 4.6d)**. However, the improper excavation of quarries is an enhancing factor to MM, taking into consideration the impact of such phenomena on different quarries types (sand or rock).

Among the thirty-eight types of soils dominating the study area, five show a high mass movement frequency (> 5%) (**Figure 4.6e)**: sandy soils (no. 11) (19%), gravel and massive landslides (no. 3) (14%), red discontinuous terra rossa soils (no. 6) (13%), mixed soils on alternating marl, limestone and sandstone (no. 20)/white rendzina (no. 22) (11%), mixed soils on alternating marl, limestone, sandstone and basalt (no. 21) (9%) and association of terra rossa and dolomitic sand (no. 6-d) (6%). Sandy soils are the most unstable because they develop pore water pressures. Terra rossa and white rendzina are also unstable due to their high clay content, making them susceptible to compression and volume change. The others are non-uniform and heterogeneous with many discontinuities.

Figure 4.6. Relation of mass movement frequency with geological/soil parameters.

a) Lithology

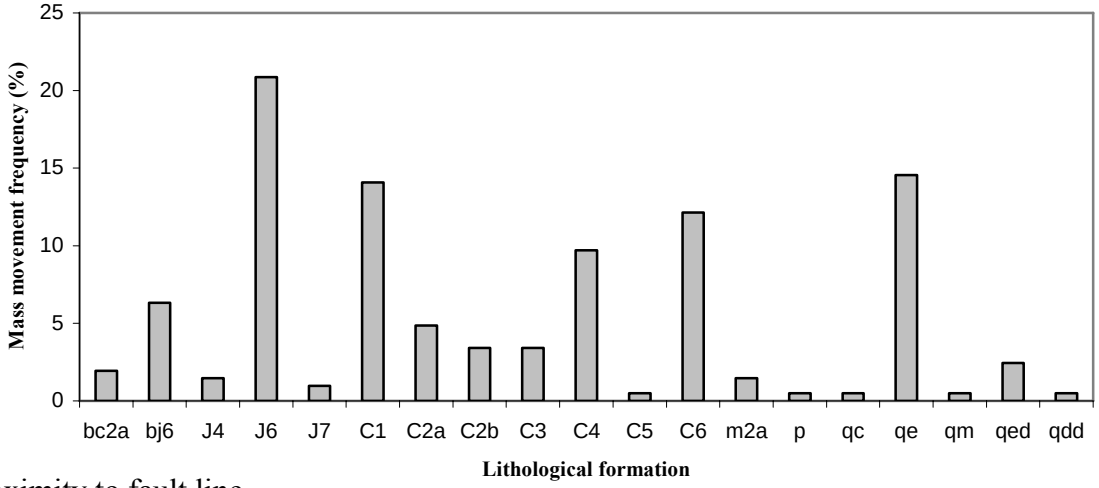

b) Proximity to fault line

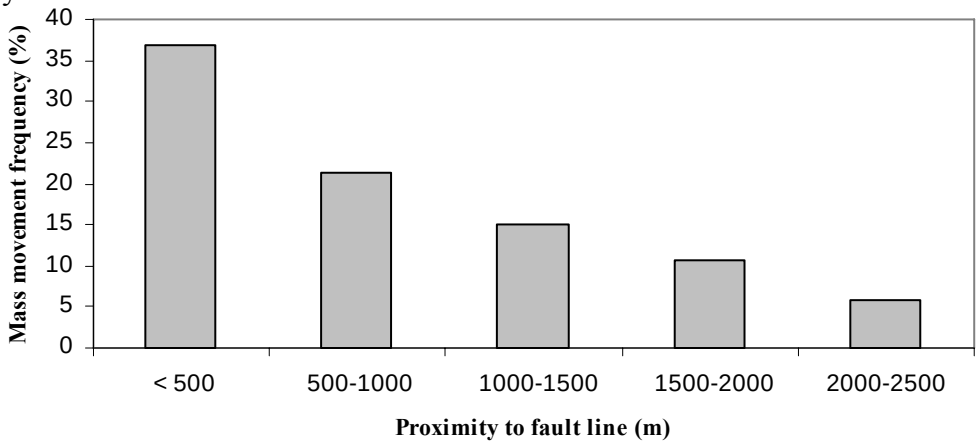

c) Karst

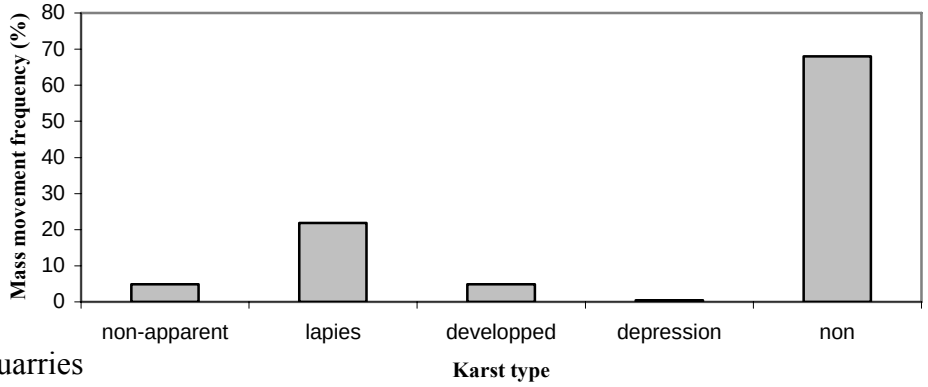

d) Proximity to quarries

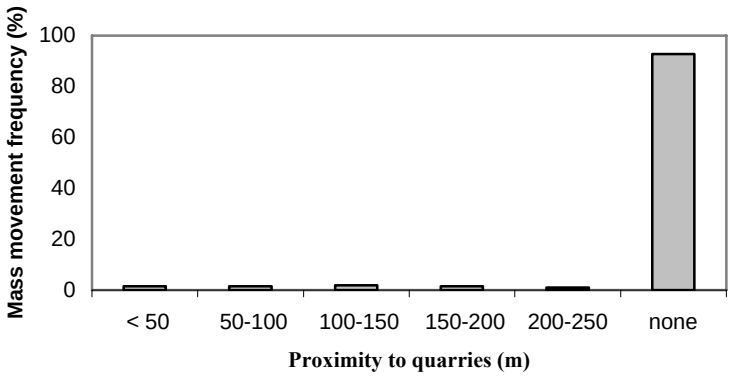

e) Soil type

**** see Table 2.3-Chapter II for soil number illustration***

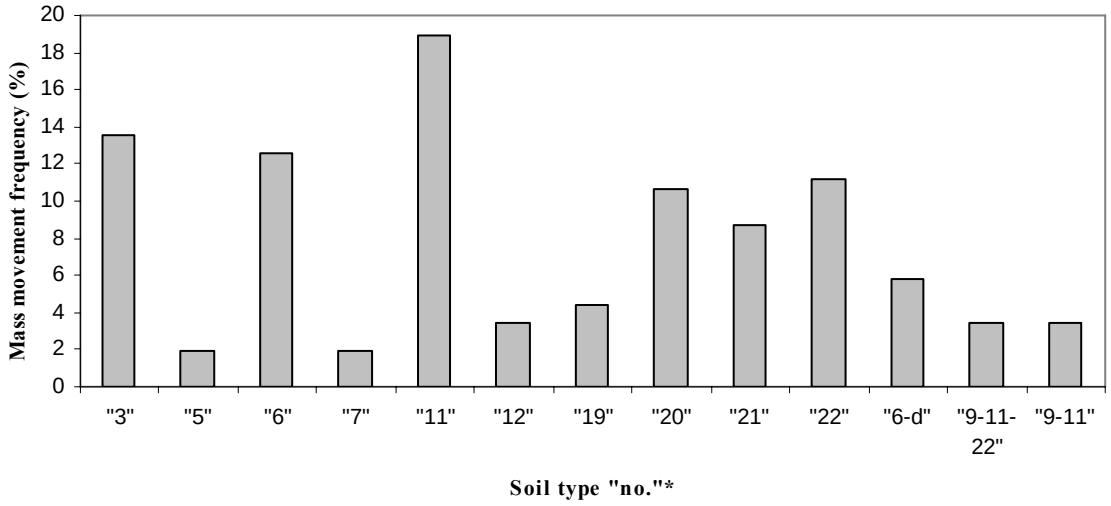

5.1.4. Relation between hydrologic/climatic parameters and MM

The maximum number of MM events (24%) occurred within a distance of approximately 0 to 50 m from a given watercourse **(Figure 4.7a)**. Farther away MM occurrences gradually decrease. This observation coincides with the fact that watercourses change the near- by morphology by forming valleys and gullies that favor mass movement. In addition, during high precipitation, debris and soil material in their proximity get over saturated very rapidly. This leads to an increase in slope material load and gravitational force that favor landslide occurrences.

Underground water flow plays an important role in triggering MM in the rainy season. This explains the presence of MM, even though of low frequency, near springs locations **(Figure 4.7b)**. In the study area, around 95% of MM are occurring at a distance from water sources exceeding 40 m. This is due to the heterogeneous cause of triggering that can be related to rainfall, seismic events, flooding, etc.

The distribution of mass movement frequency with the corresponding rainfall quantity is indicated in **Figure 4.7c**. It shows higher frequencies for quantities varying between 1000 and 1100 mm (25%), 1200-1300 mm (21%) and >1400 mm (20%) than quantities oscillating between 800-1000 mm, 1100-1200 mm and 1300-1400 mm. This indicates the absence of a solid relation between mass movement and rainfall quantity, even though the latter is a major cause triggering parameter. But the relationship between MM and rainfall quantity should not be isolated and must be correlated with other important parameters such as lithology. Therefore, it will be necessary in the future when it becomes available to take into consideration the rainfall intensity which seems to be more reliable, especially that in Lebanon, and in spite of the reduced total amounts of precipitation, rainfall is becoming more characteristically episodic and torrential. The resultant impact of this type of climate is to promote deterioration by inducing wetting and drying, thus expansion and contraction of unconsolidated slope covers possibly leading to failure.

Figure 4.7. Relation of mass movement frequency with hydrologic/climatic parameters.

a) Drainage distance

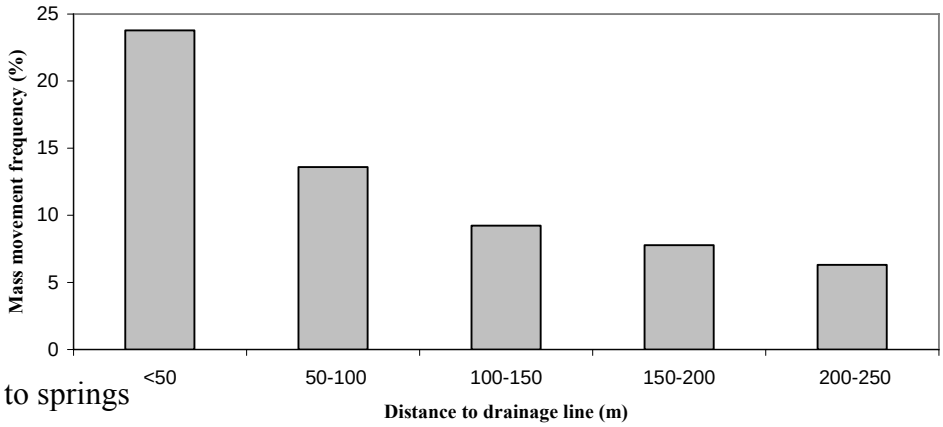

b) Proximity to springs

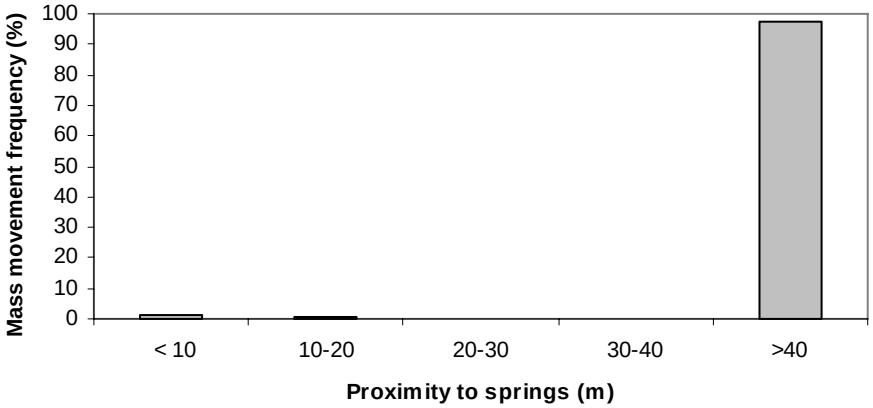

c) Rainfall

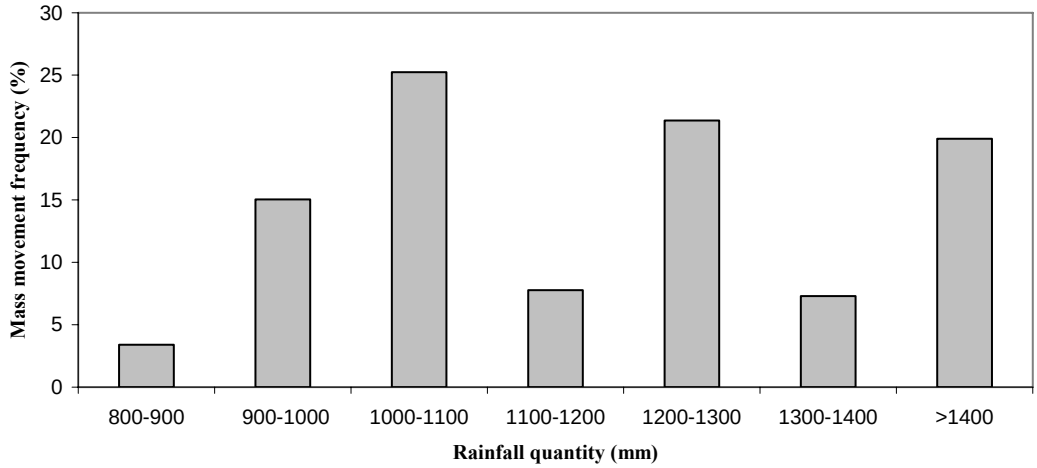

5.1.5. Relation between anthropogenic influence and MM

The correlation between land cover/use and mass movement frequency is described in **Figure 4.8a** showing that the frequency is highest on bare soils. In fact, the barren (least vegetated) areas are those that tend to be the most prone to mass movement activity. As the vegetation density increases, the stability of soil tends to increase. Vegetation limits the movement of rock debris along slopes. Where the vegetation cover is sparse or there are only shrubs species, the slow movement of the rock debris can still be detected from the curving at the bases of plant stems and from soil degradation (Pellegrini and Surian, 1996).

In addition, forests play an important role in the reduction of mass movements depending on two major elements: the umbrella medium and the surface medium. The first is expressed as water retention by canopy cover (Bou Kheir *et al.*, 2001b, 2003).This in turn depends on the leaves size and density, the higher they are the less impact of water on the soil surface. In the study area, broadleaf trees such as *Quercus infectoria* and *Abies cilicica* loose their leaves in the rainy periods. While the coniferous trees such as *Pinus brutia*, *Pinus pinea*, *Pinus halepensis* are abundant with a dense distribution that can serve as protective medium against rainfall. The second medium is the surface body itself, which acts as a tightening agent through roots. On the other hand, the high frequency of mass movements in agricultural areas, especially those cultivated with fruit trees, is due to the fact that those trees occur on non-maintained terraces and may be close to other susceptible areas. In addition, some of these areas receive abundant water from irrigation, and the saturated soil conditions likely result in increased likelihood of MM. Other factors could also contribute, i.e. depth of soil profile, grading, drainage practices, etc.

The information values of "presence of artificial cut (roads)" are systematically high for the MM data sets, pointing out the importance of anthropogenic influence on slope instability in the study area. There is an increase of MM occurrence with an increase in the proximity to road construction, especially at a buffer ranging between 50 and 100 m, and then MM frequency decreases eventually **(Figure 4.8b)**. The maintenance implementation, if it is there, is usually done near road cuts, and unfortunately does not exist after a certain distance from road networks.

Figure 4.8. Relation of mass movement frequency with anthropic data.

a) Land cover use

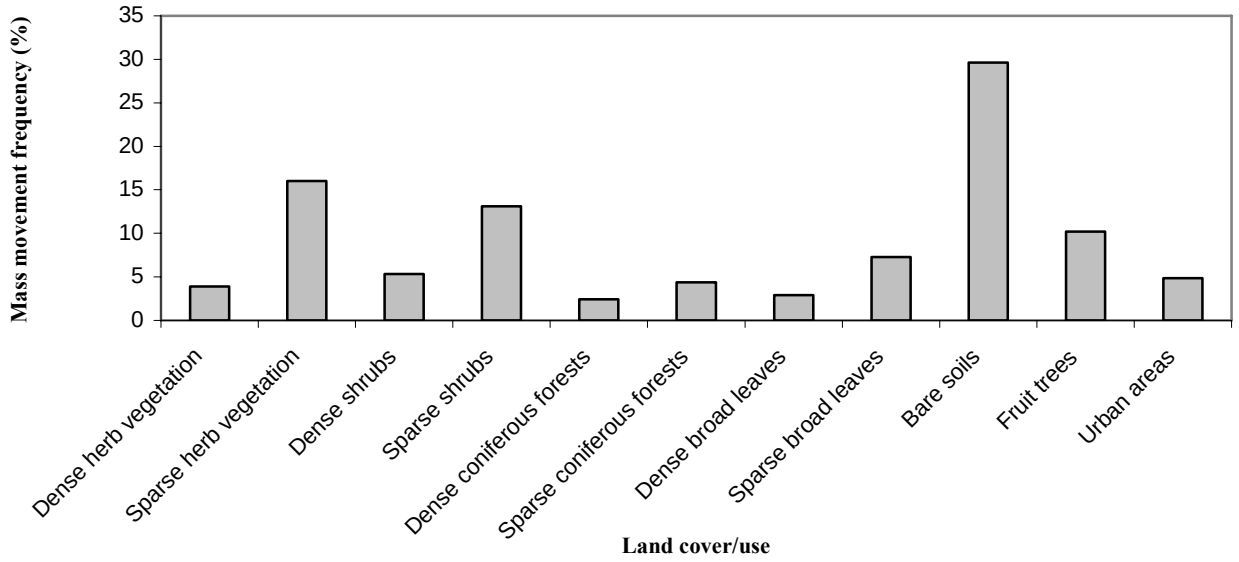

b) Proximity to roads

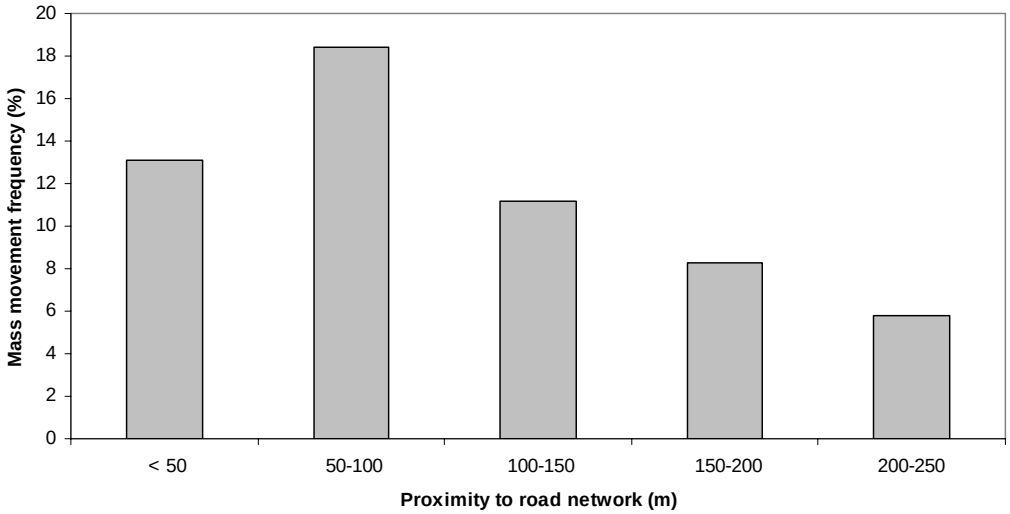

5.1.6. Relation between natural hazards and MM

Natural hazards (seismic events, floods and forest fires) are triggering factors and not predisposition factors as are most of the others. Vibrations originating from earthquakes **(Figure 4.9a)**, as well as floods **(Figure 4.9b)** and forest fires **(Figure 4.9c)** have proved conducive to MM in some locations of the study area. For instance, there are considerable amounts of MM allocated in zones of high seismic activity, while in particular cases, we can detect MM locations induced by floods or forest fires.

Figure 4.9. Relation of mass movement frequency with natural hazards.

a) Earthquake occurrence

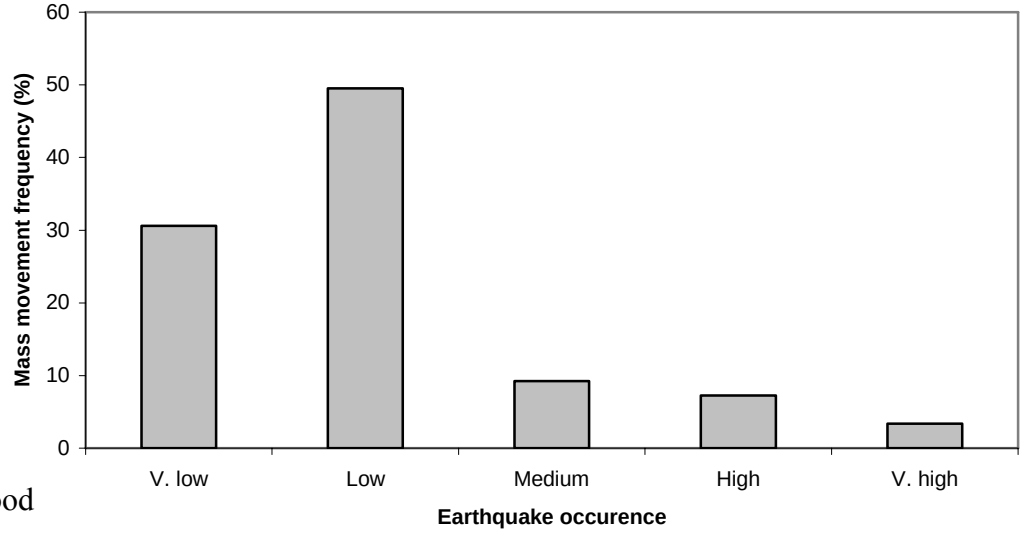

b) Flood

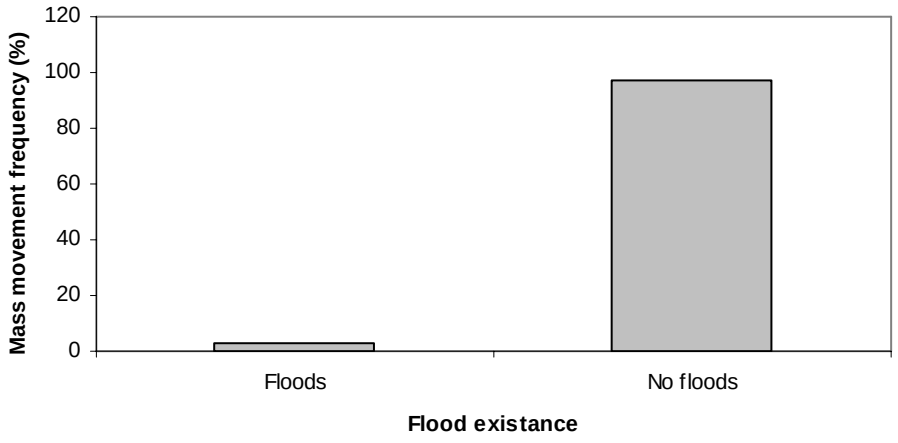

c) Forest fire

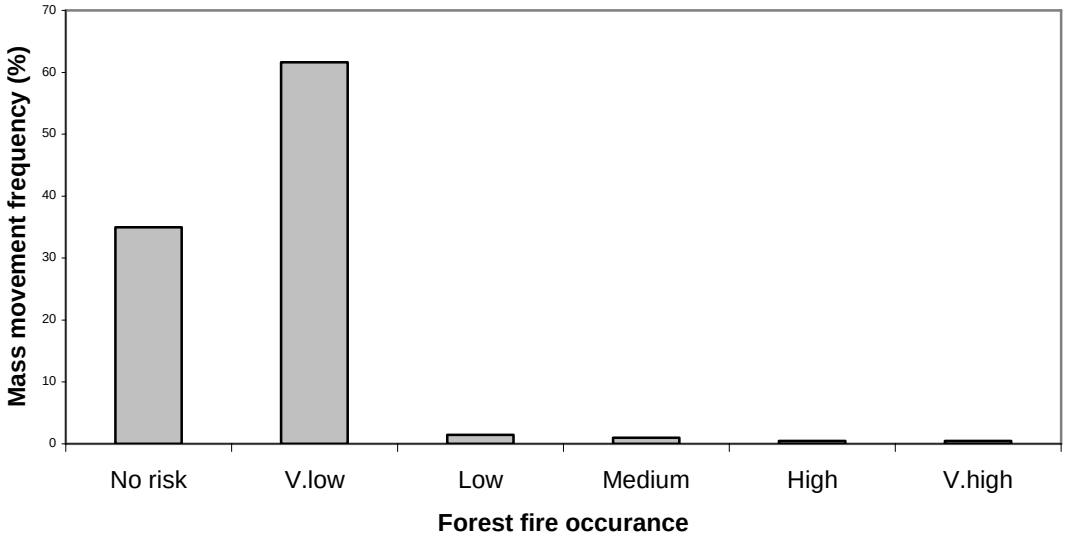

5.2. Bivariate GIS statistical correlations obtained

5.2.1. Levels of correlation significance

A correlation matrix (**Table 4.3**) between the seventeen parameters affecting mass movements was obtained. The analysis of this matrix indicates that the susceptibility of the terrain to mass movements includes all the correlated parameters which are inherent to the terrain itself, but are acting with different weights and levels of significance (1% or 5%).

The obtained values vary between -1 and +1, with a positive correlation indicating that the ranks of both parameters increase together, whilst a negative correlation indicates that as the rank of one variable increases, the other one decreases. As a result, some parameters are correlated several times with other parameters at 1% level of significance (major correlation), while others are correlated but at lower level of significance (5% - minor correlation) **(Table 4.4).** The number of relationships between the seventeen parameters is equal to 136, obtained through the following formula:

$$\frac{(\text{Number of parameters})^2 - \text{Number of parameters}}{2} = \frac{(17)^2 - 17}{2} = 136$$

Among these relationships, 12 correlations are found at high level of significance (1%) and 27 at low level (5%). However, one parameter can be correlated with two different parameters, and those will be also correlated together, all of the three influencing the occurrence of MM. As an example, lithology is highly correlated to the distance to drainage line from one side and to the distance to water courses (springs) from the other side; drainage lines and springs being also highly correlated.

5.2.2. Parameters with major correlations (1%)

Among the correlation matrix parameters, lithology seems to be the most significant parameter for mass movement occurrence within the study area for two reasons: 1) it is the most correlated (ten times as shown in the matrix) with the other parameters and 2) it is highly correlated with those parameters at 1% level of significance (seven times). Those correlations can be summarized as follows: lithology-proximity to fault line (0.275), lithology-karst (0.268), lithology-distance to water sources (springs) (0.222), lithology-soil type (0.189), lithology-distance to quarries (0.186), lithology-distance to drainage line (0.179) and lithology-floods (0.176).

It is important to mention that the studied mass movements are those in the lithologies from where they moved or detached, and not towards where they deposited. It is the location of the initial movement that decides the crucial unstable lithology. Lithology is highly correlated with the proximity to fault zone because faults can trigger mass movements by fracturing of rock and soil masses, causing the opening of numerous cracks and inducing physical changes in sensitive sediments. Obviously, active faults should be more important than non-active ones in inducing mass movements, but their detection is out of the scope of this study, though it is of major concern nowadays (Fleury *et al.*, 1999; Gomez *et al.*, 2001).

Lithology is also correlated to karst but to a less extent than faults. Different karst types (i.e. depressions, lapiez, developed karst and non-apparent karst) occur on specific lithological formation as observed in the field, leading to certain types of MM. For example, lapiez developed on the dolomite and dolomitic limestone of the Jurassic witness

considerable number of block and rock falls (see Figure 2.3), while non-apparent karst characterizing marly and chalky limestone of Miocene formation can induce slides.

In addition to the act of water on rocks like limestone in dissolving and enlarging fractures, the outlets of springs may provoke MM under certain conditions. An example is illustrated in **Figure 4.10**, where water percolates through massive, fractured and highly jointed limestone and seeps out as springs on the underlying clay-bedded materials. On long term, these soft materials are washed out creating tensions on the upper block which will collapse (block falls). The correlation between lithology and soil can be explained by the high relationship existing between the soil properties and the parent rocks. Soils may move easily if the rock is friable and susceptible to movement (explaining the occurrence of mass movements). Quarries developed on hard rocks (dolomites and limestone) reshape the natural landscape and activate the occurrence of rock falls, while those affecting soft formations increase debris falls. A good correlation was also obtained between lithology and distance to drainage line as well as between lithology and floods in inducing mass movements. This can be attributed to the fact that the more the drainage network is in hard rocks at the surface, the more the infiltration capacity. This also depends on rock type. If a large quantity of water is infiltrated, the potential of land instability tends to increase, while if there is no infiltration, the part of deep surface erosion is increased, i.e. more drainage lines.

Other parameters can also be correlated at high level of significance (1%) in decreasing order as follows: proximity to faults-seismic events (0.256), karst-spring (0.227), floods-slope gradient (0.212), distance to drainage line-floods (0.212), distance to drainage line-distance to water sources (0.177) and land cover/use-proximity to roads (0.176).

Earthquakes occur during sudden movements along faults. During long period of slow deformation, elastic strain builds up between the rock bodies on opposite sides of a fault. This deformation near faults, and the earthquakes can activate the occurrence of mass movements. Karst types and distance to water sources (springs) are highly correlated since diverse types of springs (e.g., karst springs) characterize different types of karstic terrains affecting MM processes. Floods are common on flat or nearly undulated areas, and activate the gradual movement of material down the slope. Their occurrence is highly related to the distribution of drainage system. The higher the drainage density, the lower the infiltration, the faster the movement of surface flow and materials, and vice-versa. Land cover/use shows a high correlation with proximity to roads because roads constructed in dense forests may increase the slope failures.

5.2.3. Parameters with minor correlations (5%)

At a lower level of significance (5%), correlations are reflected between parameters, but they are of less importance. These correlations can be summarized as follows: elevation-karst (0.121), elevation-rainfall quantity (0.112), slope gradient-karst (0.136), slope gradient-distance to quarries (0.119), slope gradient-soil (0.139), slope gradient-proximity to roads (0.121), slope aspect-land cover/use (0.160), slope aspect-fire (0.127), slope curvature-lithology (0.125), slope curvature-soil (0.112), slope curvature- distance to drainage line (0.128), lithology-proximity to roads (0.111), lithology-seismic events (0.153), distance to faults-distance to quarries (0.125), distance to water sources-proximity to faults (0.133), distance to faults-proximity to roads (0.156), karst-soil (0.135), karst-distance to drainage line (-0.156), distance to quarries-distance to water sources (0.156), distance to quarries-land cover/use (-0.156), distance to quarries-seismic events (0.169), soil-distance to water sources (0.145), soil-land cover/use (0.167), soils-floods (0.116),

Table 4.3. Correlation matrix between the seventeen used parameters affecting mass movements.

Coefficient of correlation	ELE	SLG	SLA	SLC	LITH	FAU	KAR	QUA	SOIL	DRA	SPRI	RAIN	LAND	ROAD	SEI	FLO	FIRE
ELE	1	0.011	0.061	0.013	0.001	0	0.121	0.071	0.051	0.005	0.027	0.112	0.009	0.013	0	0.003	0.013
SLG	0.011	1	-0.014	0.027	-0.089	-0.059	0.136	0.119	0.139	-0.082	0.078	-0.057	0.008	0.121	0.013	0.065	0.017
SLA	0.061	-0.014	1	0.007	-0.056	-0.053	0.007	0.015	-0.059	0.029	0.013	0	0.16	0.003	0	0.011	0.127
SLC	0.013	0.027	0.007	1	0.125	0.013	0.002	0.075	0.112	0.128	0.007	0.072	0.055	0.022	0.008	0.067	0.001
LITH	0.001	-0.089	-0.056	0.125	1	0.275	0.268	0.193	0.189	0.179	0.222	-0.001	-0.081	0.111	0.153	0.176	0.002
FAU	0	-0.059	-0.053	0.013	0.275	1	0.033	0.125	0.026	0.079	0.133	0.002	-0.019	0.156	0.256	0.032	0.015
KAR	0.121	0.136	0.007	0.002	0.268	0.033	1	0.005	0.135	-0.156	0.227	0.003	0.021	0.032	0.05	0.051	0.035
QUA	0.071	0.119	0.015	0.075	0.193	0.125	0.005	1	0.101	0.009	0.156	0.022	-0.156	0.07	0.169	0.003	0.065
SOIL	0.051	0.139	-0.059	0.112	0.189	0.026	0.135	0.101	1	0.033	0.145	0.058	0.167	0.031	0.033	0.116	0.007
DRA	0.005	-0.082	0.029	0.128	0.179	0.079	-0.156	0.009	0.033	1	0.177	0.105	0.063	0.068	-0.013	0.212	0.002
SPRI	0.027	0.078	0.013	0.007	0.222	0.133	0.227	0.156	0.145	0.177	1	0.116	0.007	0.013	0.002	-0.037	-0.017
RAIN	0.112	-0.057	0	0.072	-0.001	0.002	0.003	0.022	0.058	0.105	0.116	1	0.005	0.002	0.015	0.079	0.088
LAND	0.009	0.008	0.16	0.055	-0.081	-0.019	0.021	-0.156	0.167	0.063	0.007	0.005	1	0.176	0.013	0.135	0.111
ROAD	0.013	0.121	0.003	0.022	0.111	0.156	0.032	0.07	0.031	0.068	0.013	0.002	0.176	1	0.001	0.013	0.015
SEI	0	0.013	0	0.008	0.153	0.256	0.05	0.169	0.033	-0.013	0.002	0.015	0.013	0.001	1	0.091	0.003
FLO	0.003	0.065	0.011	0.067	0.176	0.032	0.051	0.003	0.116	0.212	-0.037	0.079	0.135	0.013	0.091	1	0.001
FIRE	0.013	0.017	0.127	0.001	0.002	0.015	0.035	0.065	0.007	0.002	-0.017	0.088	0.111	0.015	0.003	0.001	1

ELE = elevation; SLG = slope gradient; SLA = slope aspect; SLC = slope curvature; LITH = Lithology; FAU = Proximity to fault zone; KAR = Karst type; QUA = distance to quarries; SOIL = soil type; DRA = distance to drainage line; SPRI = distance to water courses; RAIN = rainfall quantity; LAND = land cover/use; ROAD = distance to roads; SEI = seismic events; FLO = floods; FIRE = forest fires

Correlation is significant at confidence level: 1% (value ≥ |0.76|), 5% (value ≥ |0.101| and < |0.76|)

Table 4.4. Number of correlations between the utilized parameters.

Parameter	Number of times the other parameters are		
	correlated at 1%	correlated at 5%	non-correlated
Elevation	-	2	14
Slope gradient	-	4	12
Slope aspect	0	2	14
Slope curvature	-	3	13
Lithology	7	3	6
Proximity to fault line	2	3	11
Karst type	2	4	10
Distance to quarries	1	5	10
Soil type	1	6	9
Distance to drainage line	3	3	10
Distance to water sources (springs)	3	4	9
Rainfall quantity	-	3	13
Land cover/use	1	5	10
Proximity to roads	1	3	12
Seismic events	1	2	13
Floods	2	2	12
Forest fires	-	2	14

Figure 4.10. Sketch diagram (a) illustrating the act of springs in triggering MM (b), Hammana area (Mount Lebanon).

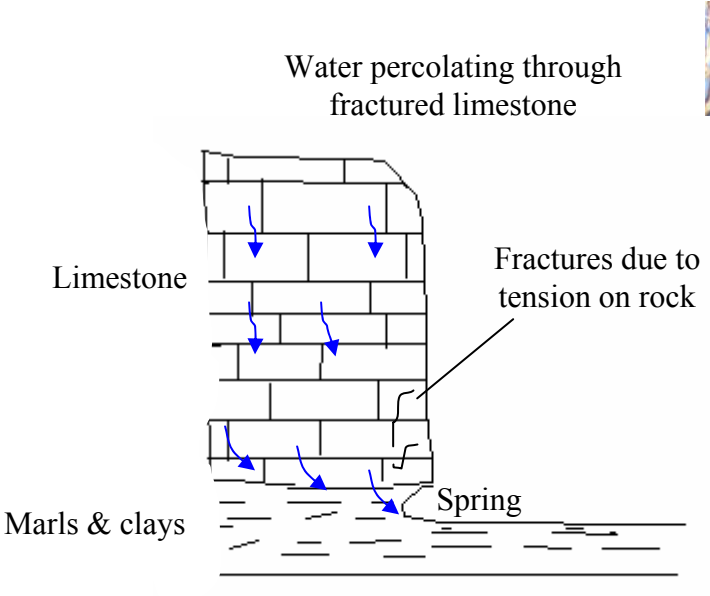

a) The seeping of water in the clay materials will increase the tension on the above rocks (limestone) resulting in MM

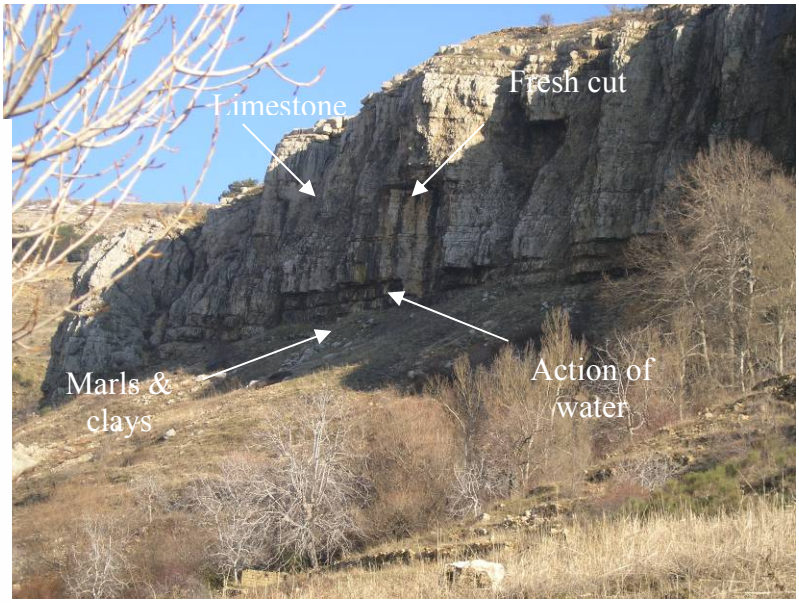

b) Photograph showing the action of water in inducing rock falls

distance to drainage line-rainfall quantity (0.105), distance to water sources-rainfall quantity (0.116), land cover/use-floods (0.135), and land cover/use-forest fires (0.111).

We notice an increase of rainfall with altitude (0.112) which leads to a consequent increase in the number of failures. In addition, karst terrains are commonly found at high elevated areas (0.121) and the action of snow in these areas increases the weathering of rocks, and the potentials of material slipping.

Slope gradient is quasi-similarly correlated with karst (0.136), distance to quarries (0.119) and roads (0.121) because of the repetitive presence of karst terrains and quarries on steep areas and the construction of roads in these areas, commonly found in Mount Lebanon. All these activities are common cause of collapse. The natural vegetation dominating the study area is grown on specific soil types (0.167) constituting a given landscape unit that can be susceptible to mass movements occurrence. Soils can also enhance mass movements due to their geomorphic situation (0.139). The steepest slopes constitute most of the erosional zone, while the relatively low lands host the rock debris and earth materials resulting from mass movements.

Slope aspect is strongly related to the microclimate (dry or wet) which, by itself, affects the vegetation cover, soil formation and erosion intensity (0.160). In addition, fire occurrence and propagation is conditioned by the direction of slope (0.127), a rapid inflammation is noticed on slopes facing to the south and south-east in the study area. A fire can activate the probability of MM through the reduction of vegetation cover (land cover/use-forest fires 0.111).

Slope curvature shows a good correlation with distance to drainage line (0.128), lithology (0.125) and soil (0.112) at a decreasing order. In fact, concave areas concentrate water, and this concentration reaches higher levels if certain lithological formations and soil types are predominant, and favors unstable conditions. Seismic events as well as constructed roads affecting soft rocks can aggravate the sliding and falling processes to a wide extent.

If a quarry is excavated on a faulted terrain (0.125) or near water sources (0.133), the probability of MM will increase severely. The proximity to major faults affects the development of slope instability, specifically once faults are cutting near roads (0.156). On karst terrains, specific soil types are developed (e.g., red mountainous soils or terra rosa) (karst-soil 0.135) and the distribution of drainage system (-0.156) is localized. Quarries are destroying the natural environment (distance to quarries-land cover/use -0.156), once coupled with seismic events (0.169), they can aggravate the MM occurrence to a wide extent.

A close correlation exists between quarries and water sources (0.156). The dewatering of quarries causes a general lowering of the water table resulting in subsidence (0.156). A close correlation exists also between rainfall quantity and distance to drainage line (0.105) from one side and between rainfall quantity and distance to water sources (0.116). Prolonged rainfall can increase the water content of slope materials leading eventually to floods and slope failure along a weak slip surface and downslope mass movement will occur. In unsaturated material, the internal voids or pores of the soils will be filled with compressible air (soil-distance to water sources 0.145). If the slope suffers from additional loading, for instance building construction, the mineral grains will be compressed more tightly and additional strength will result. However, if the pores are filled with water, the frictional strength is reduced and any external loading will increase the pore water pressure. If these pore pressures can not be relieved by water moving to an unsaturated area of the material, the solid grains begin to slip (e.g., if an expandable clay mineral like montmorillonite is available). When the soil is wet due to flooding (0.116) and once saturated (e.g. clays), it can behave like a liquid, rapidly moving initiating mudflows.

5.2.4. Parameters without any correlation

Some parameters do not show any correlation between each other, even though some of them can be correlated in some specific cases and in certain locations. For example, rainfall quantity is not correlated with floods; however huge amounts of torrential rainfall in a short duration (i.e. rainfall intensity) can lead to flooding. The number of non-correlations shown in Table 4.3 of parameters with each other can illustrate the weight of influence of each of these parameters in inducing MM.

Elevation, slope aspect and fires are correlated 2 times with other parameters, while they are not correlated fourteen times. Elevation is correlated with two parameters (karst and rainfall quantity), slope aspect the same (correlated with land cover/use and fires) and forest fires show correlation with slope aspect and land cover/use.

At a decreasing order of non-correlation, one can distinguish: elevation/slope aspect/forest fires (14 times non correlated), slope curvature/rainfall quantity/seismic events (13 times non correlated), slope gradient/proximity to roads/floods (12 times), proximity to faults (11 times), karst/distance to quarries/land cover-use/distance to drainage line (10 times), soil type/distance to water sources (9 times) and lithology (6 times) **(Table 4.4)**. When the number of non-correlations increases, the weighting of the parameter decreases. Thereof, lithology is the highest influencing parameter in inducing MM while elevation, slope aspect and forest fires are acting similarly with minor weights.

5.3. Low and high effect classes on MM occurrence

Table 4.5 summarizes the most and lowest effect classes of each parameter depending on the GIS univariate statistical analysis. Summing up, MM are more likely to occur in steep faulted unforested slopes facing to the south west, covered with sandy soils, and preferably in concave curvatures.

6. Conclusion

This chapter has shown the design and construction of spatial databases that consider MM-related factors. The databases as well as the accurate detection of the location of MM (chapter III) are crucial for MM susceptibility and hazard analysis. I have used the common univariate statistical correlations to determine simple relations between classes of each terrain parameter and MM occurrence. I have also used the bivariate GIS statistical correlations in order to define dual relations between the parameters and to detect the most related significant ones. Lithology is the predominant factor for mass movements. This may be due to the fact that most mass movements start near stratigraphic contacts (i.e. different lithologies and from groundwater influence), or at fractured cliffs, or where rock or surficial cover is weak and unconsolidated as observed in the field and explained in this chapter. Other parameters can have an influence on MM but to a lesser extent. Some of them are acting with a similar weight [those separated by (/)] as follows. These can be summarized as follows, in a decreasing order of importance: soil type/distance to water sources; karst/distance to quarries/land cover-use; proximity to faults; slope gradient/proximity to roads/floods; seismic events; elevation/slope aspect/forest fires.

This statistical weighting of terrain parameters corresponds on the whole with analysis of field observations. Thus, these results will be applied in building regional MM hazard prediction models, preventing dependency on the only skill and experience of different investigators in assuming the most important terrain parameters. In addition, they can be

easily transferred to other Mediterranean countries sharing similar geoenvironmental conditions.

Table 4.5. The most and lowest effect classes of each parameter on the occurrence of MM.

Most effect classes	Lowest effect classes
Elevation – Higher sloping plateaus (500-1500 m)	Elevation – Plain (< 100 m)
Slope gradient – (28-89°)	Slope gradient – (0-1°)
Slope aspect – (South West)	Slope aspect – (East)
Slope curvature – (concave)	Slope curvature – (rectilinear)
Lithological formation – (J6)	Lithological formation – C5, qc, p
Proximity to fault zone – (< 500 m)	Proximity to fault zone – (2000-2500 m)
Karst type – (lapies)	Karst type – (depressions)
Distance to quarries – (100-150 m)	Distance to quarries – (200-250 m)
Soil type – (sandy soils)	Soil type – (rubified coastal sand; continuous red mountainous soils)
Distance to drainage line – (< 50 m)	Distance to drainage line – (200-250 m)
Distance to water sources – (> 40 m)	Distance to water sources – (20-30; 30-40)
Rainfall quantity – (1000-1100 mm)	Rainfall quantity – (800-900 mm)
Land cover/use – bare soils	Land cover/use – (dense coniferous forests)
Proximity to roads – (50-100 m)	Proximity to roads – (200-250 m)

- V -

Comparative evaluation of mass movement Susceptibility and hazard mapping in the Study area

CHAPTER V
Comparative evaluation of mass movement Susceptibility and hazard mapping in the Study area

1. Introduction

After mass movements (MM) have been mapped, the intervening factors sorted, the main problem in MM studies is to produce susceptibility and hazard maps. These maps are of extreme importance for engineers, earth scientists and planners for several reasons: (1) They can identify and delineate unstable hazard-prone areas, so that the environmental regeneration programs can be initiated to adopt suitable mitigation measures; (2) They help planners to choose favorable locations for site development schemes, such as building and road construction. Even if hazardous areas can not be avoided altogether, their recognition in the initial stages of planning may help to adopt suitable precautionary measures.

The basic concept of MM "susceptibility" (Radbruch, 1970; Brabb *et al.*, 1972; Augusto, 2004) includes the spatial distribution of preconditioning factors related to the instability processes that determine zones of MM-prone areas without any temporal implication. On the other hand, MM "hazard" zones are defined as zones where MM of various magnitudes have a probability to occur over given timescales, obtained by superimposing instable susceptible areas with the existent effective triggering factors, induced either by natural events or by human intervention.. The objective is to map where MM are susceptible to occur, and to assess the hazards probability and magnitude. In this chapter V, a newly adapted mathematical decision-making method – Valuing Analytical Bi-Univariate (VABU) method – will be used for such mapping, which allows both qualitative (subjective) and quantitative (objective) assumptions. It is based on numerical expressions of the relationship between controlling factors and MM hazards. It also produces susceptibility maps portraying the spatial distribution of possible MM, and predicts the frequency of MM of various magnitudes. The study area, located in the Mediterranean slopes of central to northern Lebanon will be mapped at a scale of 1:50,000. The proposed VABU method in this study is compared with two other statistical methods – the valuation area accumulation method (VAA), and the Information Value method (InfoVal) that are commonly used worldwide for MM susceptibility/hazard mapping. Furthermore, the three methods were validated using field data on existent MM, and the accuracy and reliability of each method will be determined, ending by finding the most effective one to be adopted in MM susceptibility/hazard studies.

2. Factors of susceptibility/hazard mapping

The seventeen parameters prepared in Chapter IV will be used as input data in MM susceptibility/hazard mapping. MM susceptibility will be obtained through the integration of thirteen parameters considered as preconditioning factors governing the stability conditions of the terrain as follows: 1) elevation, 2) slope gradient (or slope angle), 3) slope aspect, 4) slope curvature, 5) lithology, 6) proximity to fault line, 7) karst type, 8) distance to quarry, 9) soil type, 10) distance to drainage line, 11) distance to spring, 12) land cover/use and 13) proximity to road. Whereas, MM hazards will be determined by integrating these thirteen preconditioning parameters and the four triggering ones, i.e. rainfall quantity, seismic events, floods and forest fires. Some preconditioning factors such as distance to spring and proximity to road could have a triggering effect but under specific conditions. For example, new road excavations can activate MM occurrence, as well as the presence of temporary water springs

acting only when the groundwater body is at its best. This could be studied more deeply at local scale and not at regional one as in our case.

3. Methods of susceptibility/hazard mapping

3.1. The valuing analytical bi-univariate method (VABU)

In this study, I propose a new method called "**Valuing Analytical Bi-Univariate accumulation method (VABU)**" for susceptibility/hazard mapping. This method shares some similarities with the "weighted rating combination method" developed by the United States Geological Survey (USGS, 1967) and expanded by many others (Davidson, 1982; Khawlie, 1986) in assessing land use planning. It resembles also the "analytical hierarchical process" (AHP) developed by Saaty (1988) that was used by several researchers for landslide susceptibility mapping (Barredo *et al.*, 2000; Mwasi, 2001; Nie *et al.*, 2001). The difference is that the latter (AHP) considers only one-level weighting system, developed by collecting expert opinions (i.e. not calculated on statistical basis).

The VABU method that will be developed in this study consists of applying primary- and secondary-level weights. The primary-level weights (named rates) are weights given to each class of a parameter on the basis of the univariate results obtained in Chapter IV **(Table 5.1)**. The secondary-level weights that can capture the relative importance of one parameter relative to another were established on the basis of the bivariate statistics calculated also in Chapter IV **(see Table 4.3).** This technique of simplifying the influence of all parameters in a pair-wise comparison (couple of parameters or what is called bivariate analysis) can facilitate the weighting process. It was described by Saaty and Vargas (2001) in the context of decision making processes. It was also used by Juang *et al.* (1992) to map slope failure potential using fuzzy sets, and by Ayalew *et al.* (2004) to map landslide susceptibility.

Thereof, I converted the statistical results obtained in Chapter IV for MM susceptibility/hazard mapping in a GIS system as follows. First of all, I assigned into the "attribute table" of each class in each parameter map expressed by a shapefile (vector mode) the MM frequency values shown on the plotted histograms of chapter IV. As for example, I attributed a value of 4.37 for the slope gradient class ranging between 0 and 1°, and a value of 34.96 for that ranging between 28 and 89° **(Figure 5.1)**. These MM frequency values are considered as the primary level-weights of the VABU method.

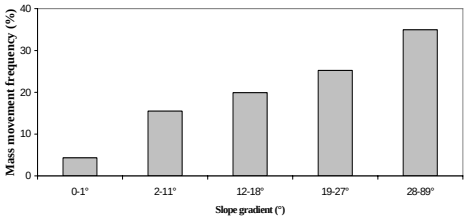

Slope gradient classes	Rate value
0-1◦	4.37
2-11◦	15.53
12-18◦	19.90
19-27◦	25.24
28-89◦	34.96

Figure 5.1. Conversion of univariate histogram on slope gradient to primary-level weight (rate) in the VABU method.

Table 5.1. The calculated statistics of VABU, VAA and InfoVal methods.

[*rate values are attributed to our proposed method (VABU), **VAA index are values calculated for valuing accumulation area method (VAA) and ***InfoVal values are calculated according to information value method (InfoVal)]

Layer parameter	Class	Rate value*	VAA index**	InfoVal***
Elevation	Coastal plain (< 100 m)	0.97	-29.62	1.40
	Lower slopes (100-500 m)	21.84	-1.99	-0.41
	Higher sloping plateaus (500-1500 m)	53.89	15.63	0.18
	Piedmonts (900-1500 m)	3.40	16.72	-0.81
	Elevated crests (> 1500 m)	19.90	-21.59	0.16
Slope gradient	0-1◦	4.37	-40.35	-1.50
	2-11◦	15.53	-22	-0.59
	12-18◦	19.90	-11.27	-1.17
	19-27◦	25.24	37.62	-0.01
	28-89◦	34.96	227.45	2.05
Slope aspect	Non oriented	3.40	-37.72	-1.39
	North (N)	6.80	-27.43	-1.49
	North-East (NE)	8.25	11.1	0.22
	East (E)	4.37	-13.89	-0.79
	South-East (SE)	9.71	-1.82	-0.65
	South (S)	18.45	45.98	1.17
	South-West (SW)	20.39	59.06	0.67
	West (W)	18.92	23.96	0.52
	North-West (NW)	9.71	-27.57	-1.65
Slope curvature	Concave	67.96	46.62	0.44
	Convex	28.64	-26.24	-0.30
	Rectilinear	3.40	-47.02	-1.18
Lithology *(shown as symbols of geological stages)- see Table 2.1.*	bc2a	1.94	94.435	-0.69
	bj6	6.31	260.53	1.49
	J4	1.46	-54.93	-0.98
	J6	20.87	23.13	0.008
	J7	0.97	31.2	0.89
	C1	14.08	56.66	0.56
	C2a	4.85	46.02	0.05
	C2b	3.40	-3.15	-0.35
	C3	3.40	0.49	-0.07
	C4	9.71	-29.14	-1.50
	C5	0.49	-54.96	-1.53
	C6	12.14	268.42	1.14
	m2a	1.46	588.85	0.97
	p	0.49	-27.62	-0.36
Lithology (continue)	qc	0.49	2.33	-0.34
	qe	14.53	267.03	1.64
	qm	0.49	-109.86	5.95
	qed	2.43	717.87	2.99
	qdd	0.49	-19.01	-0.28

Table 5.1 ***(continue)***

Layer parameter	Class	Rate value*	VAA index**	InfoVal***
Proximity to fault line	< 500 m	36.89	27.45	0.002
	500-1000 m	21.36	9.44	-0.15
	1000-1500 m	15.05	6.29	-0.003
	1500-2000 m	10.68	0.98	-0.41
	2000-2500 m	5.83	-34.27	1.19
Karst type	Non apparent	4.85	-158.3	-1.64
	Lapies	21.85	-706.3	-0.02
	Developed	4.85	-269.64	0.10
	Depressions	0.49	71.25	-3.37
	None	67.96	222	0.26
Distance to quarry	< 50 m	1.46	47.99	-0.18
	50-100 m	1.46	120.61	-0.20
	100-150 m	1.94	107.34	-0.08
	150-200 m	1.46	26.14	0.45
	200-250 m	0.97	-20.36	-0.06
Soil type *(refer to Table 2.3 for soil no.)*	Gravel and massive landslides (no. 3)	13.59	147.07	1.74
	Decalcified and rubified coastal sand (no. 5)	1.94	80.85	-0.34
	Discontinuous red mountainous soils (no. 6)	12.62	-35.43	-0.27
	Continuous red mountainous soils (no. 7)	1.94	-37.49	-1.98
	Sandy soils (no. 11)	18.93	135.43	0.40
	Continuous grey soils (no. 12)	3.40	159	-0.09
	Mixed soils on marl with bedded limestone (no. 19)	4.37	-9.54	0.47
	Mixed soils on alternating marl, limestone and sandstone (no. 20)	10.68	11.55	0.13
	Mixed soils on alternating marl, limestone, sandstone and basalt (no. 21)	8.74	78.67	0.53
	White rendzina (no. 22)	11.17	-173.79	0.85
	Discontinuous red mountainous soils-dolomitic sand (no. 6-d)	5.83	104.76	0.47
	Yellowish mountain soils-sandy soils (no. 9-11)	3.40	3.29	-0.66
	Yellowish mountain soils-sandy soils-white rendzina (no. 9-11-22)	3.40	57.85	-0.50
Distance to drainage line	< 50 m	23.79	-47.92	1.30
	50-100 m	13.59	17.74	0.60
	100-150 m	9.22	-10.58	-0.90
	150-200 m	7.77	-7.92	-0.58
	200-250 m	6.31	-20.73	-0.21
Distance to water sources (springs)	< 10 m	1.46	-37.35	1.7837
	10-20 m	0.97	15.62	0.0124

Table 5.1 ***(continue)***

Layer parameter	Class	Rate value*	VAA index**	InfoVal***
	20-30 m	0.00	-9999 (nil)	-9999 (nil)
	30-40 m	0.00	-9999 (nil)	-9999 (nil)
Rainfall quantity	600-700 mm	-53.86	-54.93	-9999 (nil)
	700-800 mm	-53.86	-54.93	-9999 (nil)
	800-900 mm	3.40	-129.12	-1.36
	900-1000 mm	15.05	9.15	-0.20
	1000-1100 mm	25.24	24.77	0.12
	1100-1200 mm	7.77	-26.27	-0.62
	1200-1300 mm	21.36	31.2	-0.02
	1300-1400 mm	7.28	-7.12	0.05
	> 1400 mm	19.90	47.96	1.12
Land cover/use	Dense herbaceous vegetation	3.88	-28.92	0.51
	Sparse herbaceous vegetation	16.02	-2.26	0.14
	Dense shrubs	5.34	65.81	-2.93
	Sparse shrubs	13.11	-14.94	0.83
	Dense coniferous forests	2.43	8.68	-0.30
	Sparse coniferous forests	4.37	-20.24	-0.36
	Dense broadleaves forests	2.91	-20.68	0.38
	Sparse broadleaves forests	7.28	-12.56	-0.17
	Bare soils	29.62	154.25	1.35
	Fruit trees	10.19	-17.10	-0.48
	Urban areas	4.85	-54.93	-0.36
Proximity to road	< 50 m	13.11	3.08	2.93
	50-100 m	18.45	109.32	1.50
	100-150 m	11.17	78.2	0.50
	150-200 m	8.25	35.89	-0.03
	200-250 m	5.83	1.4	-0.13
Seismic events	Very low	30.58	-14.73	-0.04
	Low	49.52	71.6	0.38
	Medium	9.22	-13.61	-0.19
	High	7.28	3.88	0.07
	Very high	3.40	1.38	0.07
Floods	Presence of floods	2.91	-35.69	-1.19
	Absence of floods	97.09	3.29	0.06
Fire	No risk	34.95	-50.87	-0.4860
	Very low risk	61.64	10.95	0.3184
Fire *(continue)*	Low risk	1.46	-16.58	-0.85
	Medium risk	0.97	169.03	-0.82
	High risk	0.49	785.41	0.31
	Very high risk	0.49	2249.22	0.61

Secondly, I imported the results of bivariate correlations shown in **Table 4.3** (Chapter IV) and I separated them in two tables, considering for the first one the values of the preconditioning parameters, and for the second, the values of the triggering ones. Afterwards, I converted these values to secondary level weights using the arithmetic mean method as follows.

The influence of a parameter in comparison with another parameter is read along columns. For that, I summed up the values of each column **(Table 5.2)**, and I divided then the values of each couple of parameters by the calculated sum value of the same parameter column. As for example, the sum value of the elevation parameter column is equal to 1.472 calculated by summing the values of all couple of parameters shown in this column, i.e. elevation - elevation (1), slope gradient - elevation (0.011), slope aspect - elevation (0.061), slope curvature - elevation (0.013), lithology - elevation (0.001), proximity to fault - elevation (0.089), karst - elevation (0.121), distance to quarry - elevation (0.071), soil type - elevation (0.051), distance to drainage line - elevation (0.005), distance to spring - elevation (0.027), land cover/use - elevation (0.009), and proximity to road - elevation (0.013) **(Table 5.2)**. The division of the slope gradient-elevation value (0.011) for example by the sum value of the column (1.472) will lead to a new value (0.00747), that will be summed with the other values calculated in the same way along the row, and a mean value will be calculated **(Table 5.3)**. The mean calculated values along rows are considered as secondary weight-levels attributed to each parameter.

Similarly using the same way, I calculated the secondary-level weights of the triggering parameters useful for building the hazard maps, with the establishment of two new matrices **(Tables 5.4 and 5.5)**. Once the calculation of the secondary level-weights was performed statistically, I assigned these weights to the parameter maps using the "Weighted Overlay tool" of the ArcGIS 9.2 Model Builder. For that, and in order to achieve easy computation, I converted all vector maps to raster files with 30 m pixel size. I chose this pixel size in order to attain susceptibility/hazard maps with 1:50,000 cartographic scale, by applying the following equation: S = 1/X, with S = scale of representation and X = 2r x 10^3 [r is the pixel resolution (size) in meters] (Girard and Girard, 1999). At a later stage, I applied two different equations for determining susceptible **(eq. 1)** and hazardous **(eq. 2)** areas.

$$\text{MM SUSCEPTIBILITY } (MM_s) = \sum_{i=1}^{n} PP_i * w_i \quad \text{(eq. 1)}$$

Where PSP = preconditioning parameters, and w = secondary-weight level given to each parameter

$$\text{MM HAZARD } (MM_h) = [\sum_{i=1}^{n} TP_i * w_i] * MM_s \quad \text{(eq. 2)}$$

Where TSP = triggering parameters, w = secondary-weight level given to each parameter, and MM_s = MM susceptibility

Table 5.2. Summing up the bivariate values of preconditioning parameters obtained in Chapter IV for calculating the secondary weight levels characterizing the MM susceptibilities produced by VABU method.

Coefficient of correlation	ELE	SLG	SLA	SLC	LITH	FAU	KAR	QUA	SOIL	DRA	SPRI	LAND	ROAD
ELE	1	0.011	0.061	0.013	0.001	0.089	0.121	0.071	0.051	0.005	0.027	0.009	0.013
SLG	0.011	1	-0.014	0.027	-0.089	-0.059	0.136	0.119	0.139	-0.082	0.078	0.008	0.121
SLA	0.061	-0.014	1	0.007	-0.056	-0.053	0.007	0.015	-0.059	0.029	0.013	0.16	0.003
SLC	0.013	0.027	0.007	1	0.125	0.013	0.002	0.075	0.112	0.128	0.007	0.055	0.022
LITH	0.001	-0.089	-0.056	0.125	1	0.275	0.268	0.193	0.189	0.179	0.222	-0.081	0.111
FAU	0.089	-0.059	-0.053	0.013	0.275	1	0.033	0.125	0.026	0.079	0.133	-0.019	0.156
KAR	0.121	0.136	0.007	0.002	0.268	0.033	1	0.005	0.135	-0.156	0.227	0.021	0.032
QUA	0.071	0.119	0.015	0.075	0.193	0.125	0.005	1	0.101	0.009	0.156	-0.156	0.07
SOIL	0.051	0.139	-0.059	0.112	0.186	0.026	0.135	0.101	1	0.033	0.145	0.167	0.031
DRA	0.005	-0.082	0.029	0.128	0.179	0.079	-0.156	0.009	0.033	1	0.177	0.063	0.068
SPRI	0.027	0.078	0.013	0.007	0.222	0.133	0.227	0.156	0.145	0.177	1	0.007	0.013
LAND	0.009	0.008	0.16	0.055	-0.081	-0.019	0.021	-0.156	0.167	0.063	0.007	1	0.176
ROAD	0.013	0.121	0.003	0.022	0.111	0.156	0.032	0.07	0.031	0.068	0.013	0.176	1
SUM	1.472	1.395	1.113	1.586	2.334	1.798	1.831	1.783	2.07	1.532	2.205	1.41	1.816

ELE = elevation, SLG = slope gradient, SLA = slope aspect, SLC = slope curvature, LITH = lithology, FAU = proximity to fault line, KAR = karst type, QUA = distance to quarries, SOIL = soil type, DRA = distance to drainage line, SPRI = distance to water sources (springs), LAND = land cover/use, ROAD = proximity to roads

Table 5.3. Arithmetic mean values (secondary weight levels) of preconditioning parameters characterizing the MM susceptibilities produced using VABU method.

	ELE	SLG	SLA	SLC	LITH	FAU	KAR	QUA	SOIL	DRA	SPRI	LAND	ROAD	Mean	%
ELE	0.67934	0.00788	0.05481	0.00820	0.00043	0.04949	0.06609	0.03982	0.02464	0.00326	0.01224	0.00638	0.00716	**0.0564**	**6.35**
SLG	0.00747	0.71685	0.01258	0.01702	0.03813	0.03281	0.07428	0.06674	0.06715	0.05352	0.03537	0.00567	0.06663	**0.0702**	**7.91**
SLA	0.04144	0.01004	0.89847	0.00441	0.02399	0.02948	0.00382	0.00841	0.02850	0.01893	0.00590	0.11348	0.00165	**0.0699**	**7.87**
SLC	0.00883	0.01935	0.00629	0.63052	0.05356	0.00723	0.00109	0.04206	0.05411	0.08355	0.00317	0.03901	0.01211	**0.0565**	**6.36**
LITH	0.00068	0.06380	0.05031	0.07881	0.42845	0.15295	0.14637	0.10824	0.09130	0.11684	0.10068	0.05745	0.06112	**0.0857**	**9.65**
FAU	0.06046	0.04229	0.04762	0.00820	0.11782	0.55617	0.01802	0.07011	0.01256	0.05157	0.06032	0.01348	0.08590	**0.0673**	**7.58**
KAR	0.08220	0.09749	0.00629	0.00126	0.11482	0.01835	0.54615	0.00280	0.06522	0.10183	0.10295	0.01489	0.01762	**0.0689**	**7.76**
QUA	0.04823	0.08530	0.01348	0.04729	0.08269	0.06952	0.00273	0.56085	0.04879	0.00587	0.07075	0.11064	0.03855	**0.0696**	**7.84**
SOIL	0.03465	0.09964	0.05301	0.07062	0.07969	0.01446	0.07373	0.05665	0.48309	0.02154	0.06576	0.11844	0.01707	**0.0699**	**7.87**
DRA	0.00340	0.05878	0.02606	0.08071	0.07669	0.04394	0.08520	0.00505	0.01594	0.65274	0.08027	0.04468	0.03744	**0.0712**	**8.02**
SPRI	0.01834	0.05591	0.01168	0.00441	0.09511	0.07397	0.12397	0.08749	0.07005	0.11554	0.45351	0.00496	0.00716	**0.0660**	**7.43**
LAND	0.00611	0.00573	0.14376	0.03468	0.03470	0.01057	0.01147	0.08749	0.08068	0.04112	0.00317	0.70922	0.09692	**0.0744**	**8.38**
ROAD	0.00883	0.08673	0.00269	0.01387	0.04756	0.08676	0.01748	0.03926	0.01498	0.04439	0.00589	0.12482	0.55066	**0.0614**	**6.92**

ELE = elevation, SLG = slope gradient, SLA = slope aspect, SLC = slope curvature, LITH = lithology, FAU = proximity to fault line, KAR = karst type, QUA = distance to quarries, SOIL = soil type, DRA = distance to drainage line, SPRI = distance to water sources (springs), LAND = land cover/use, ROAD = proximity to roads

Table 5.4. Summing up the bivariate values of triggering parameters obtained in Chapter IV for calculating the secondary weight levels characterizing the MM hazards produced by VABU method.

Coefficient of correlation	RAIN	SEI	FLO	FIRE
RAIN	1	0.015	0.079	0.088
SEI	0.015	1	0.091	0.003
FLO	0.079	0.091	1	0.001
FIRE	0.088	0.003	0.001	1
SUM	**1.182**	**1.109**	**1.171**	**1.092**

RAIN = rainfall quantity, SEI = seismic events, FLO = floods, FIRE = fire hazard

Table 5.5. Arithmetic mean values (secondary weight levels) of triggering parameters characterizing the MM hazards produced by VABU method.

	RAIN	SEI	FLO	FIRE	MEAN	Corresponding weight
RAIN	0.8460237	0.0135257	0.0674637	0.0805861	**0.059271**	**25.18**
SEI	0.0126904	0.9017133	0.0777114	0.0027473	**0.058521**	**24.87**
FLO	0.0668359	0.0820559	0.853971	0.0009158	**0.059046**	**25.09**
FIRE	0.0744501	0.0027051	0.000854	0.9157509	**0.058456**	**24.84**

****RAIN = rainfall quantity, SEI = seismic events, FLO = floods, FIRE = fire hazard***

3.2. Valuing area accumulation method (VAA)

In addition to the proposed designed method (VABU), I applied another method (***valuing area accumulation method - VAA***) that was commonly used elsewhere (Soeters and van Westen, 1996; Kelarestaghi, 2003) for susceptibility/hazard mapping. This VAA method depends on a mathematical index, subtracting the MM frequency occurrence of each class of each parameter by the density of MM in the studied area **(eq. 3 & 4)**:

VAA index = 1000 (A/B) – 1000 (C/D) (eq. 3)

Where VAA index = Valuing area accumulation method index
A = the number of MM in each class of parameters;
B = the area of each class of parameters;
C = the number of total MM in the study area = 202 (in our case study);
D = the total area of the studied region = 3750 km^2 (in our case study)

→ VAA index = 1000 (A/B) – 1000 (202/3750) (eq. 4)
→ VAA index = 1000 (A/B) – 53.86 (eq. 4)

This index was calculated for each class of each parameter **(Table 5.1)**. Afterwards, the preconditioning parameters were overlaid together summing pixel values and resulting in a MM susceptibility map. The intersection of the susceptibility map with the triggering parameters results in a hazard map of the area.

2.3. Information value method (InfoVal)

MM susceptibility/hazard assessment was fulfilled also using a data-driven approach – the **Information Value Method (InfoVal)**, which represents the third method considered in this study. It depends, similarly to the valuing area accumulation method (VAA), on the probability of MM occurrence within a certain area of each class of a parameter, but using different formula index. The index in this case represents a logarithm used to take care of the large variation in the weights (Saha *et al.*, 2005), and differs from the previous VAA and VABU methods by using the areas occupied by MM rather than their numbers. It can be derived using the following equation (Yan, 1988; Wu *et al.*, 2001) **(eq. 5 & 6)**:

$$InfoVal = \ln\left(\frac{Densclass}{Densmap}\right) \quad \textbf{(eq. 5)}$$

$$InfoVal = \ln\frac{Npix(Si)/Npix(Ni)}{\sum_{i=1}^{n} Npix(Si) / \sum_{i=1}^{n} Npix(Ni)} \quad \textbf{(eq. 6)}$$

Where InfoVal is the weight given to the i^{th} class of a particular parameter layer (e.g., red mountainous soils in the thematic layer "soil type"),
Densclass is the MM density within the parameter class,
Densmap is the MM density within the entire parameter layer,
Npix(Si) is the number of MM pixels in a certain parameter class,
Npix(Ni) is the total number of pixels in a certain parameter class, and
n is the number of classes in a parameter map.

Thus, I calculated the weight for various classes in each parameter **(see Table 5.1)**. I overlaid then the preconditioning parameters to prepare a susceptibility map. Once obtained, this map is multiplied by the triggering parameters, and a hazardous map is derived.

4. Classification of MM susceptibility/hazard maps

Once I constructed the susceptibility/hazard raster layer maps using the three described methods previously (VABU, VAA and InfoVal), I tried to divide the pixel histograms of these maps in different classes. This division is not an easy task, based commonly in the literature on expert opinions (Guzetti *et al.*, 1999; Lee and Min, 2001; Dai and Lee, 2002; Ohlmacher and Davis, 2003). But, this type of changing continuous data into two or more classes in a subjective way (expert opinions) does not take into account the relative position of a case within the susceptibility/hazard maps, and is neither fully automated nor statistically tested. In this study, I have considered four classification systems that use quantiles, natural breaks, equal intervals and standard deviations, and attempted to choose the one that best suits the information and the scale of present investigation.

A few trials showed that the quantile-based classification system has a disadvantage in that it places widely different values in the same class. The use of natural breaks is good when there are big jumps in data values, which is not the case in our susceptibility/hazard maps. Using equal intervals was also found not to be helpful because it emphasizes one class relative to others. The standard deviation method has a certain merit in that it uses the mean to

generate class breaks, and allows dividing the susceptibility/hazard maps into five classes of MM susceptibility/hazard maps, respectively: very low, low, medium, high and very high by adding or subtracting one standard deviation at a time. This allows adjusting objectively the class boundaries and refining suitable susceptibility/hazard maps.

5. Comparison and validation of the obtained susceptibility/hazard maps

After the construction and categorization of the susceptibility/hazard maps in five classes each (very low, low, medium, high and very high), a comparative evaluation of these maps was performed on attribute and spatial basis, as well as by considering correspondence analysis as explained at a later stage. The attribute evaluation basis considers the total number of polygons and the total perimeter in each obtained map, in addition to the number of polygons and the covered area in each class of the obtained map. Whereas, the spatial evaluation basis pertains to compare the percentages of polygons and areas characterizing the three susceptibility maps on one side, and the three hazard maps on the other side. The correspondence analysis is an automated comparison between susceptibility maps or hazard maps produced using the three different methods (VABU, VAA and InfoVal), that permits the assessment of the degree of coincidence between these maps. It seems important in checking if the same areas are witnessing the same MM susceptibility/hazard class or different ones.

In addition to the comparison, I validated the three obtained susceptibility maps by subtracting an independent dataset from the considered mass movements detected through the interpretation of satellite imageries (Chapter III) and verified in the field. The withheld dataset of 40 field sites (~ 20% of the total number of MM detected in the study area) was obtained by applying a stratified random sampling using VBA (Visual Basic) script attached customized for ArcGIS 9.2. Afterwards, I checked the location of these sites within the different classes of the susceptibility maps, and I calculated the accuracy of each map by dividing the number of sites falling in the high and very high classes by the total number of sites. The map with the highest accuracy demonstrates the usefulness of the used method, that must be adopted in future studies for predicting MM susceptible and hazardous areas.

6. Results and discussion

6.1. Attribute and spatial analysis of MM susceptibility maps

The MM susceptibility maps are built using the three different methods applied on the thirteen preconditioning parameters. The first map (map 1 – **Figure 5.2**) obtained through the implementation of the newly designed valuing analytical bi-univariate method (VABU – method 1), comprises the same classes as the maps constructed using valuing area accumulation method (VAA – map 2 and method 2) **(Figure 5.3)** and depending on the Information value method (InfoVal – map 3 and method 3) **(Figure 5.4)**. These maps rank the terrain stability of the studied area into five classes ranging from stable (very low susceptibility) to unstable (very high susceptibility). A colour scheme was applied on these classes relating stronger colours (red, orange and yellow) to unstable and marginally unstable areas and cool colours (blue and green) to more stable ones. This colour scheme is adopted in similar studies (Spieker and Gori, 2000; 2003a, b).

The medium MM susceptibility class (no. 3) covers the largest area in the produced maps 1 and 2 (around 37% each), whereas 62% of the region is covered by the very low class in map 3 **(Tables 5.6, 5.7 and 5.8)**.

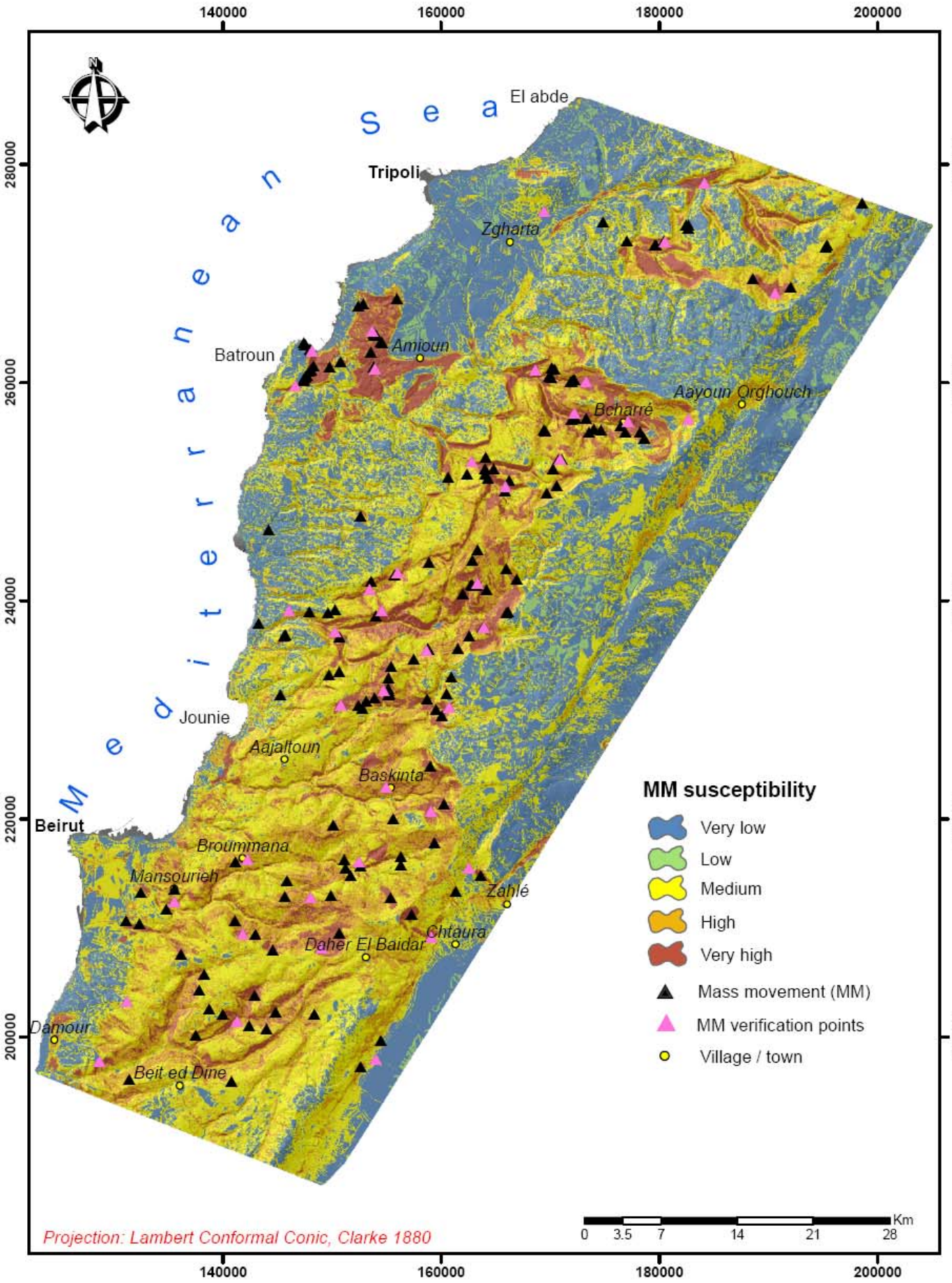

Figure 5.2. Mass movement (MM) susceptibility map derived from VABU method.

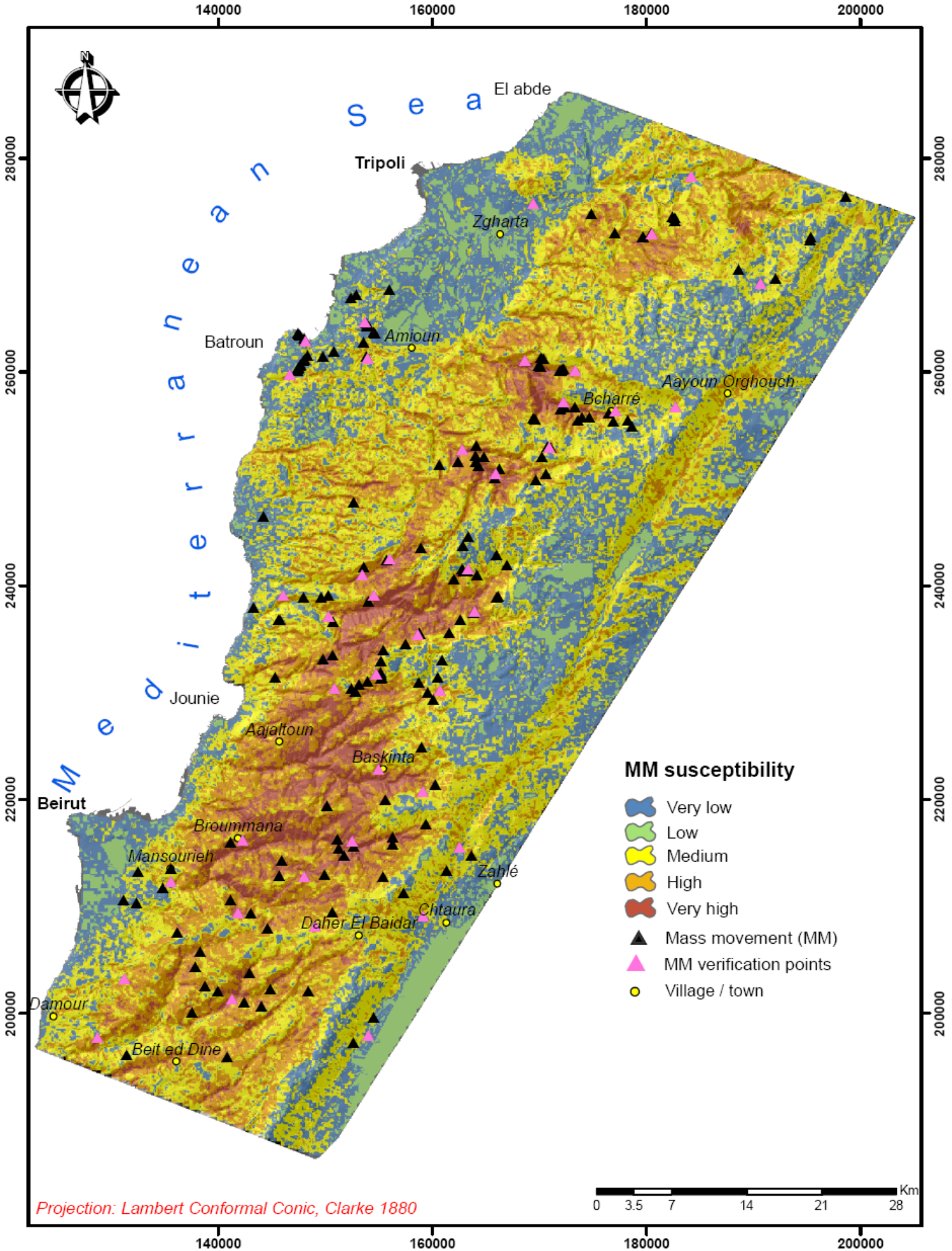

Figure 5.3. Mass movement (MM) susceptibility map derived from VAA method.

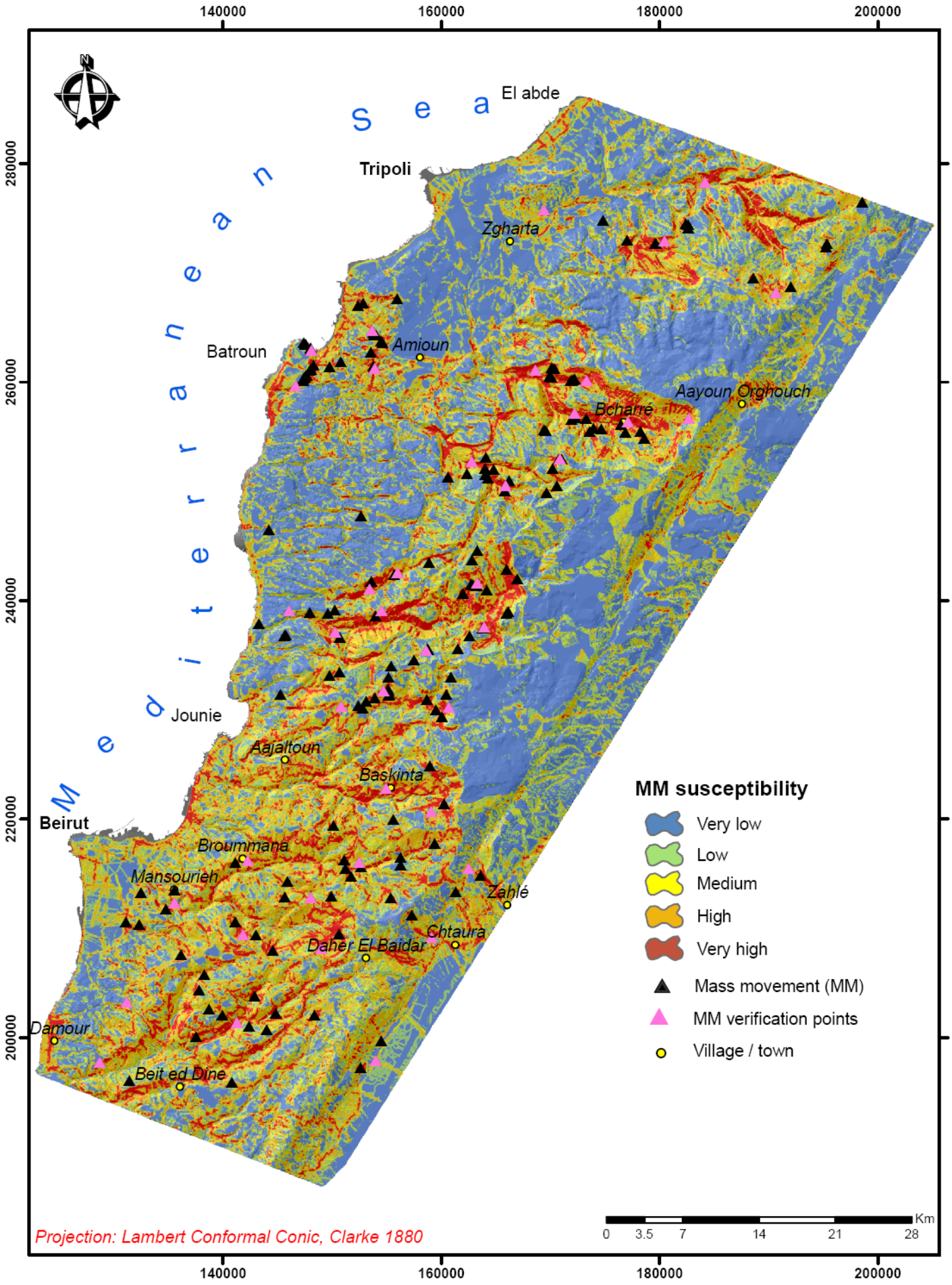

Figure 5.4. Mass movement (MM) susceptibility map derived from InfoVal method.

The very low (no. 1) to low (no. 3) susceptibility classes have nearly equal areas in both maps 1 and 2 to the high (no. 4) and very high (no. 5) classes [(classes 1 & 2 – 35%, classes 4 & 5 – 28% on map 1) and (classes 1 & 2 – 31.5%, classes 4 & 5 – 31% on map 2)]; while in map 3, the low susceptibility class occupies a similar area than high and very high classes (i.e. low class – 6.5%, high class – 0.5% and very high class – 6%). Methods 1 (VABU) and 2 (VAA) disperse susceptibility of the terrain in close equal class areas, while InfoVal often underestimates the susceptibility; this can be considered as a negative point for management planning considerations because the possibility of overlooking actual MM decreases.

Table 5.6. Number of polygons and covered areas by the five susceptibility classes obtained using valuing analytical bi-univariate VABU method (method 1 and map 1).

Pixel value range	Susceptibility class (no.)	Polygons		Areas	
		Number of polygons	% of polygons	Covered area (km^2)	% of covered area
0.9618 to 6.2010	Very low (1)	13234	20%	1256	33%
6.2010 to13.5828	Low (2)	3724	5.5%	81	2%
13.5828 to 17.2737	Medium (3)	23093	34%	1376	37%
17.2737 to 20.9647	High (4)	19529	29%	703	19%
20.9647 to 25.3378	Very high (5)	7755	11.5%	334	9%

The highest number of polygons is shown on map 1 (VABU) (i.e. 67335 polygons) versus 24132 polygons in map 2 (VAA), and 46067 polygons in map 3 (InfoVal) **(Table 5.9)**. Therefore, the use of VABU method increases the number of polygons by 64%, once compared to method 2 (VAA) and by 31.5% if method 3 (InfoVal) is considered **(Table 5.9)**. This indicates an important spatial transformation through differentiating more the areas characterized by different MM susceptibility levels. The perimeter (polygons' boundaries) of the total number of polygons is another proof on this finding. In fact, the total perimeter in the MM susceptibility map of method 1 (VABU) is equal to 60896 km, while in the maps of methods 2 (VAA) and 3 (InfoVal) it is 38234 km and 46309 km, respectively. The increase in the perimeter in map 1 is varying between 14587 km (24% - map 3) and 22662 km (around 37% - map 2). It is important to mention that the difference in polygons' number between maps 2 and 3 is 48%, highlighting the effect of the adopted methodology in modifying the result.

Table 5.7. Number of polygons and covered areas by the five susceptibility classes obtained using valuing area accumulation (VAA) method (method 2 and map 2).

Pixel value range	Susceptibility class (no.)	Polygons		Areas	
		Number of polygons	% of polygons	Covered area (km^2)	% of covered area
-446.9299 to -328.7560	Very low (1)	5577	23%	938	25%
-328.7560 to -119.6680	Low (2)	2376	10%	247	6.5%
-119.6680 to -89.4199	Medium (3)	7115	30%	1408	37.5%
-89.4199 to -298.5079	High (4)	6128	25%	893	24%
-298.5079 to -1155.449	Very high (5)	2936	12%	264	7%

Table 5.8. Number of polygons and covered areas by the five susceptibility classes obtained using information value (InfoVal) method (method 3 and map 3).

Pixel value range	Susceptibility class (no.)	Polygons		Areas	
		Number of polygons	% of polygons	Covered area (km^2)	% of covered area
-14.4547 to -7.0639	Very low (1)	10306	22.5%	2337	62%
-7.0639 to -0.7398	Low (2)	7151	15.5%	244	6.5%
-0.7398 to 2.4221	Medium (3)	18191	39.5%	932	25%
2.4221 to 5.5841	High (4)	1446	3%	20	0.5%
5.5841 to 14.9982	Very high (5)	8973	19.5%	217	6%

Table 5.9. Spatial comparison (number of polygons and total perimeter) between the three obtained susceptibility maps.

Susceptibility maps	Total number of polygons (NP)	Total perimeter (TP) (km)	Difference between maps				
				NP	% NP	TP (km)	% TP
Map 1 (VABU)	67335	60896	**Map1/Map2**	43203	64%	22662	37%
Map 2 (VAA)	24132	38234	**Map1/Map 3**	21268	31.5%	14587	24%
Map 3 (InfoVal)	46067	46309	**Map2/Map3**	21935	48%	8075	17%

The comparative analysis between the three produced susceptibility maps indicates that the polygons' difference reaches the same values (-26% to 10%) once maps 1 and 3 are compared from one side, and maps 2 and 3 from the other side (-22% to 9.5%) **(Table 5.10)**. However, these values are decreasing if map 2 is compared to map 1 (i.e. -4% to +4.5%). Thus, MM susceptibility classes are distributed in a uniform manner, and only some polygons change from one map to another allowing for varying the obtained results between MM susceptibility maps.

Nevertheless, the comparison of MM susceptibility class areas' indicates a close difference between maps 2 and 1 (i.e. -8% to +4.5%), demonstrating analogous areal coverage **(Table 5.11)**. For the class areas' relations between maps 3/1 or 3/2, bigger values are noticed (maps 3/1: -18.5% to 29%, maps 3/2: -23.5% to 37%).

Table 5.10. Spatial comparison between the percentages of polygons characterizing the three susceptibility maps.

Class	Map 2 versus Map 1*	Map 3 versus Map 1	Map 3 versus Map 2
Very low (1)	+3%	+2.5%	-0.5%
Low (2)	+4.5%	+10%	+5.5%
Medium (3)	-4%	+5.5%	+9.5%
High (4)	-4%	-26%	-22%
Very high (5)	+0.5%	+8%	+7.5%
TOTAL	**-4% to +4.5%**	**-26% to 10%**	**-22% to 9.5%**

*The positive values (+) indicate an increase in the number of polygons in map 2, once compared with map 1; while the negative values (-) represent a decrease in the polygons' number.

Table 5.11. Spatial comparison between the percentages of areas characterizing the three susceptibility maps.

Class	Map 2 versus Map 1	Map 3 versus Map 1	Map 3 versus Map 2
Very low (1)	-8%	+29%	+37%
Low (2)	+4.5%	+4.5%	0%
Medium (3)	+0.5%	-12%	-12.5%
High (4)	+5%	-18.5%	-23.5%
Very high (5)	-2%	-3%	-1%
TOTAL	**-8% to +4.5%**	**-18.5% to +29%**	**-23.5% to +37%**

6.2. Correspondence analysis of MM susceptibility maps

An automated comparison between the three MM susceptibility maps was conducted to check if the same areas witness the same MM susceptibility level **(Tables 5.12, 5.13, 5.14).** This is of crucial importance in the evaluation of the used methodologies. Coincidences between maps 1 and 2 on one side, and maps 1 and 3 on the other side are equal to 47.5% and 54%, respectively. These coincidences were calculated by dividing the sum of areas to which the classes of maps correspond strictly (1783 km^2 – maps 1/2 and 2012 km^2 – maps 1/3, in grey on the diagonals of the contingency tables) on the total area of the studied region (3750 km^2) **(Tables 5.12 and 5.13)**. The comparison between maps 2 and 3 reveals a poorer agreement between MM susceptibility classes (38%) **(Table 5.14)**.

Table 5.12. Comparison (in km^2) between MM susceptibility map 1 (VABU) and MM susceptibility map 2 (VAA).

Susceptibility classes (km^2)	**Map 2**						
Map 1	**1**	**2**	**3**	**4**	**5**	**TOTAL**	**Producer's degree of coincidence (%)**
1	555	30	261	54	30	930	**60%**
2	175	44	22	3	44	288	**15%**
3	5	426	892	244	5	1572	**57%**
4	0	87	376	292	0	755	**39%**
5	0	3	94	108	0	205	**0%**
TOTAL	735	590	1645	701	79		
User's degree of coincidence (%)	**75.5%**	**7%**	**54%**	**42%**	**0%**	**Overall coincidence = 1783/3750 = 47.5%**	

Table 5.13. Comparison (in km^2) between MM susceptibility map 1 (VABU) and MM susceptibility map 3 (InfoVal).

Susceptibility classes (km^2)	**Map 3**						
Map 1	**1**	**2**	**3**	**4**	**5**	**TOTAL**	**Producer's degree of coincidence (%)**
1	978	179	89	8	0	1254	**78%**
2	42	37	1	0	0	80	**46%**
3	28	661	653	39	1	1382	**47%**
4	0	78	290	330	4	702	**47%**
5	0	66	161	91	14	332	**4%**
TOTAL	1048	1021	1194	468	19		
User's degree of coincidence (%)	**93%**	**3%**	**55%**	**70.5%**	**74%**	**Overall coincidence = 2012/3750 = 54%**	

Table 5.14. Comparison (in km^2) between MM susceptibility map 2 (VAA) and MM susceptibility map 3 (InfoVal).

Susceptibility classes (km^2)	Map 3						
Map 2	**1**	**2**	**3**	**4**	**5**	**TOTAL**	**Producer's degree of coincidence (%)**
1	690	114	113	15	0	932	**74%**
2	63	166	14	1	0	244	**68%**
3	57	940	364	53	4	1418	**26%**
4	8	449	231	196	8	892	**22%**
5	0	80	128	50	6	264	**2%**
TOTAL	818	1749	850	315	18		
User's degree of coincidence (%)	**84%**	**9%**	**43%**	**62%**	**33%**	**Overall coincidence = 1422/3750 = 38%**	

However, if we take into consideration the MM susceptibility classes separately, the degree of coincidence can increase in some cases. But this degree differs significantly between the producer of the map and its user. Areas attributed to the very low susceptibilities are showing very high coincidence either for the producer or the user varying between 60 and 93% depending on the considered maps (maps 1/2 and maps 1/3). Very high MM susceptibility classes are less matched than very low ones, showing coincidences degrees varying between 0 and 74% for the user; and 0 and 4% for the producer. Intermediate classes also reveal a poorer agreement than the extreme stable ones. This agreement oscillates between 3 and 70.5% for the user and 15 and 68% for the producer. For the relations between maps 1 and other maps (2 and 3), the lowest producer's and user's degrees of coincidence characterize class 2 (low MM susceptibility). The highest producer's degree of coincidence characterizes the unit 3 (medium class) being equal to 57% (maps 1/2) and 47% (maps 1/3), respectively; while the highest user's one is dedicated to different units depending on the used methodology (medium class – 54% if map 2 is compared to map 1; and high class – 70.5% in the produced maps 1/3). The overall comparison indicates that the relation between the map produced using the newly designed method (VABU) (map 1) and the map obtained through the implementation of InfoVal method (map 3) is more convenient than that between maps 1/2 or maps 2/3. This is due to the fact of having different origin of the applied methodologies – the good accord between maps of the methods 1 and 3 proves the usefulness of using primary and secondary level weights on MM locations if their covered areas are difficult to obtain. This is more effective than considering indices taking into consideration frequencies rates of MM locations.

6.3. Spatial and attribute analysis of MM hazard maps

Three maps of MM hazard **(Figures 5.5, 5.6 and 5.7)** were also elaborated by integrating the obtained MM susceptibility maps using three different methods (VABU, VAA and InfoVal) and the triggering factors (rainfall quantity, seismic events, forest fires and floods).

The medium hazard class (no. 3) is occupying the largest area (1761 km^2 or 48%) in map 1a (VABU) **(Figure 5.5, Table 5.15)**, whereas the very low class (no. 1) dominates in map 3a (2004 km^2 or 53%) **(Figure 5.7, Table 5.17)**. The low (no. 2) and medium (no. 3) hazard classes cover nearly similar areas in map 2a: class 2 – 1172 km^2 (31%) and class 3 – 1065 km^2 (28%) **(Figure 5.6, Table 5.16).**

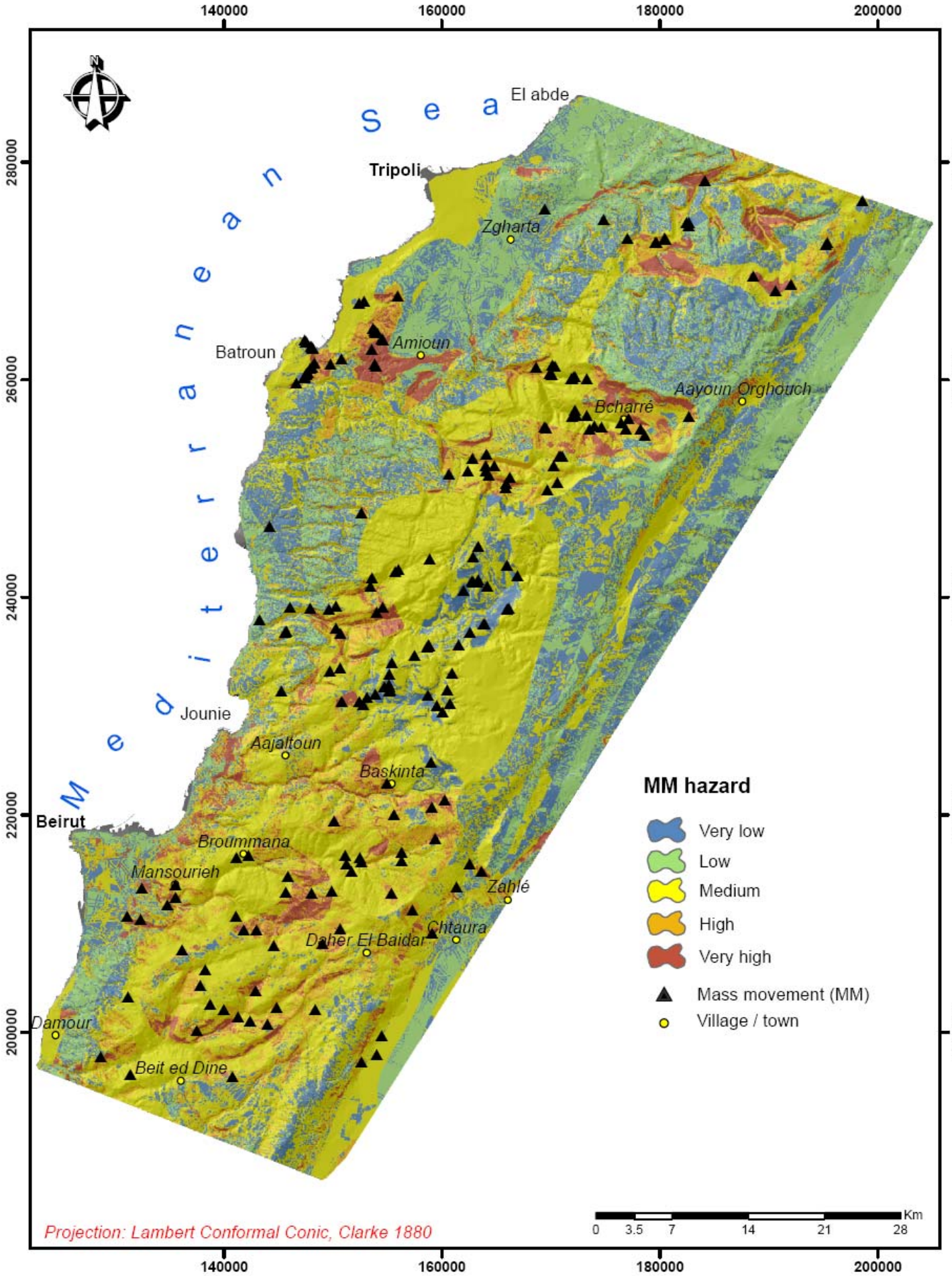

Figure 5.5. Mass movement (MM) hazard map derived from VABU method.

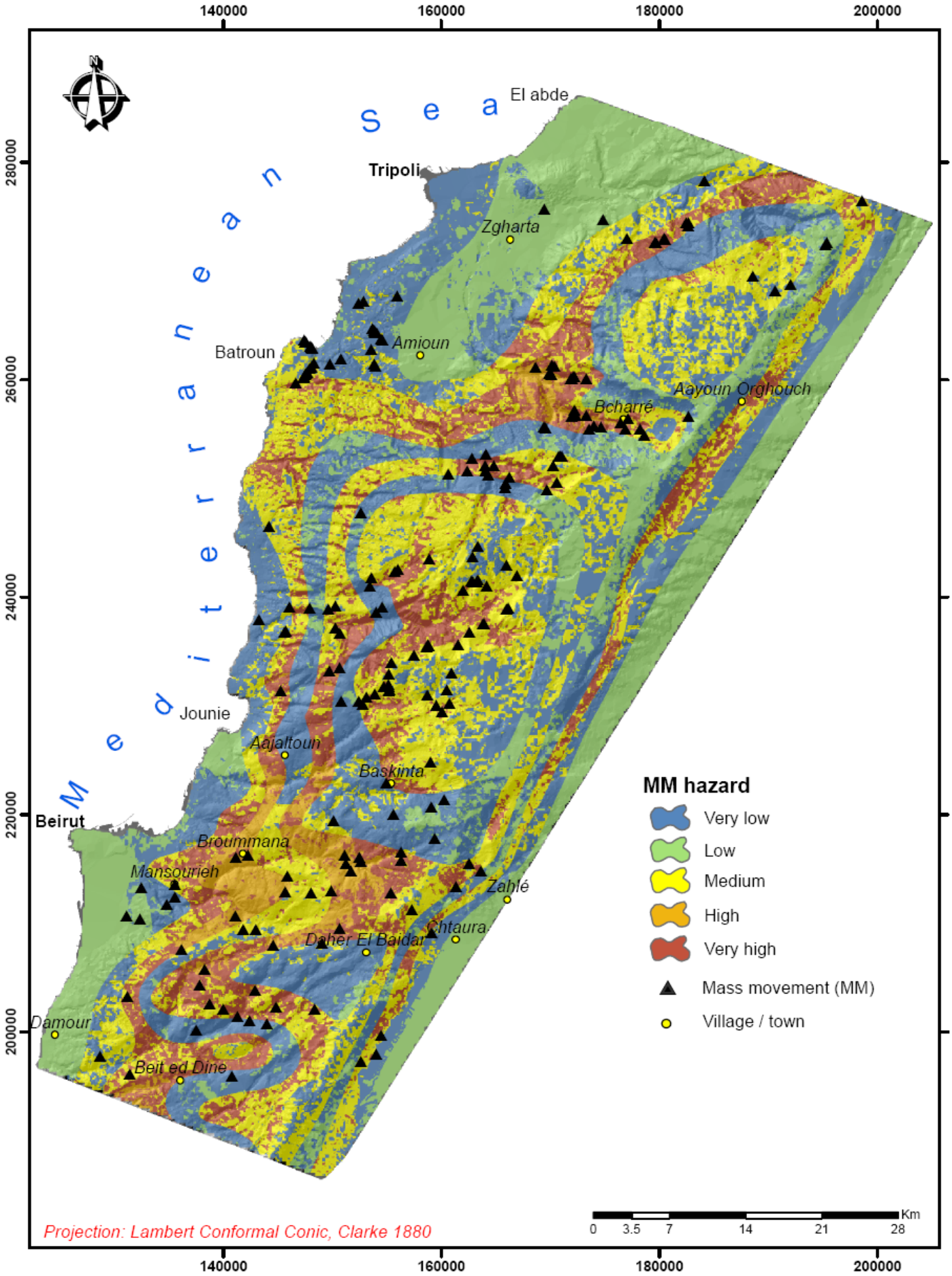

Figure 5.6. Mass movement (MM) hazard map derived from VAA method.

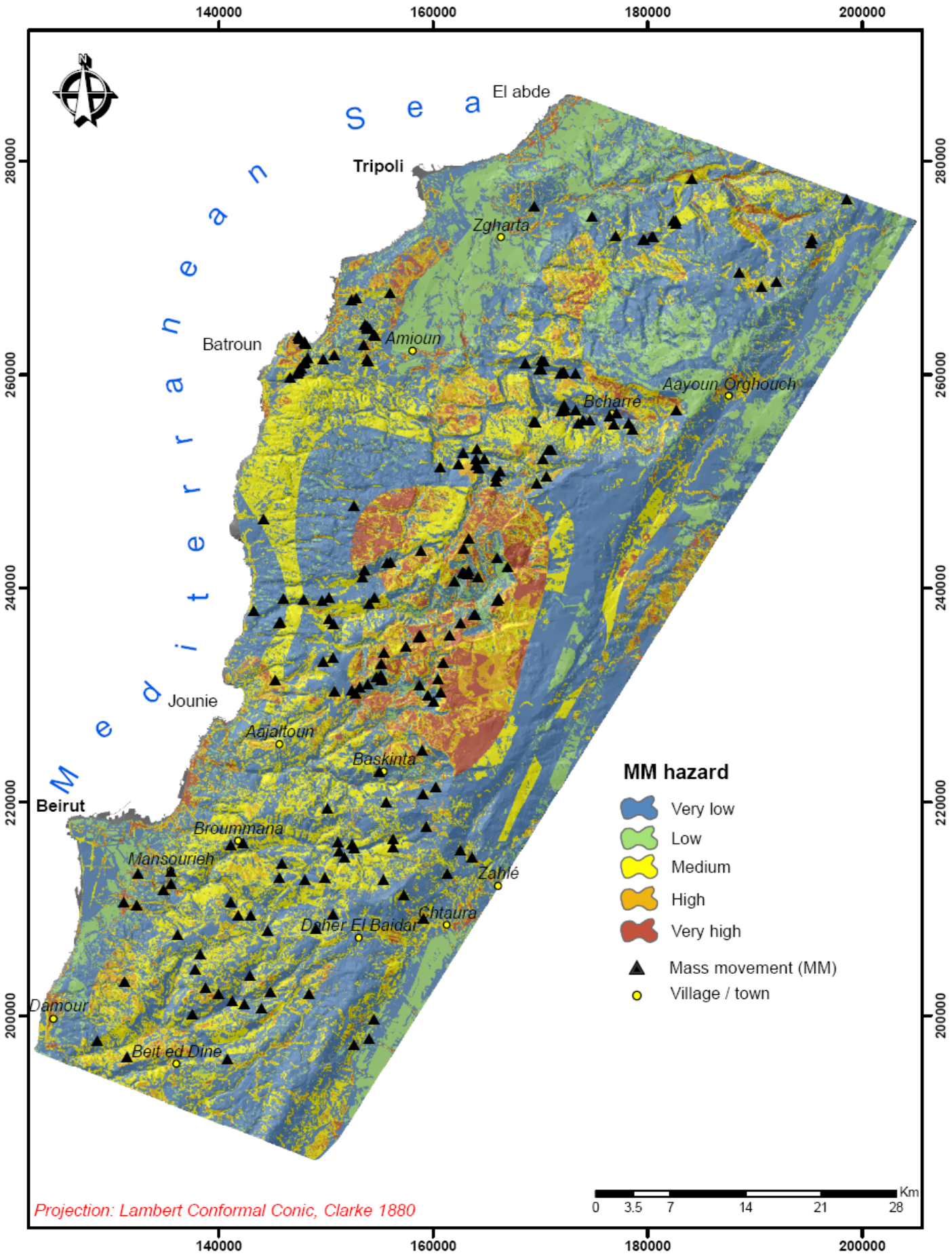

Figure 5.7. Mass movement (MM) hazard map derived from InfoVal method.

While the high to very high hazard classes characterize good portions of the three maps: map 1a – 14%, map 2a – 18% and map 3a – 12.5%, highlighting the high probable occurrence of the MM dangerous event and pushing authorities to design management protective plans.

Table 5.15. Number of polygons and covered areas by the five hazard classes obtained using valuing analytical bi-univariate method (VABU - method 1 and map 1a).

Hazard class (no.)	Polygons		Areas	
	Number of polygons	% of polygons	Covered area (km^2)	% of covered area
Very low (1)	9014	12%	610	16%
Low (2)	24705	34%	839	22%
Medium (3)	19369	26%	1761	48%
High (4)	15655	21%	348	9%
Very high (5)	5006	7%	192	5%

The highest number of polygons is shown in the first map (VABU) for the MM low hazard class (34%) **(Table 5.15)**, while it characterizes the medium class (38%) in the map 3a (InfoVal) **(Table 5.17)**. The low, medium and high hazard classes are distributed equally in the three maps (map 1a – 81%, map 2a – 79.5%, map 3a – 71.5%). The high to highest MM hazard classes are dispersed similarly in the three maps (map 1a – 28%, map 2a – 31%, map 3a – 30.5%).

Table 5.16. Number of polygons and covered areas by the five hazard classes obtained using valuing area accumulation method (VAA - method 2 and map 2a).

Hazard class (no.)	Polygons		Areas	
	Number of polygons	% of polygons	Covered area (km^2)	% of covered area
Very low (1)	1842	13.5%	861	23%
Low (2)	3731	27.5%	1172	31%
Medium (3)	3854	28%	1065	28%
High (4)	3273	24%	518	14%
Very high (5)	898	7%	134	4%

Table 5.17. Number of polygons and covered areas by the five hazard classes obtained using information value method (InfoVal – method 3 and map 3a).

Hazard class (no.)	Polygons		Areas	
	Number of polygons	% of polygons	Covered area (km^2)	% of covered area
Very low (1)	16620	21%	2004	53%
Low (2)	8472	10.5%	433	11.5%
Medium (3)	30823	38%	854	23%
High (4)	5939	7.5%	172	4.5%
Very high (5)	18345	23%	287	8%

If one takes into consideration the total number of polygons for the three maps, the first one (map 1a) gives the highest number (73749) **(Table 5.18).** The latter is 81% higher than map 2a, whereas it differs only by 8% once compared to map 3a. The comparison between maps

2a and 3a demonstrates a huge difference in the number of polygons, reaching 83%. On the other hand, maps 1 and 2 have the widest difference (22170 km or 60%) in the polygons' boundaries (perimeter). This difference is reduced once maps 1a and 3a are compared, valuing 30% **(Table 5.18)**. This demonstrates a closer agreement between MM hazard maps produced using methods 1 and 3. This agreement resembles that obtained comparing MM susceptibilities. However, the spatial comparison between the areas characterizing MM hazard classes for the considered three maps oscillates between -25% and +31% if map 3a is compared to map 1a **(Table 5.19)**. This difference is the highest, since values ranging between -20% and +9% characterize the couple constituted by maps 1a and 2a, and varying from -19.5% to +30% if maps 3a and 2a are compared. The number of polygons attributed for each MM hazard class in each map is also differing, and this difference is mostly seen for the couple 3a/2a (polygons' difference; -23.5% to 16%), versus polygons intervals ranging between -6.5% and +1.5% (couple 2a/1a), and -13% and 12% (couple 3a/1a), respectively **(Table 5.19)**. This differential matching between MM hazard maps explains the significance of the adopted methodology in projecting diverse results.

Table 5.18. Spatial comparison (number of polygons and total perimeter) between the three obtained hazard maps.

Hazard maps	**Total number of polygons (NP)**	**Total perimeter (TP) (km)**	**Difference between maps**				
				NP	**% NP**	**TP (km)**	**% TP**
Map 1a (VABU)	73749	56025	**Map1a/Map2a**	60151	81%	33855	60%
Map 2a (VAA)	13598	22170	**Map1a/Map3a**	6450	8%	16994	30%
Map 3a (InfoVal)	80199	39031	**Map2a/Map3a**	66601	83%	16861	43%

Table 5.19. Spatial comparison between the percentages of polygons characterizing the three hazard maps.

Class	**Map 2a versus Map 1a**	**Map 3a versus Map 1a**	**Map 3a versus Map 2a**
Very low (1)	+1.5%	-1.5%	+9%
Low (2)	-6.5%	-13%	-23.5%
Medium (3)	+2%	+12%	+12%
High (4)	+3%	+2%	-13.5%
Very high (5)	0%	+0.5%	+16%
TOTAL	**-6.5% to +1.5%**	**-13% to 12%**	**-23.5% to +16%**

Table 5.20. Spatial comparison between the percentages of areas characterizing the three hazard maps.

Class	**Map 2a versus Map 1a**	**Map 3a versus Map 1a**	**Map 3a versus Map 2a**
Very low (1)	+7%	+37%	+30%
Low (2)	+9%	-10.5%	-19.5%
Medium (3)	-20%	-25%	-5%
High (4)	+5%	-4.5%	-6%
Very high (5)	-1%	+3%	+0.5%
TOTAL	**-20% to +9%**	**-10.5% to +37%**	**-19.5% to +30%**

6.4. Correspondence analysis between MM hazard maps

The comparison (in km^2) of classes belonging to the hazard maps produced using the three different methods permits the assessment of the degree of coincidence between the different MM hazard couples (1a/2a, 1a/3a and 2a/3a) **(Tables 5.21, 5.22, 5.23)**. The contingency tables point out to the similarity degrees between maps 1a and 2a of 39%, maps 1a and 3a of 44%, and maps 2a and 3a of 36.5%, reflecting the major effect played by considering different methodologies in modifying the result. The highest coincidence for both susceptibilities and hazard maps is corresponding to the couple integrating methods 1 and 3 (54% in the case of susceptibilities and 44% for the hazard maps). This proves the usefulness of considering primary and secondary weight levels in assessing MM hazards, if MM locations are only acquired without any possibility of measuring areas covered by MM events. Areas without any probable occurrence of MM event (class 1 – very low) show high coincidence either for the producer or the user, varying between 44% to 77% -depending on the couple of maps compared (1a/2a, 1a/3a, 2a/3a). Intermediate classes (low and medium) reveal also better agreement than high ones. This agreement oscillates between 27% and 61% for the user, and 28.5% and 63.5% for the producer. High classes are better matched for both user and producer between maps 1a and 3a than for other maps (1a/2a or 2a/3a), indicating a closer relation between VABU and InfoVal methods if the probability of MM occurrence is high.

Table 5.21. Comparison (in km^2) between MM hazard map 1a (VABU) and MM hazard map 2a (VAA).

Hazard classes (km^2)	**Map 2a**						
Map 1a	**1**	**2**	**3**	**4**	**5**	**TOTAL**	**Producer's degree of coincidence (%)**
1	432	220	139	34	33	858	**50%**
2	153	348	463	143	113	1220	**28.5%**
3	19	264	619	85	34	1021	**61%**
4	0	53	389	67	9	518	**13%**
5	0	0	115	17	1	133	**0.75%**
TOTAL	604	885	1725	346	190		
User's degree of coincidence (%)	**71.5%**	**39%**	**36%**	**19%**	**0.5%**	**Overall coincidence = 1467/3750 = 39%**	

Table 5.22. Comparison (in km^2) between MM hazard map 1a (VABU) and MM hazard map 3a (InfoVal).

Hazard classes (km^2)	**Map 3a**						
Map 1a	**1**	**2**	**3**	**4**	**5**	**TOTAL**	**Producer's degree of coincidence (%)**
1	429	299	77	33	19	857	**50%**
2	91	702	210	97	67	1167	**60%**
3	32	451	367	103	68	1021	**36%**
4	7	249	199	100	17	572	**17%**
5	0	30	55	8	40	133	**30%**
TOTAL	559	1731	908	341	211		
User's degree of coincidence (%)	**77%**	**40.5%**	**40%**	**29%**	**19%**	**Overall coincidence = 1638/3750 = 44%**	

Table 5.23. Comparison (in km^2) between MM hazard map 2a (VAA) and MM hazard map 3a (InfoVal).

Hazard classes (km^2)	Map 3a						
Map 2a	**1**	**2**	**3**	**4**	**5**	**TOTAL**	**Producer's degree of coincidence (%)**
1	265	299	23	12	8	607	**44%**
2	104	535	139	48	16	842	**63.5%**
3	53	851	540	183	131	1758	**31%**
4	4	209	114	19	5	351	**5%**
5	3	89	67	21	12	192	**6%**
TOTAL	429	1983	883	283	172		
User's degree of coincidence (%)	**62%**	**27%**	**61%**	**7%**	**7%**	**Overall coincidence = 1371/3750 = 36.5%**	

6.5. Examination of reliability of MM susceptibility maps

The reliability of MM susceptibility maps depends mostly on the amount and quality of available data, the working scale and the selection of the appropriate methodology of analysis and modelling. It was shown previously that the used three methods lead to different MM susceptibility/hazard maps in the study area, and the misclassification exists inevitably, which could be discussed to validate the resultant maps useful for planning, land development, and decision-making.

Therefore, I performed the validation of these maps by eliminating 20% of the measured MM locations (40) in the mentioned overall calculations. Those points considered as reference points were delineated on the MM susceptibility maps, and accuracies were calculated. The latter denote the number of correctly classified ground truth points in the high to very high MM susceptibility classes divided by the total number of points **(Table 5.24)**. The overall accuracies are equal to 77.5% (method 1 - VABU), 52.5% (method 2 - VAA) and 67.5% (method 3 - InfoVal), respectively. However, the highest accuracy is manifested for VABU method (77.5%), and is statistically good because the adjustments correspond to 70-80% (Lillesand and Kiefer, 1994), with a minimum quantity of errors. Accurate results are defined also for method 3 (InfoVal). Despite some noticed confusions, it could be more countable than method 2, where mismatching exists between the occurred MM and the very low to low classes.

Table 5.24. Accuracies of MM susceptibilities maps produced using three different methods (method 1 – VABU, method 2 – VAA, method 3 – InfoVal).

	Very low	Low	Medium	High	Very high	Accuracy
Map 1	2*	0	7	10	21	77.5%
Map 2	6	4	9	14	7	52.5%
Map 3	1	1	11	6	21	67.5%

* Number of field points matching modeled MM susceptibility classes.

6.6. Advantages and problems of the MM used methods

The obtained results demonstrate a high degree of accuracy for the VABU method, and hence it can be adopted as a predictive method to produce reliable maps of MM susceptibility/hazard in the area of interest. Such maps are unavailable for Lebanon, and are extremely useful for prevention and planning for regional land use and construction. The process of input, calculation and output of this method could be understood easily. It depends on some identical computations (primary weight levels or rates) as method 2 (VAA), but it considers secondary level weights and arithmetic means rather than given computing indices. Both methods 1 (VABU) and 2 (VAA) are established using MM locations, but the accuracy of method 1 proved to be higher. Methods 1 (VABU) and 3 (InfoVal) give close results, however, method 1 is somewhat simplistic and does not necessitate detailed measurements of MM, constrained by further availability of money and time. These "detailed measurements" are difficult to implement in several developing countries, with limited amount of sources – i.e. satellite imageries with very high resolution needed for exact areal coverage of MM calculations or with undulated inaccessible topography, rendering the collection of MM areas very hard.

Thus, the consideration of two weight levels (primary and secondary) in the VABU method allows a better reflection of the local conditions. This method can easily be extrapolated to all the country if the functional capacities of GIS are used. Some preconditioning parameters – elevation, slope gradient, slope aspect, slope curvature, lithology, proximity to fault line, karst type, soil type, distance to drainage line, and distance to springs – are more persistent with time than the other parameters, i.e. land cover/use, distance to quarries and proximity to roads, which must be updated and can change through the years.

However, many difficulties have been encountered. The use of one-lumped value for rainfall parameter in MM modeling is sometimes an oversimplification of the real situation in which rainfall shows complex spatial and temporal patterns. Future study should focus on capturing this variability through the utilization of rainfall intensity and its incorporation in MM methods. In addition, the paucity on the distributive occurrence of seismic events can minimize the quality of the produced MM hazard maps. Those can be improved by including the vertical and lateral displacement of blocks which leads to better evaluation of hazardous areas.

7. Conclusion

MM susceptibility and hazard maps were produced for the first time in the central to northern part of Lebanon using different statistical methods, i.e. VABU, VAA and InfoVal that have been compared and validated in the field. The first one (VABU), proposed in the frame of this thesis, depending on the primary and secondary weight levels, proves its capability and shows higher accuracies than the other tested statistical methods (i.e. VAA and Info Val).

Therefore, the VABU method can be adopted in Lebanon for a generalized mapping of MM hazards, being simple, easily implemented and realistic. The medium chosen scale map 1:50,000 is appropriate principally for agencies dealing with municipal planning, and studies for local engineering works. However, it may be less useful at the site – specific scale where local geological heterogeneities may prevail. Consequently, detailed (>1:5,000) and large scales (1:5,000-1:10,000) can be executed in the future as follows. The detailed scale (> 1:5,000) can help mainly companies or municipal agencies dealing with hazards on individual sites with a maximum area of several hectares. The large-scale (1:5,000-1:10,000) maps can

be used for problems of local slope instability, for planning of infrastructure, housing, and industrial projects.

Additionally, if the factors relevant to vulnerability of buildings and other property were available, risk analysis could also be done. Fortunately, the MM-related spatial database for morphology, soil, forest, hydrology and geology is already available for most areas of Lebanon, so the MM analysis can be done quickly and cheaply for all of Lebanon.

- VI -

Spatial representation and volumetric mapping of block falls using GIS-based decision-tree models

CHAPTER VI
Spatial representation and Volumetric Mapping of block falls using GIS-based decision-tree models

1. Introduction

After the production of susceptibility and hazard maps for mass movements (MM) in general (whatever type of MM is) occurring in the study area with five classes each (very low, low, medium, high and very high) (Chapter V), I tried to map the predicted volume of block falls in the frame of a Geographic Information System (GIS). I have performed this mapping for several reasons: 1) block falls are widely distributed in the Mediterranean region, affecting life and properties severely; and 2) although of the danger effect of block falls, most studies have been done worldwide on landslide research, and there is a little on evaluating other types of MM, especially block/rock falls (Abbot *et al.*, 1998; Ayala *et al.*, 2003; Baillifard, *et al.*, 2004; Calcaterra *et al.*, 2004; Guzzetti *et al.*, 2004).

The constructed map in this chapter will describe the potential size of block falls (volume in m^3) in each location depending on field measurements of existing ones (what is called predictive mapping). The concept of volumetric mapping of block falls differs therefore from MM susceptibility and hazard maps, the first one (block falls) is quantitative with volumes in m^3, inexistent until now in Lebanon; while the latter (susceptibility and hazard) are categorized with five level classes.

I have used the decision-tree method for producing the volumetric map of block falls, since this method is machine learning, probabilistic and non-parametric. The concept of decision-trees is old (~ 40 years), but its utilization was impractical until the development of modern and high-speed computers with a high capacity to analyze large sets of data records. The decision-tree method has been extensively exploited for vegetation mapping (Lees and Ritman, 1991; Franklin, 1998), ecological modeling (Michaelsen *et al.*, 1994), gully erosion modeling (Bou Kheir *et al.*, 2007a), soil mapping (Bou Kheir *et al.*, 2007b), and in remote sensing studies (e.g. land use classification based on threshold values of various band data) (Huang and Jensen, 1997; Friedl *et al.*, 1999). However, its use in predictive estimate of the block falls is still at its early stages.

In this context, this chapter focuses on building decision-tree models for mapping the volume of block falls in a study site within Lebanon. These models comprise a set of rules to classify (predict) a dependent target variable (volume of predicted block falls in m^3) using the values of independent variables (predictors). The predictor variables are both ordinal (elevation, slope angle, slope aspect, slope curvature, proximity to fault line, distance to the drainage line, proximity to roads) and nominal (lithology, karst type, soil type, land cover/use). These variables are selected from those considered in building susceptibility and hazard maps in Chapter V due to the necessity of obtaining landscape unit on which the results of decision-tree models will be converted to predictive volumetric map of block falls. The landscape unit concept is used in many natural environmental surveys worldwide since it refers to the portion of land surface which contains a set of ground conditions which differ from the adjacent units across definable boundaries (Hansen, 1984), or what is called as a spatially homogeneous domain, in terms of both instability factor characteristics and MM degree (Meijerink, 1988; Hansen *et al.*, 1995). Accordingly,

the rainfall quantity, the distance to quarries, seismic events, floods, forest fires and distance to sources were excluded in building our decision-tree models.

2. Reasons for using decision-tree modeling

The decision-tree model is a logical model (deductive reasoning) represented as a binary (two-way split) tree that shows how the value of a variable – named target variable – can be predicted by using the values of a set of predictor variables. It has a number of advantages when compared to numerically oriented techniques such as linear and nonlinear regression (function fitting), logistic regression, artificial neural networks ANNs (also called multilayered perceptron) and genetic algorithms. Decision-trees are easy to build and interpret, and can automatically handle interactions between both continuous (ordinal, interval) and categorical (nominal) variables. Linear regression, for instance, is appropriate only if the data can be modeled by a straight line function, which is often not the case. Also, linear regression cannot easily handle categorical variables, nor is it easy to look for interactions between variables. As with linear regression, nonlinear and logistic regressions are not well suited for categorical variables.

Decision-trees can identify the most decisive variables, which are those that are used for creating the splits near the top of the tree. In addition, they do not require the specification of the form of a function to be fitted to the data as is necessary for other competing procedures (e.g. non linear regression).

Artificial Neural Networks (ANNs) are often compared to decision-trees models because both methods can model data that have nonlinear relationships between variables, and both can handle interactions between variables. They have been used also for modelling soil collapse (Basma and Kallas, 2004; Binaghi *et al.*, 2004). However, neural networks have a number of drawbacks. They do not present an easily understandable model allowing researchers to get the full explanation of the underlying nature of the data being analyzed. In addition, they handle only binary categorical input data, and not those with multiple classes. It is difficult also to incorporate a neural network model into a computer system without using a dedicated interpreter for the model. In contrast, once a decision-tree model has been built, it can be converted to statements that are implemented easily in most computer languages without requiring a separate interpreter.

Moreover, decision-trees can identify a target (dependent) variable. This is not possible with unsupervised machine learning methods like cluster analysis, factor analysis (principal component analysis) and statistical measures, which treat all variables equally without predicting the value of a variable. These methods rather look for patterns, groupings or other ways to characterize the data that may lead to the understanding of the way the data interrelate. In addition, decision-trees can indicate the relative weight of each predictor variable in explaining the training data, while bivariate analysis demonstrates only the implication of a couple of predictor variables against the target variable. Therefore, if the goal of an analysis is to predict the value of some variable, then decision-tree modelling is a recommended approach. *But predicting the future remains a hard task, even with decision-trees.*

3. Modeling approach

3.1. Workflow

I have mapped the volumetric size of block falls in several steps: 1) I have measured first the dimensions of existing block falls (target dependent variable) detected through the interpretation of satellite imageries (Chapter III); 2) I intersected after the block fall layer information (point location) with the maps of predictor independent parameters (i.e. elevation, slope angle, slope aspect, slope curvature, proximity to fault line, distance to the drainage line, proximity to roads, lithology, karst type, soil type, and land cover/use) prepared in Chapter IV. The result of this intersection was a layer of the block fall locations and the corresponding parameters in an attribute table related to it. This table was saved in an ASCII format for software considerations; 3) I performed on this ASCII file several decision-tree models (as explained below); and 4) I converted the model that explains the highest variance in block falls to a predictive volumetric map of block falls under GIS environment and using landscape analysis (explained below).

3.2. Study site

I selected a part of the study area that is located at the northern to central Lebanese Mediterranean slopes for developing and testing the decision-tree methodology because it comprises several terrains that witness with major block falls, and since it was uneasy to measure all falls in the area for reasons of time, cost and access. The selected part covers only 20% (762 km^2) of the studied area in this thesis (3750 km^2). This part (study site) is bounded by Hazerta village in the north east, Biaqout village in the north-west, and Nahr Damour to the south **(Figure 6.1).** It comprises also most of the rock units (29 units) prevailing in the whole studied area.

The massive, thick bedded, highly fissured (or fractured), jointed and well karstified dolomite, limestone and dolomitic limestone of the Kimmeridgian form around 30% of the site, followed in importance by the fractured sandstones with intercalations of silts and clays of the Neocomian-Barremian (17%). The massive, jointed, partially karstified limestone and dolomitic limestone the late Aptian (c2b – muraille blanche), the thin bedded marly limestone of the Albian (C3), and the highly fractured and jointed limestone and dolimitic limestone outcrops of the Cenomanian (C4) are covering with an equal distribution (around 11% each) **(see Table 2.1 for more details – Chapter II).**

A total of 23 different soil units were identified on the available soil map (Gèze, 1956) of which 17 are soil series and six are soil associations. Only three of them cover 71% of the study area (discontinuous red mountainous soils - 20%, sandy soils – 17% and mixed soils on alternating marl, limestone and sandstone – 34%). 26% of the study area has slope angles exceeding 18°. The percentage of concave and convex areas is quasi-similar (43% each). Lapiez are more dominant (18%) than areas with developed karst such as karren and other surface dissolution features with relatively small exposures (6%), although the largest part of the area is made of non-karstic terrain (76%). Elevations range between less than 500 m and 2000 m. Shrub and grasslands occupy 28% of the site; bare lands and forests make 22% and 12%, respectively.

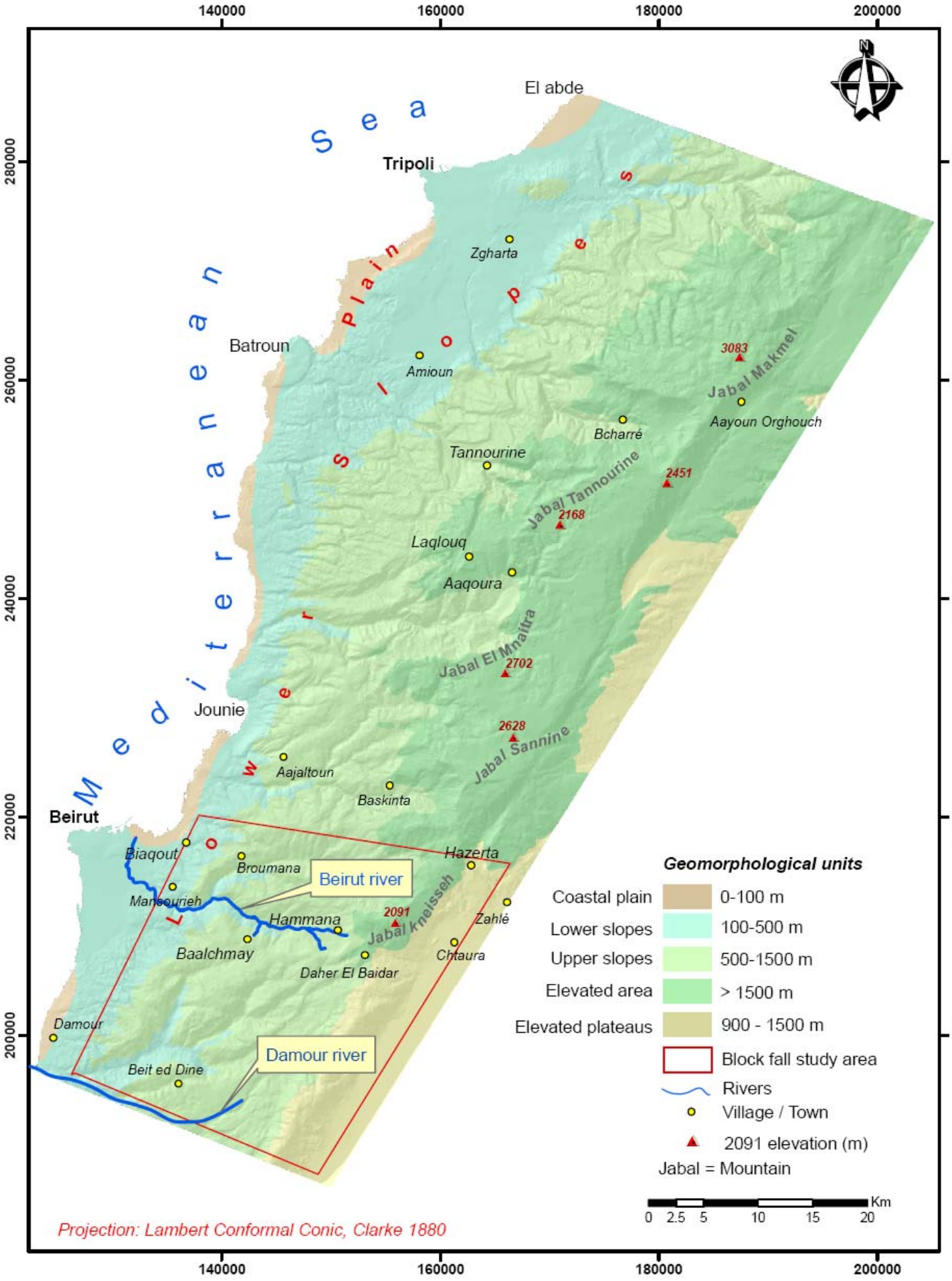

Figure 6.1. Selected site location for block fall in the study area.

3.3. Field survey

I have made a field survey involving detailed measurements of existing block falls in the selected study site, that were detected through interpretation of satellite imageries (Chapter III). Geographic locations of the falls were determined using a global positioning system (GPS) with 10 m precision. For each block fall accumulation area, the dimensions [cross sectional area (length x width) and average thickness] were measured using a tape **(Figure 6.2)**. The thickness for each block fall accumulation area was obtained by splitting this area into several parts depending on the height of blocks within it (i.e. huge block falls or small materials). The height of blocks was measured in each part, and according to the proportion of these aggregates (huge or small blocks) in each accumulation area, the average thickness was calculated. For example, block fall accumulation area no. 25 occurring in Ramlieh region covers an area of 1400 m^2 (70 m x 20 m) and can be divided into four parts according to the height of blocks within it, i.e. part a **(Figure 6.2)** [height (h) = 6 m, proportion (p) = 15% of the area)], part b (h = 10 m, p = 25%), part c (h = 14 m, p = 20%) and part d (h = 2 m, p = 40%). The average thickness in this case (block fall accumulation area no. 25) will be equal to [(6 m x 0.15) + (10 m x 0.25) + (14 m x 0.2) + (2 m x 0.4)] = 7 m. Afterwards, the total volume (m^3) accumulated by each block fall accumulation area was calculated by multiplying the average cross sectional area by the average thickness. In the particular example case, the volume is equal to 9800 m^3 (70 x 20 x 7).

Figure 6.2. Photographs showing the volumetric measurement of block fall in the field (Ramlieh area, block fall accumulation area no. 25).

3.4. Statistical analysis

At a later stage, I intersected the block fall information layer obtained from field measurements with the various parameters layers selected in Chapter IV (elevation, slope gradient, slope aspect, slope curvature, lithology, proximity to fault line, karst type, soil type, distance to the drainage line, land cover/use, proximity to roads). This results in a "block fall layer" having at this stage an attribute table with all related parameters. This table was then converted to an ASCII file, which comprises several columns: geographic site coordinates (x, y) of the measured block fall, the volumetric size of the block fall (target variable), and various parameters (predictors) being both continuous (elevation, slope angle, slope aspect, slope curvature, proximity to fault line, distance to the drainage line, proximity to roads) and nominal (lithology, karst

type, soil type, land cover/use). For example, block fall no. 25 has a volume of 9800 m^3 and falls on elevation between 500 and 1000 m, slope angle between 11° and 18°, slope aspect towards the South-West, slope curvature being concave, lithology type J6 (dolomite and dolomitic limestone), proximity to fault zone less than 500 m, karst type dedicated to developed karst, soil type no. 6 "terra rosa", distance to drainage line between 150 and 200 m, land cover/use constituted by dense shrubs, and proximity to roads between 50 and 100 m.

I explored afterwards three sets of decision-tree models on this ASCII file in order to test which model can explain the highest variance of field measurements on existing block falls, and can be adopted therefore for mapping the volumetric size of block falls. The ideal was to find a model with the reduced number of input parameters (predictor variables), but with the highest powerful capacity (highest variance in explaining field measurements). Consequently, this exploration was based on: (1) all the parameters, (2) the topographic parameters only (elevation, slope gradient, slope aspect and slope curvature), and (3) the geologic parameters only (lithology, proximity to fault line, karst type and soil type). In addition, I built a decision-tree model by using preferentially the lithology as the initial split for cross validation, since this parameter has a major influence on the occurrence of mass movements as revealed in Chapter IV.

3.5. Building and pruning decision-tree models

Building the three trees described above comprises several steps: (1) find the best possible split through the examination of each predictor, (2) create two child nodes, and (3) determine in which child node each row goes into.

The number of splits evaluated is equal to $2^{(k-1)}$-1, where k is the number of categories of the predictor variables (parameters) (Breiman, 2001). For example, if the slope curvature with 3 classes (i.e. concave, convex and rectilinear) is considered, 3 splits are tried; if there are 5 classes (e.g. proximity to roads), 15 splits are tried. With the increase of the number of categories, there is an exponential growth of splits and computation time.

However, it is extremely important to generate trees of the optimal size since a simpler tree is easier to understand and faster to use for decision making, than larger ones. I used a minimum node size of ten in building the decision-trees. In other terms, a node will not be split with less than ten rows. This number has been used in several studies (Murphy *et al.*, 1994; Zhang and Burton, 1999).

In addition, I didn't specified the maximum tree elevation as was the case for the early programs such as AID (Automatic Interaction Detection) developed in 1963 by Morgan and Sonquist. Instead, I have grown a large tree that is over-fit for the training data and pruned it back to its optimal size (i.e. backward pruning) on the basis of a V-fold cross-validation (Berk, 2003).

The V-fold cross validation pruning method was used because of its accuracy in past studies (e.g. Breiman *et al.*, 1984; Venables and Ripley, 1994). In addition, it has several advantages once compared to other methods of validation such as random-row-holdback validation and fixed number of terminal nodes. It does not require a separate, independent dataset, which would reduce the data (field measurements on block falls) used to build the tree. It partitions the used learning dataset to build the reference unpruned tree into a number of groups called folds. A 10 V-folds value was adopted in this study, since a larger value increases the computation time and does not result in a more optimal tree (Clarke and Pregibon, 1992). V-fold cross validation is

the recommended method for small to medium size data sets, since random rows selected from the full dataset (random-row-holdback validation), which are held back do not contribute to the model as it is constructed, so the built model may be an inferior representation of the training data. However, if a given number of terminal nodes is specified, cross-validation trees are not generated, so it is much faster than doing full cross-validation on large trees; and there is no assurance that the generated tree has the optimal number of nodes.

Therefore, the 10 V-fold cross validation was adopted, and once 10 partitions are created, DTREG (decision-tree software) collects the rows in 9 of the partitions into a new pseudo-learning dataset. A test tree is built using this pseudo-learning dataset. The quality of the test tree for fitting the full learning dataset will, in general, be inferior to the reference tree because only 90% of the data was used to build it. Since the 10% (1 out of 10 partitions) of the data that was held back from the test tree built is independent of the test tree, it can be used as an independent test sample for the test tree. The 10% of the data held back when the test tree was built, is run through the test tree and the classification error for the data is computed. This error value is stored as the independent test error value for the first test tree. A different set of 9 partitions is now collected into a new pseudo-learning dataset. The partition being held back this time is selected so that it is different from the partition held back for the first test tree. A second test tree is built and its classification error is computed using the data that was held back when it was built. This process is repeated 10 times, building 10 separate test trees. In each case, 90% of the data is used to build a test tree and 10% is held back for independent testing. A different 10% is held back for each test tree. Once the ten test trees have been built, their classification error rate (known as cross validation cost) as a function of tree size has been averaged. The tree size that produces the minimum cross validation cost (error) corresponds to the optimal tree size that shall be considered to be good enough for predicting future values as the larger (reference) tree.

Using the results of the validated regression tree-model that explained the highest variance in block fall volume, the corresponding predictor spatial data were inverted under a GIS environment into a predictive map of volume occupied by block falls at their accumulation areas.

4. Results and discussion

4.1. Character of block falls' occurrence

Sixty-two block falls were found in the field, ranging from 234 m^3 to 5436 m^3, with a mean volume being equal to 2139 m^3 and a standard deviation of 1959. Most of them occur under following conditions: on elevations ranging between 500 and 1000 m (37% of block falls), with moderately steep slopes oscillating between 12 and 18° (48%), facing southward (16%), in concave (50%) forested areas of coniferous type (21%), growing over highly fissured and joined dolomites and dolomitic limestone of the Jurassic formation (24%), mixed soils on alternating marls, limestone and sandstone (48%), of highly faulted terrain (48% of block falls are occurring on a fault buffer inferior to 500 m) and non karstic (79%). In addition, the majority of block falls are away from the drainage buffer (43% of block falls on drainage buffers exceeding 250 m) and from roads cutting (56%). The block falls density is 0.08 events per km^2.

4.2. Model performance evaluation

The reference (based on all rows) regression unpruned (i.e. exploratory) tree-model (model 1a) **(Figure 6.3)** based on all the parameters correctly explained 86% of the variance with 23 total nodes (shown as rectangular boxes) and 12 terminal (or leaf) nodes, that do not have child nodes (nodes 8, 10, 11, 13, 14, 15, 17, 18, 19, 20, 22 and 23) **(Figure 6.3)**. Each node represents a set of records (rows) from the original dataset (total number of block falls being equal to 62).

The number of observations (N) per terminal node ranges from 1 to 7, and the node does not split if N is lesser than 10 observations. The mean value of the target variable (volume in m^3 of block falls) of the rows that are in a terminal node of the tree is the estimated median value. From the tree **(Figure 6.3)**, one can see that if the values of the lithological formations are attributed to C2b, J6, J7 and qe (N = 51 rows), then the estimated (average) value of the target variable is 1816 m^3; whereas, if the lithological formations are C1, C2a, C3 and C4 (N = 11 rows), then the average value of the target variable is 3638 m^3. This tree has been pruned to a more parsimonious 7-total and 4-terminal node model (model 1b - **Figure 6.4)**, explaining 50% of the variance in block falls volumes and selecting only four parameters (lithology, slope angle, soil and land cover/use). The minimum validation relative error (or validation cost) occurs with 3 nodes, being equal to 0.07 and a validation standard error of 0.0257. This validation error value is the cost relative to the cost for a tree with one node. It is the best measure of how well the tree will fit an independent dataset different from the learning dataset. The standard error represents the standard error of the validation cost value. The exploratory model based on topographic parameters (elevation, slope gradient, slope aspect and slope curvature) only (model 2a) explained 57% of the variation in block fall volume with a total number of nodes being equal to 31, of which 15 are terminal nodes **(Figure 6.5)**. But V-fold cross validation indicated that this model would classify 19% of the variation in block fall size, splitting the root node (entire group) into 2 nodes only depending on slope angle **(model 2b- Figure 6.6)**. The minimum validation relative error occurs with 2 nodes.

The relative error value is equal to 0.8538 with a standard error of 0.1022.

The exploratory tree (model 3a – **Figure 6.7**) based on geologic variables only (lithology, proximity to fault line, karst type and soil type) gave higher variance (68%) than model 2a based on topographic variables without any pruning (cross validation). The number of total (27) and terminal (14) nodes in this model were a little bit less than model 2a. This indicates that model 3a provides better predictive accuracy than model 2a, since the variance value is higher and the number of nodes is lower. With pruning (model 3b – **Figure 6.8**), the number of total and terminal nodes decreases to 5 and 3, respectively. The minimum validation relative error occurs with 3 nodes, and is equal to 0.8057 (the standard error being equal to 0.1593).

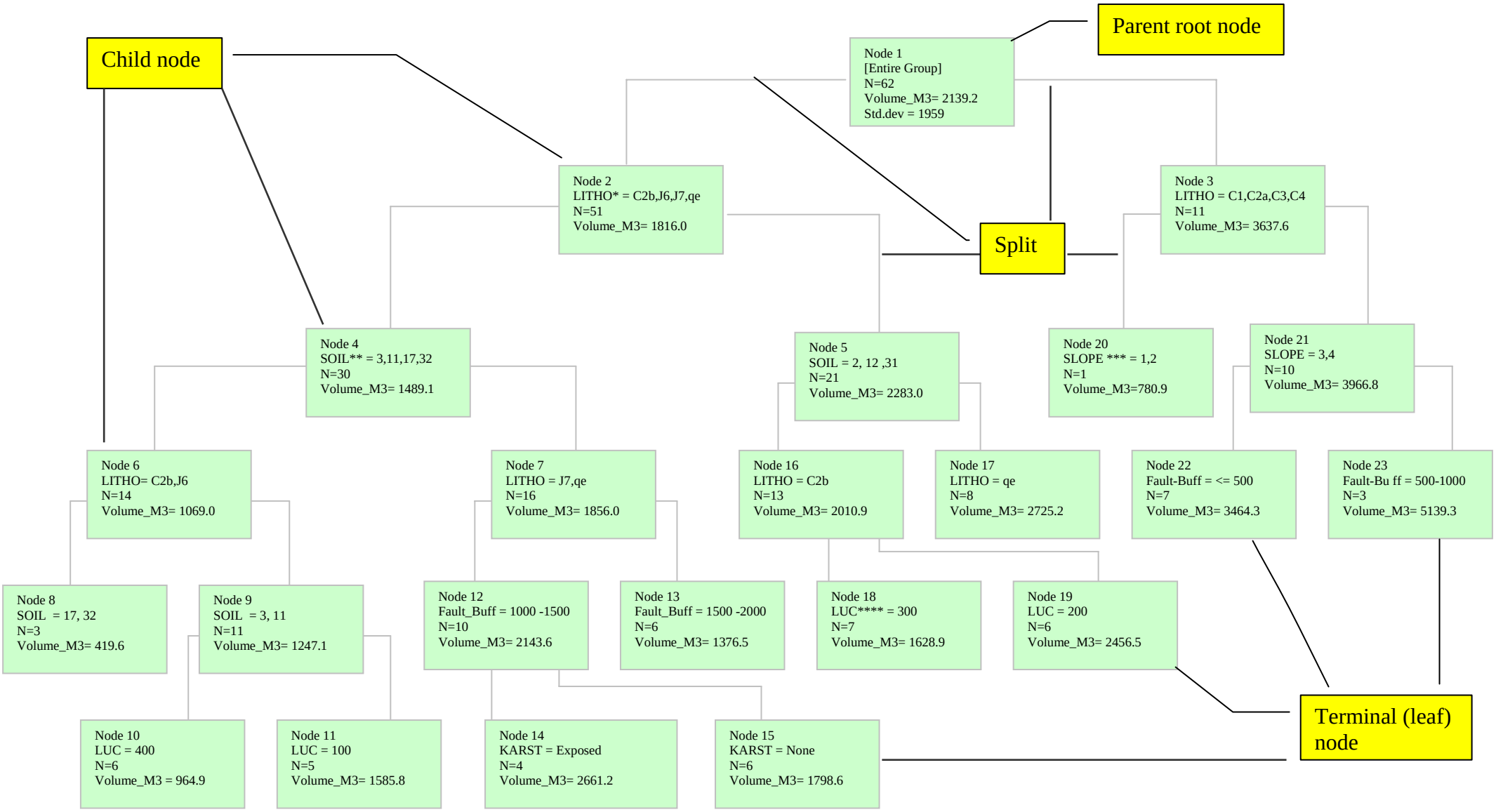

Figure 6.3. Decision-tree model explored on all parameters, without applying a pruning cross-validation test (model 1a).

(LITHO = lithology, SOIL = soil type, SLOPE = slope angle, Fault_Buff = proximity to fault line, LUC = land use/cover, KARST = karst type)
** Geological stages and ** = soil numbers are described in Chapter II*
**** Slope = 1,2,3,4 corresponds to slope angle classes 0-1º,2-11 º,12-18 º,19-27 º, and 28-90 º, respectively*
**** LUC classes 100= Artificial areas, 200 = Agricultural areas, 300 = Forests, 400 = Bare lands

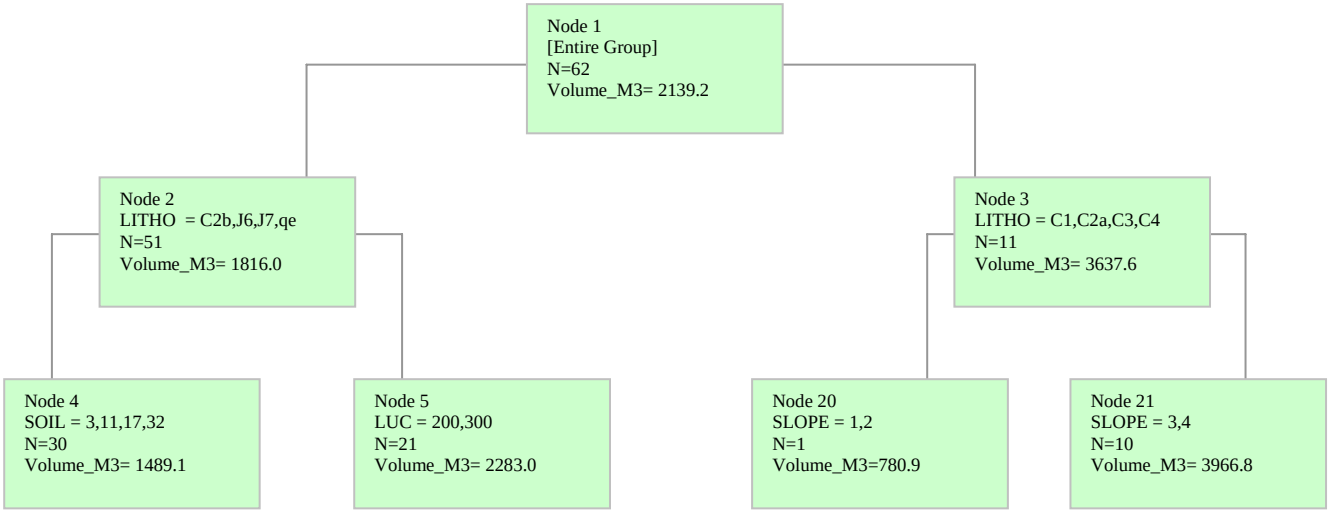

Figure 6.4. Decision-tree model explored on all parameters by applying a pruning cross-validation test (model 1b) ***(refer to Figure 6.3 for abbreviation explanation).***

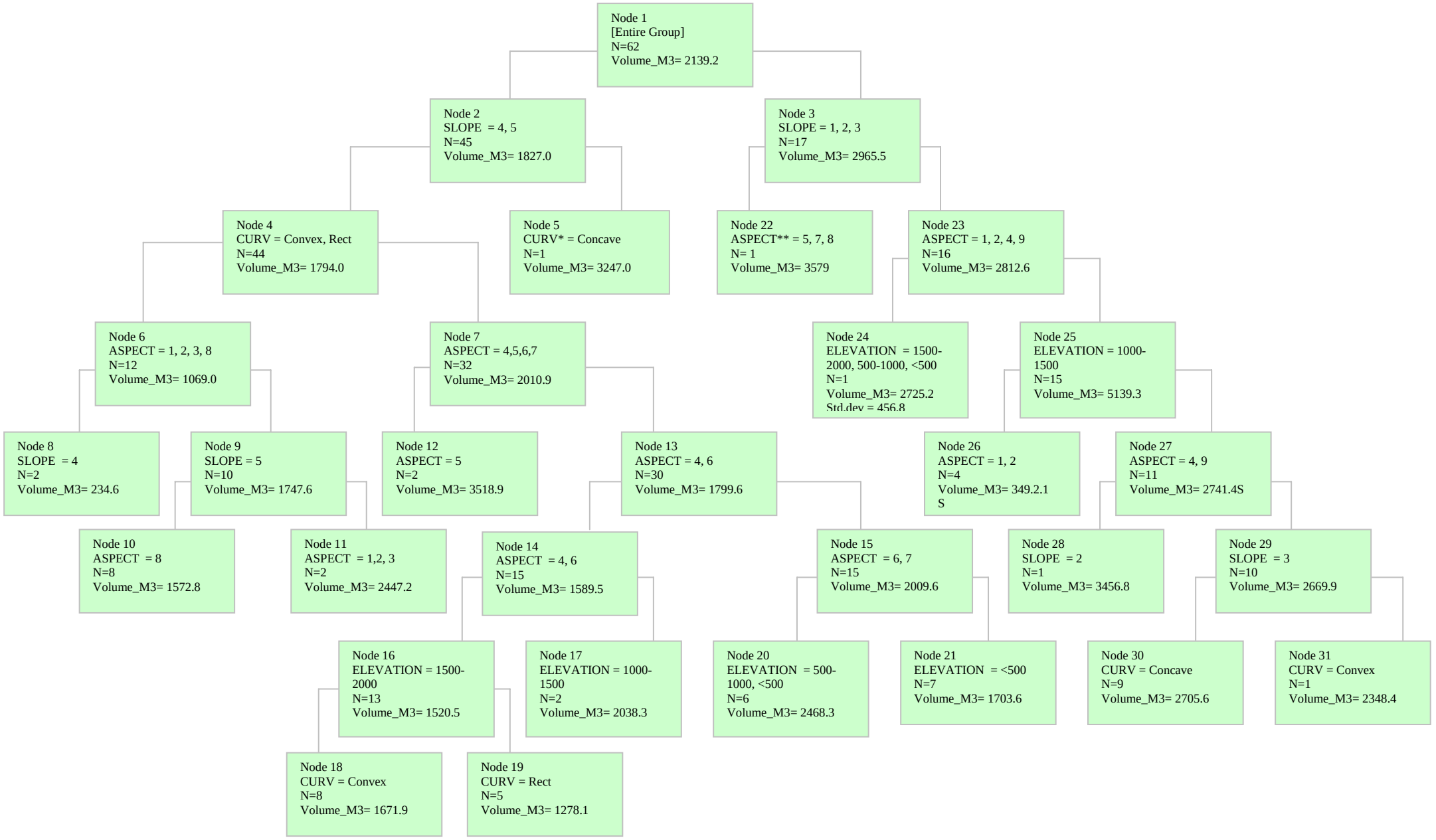

Figure 6.5. Unpruned decision-tree model explored on topographic parameters only (model 2a).

** CURV = Slope curvature (Concave, Convex, rectilinear)*

*** ASPECT = 1,2,3,4,5,6,7,8,9 corresponds to slope aspect Non oriented, N, NE, E, SE, S, SW, W, NW, respectively*

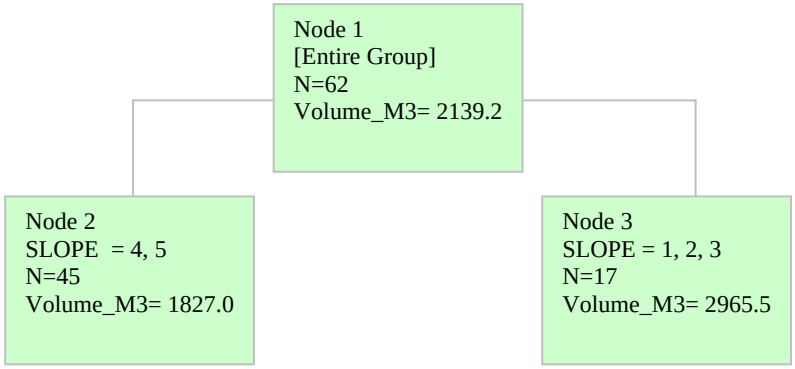

Figure 6.6. Pruned decision-tree model explored on topographic parameters only (model 2b).

The relative importance of the predictor parameters in building those trees (model 1a, model 1b, model 2a, model 2b, model 3a, model 3b) and splitting corresponding nodes is shown in **Table 6.1.**

Table 6.1. Summary characteristics of built regression tree-models [1 - based on all parameters, 2 - based on topographic parameters only and 3 - based on geologic parameters only].

Predictor variables (%)	Model 1a (exploratory tree)	Model 1b (pruned tree)	Model 2a (exploratory tree)	Model 2b (pruned tree)	Model 3a (exploratory tree)	Model 3b (pruned tree)
Elevation	0%*	0%	18%	0%	N	N
Slope gradient	70%	78%	100%	100%	N	N
Slope aspect	11%	0%	70%	0%	N	N
Slope curvature	0%	0%	50%	0%	N	N
Lithology	100%	86%	N**	N	100%	100%
Proximity to fault line	50%	0%	N	N	22%	0%
Karst type	10%	0%	N	N	10%	0%
Soil type	61%	40%	N	N	41%	49%
Distance to drainage line	0%	0%	N	N	N	N
Land cover/use	60%	50%	N	N	N	N
Proximity to roads	6%	0%	N	N	N	N
Proportion of variance explained	**86%**	**50%**	**57%**	**19%**	**68%**	**45%**
Number of total nodes	23	7	31	3	27	5
Number of terminal nodes	12	4	15	2	14	3
Minimum cost error – node number	-	0.07 – node 3	-	0.8538 – node 2	-	0.8057 – node 3

* = relative importance of predictor variables; N = not included in building the model

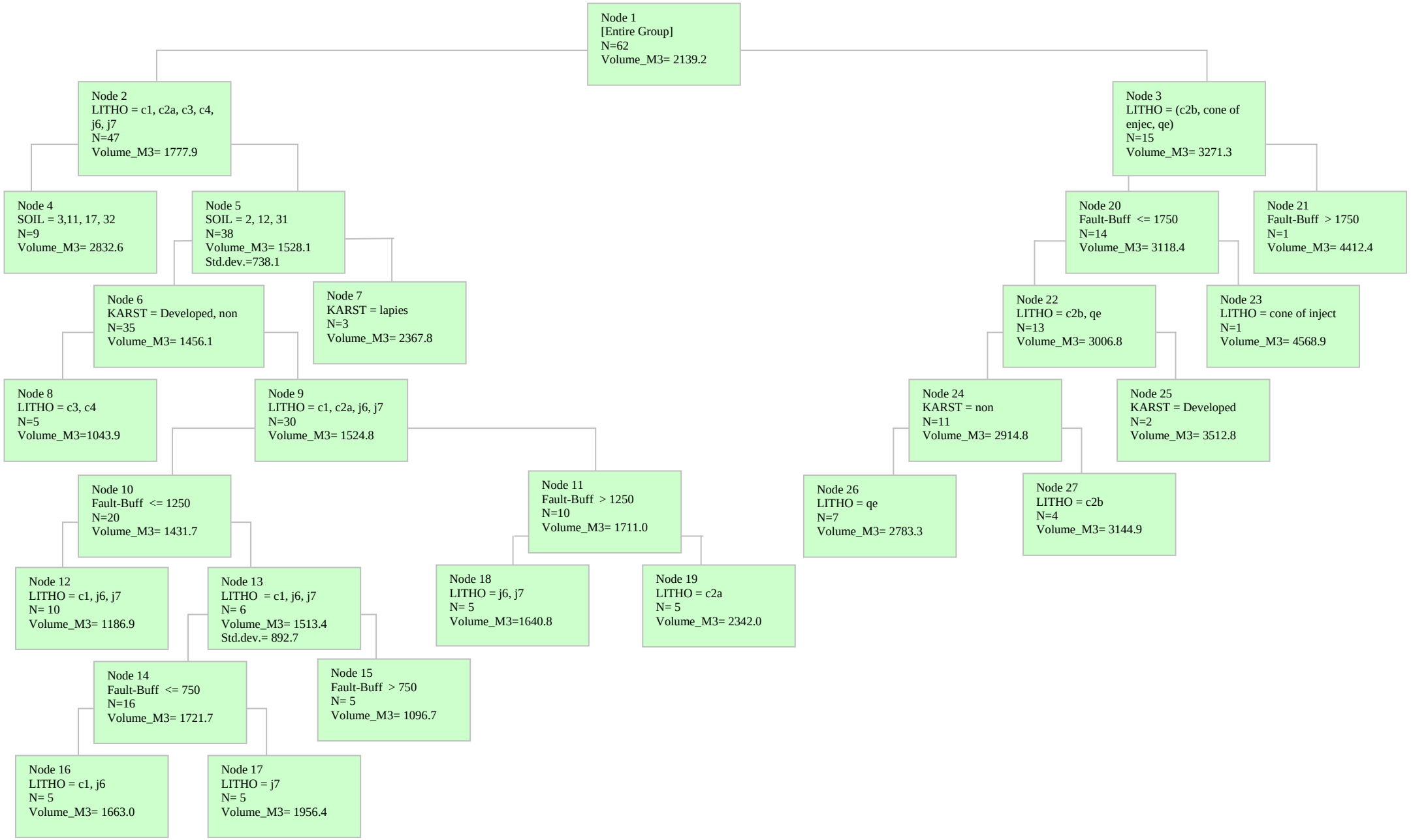

Figure 6.7. Unpruned decision-tree model explored on geologic parameters only (model 3a).

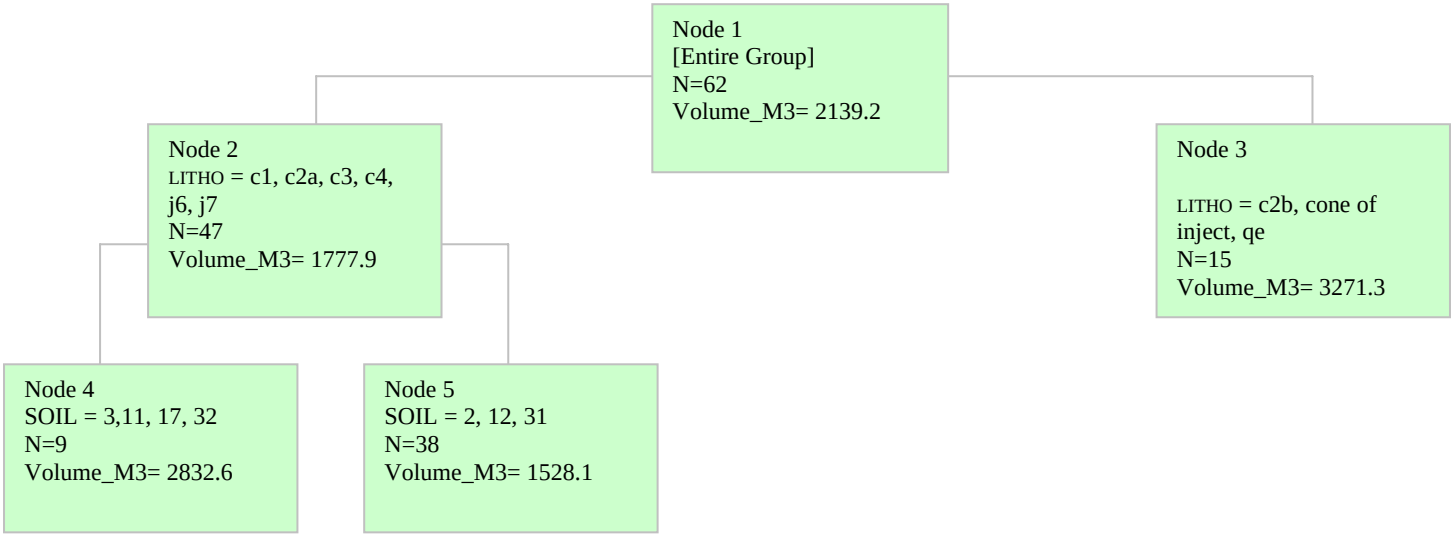

Figure 6.8. Pruned decision-tree model explored on geologic parameters only (model 3b).

As shown in this table, lithology, once considered, is presenting the highest effect on block falls' occurrence, followed by slope gradient (angle); both of them conditioning this MM event. Soil type and land cover/use are acting almost similarly (models 1a and 1b) on this occurrence. The proximity to fault line has demonstrated a certain effect if the tree is unpruned (50 %), but once pruning is affecting the tree; its effect will be masked. In the same way, slope aspect, karst type and proximity to roads are influencing the occurrence of block falls but to a lesser extent (6 to 11%). This influence became nul if the tree is pruned. Elevation and slope curvature do not intervene in building the exploratory tree. The latter shows higher contribution (50%) than the former (18%) in building the unpruned model based on topographic parameters only (model 2a).

The unpruned model based on all parameters (model 1a) is the most powerful in explaining the variance in the trained data (variance = 86%), compared to pruned and non pruned models 1b, 2a, 2b, 3a and 3b. Although, the pruned trees are easier to understand and faster to use for making decisions, the proportion of variance explained eventually decreases (i.e. non pruned model 1a – 86% variance, pruned model 1b – 50% variance; non pruned model 2a – 57% variance, pruned model 2b – 19% variance; non pruned model 3a – 68%, pruned model 3b – 45% variance). I have built "1a, 1b, 3a and 3b" models, the predictor variable, that was used statistically to generate the split from the parent root node, was the lithological formation indicating its potential role in predicting the geographic location and size of block falls. Slope gradient plays also a crucial role, with a relative importance varying between 70% (model 1a), 78% (model 1b) and 100% (models 2a and 2b).

The model constructed by using lithology as the initial split **(Figure 6.9)** explained 81% of the variance, giving close results to the exploratory reference tree-model based on all parameters (model 1a). This demonstrates the significance of the lithological formations in determining block falls' occurrence. The number of total nodes and terminal nodes is equal to 21 and 11, respectively. The relative importance of the predictor variables is represented as follows: lithology – 100%, slope gradient – 81%, land cover/use – 50%, proximity to fault line – 45%, soil type – 35% and karst type – 14%.

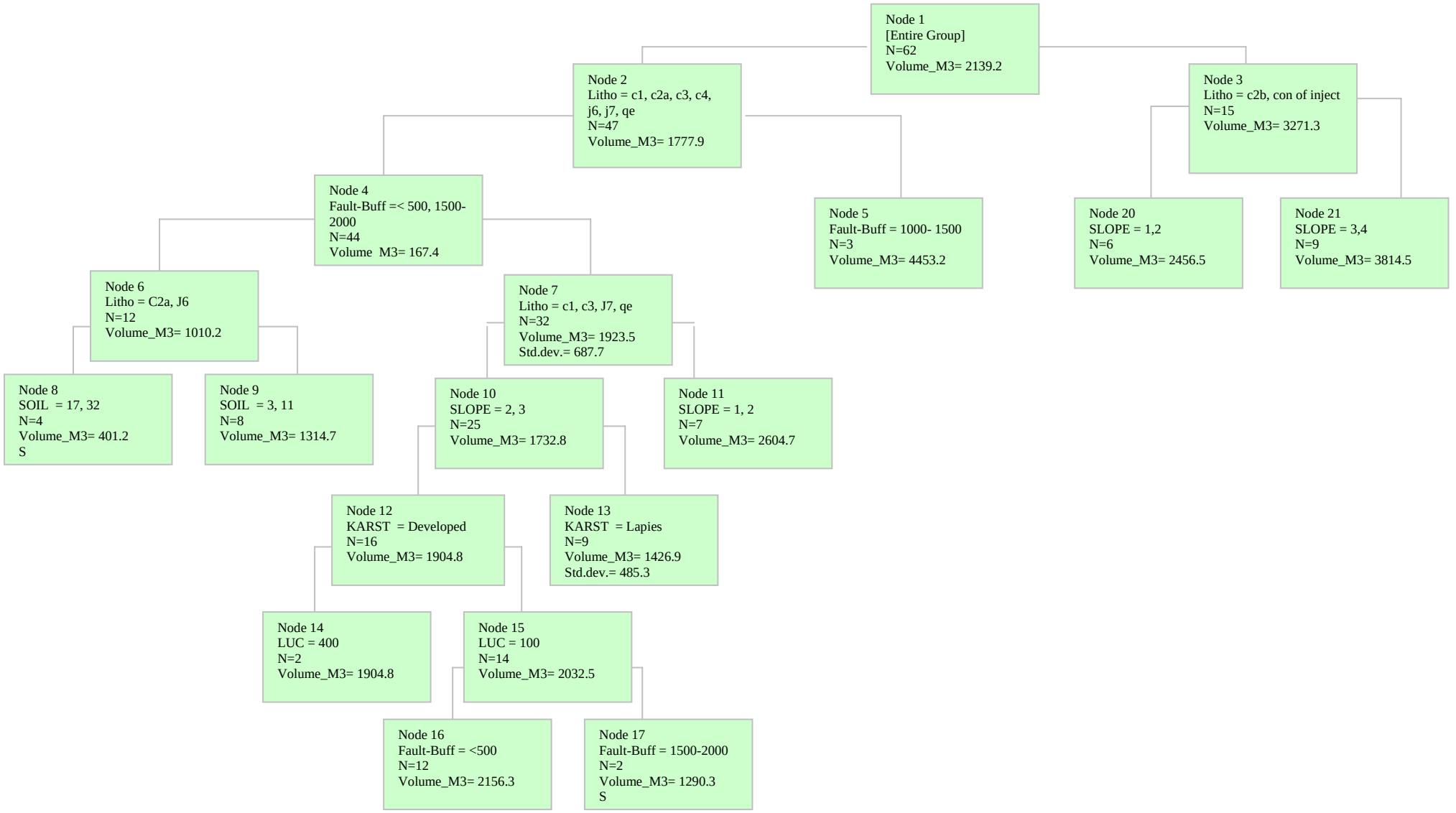

Figure 6.9. Decision-tree model built by preferring the lithological formation as initial split *(refer to Figure 6.3. for abbreviation explanation).*

4.3. Production of the volumetric map of block falls

4.3.1. Mapping block falls' volumes using the unpruned decision-trees

Depending on the obtained decision-tree models results, I used the preferred unpruned one based on all parameters (model 1a) in order to establish the volumetric map of block falls in the chosen studied site at 1:50,000 cartographic scale. This preferred model shows the highest predictive power, classifying 86% of the data correctly, and selecting six parameters with a decreasing order of importance as follows – lithology, slope gradient, soil type, land cover/use, proximity to fault line and karst type. For that, I considered the corresponding maps of these parameters as important in representing the conditions of block falls' formation if triggering factors exist (refer to introduction of this chapter). I overlaid then these maps sequentially under the GIS environment resulting in a unique-condition landscape unit map. Using the preferred decision tree-model (model 1a), I converted the landscape unit map into a predictive volumetric map of block falls [assigned as map 1 **(Figure 6.10)**]. If different end results (volumes of block falls in m^3) characterize field sites within a given landscape unit, new sub-polygons were delineated. In the case of similar results, landscape unit polygons were joined.

Afterwards, I divided the obtained volumetric map of block falls into six volume classes having an equal range of distribution i.e. nil (class 1) indicating the absence of block falls, very low volume (class 2 – volume being less than 1000 m^3), low volume (class 3 – volume ranging between 1000 and 2000 m^3), medium volume (class 4 – 2000 m^3 < volume < 3000 m^3), high volume (class 5 – 3000 m^3 < volume < 4000 m^3), and very high volume (class 6 – volume > 4000 m^3). This division seems necessary for prioritization of needed measurements to reduce the occurrence of harmful block falls. In this volumetric map, class 1 covers the largest area (64%) being dispersed in the studied region **(Table 6.2)**. The very low volume (class 2) of block falls occurs similarly in all parts of the studied site, occupying 17%. Class 3 (low volume) covers a small portion (3%), shown as small patches in the region. The medium volume (class 4) occupies a very small coverage (around 1%). The high (class 5) to very high (class 6) volumes of block falls have nearly equal areas (class 5: 8% and class 6: 7%) and are found as associated classes in the whole region. This indicates a widespread possibility of large volume of block falls if the terrain is attributed to the high volume class and no conservation practices are applied.

4.3.2. Mapping block falls' volumes using the pruned decision-trees

Even though the built pruned decision-trees models give less accurate results than pruned ones, since the explained variance is decreasing dramatically (model 1b – 50%, model 3b – 45% and model 2b – 19%), they can be useful for predicting the occurrence of block falls for two reasons: (1) they are easier to understand (smaller number of nodes) and (2) they are constructed using a small number of parameters. This is crucial for several developing countries lacking of detailed spatial data. For this reason, I prepared another block falls' map **(map 2 - Figure 6.11)** using the results of the most powerful pruned tree (model 1b) with 4 terminal nodes and 4 inherent parameters (lithology, slope gradient, land cover/use and soil type). It comprises the same classes as map 1 at the exception of class 6 (very high volume). The number of polygons decreases by 37% in map 2 compared with map 1 indicating an important spatial transformation **(Table 6.2)**.

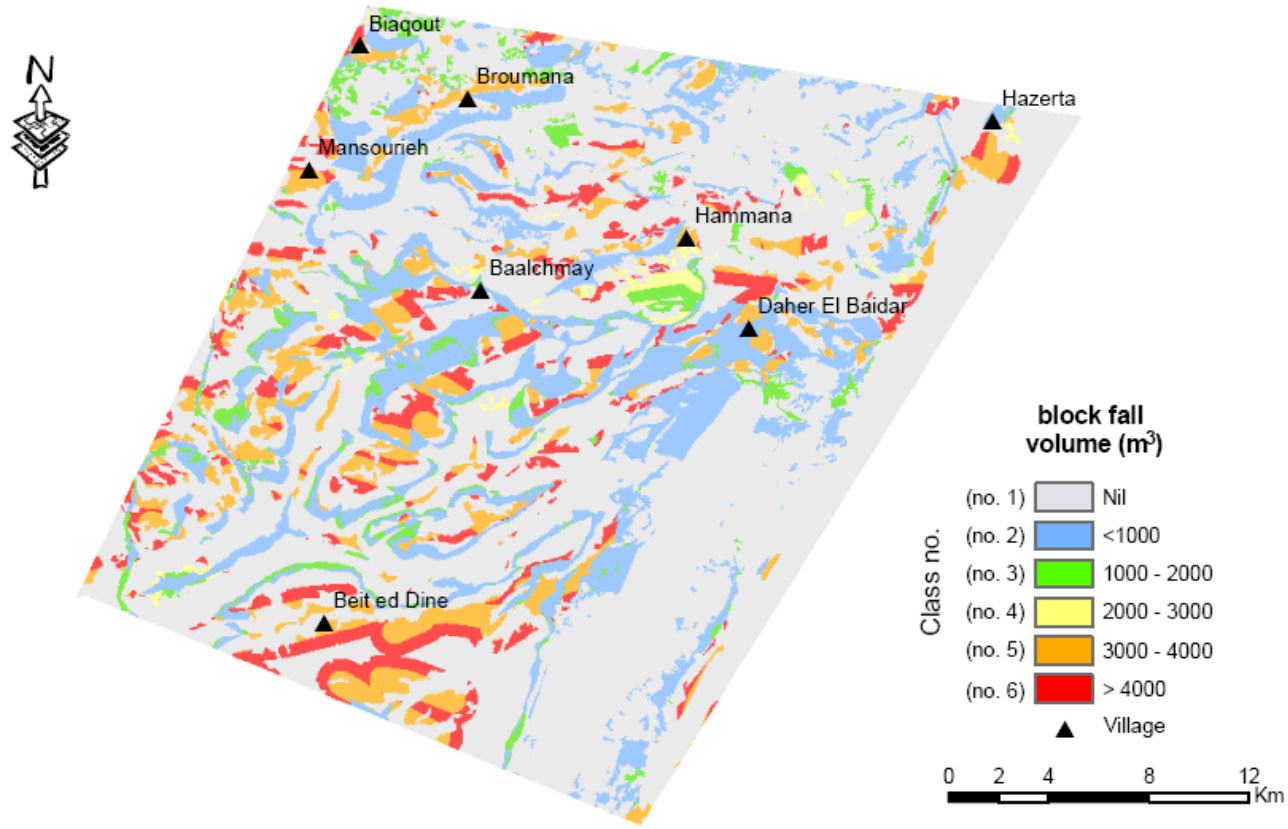

Figure 6.10. Predictive block falls' map based on all parameters of the unpruned decision-tree model (model 1a).

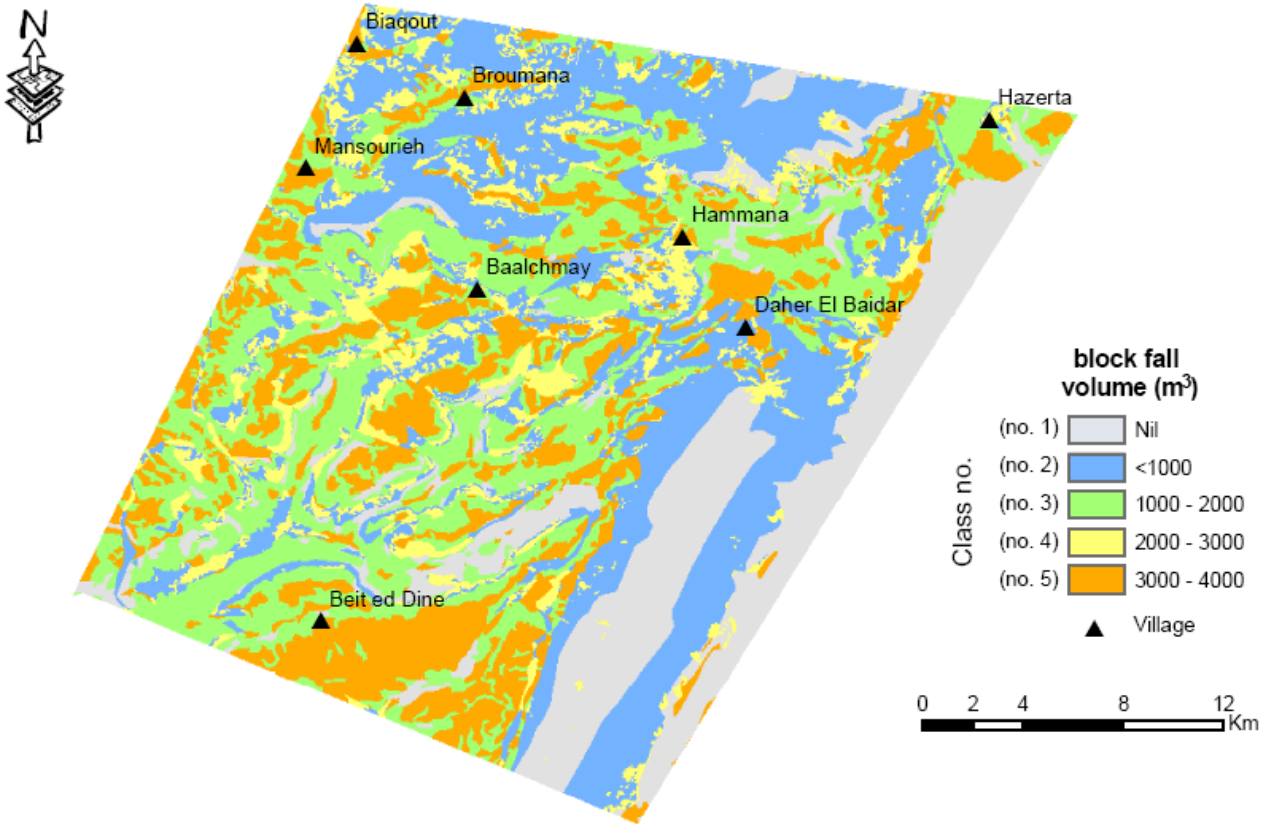

Figure 6.11. Predictive block falls' map based on all subparameters of the pruned decision-tree model (model 1b).

The areas of very low, low, medium and high classes increase on map 2, against a big decrease of the nil class area (by 46.5%) **(Table 6.2).** Pruned predictive modeling often overestimates block falls volumes, while underestimation is rare. This can be considered as a positive point for management planning considerations because the possibility of overlooking actual volumes decreases.

4.3.3. Comparison between volumetric block falls' maps produced using unpruned and pruned decision-trees

The perimeter (polygons' boundaries) of the total number of polygons in the block falls' map 1 is equal to 22873 km, while in the block falls' map 2, it is 20391 km. The decrease in the perimeter in map 2 is equivalent to 2482 km (around 11%). Therefore, map 1 established from the unpruned model based on all parameters presents more spatial coverage details, differentiating more the areas characterized by a different block fall volume level.

The comparison (in km^2) of classes belonging to the two maps permits the assessment of the effect of pruning on block falls mapping **(Table 6.3)**. In this contingency table, the sum of areas to which the classes of map 1 and map 2 correspond strictly (340 km^2, in grey on the diagonal of the table) is divided by the total area of the studied region (762 km^2). The table shows a similarity degree between the 2 maps of 45%, reflecting the major effect played by taking into account additional parameters in modifying the result. The comparative analysis between maps 1 and 2 demonstrates the usefulness of map 1 in predicting block falls volume at more detailed scale than map 2; however the latter (map 2) can be used for a rapid estimation of block falls susceptible areas being constructed from four parameters only. In addition, if close classes (nil, very low, low) are merged together in one class (low for example); the similarity degree will increase considerably (77%). This indicates that map 2 will be useful with 4 classes only (i.e. low, medium, high and very high).

Table 6.2. Comparison of polygons' number and areas of volume of block falls classes in the constructed maps 1 and 2.

Block fall volume class	Map 1		Map 2		Comparing Map 2 with Map 1	
	Number of polygons (%)	Occupied area	Number of polygons	Occupied area	Number of polygons	Occupied area
Nil	12122 **(62%)**	491 km^2 **(64%)**	2049 **(16.5%)**	132 km^2 **(17.5%)**	-45.5%	-46.5%
Very low	3146 **(16%)**	130 km^2 **(17%)**	2302 **(18.5%)**	209 km^2 **(27%)**	+2.5%	+10%
Low	912 **(5%)**	26 km^2 **(3%)**	3660 **(29%)**	195 km^2 **(26%)**	+24%	+23%
Medium	295 **(1%)**	7 km^2 **(1%)**	1712 **(14%)**	77 km^2 **(10%)**	+13%	+9%
High	1778 **(9%)**	62 km^2 **(8%)**	2683 **(22%)**	149 km^2 **(19.5%)**	+13%	+11.5%
Very high	1339 **(7%)**	46 km^2 **(7%)**	-	-	-7%	-7%
TOTAL	19592	-	12406	-	-37%	-

Table 6.3. Error matrix of the two block falls' maps.

Class of block falls volume		Map 2						
		Nil	**Very low**	**Low**	**Medium**	**High**	**Very high**	**TOTAL**
Map 1	**Nil**	132	70	160	17	40	0	491
	Very low	0	122	0	45	0	0	130
	Low	1	14	35	11	0	0	26
	Medium	0	2	0	5	0	0	7
	High	0	0	0	0	0	62	62
	Very high	0	0	0	0	0	46	46
	TOTAL	133	208	195	78	40	108	762

Numbers correspond to km^2;
Similarity degree between the two maps is equal to (340/ 762)*100 = 45%

4.4. Advantages and problems of the preferred decision-tree model

The preferred decision-tree model (model 1a) defines a map of block falls volume with six classes for a region situated in the central part of Lebanon. Such a map is unavailable in Lebanon, as well as in many countries. It represents the result of modeling from geoenvironmental characteristics and can meet the scientific needs of researchers and decision makers for exploring land problems.

The model explained 86% of the variance in block falls' volume for a series of field sites in a selected study area (762 km^2). The variance explained can be ameliorated using other details within the predictor variables such as geomechanical parameters (e.g., dip direction, spacing of discontinuities, roughness, infilling, weathering, rock mass strength, etc.). This is an important future research topic since the importance of such variables in explaining additional variance can be tested. This model can be extrapolated to other areas in the country if the functional capacities of GIS are used, because they allow the integration of several maps (i.e. lithological formation, slope gradient, soil type, land use/cover, proximity to fault line and karst type) for producing landscape units' maps of these areas, on which block falls measurements can be determined.

The concept of decision-tree modeling can also be tested for other mass movement types (e.g. landslides and earth flows) if the volumes of failure types are calculated. However, a major difficulty is encountered related to the coarse scale of the exiting soil map at 1:200,000 used for constructing the landscape unit map.

5. Conclusion

The established decision-tree models enabled, for the first time, mapping of predicted block falls' volumes in a region of Lebanon at a scale of 1:50,000, based on geoenvironmental characteristics (e.g. topography, geology, soil and land cover/use). The modeling approach was easily implemented with available GIS software, and is suitable for data exploration and predictive block falls' volumetric mapping. It is explicit and can be critically evaluated and revised when necessary. It can be also extrapolated easily to other Mediterranean countries undergoing socio-economic change.

This decision-tree approach did not produce volumetric maps of block falls with accuracies substantially higher than those reported in the literature for other methods

and/or models (Selby, 1980; Romana, 1985; Bieniawski, 1993; Irigaray *et al.*, 2003; Marquinez *et al.*, 2003; Dorren and Heuvelink, 2004). However, it can be considered as quick, simple, realistic and informative method for combining geoenvironmental variables in order to generate maps describing the potential size of block falls (predictive maps). These maps can be used to prioritize the choice of study areas for further measurement and modeling, and may in the short-term help with the selection and adoption of measures to reduce the occurrence of the harmful block falls. Although the chosen scale of these maps (1:50,000) seems to be sufficient for estimating the volume of the block falls to consider strategies for land protection, the maps can be improved for more localized hazard assessment if more detailed data sets are available [higher resolution DEMs and more detailed GIS parameter maps (predictors)].

- VII -
Preliminary testings for Monitoring Mass Movements

CHAPTER VII

Preliminary testings for monitoring mass movements

1. Introduction

Monitoring is essential to understand the dynamic behavior of mass movements (MM) and to reduce their risk. It may help to detect early indications of catastrophic movement. It provides immediate (real time monitoring) notification of landslide activity, possibly saving lives and property. Continuous information from monitoring also provides a better documentation of MM behavior, enabling scientists and engineers to create more effective designs for the physical processes that trigger and control MM.

Usually, the measurement of surficial displacement is the simplest way to observe the history and analyze the kinematics of the movement. Measurements have to be made efficiently in terms of time, manpower and budget. In the past, a variety of surveying techniques were used to detect the surficial movements of unstable areas (Mikkelsen, 1996). For example, tapes and wire (extensometers and clinometers) devices have been used to measure changes in distance between points or crack walls (Gulla *et al.*, 1988). Levels, theodolites, Electronic Distance Measurement (EDM), Time Domain reflectometry (TDR) and total station measurements provide both the coordinates and changes of target, control points and MM features (Ashkenazi *et al.*, 1980). In addition, aerial or terrain photogrammetry provides point coordinates contour maps and cross-section of the landslides. Photogrammetry compilation enables a quantitative analysis of the change in slope morphology and also the determination of the movement vectors (Hansen, 2001).

In the course of a little more than two decades, new methods for MM monitoring have developed; mainly ground-based and space borne radar interferometry, Light Detection and Ranging (LIDAR) and Global Positioning System (GPS). A comprehensive summary of the main measurements methods and their precisions is shown in **Table 7.1.**

Table 7.1. Overview of methods used in measuring surface displacement and their precision (Mikkelsen, 1996).

Method	Typical range	Results	Typical precision
GPS	Variable (< 20 km)	ΔX, ΔY, ΔZ	5-10mm + 1-2ppm*
Elec. Dist. Meas. (EDM)	Variable (1-14 km)	ΔX, ΔY, ΔZ	1-5mm + 1-5ppm*
Extensometer	< 10 – 80 m	Δdistance	0.3 mm/30m
Surveying triangulation	<300 -1000m	Δdistance	5-10mm
Surveying traverse	Variable	ΔX, ΔY, ΔZ	5-10mm
Geometrical Leveling	Variable	ΔZ	2-5mm/km
Precise Geometrical level	Variable	ΔZ	0.2-1 mm/km
Terrestrial photogrammetry	Ideally < 100 m	ΔX, ΔY, ΔZ	20 mm from 100m
Aerial photogrammetry	H_{flight} < 500m	ΔX, ΔY, ΔZ	10 cm

N.B. 1ppm means one part per million or 1 additional millimeter per kilometer of measured line
ΔX, ΔY, ΔZ are measurements of the distance in the (x, y coordinates), z being the elevation.

Interferometry from Synthetic Aperture Radar (InSAR) using earth-orbiting spacecrafts provide a new tool to map topography and deformation of the earth's surface. Interferometry allows the construction of digital elevation models of meter-scale accuracy. If the earth's surface is deformed between two radar image acquisitions of different times, a map of the surface displacements with tens-of-meters resolution and sub-centimeter accuracy can be constructed.

Synthetic Aperture Radar (SAR) systems that are used directly on the ground have recently also proved to be a monitoring tool for measuring not only MM, but also the seasonal movement in dams (Tarchi *et al.*, 2003), and for carrying out displacement measurements during the static test of bridges (Pieraccini *et al.*, 2001). Nevertheless, the ground-based installation has some drawbacks compared with satellite sensors; the most relevant being the necessity of finding a site suitable for installation. Furthermore, the site should be chosen in such a way that the movement component along the line of sight is not too small to be detected. Another relevant limitation of this technique is that the area which the ground-based installation can monitor is rather limited and typically covers a single landslide, whereas a satellite sensor is potentially able to monitor a much larger area. But, one of the main advantages of ground-based radar installation is that several radar data sets can be taken in one day, so coherence is always rather high and a displacement time-pattern can be well described.

Land-based LIDAR allows getting high resolution terrain digital models. They are very useful for monitoring quantitatively hard reachable areas of difficult access where MM occurred. The generated point cloud (which is a 3D image consisting of millions of laser shots that has exact range and location) allows a high precision reconstruction of an unstable area as, for example, a rock slope or a generically landslide phenomenon, permitting to perform comparisons between successive surveys from a morphologic or analytic (volumetric) point of view. Airborne LIDAR scanners (using airplanes or helicopters) constitute also a well established method for MM surveying.

On the other hand, the Global Positioning System (GPS) is fully operational and has spread world wide. The GPS technology has shown that it is capable to monitor sub-centimeter deformations of ground movement. Moreover, the GPS equipments are reliable, cheap, fast, easy to use and do not require line-of-sight between stations compared to conventional instruments. New hardwares, field procedures and softwares have also been developed to assist users in data collection and processing. Thus, the GPS equipment is more advanced and used for a wide range of monitoring applications.

In this chapter the application of two monitoring methods in the study area, the space borne InSAR and the GPS, is exposed and the preliminary results are discussed.

2. Interferometric synthetic aperture radar (InSAR)

2.1. Background

Conventional radar (radio detection and ranging) imaging is a technique in which a target is illuminated with electromagnetic waves of microwave frequency (cms) and the backscattered signal is used to deduce information about the target. Such conventional "real-aperture" radar moving in space would generate a rough two dimensional image with a resolution of about 5–10 km of the target area as the radar sweeps the area of interest. SAR (synthetic aperture radar) is more complex and,

combines signal processing techniques, together with recording of satellite orbit information, which "synthesize" a larger antenna in order to produce a much-higher-resolution (tens of meters) radar image. SAR processing significantly improves the resolution of point targets in both the cross-track (range) and along-track (azimuth) direction by better focusing the radar echoes (Elachi, 1988; Curlander and McDonough, 1991). Typical image point (pixel) spacing in space-based SAR image is 20-100 m within a 100 km wide swath.

Most SAR applications make use of the amplitude of the return signal, and ignore the phase data. However interferometry uses the phase of the reflected radiation. Since the outgoing wave is produced by the satellite the phase is known, and can be compared to the phase of the return signal. The phase of the return wave depends on the distance to the ground, since the path length to the ground and back will consist of a number of whole wavelengths plus some fraction of a wavelength. This is observable as a phase difference or phase shift in the returning wave. The total distance to the satellite (i.e. the number of whole wavelengths) is not known, but the extra fraction of a wavelength can be measured extremely accurately **(Figure 7.1)**.

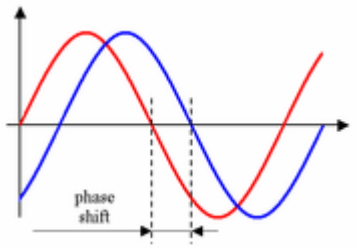

Figure 7.1. Showing phase difference in returning wave length.

In practice, the phase is also affected by several other factors, which together make the raw phase return in any one SAR image essentially arbitrary, with no correlation from pixel to pixel. To get any useful information from the phase, some of these effects must be isolated and removed. Interferometry uses two images of the same area taken from the same position (or for topographic applications slightly different positions) and finds the difference in phase between them, producing an image known as an interferogram. This is measured in radians of phase difference and, due to the cyclic nature of phase, is recorded as repeating fringes which each represent a full 2π cycle.

Two SAR data sets, especially the recorded phase information, can be combined to produce a simple radar interferogram, which can reveal information about the third dimension (elevation) of the target area. With three SAR data sets it is possible to measure small changes in the range distance that occurred during the two acquisitions intervals. After SAR focusing, the radar image is a two-dimensional record of both the amplitudes and the phases of the returns from targets within the imaging area. The amplitude is a measure of target backscatter, whereas the phase encodes changes at the surface (e.g., mass movements) as well as a term proportional to the range to the target. As mentioned before InSAR uses the phase information of two SAR scenes to determine the phase difference between each pair of corresponding scene points, thus producing an interferogram. Therefore, if two SAR scenes of a target area are available and can be precisely aligned with the precision of a fraction of a pixel width, the difference in phase of each scene point can be determined. If the difference in phase is taken from two scenes acquired from slightly different viewing angles, it provides information about changes in range between location of sensor in space and

targets on the ground **(Figure 7.2)**. In a SAR interferogram from two scenes, fringes from phase differences may appear (this is called simple interferometry). By compensating for the topography, these fringes become clearly visible and indicate very small relative movements of the ground surface (of the order of millimeters or centimeters). This is called differential interferometry. Interestingly, the first applications of InSAR were in earth-based studies of topography of the Moon and Venus (Zisk, 1972; Rumsey *et al*., 1974). The phase difference of two scenes taken from the same viewpoint, but at different times (so at different locations of Earth) can precisely measure differences of the returned phase. Both interferometry techniques (simple and differential) open up many new potential application areas for spaceborne SAR data in disciplines such as cartography, volcanology, structural geology, glaciology, and geotechnics, and for work relevant to land subsidence and landslide monitoring (Barbieri and Lichtenegger, 2005; Catani *et al.*, 2005; Dhont *et al.*, 2005).

Thereof, differential interferometry applied to MM is based on the phase comparison between two SAR images acquired before and after a deformation event and referred to a DEM. If the earth's surface moved toward or away from the radar between the two imaging passes, phase changes that result can be measured with a precision corresponding to millimeter-level displacements. The interferogram amplitude (brightness) is the product of the image backscatter amplitudes. Interferograms are often displayed overlaying the brightness rendered in grayscale, and phase as color, where each cycle of color, or fringe, represents a phase change to 2π radians.

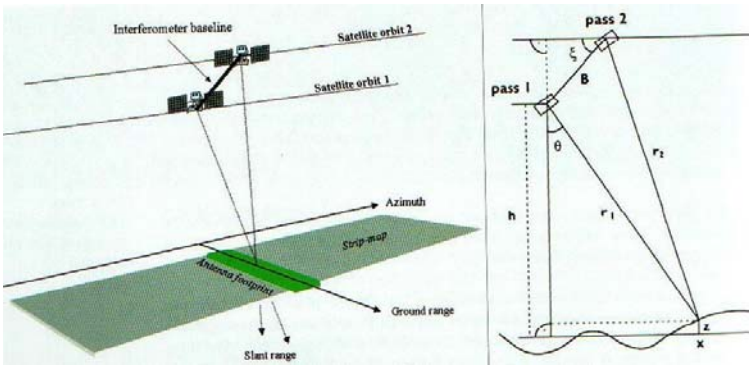

Figure 7.2. Interferometric imaging geometry, two passes pointing to one resolution element (Barbarie and Lichtenegger, 2005).

2.2. Producing interferograms

The production of an interferogram is in principle a straightforward procedure (Burgmann *et al.*, 2000). The processing chain used to produce interferograms varies according to the software used and the precise application, but will usually include some combination of the following steps (Figure 7.3): Two SAR images are required to produce an interferogram; these may be obtained pre-processed, or produced from raw data by the user prior to InSAR processing. The two images must first be co-registered, using a correlation procedure to find the offset and difference in geometry between the two amplitude images. One SAR image is then re-sampled to match the geometry of the other, meaning each pixel represents the same ground area in both images. The interferogram is then formed by cross-multiplication of each pixel in the two images, and the interferometric phase due to the reference ellipsoid is removed, a

process referred to as flattening. For deformation applications a DEM can be used in conjunction with the baseline data to simulate the contribution of the topography to the interferometric phase, this can then be removed from the interferogram.

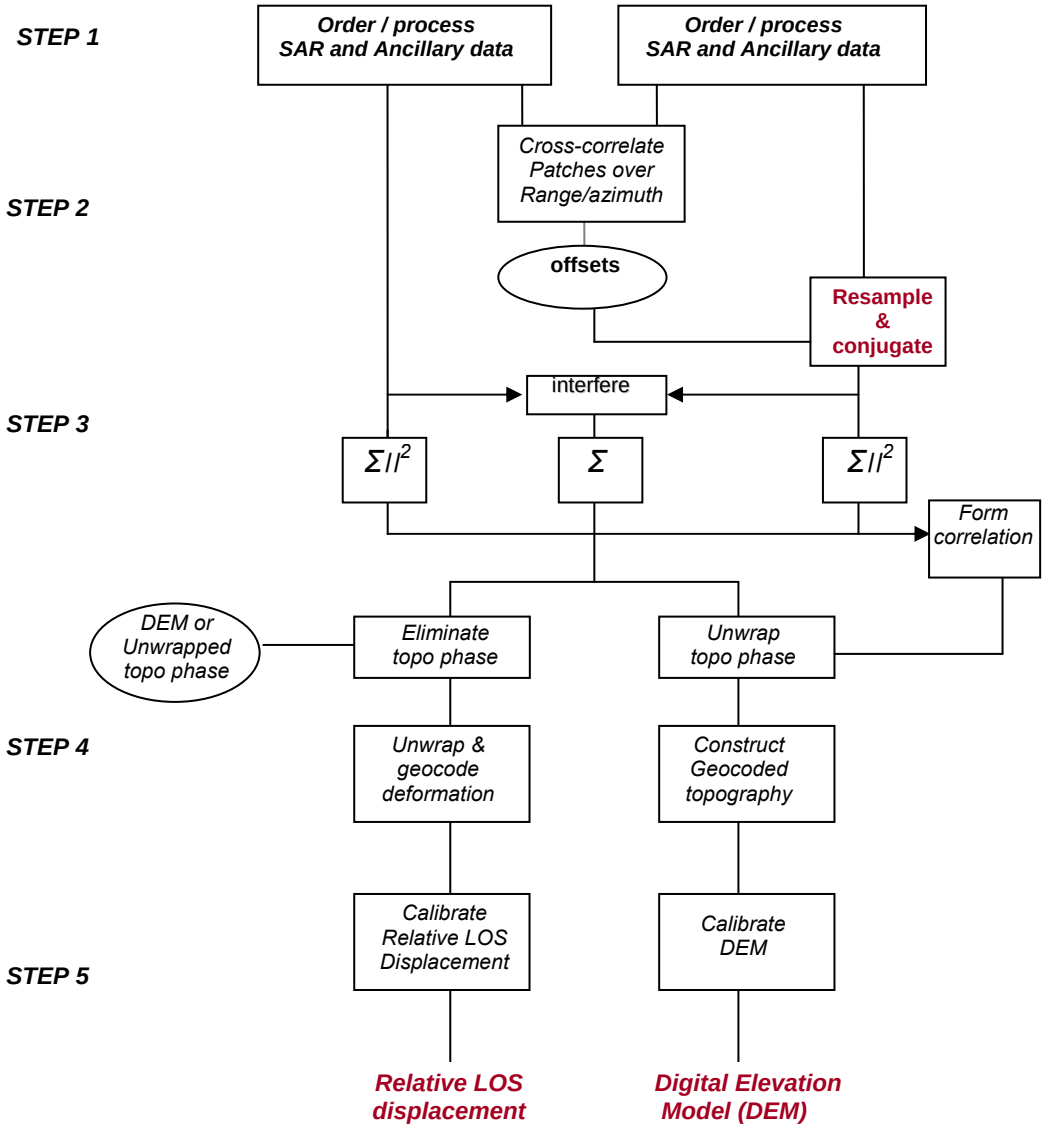

Figure 7.3. A Schematic outlining steps in processing SAR data for interferometric applications.
Step 1 entails ordering, cleaning, and processing SAR data and ancillary data. Step 2 determines the coregistration offsets between the images. If orbits are accurate to 1/20 pixel, this can be done without using the SAR data. If not, the SAR data are cross correlated to determine the offsets. Step 3 resamples and forms the interferogram and correlation. The outer boxes with the summation symbols in this step represent averaging the power of nearby pixels. The center summation box represents averaging the interferogram. These averages are required to estimate the correlation. Step 4 unwraps the phase and produces the geophysical measurement. Step 5 is calibration of the measurement (Burgmann et al., 2000).

Once the basic interferogram has been produced, it is commonly filtered using an adaptive power-spectrum filter to amplify the phase signal. For most quantitative applications the consecutive fringes present in the interferogram will then have to unwrapped, which involves interpolating over the 0 to 2π phase jumps to produce a

continuous deformation field. At some point, before or after unwrapping, incoherent areas of the image may be masked out. The final processing stage involves geocoding the image, which involves resampling the interferogram from the acquisition geometry (related to direction of satellite path) into the desired geographic projection.

2.3. Permanent scatter techniques

For the interferometric process to work successfully, a degree of similarity or correlation must exist in the surface properties between the two image acquisitions. In most parts of the world, particularly temperate regions, correlation between images will degrade with time due to changing/moving vegetation, differing climatic conditions - termed 'temporal decorrelation'. Correlation tends to remain good in arid, desert regions where little change occurs. An output from the processing chain is a coherence image, and this represents the correlation that exists between corresponding pixels of the two images - lighter pixels showing good correlation (e.g. arid, dry land cover), and darker pixels showing bad correlation (e.g. water, changing vegetation).

Techniques for reducing this error are by stacking multiple independent observations called Corner Reflectors or Permanent Scatterers (Wegmuller and Strozzi, 2000; Berardino *et al.*, 2003). Ferretti et al. (2001) proposed examining interferometric phases from stable, point-like reflectors and demonstrated that large numbers of such reflectors could be identified in stacks of ERS data, particularly in built up areas. For point targets (permanent scatters) no spatial decorrelation happens, permitting interpretation of the interferometric phase of pairs with long baselines. Obviously same reflectors must remain stable over the time period of interest, enough to permit analysis of the phase history. Based on these ideas, one important objective of the permanent scatterers is to achieve a more complete use of the available data. Through the use of point targets, interferometric pairs with long baselines can be used. Consequently, more observations are available permitting reduction of errors resulting from the atmospheric path delay and leading to better temporal coverage. Concerning the spatial coverage, it is expectated that a few point targets may also be found in non-urban areas, permitting extension of the spatial coverage.

The phase model used in permanent scattrers techniques, or the so called IPTA (Interferometric Point Target Analysis), is the same as that used in conventional interferometry. The unwrapped interferometric phase is expressed as the sum of a topographic phase, a deformation phase, a differential path delay phase (also called atmospheric phase), and phase noise (or decorrelation) terms. In the interferometric point target analysis the interferograms, unwrapped phases, topographic heights, deformation rates, residual phases associated with the atmosphere and others, are only interpreted for the selected points. The permanent scattrers (IPTA) processing begins by assembling the images. A stack of co-registered Single Look Complex image SLC (Phase and amplitude combination in a single image file), with reference image (RSLC) using ancillary data for each image having in it the image orbit parameters is performed. To specify which pairs shall be considered in the interferometric data stacks a parameter text file (itab) is prepared. Furthermore, a preliminary Digital Elevation Model (DEM) is used, can be the DEM deduced from the InSAR.

Based on the registered SLCs, a candidate list of point targets (plist) is determined. Criteria for an initial selection of point target candidates include low temporal variability of the backscattering coefficient. For the candidate points the SLC values are extracted and written to a point data stack. For convenient access the related SLC parameter files are stored in a single binary file (ppar). Initial estimates of

the interferometric baselines are calculated from the available orbit state vectors. All the baseline information is also stored in a single binary file (phase). Next, the differential interferograms are calculated. This is done by simulation of the unwrapped interferometric phase based on the currently available information, i.e. the initial baselines and the available DEM. Typically, no information on deformation and atmospheric phase delay is available at this stage. For each selected interferometric pair this simulation is calculated and subtracted from the interferogram. Depending on the accuracy of the assumed model parameters, the quality of the candidate points, and the baselines, these differential interferograms may look smooth or very noisy. In the next step the stack of differential interferograms is analyzed.

The phase standard deviation includes terms related to noise phase, atmospheric phase, deformation phase, and baseline errors. Except for noise phase, these terms depend all on the distance between the two points. The regression is further improved and made more robust by also considering linear phase dependence with time, equivalent to a constant deformation rate. The results from the regression analysis are height corrections, linear deformation rates, a quality measure, residual phases, and the unwrapped interferometric phase. These are used to improve the model. The height corrections, for example, are added to the DEM heights used in the simulation. The residual phase contains the atmospheric phase, which is related to the path delay heterogeneity at the two acquisition times of the pair, as well as non-linear deformation and error terms. An important aspect of the IPTA concept is the possibility of a step-wise, iterative improvement of different parameters. Main improvements include the consideration of a height correction, a deformation rate, a baseline refinement, atmospheric phase terms, and extension of the point list. The objective of the extension of the point list is to include as many points as possible. The evaluation of the quality of potential additional points can be done more reliably and efficiently if the improved model for the validated points is already available. (GAMMA- IPTA, user guide).

2.4. Data processing

Nineteen ERS-1 and ERS-2 SAR scenes, of track 78 and frame 2925 acquired in a span of eleven years (1992 – 2000) were tested. In the first phase (preparing the interferograms), image couples of relatively small perpendicular baselines were used **(Table 7.2)**. The ERS imageries were processed using Interferometric SAR Processor (ISP) module of GAMMA software. The starting point for generating an interferogram is a couple of Single Look Complex (SLC) images, this was done on each selected couples, respectively **(Table 7.3)**.

The first step is done by preparing the raw data, linking this data to the working directories, defining data in one geometry, and creating the parameter files (Annex 1-a). The second step is the offset estimates. First the offset file is created, after an initial range and azimuth offsets between the two SLC images are estimated based on image intensity cross-correlation, a precise estimation of offset polynomials based on the image intensity is calculated. The result determine a field of registration

Table 7.2. Table showing some of the ERS data couples and their corresponding perpendicular baselines used in the ISP processing.

		E1	E1	E1	E1	E1	E1	E1	E1	E1	E1	E2	E2	E2	E2	E2	E2	E2	E2	E2	E2
		4732	**5233**	**6235**	**11245**	**11746**	**20607**	**21609**	**22110**	**25116**	**32631**	**934**	**1936**	**2437**	**5443**	**6445**	**12958**	**15964**	**21976**	**26986**	**42016**	**42517**
E1	**4732**	0	609	-716	-222	-220	1095	-830	12	398	351	-1234	905	527	-297	-143	79	93	755	-551	578	-1495
E1	**5233**	609	0	-107	-831	389	486	-221	-597	1007	-258	-625	296	1136	-906	466	-530	702	146	58	-31	-886
E1	**6235**	716	-107	0	-938	496	379	-114	-704	1114	-365	-518	189	1243	-1013	573	-637	809	39	165	-138	-779
E1	**11245**	-222	831	-938	0	-442	1317	-1052	234	176	573	-1456	1127	305	-75	-365	301	-129	977	-773	800	-1717
E1	**11746**	220	389	-496	-442	0	875	-610	-208	618	131	-1014	685	747	-517	77	-141	313	535	-331	358	-1275
E1	**20607**	1095	-486	379	-1317	875	0	265	-1083	1493	-744	-139	-190	1622	-1392	952	-1016	1188	-340	544	-517	-400
E1	**21609**	830	-221	114	-1052	610	265	0	-818	1228	-479	-404	75	1357	-1127	687	-751	923	-75	279	-252	-665
E1	**22110**	12	597	-704	-234	-208	1083	-818	0	410	339	-1222	893	539	-309	-131	67	105	743	-539	566	-1483
E1	**25116**	-398	1007	-1114	176	-618	1493	-1228	410	0	749	-1632	1303	129	101	-541	477	-305	1153	-949	976	-1893
E1	**32631**	351	258	-365	-573	131	744	-479	-339	749	0	-883	554	878	-648	208	-272	444	404	-200	227	-1144
E2	**934**	1234	-625	518	-1456	1014	-139	404	-1222	1632	-883	0	-329	1761	-1531	1091	-1155	1327	-479	683	-656	-261
E2	**1936**	905	-296	189	-1127	685	190	75	-893	1303	-554	-329	0	1432	-1202	762	-826	998	-150	354	-327	-590
E2	**2437**	-527	1136	-1243	305	-747	1622	-1357	539	-129	878	-1761	1432	0	230	-670	606	-434	1282	-1078	1105	-2022
E2	**5443**	-297	906	-1013	75	-517	1392	-1127	309	101	648	-1531	1202	230	0	-440	376	-204	1052	-848	875	-1792
E2	**6445**	143	466	-573	-365	-77	952	-687	-131	541	208	-1091	762	670	-440	0	-64	236	612	-408	435	-1352
E2	**12958**	79	530	-637	-301	-141	1016	-751	-67	477	272	-1155	826	606	-376	-64	0	172	676	-472	499	-1416
E2	**15964**	-93	702	-809	-129	-313	1188	-923	105	305	444	-1327	998	434	-204	-236	172	0	848	-644	671	-1588
E2	**21976**	755	-146	39	-977	535	340	-75	-743	1153	-404	-479	150	1282	-1052	612	-676	848	0	204	-177	-740
E2	**26986**	551	58	-165	-773	331	544	-279	-539	949	-200	-683	354	1078	-848	408	-472	644	204	0	27	-944
E2	**42016**	578	31	-138	-800	358	517	-252	-566	976	-227	-656	327	1105	-875	435	-499	671	177	27	0	-917
E2	**42517**	1495	-886	779	-1717	1275	-400	665	-1483	1893	-1144	261	-590	2022	-1792	1352	-1416	1588	-740	944	-917	0

Table 7.3. Image couples used for the processing and their corresponding baselines.

ERS-1	ERS-2	⊥ Baseline
21609	01936	75 m
20607	00934	-139 m
11746	06445	77 m
25116	05443	101 m
04732	12598	79 m

offsets (file*.offs) and a corresponding quality measured field (*.snr) (Annex 1-b), based on these, the bilinear registration offset polynomial (fine registration) is then determined using a least square error method (Annex 1-c). The final stage of step 2 is to compute normalized interferogram and register intensity images. This is done through the interpolation of the slave image (the second SLC or image) in the master (the first SLC or image) geometry using offset polynomial (estimated in offset_fit, Annex 1-d). The third step starts by initial estimation for the baseline, then the removal of the phase trend expected for a smoothed curved earth (ellipsoid) from the interferogram. The result is a flattened interferogram (**Figure 7.4**) (Annex 1-e). A phase simulation is then performed from the flattened interferogram to produce a wrapped interferogram. Finally we subtract the topographic phase from the wrapped interferogram and a wrapped phase without topography is deduced (Annex 1-f).

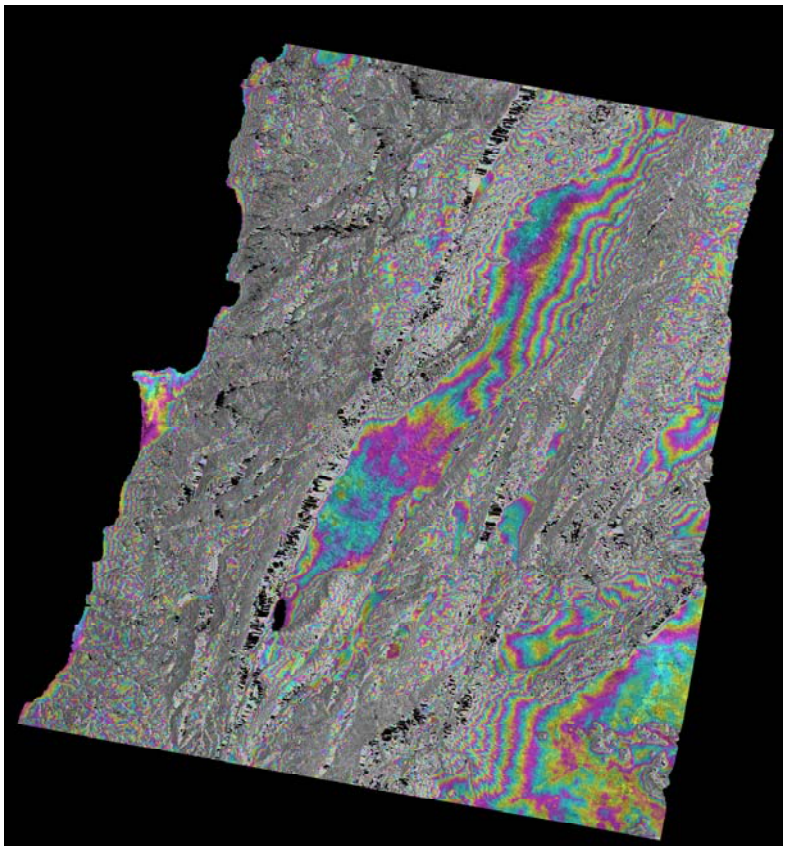

Figure 7.4. Flattened interferogram e120607_e200934.flt, one color cycle corresponds to 2 and pi interferometric phase.

Step four consists in: 1) iterative filtering is run on the wrapped interferogram (without topography) to reduce the phase noise and the discontinuity; 2) Unwrap the phase (without topography); 3) add the topographic phase back to generate a complete unwrapped interferogram (with topography, deformation, and curved earth), which is done essentially to improve baseline estimate (Annex 1-g). The fifth step starts by extracting the GCPs for improving baseline estimates, and this is followed by baseline calculation. The result is used to estimate the topographic phase accurately. Finally, this accurate deduced topographic phase is subtracted from the complete unwrapped interferogram (Annex 1-h, **Figure 7.5**).

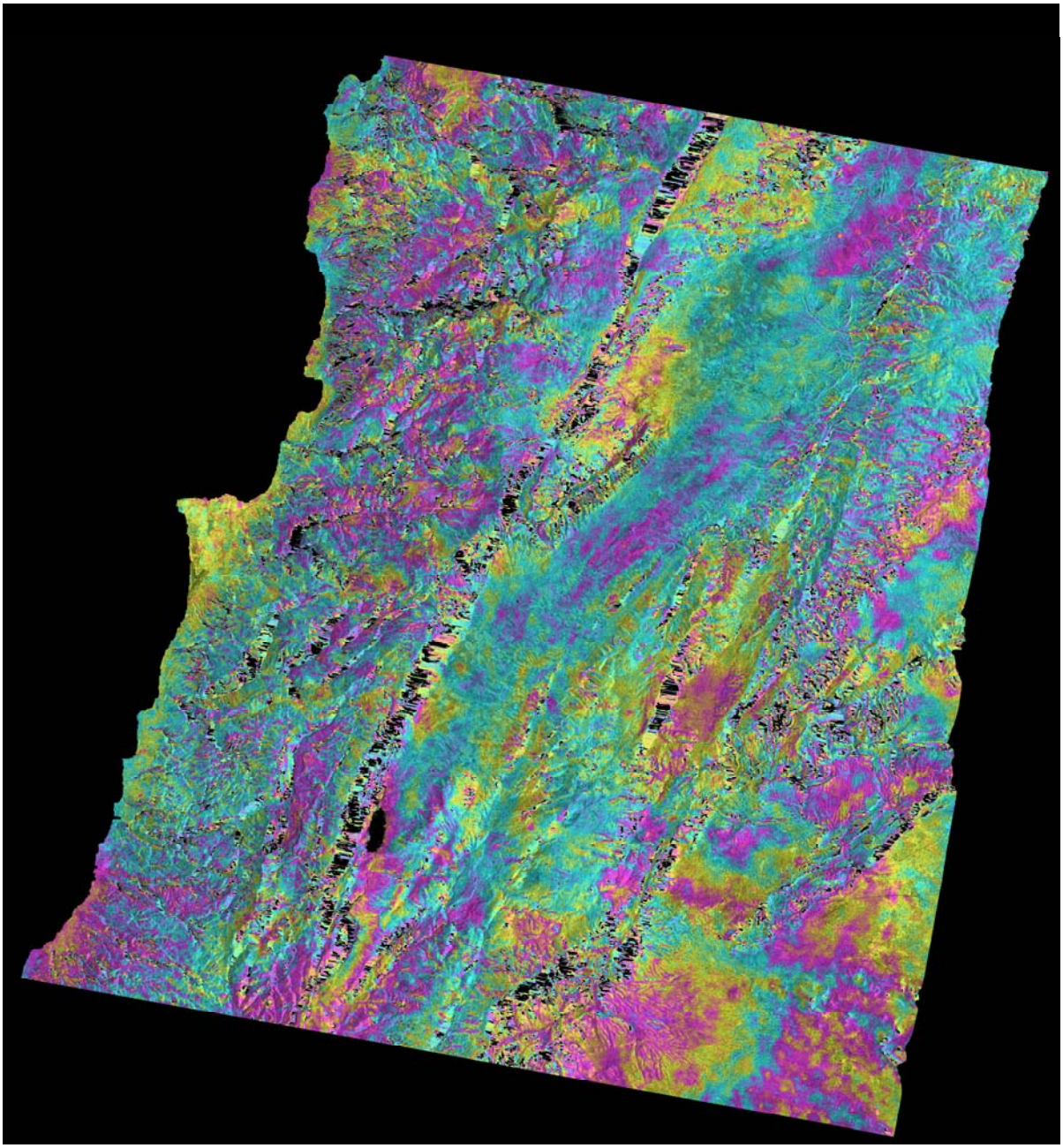

Figure 7.5. Differential interferogram (e120607_e200934.unw_dif), showing phase due to deformation, the time interval between the two images is one day.

In the second phase of processing, an Interferometric Point Target Analysis (IPTA) was conducted. Since all the available data would be used in the processing, and due to storage capacities, three areas were selected for the analysis: Hammana and Aaqoura in Lebanon, and Bloudan in Syria. These three areas were selected because they experienced large MM (**Figure 7.6**). It is essential to say that the phase model used for IPTA is the same as conventional interferometry. As mentioned before, the unwrapped interferometric phase ϕ_{unw} is expressed as the sum of topographic, deformation, atmospheric phase, and phase noise (or decorrelation) terms that can be stated in the following equation:

$$\phi_{unw} = \phi_{topo} + \phi_{def} + \phi_{atm} + \phi_{noise}$$

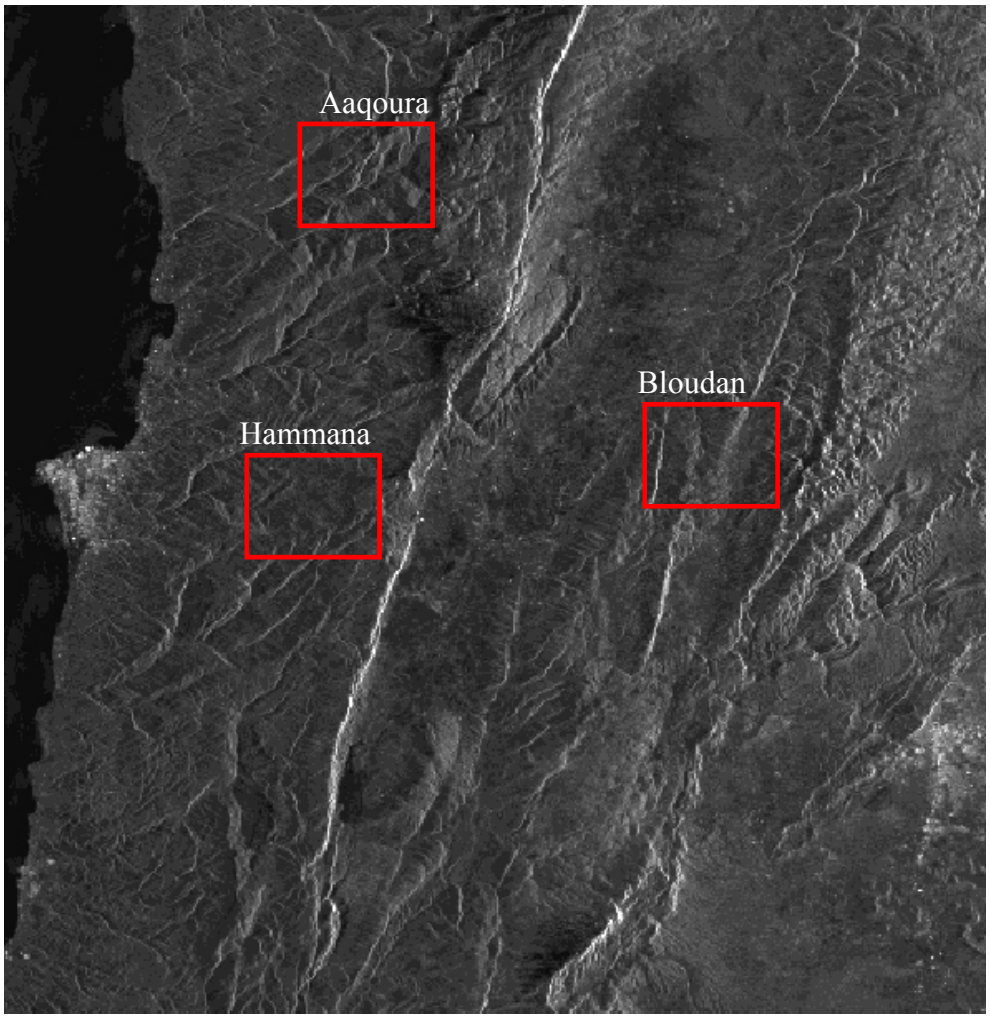

Figure 7.6. The three selected sites for IPTA processing.

Figure 7.7 shows utilized processing steps of the IPTA approach. Data input is step one in this processing. The multiple co-registered SLCs and their related ancillaries, the IPTA "itab", and the DEM are the three main inputs to the IPTA. The multiple SLCs and their related ancilliary data are prepared, linked to the working directory and the study area is selected (Annex 2). The SLC data are then corigestered and the offsets are defined. The DEM is geocoded multilook (mli) parameter files and

transformed to the SLC geometry (Annex 2). An IPTA tab "ASCII" file defining the interferometric pairs that will be investigated is then created (Annex 3).

In the second step, a point target candidate list is generated using the mean to standard deviation ratio with a specified threshold (Annex 4-a). The third step corresponds to selection of data points; this is done by evaluating the spectral correlation function and selecting points from the spectral diversity results (Annex 4 - b). In the next step (Step 4) differential interferograms are calculated. The differential interferograms are calculated by subtracting simulated (from DEM) unwrapped phases from the complex valued interferograms (**Figure 7.8a**). This is done for each interferometric pair defined in the itab and for each point defined in the point list (Annex 4-c). The unwrapped interferometric phase is estimated from the currently available knowledge on sensor (e.g., baseline), scene topography, linear deformation rates, and heterogeneity in the atmospheric path delay. At this level, the differential interferograms may look smooth or very noisy, this depend on the accuracy of the assumed parameters, the quality of the candidate points, baseline, etc..

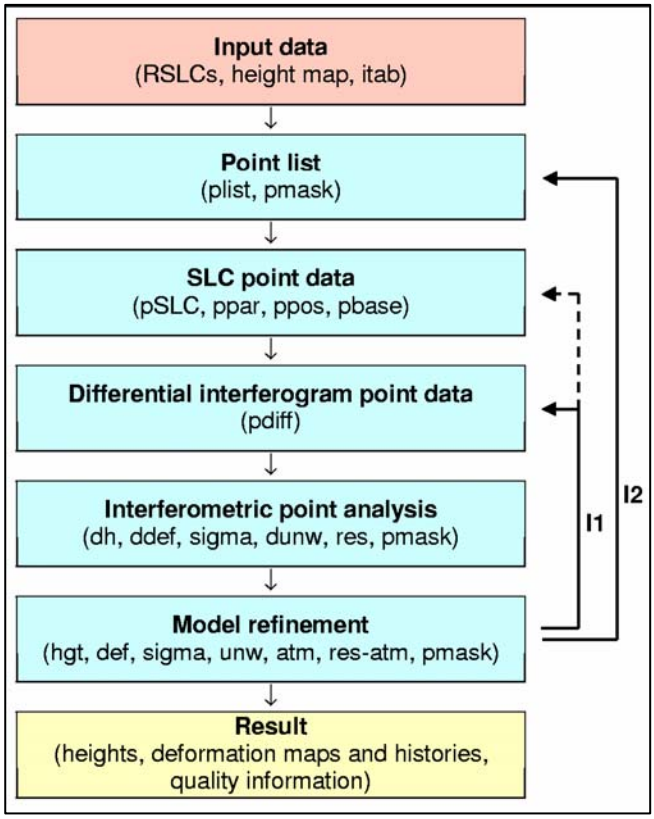

Figure 7.7. Simplified flow diagram showing IPTA processing approach (Werner *et al.*, 2003).

Step five starts by analyzing the stack of differential interferograms. In an initial run, the input provided is a point data stack of complex valued differential interferograms (**Figure 7.8b)**. There are different methods to run this regression. It can be done by running a quality control for each point in order to make an evaluation based on the phase standard deviation of the differential interferometric phase (pdiff) from the selected 2-D regression model of pairs of nearby points (Annex 4-d). Good/bad points, i.e. points with a phase standard deviation smaller/larger than the indicated threshold, are accepted/rejected. The same methodology can be utilized by

running def_mod_pt and multi_def_pt (**Figure 7.9**, Annex 4-e); the none-zero values are only assigned to points with a quality above the indicated threshold. The results from the regression analysis are used to improve and update the model (Model refinement, step six). Model refinement constitutes of height corrections, linear deformation rate corrections, point quality and atmospheric corrections. Concerning the height corrections, it is important to notice that the heights correspond to the scatterer location (phase centre) which may significantly deviate from the local terrain height. Some scatterers may be on top of buildings while others are at ground level. This also introduces significant point to point differences in the interferometric heights. This is taken into account when filtering or interpolating point based interferometric heights (IPTA user guide). The height corrections are added to the height used in the simulation (f-Annex 4). After running two height iterations (g-Annex 4), the deformation estimates in the last iteration were used to make differential interferograms so that it accounts for both topography and deformation (h-Annex 4). Then different iteration were used to estimate noise phase and atmospheric phase, this done by applying spatial and temporal filtering (i-Annex 4).

Figure 7.8. Differential interferograms of Bloudan area (IPTA processing).
(a) is based only on the SRTM heights (and initial baseline estimate). While (b) includes the DEM after the height corrections (from the first iteration of the IPTA regression), Hence the latter (b) is much flatter in terms of phase. The time span between the two scenes is about 9 months, and the perpendicular baseline is ~180 meters.

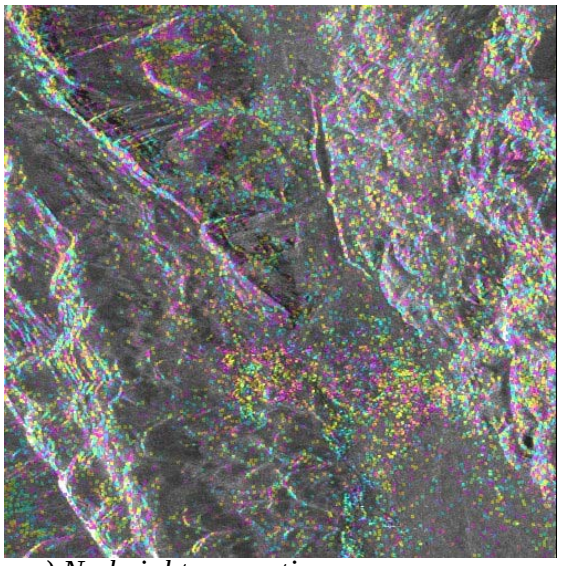

a) No height correction

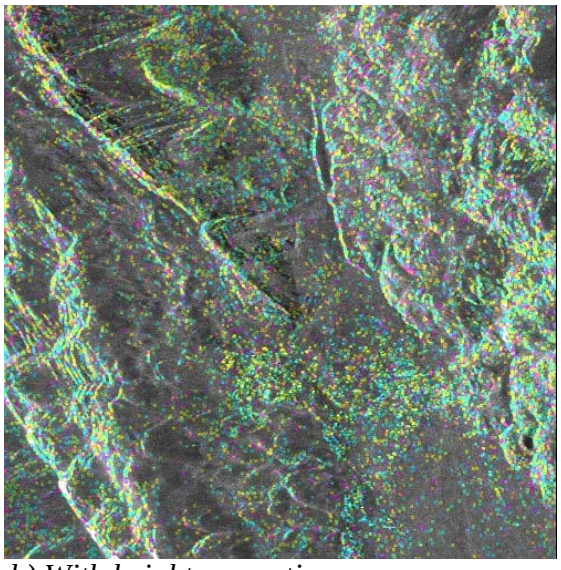

b) With height correction

Figure 7.9. Two dimensional regression analysis of differential interferometric phase difference of two points in a stack of 49 ERS interferograms.

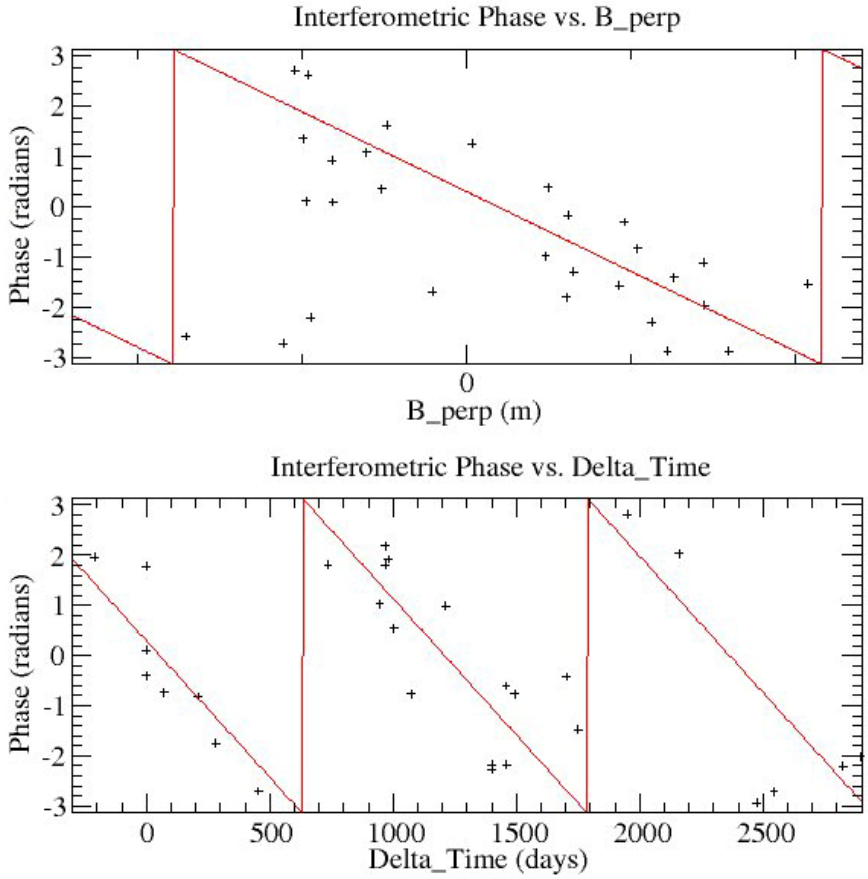

2.5. Preliminary results and discussion

All the data processing was done at the Geological Department of the Missouri University in the United States, under the supervision of Dr. Francisco Gomez. The ERS imageries purchase was supported by an NSF grant *(EAR-0439021).* It is also obvious that this present chapter is still a learning and testing step of this sophisticated technique. The InSAR application on the data sets enabled to produce a DEM of planimetric resolution 20m and altimetric accuracy of ± 20m (**Figure 7.10**). In fact the measurement of slope deformation caused by mass movement was not successful, due to the rugged topography and the looking angle. Since ERS satellites typically have a depression angle of about 23 degrees from horizontal, the look vector is rather steep (67 degrees from vertical). Hence, SAR is more sensitive to vertical motions than horizontal ones. That is, a larger horizontal motion is required to change the length of the look vector by the same amount than a smaller vertical displacement would. Other platforms with different incident angles could be tested for these types of deformations. Furthermore, the interferograms resulting from the IPTA processes lose coherence over time intervals longer than few months. Hence, it will be necessary in the future to focus on pixels that represent stable scatters, or to start by using first the IPTA with Single_Look_Complex images and then unwrap them through Interferometric SAR Processing to obtain spatially coherent interferograms. This might make the IPTA processing faster, more reliable (it does not have to use

time series to unwrap) and lead to find the baseline- and time-dependent components more precisely.

Figure 7.10. The Digital Elevation model deduced from the radar interferometry.

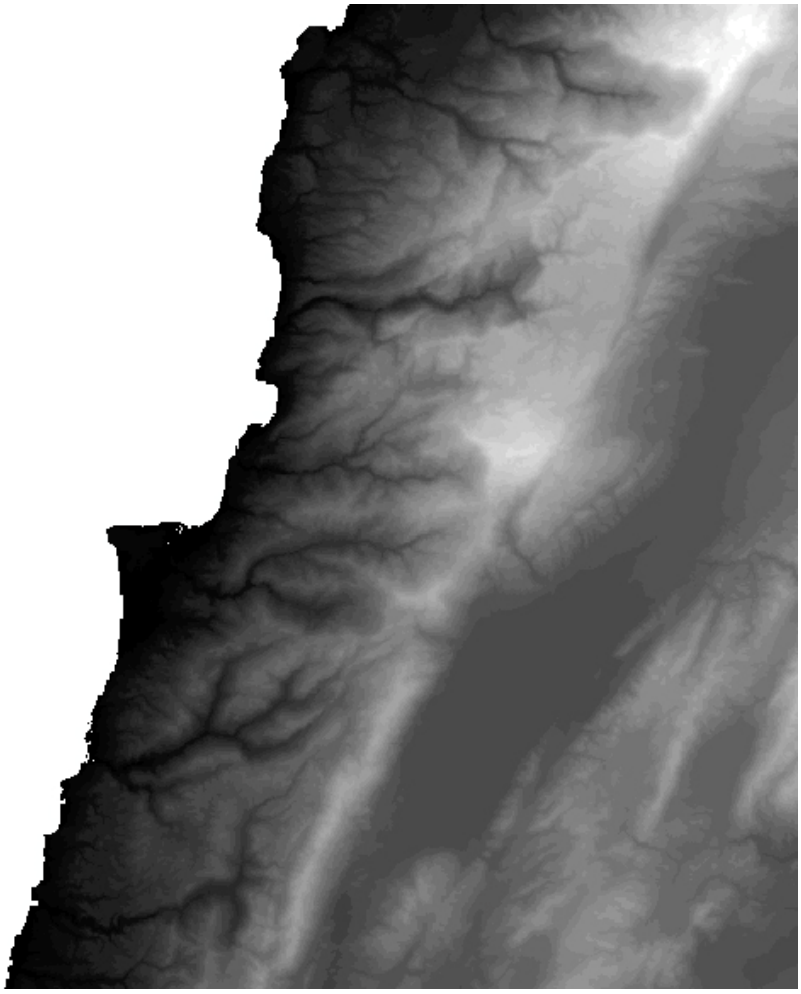

3. Global Positioning System (GPS)

3.1. Background

GPS is a radio navigation, timing and positioning system with a wide set of applications. It has become a valuable complement or extension to the conventional surveying methods (theodolite, tapes, total stations, etc). By tracking the electromagnetic waves that are sent continuously to the earth by satellites, the system can obtain the 3D coordinates (φ, λ, h or x, y, z) of any location. Field surveys are usually carried out within a frequently given period. The results are discontinuous over time, and related to the cumulative movements of the surface points.

The accuracy required for the measurement of mass movements displacement should be, in many cases, at least in the order of centimeters (Gili *et al.*, 2000). Therefore, the basic question that arises is whether the satellites orbiting 20200 km above the earth can be used to measure coordinates or displacement of landmark points located at the ground surface with centimeter accuracy. Moreover, the GPS can give the possibility of determining the relative position of points at centimetric and/or millimetric accuracy by means of fast survey operations. The application of this

technique in the so-called kinematic mode that consists in moving continuously one receiver with respect to a reference fixed station, allowing the description of the terrain surface by measuring the coordinates of points distributed on a high density irregular grid. Moreover, Static and Fast Static GPS mode provide an efficient means for determining the position at millimetric level of precision of marker points distributed along the area of interest. Continuous observations of landslide surface displacement may be performed by means of GPS permanent station monitored from a remote control centre, and the possibility of automating the main GPS operational steps (observation, collection, downloading and processing) make it possible to control landslide activity in real time.

3.2. GPS setting

Being one of the classically known areas affected by a major landslide and several other failure phenomena **(Figure 7.11)**, the Hammana region was selected in an attempt to compare the landslide conditions over time, to measure the speed, direction of the movement and to correlate the result with interferometry data (once finished).

The GPS network used in this study includes one local continuous GPS station (LAUG) located in Jbail (Mount Lebanon), a reference station and twelve survey monuments. We choose to distribute the twelve GPS monuments in order to cover the entire landslide in the form of four profiles. Each profile consists of three monuments **(Figure 7.12)**. Each reference station was mounted on top of the cliff and above the slide in a relatively stable area (**Figure 7.12)**. Additionally, it is important to mention that obstructions have limited the number of the monitoring GPS installations. The monuments at the thirteen survey sites consisted of 10 cm steel pins cemented into bedrock **(Figure 7.13a).** We distributed the sites in order to facilitate 2-D analysis of the resulting velocities. We used two sets of Trimble 5700 receivers with Zephyr Geodetic antennae atop fixed-height antenna masts in order to reduce uncertainty owing to antenna setup **(Figure 7.13b)**.

3.3. GPS campaigns

It is well known that the accuracy of the GPS based system is limited by the satellite geometry and by systematic errors such as multipath, weak satellite geometry, etc. Thereof, in order to attain good accuracy of the readings, each point was observed for two hours using one GPS set. While the other GPS set was kept observing continuously during the time span of the campaign. Hence, each campaign took four days to complete the observation of the twelve points.

Moreover, monument installation was done in September 2005. Until the time of writing of this chapter, only two campaigns were raised. The first campaign took place in April 2006, while the second was in November of the same year. The third campaign is planned in April 2007. **Therefore, NO results have been achieved till now, since the accumulation of data is not enough to perform any interpretation.**

Figure 7.11. The several failure phenomena in Hammana.

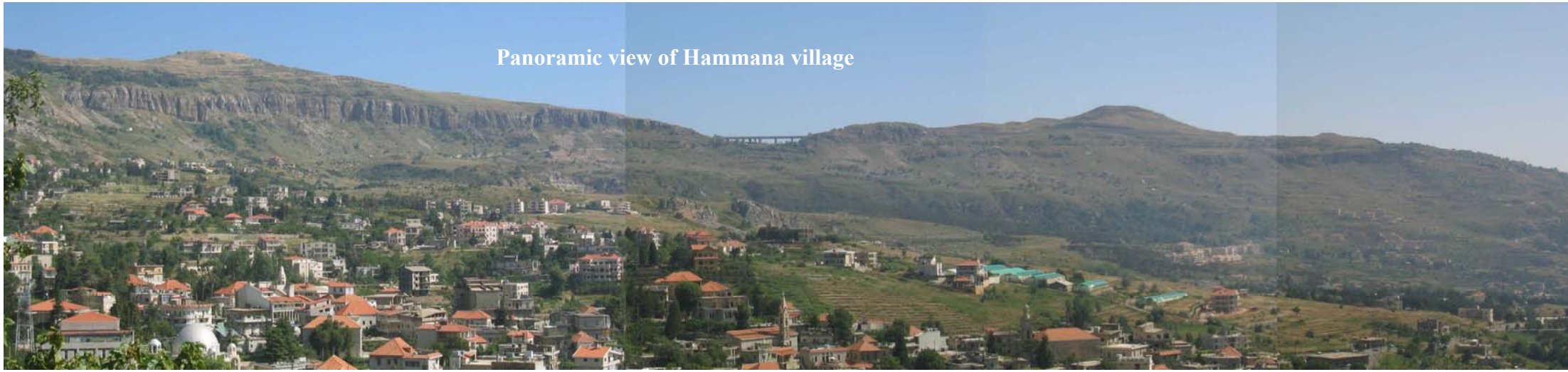

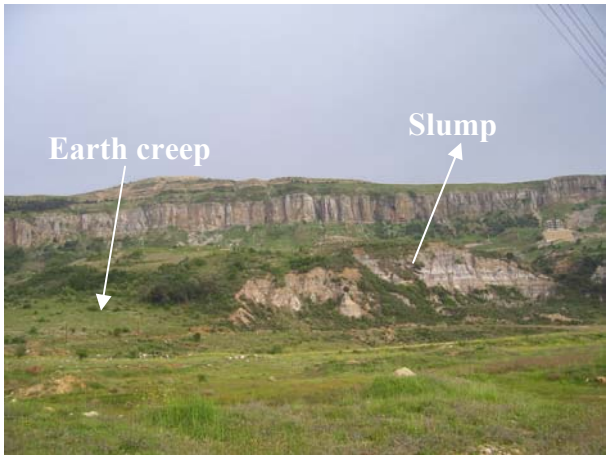

Figure 7.12. Distribution of the GPS monuments in Hammana.

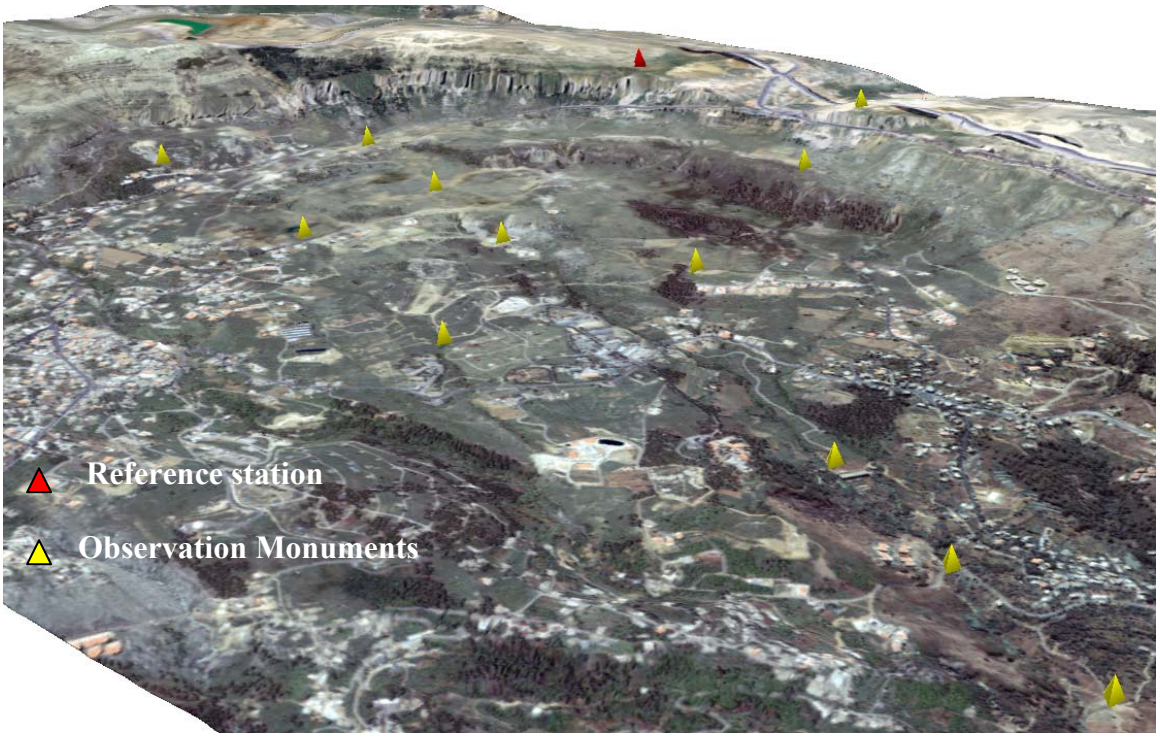

Figure 7.13. Description of the GPS survey monuments setting.

a) Drilling to insert the steel pin

b) Trimble 5700 set description

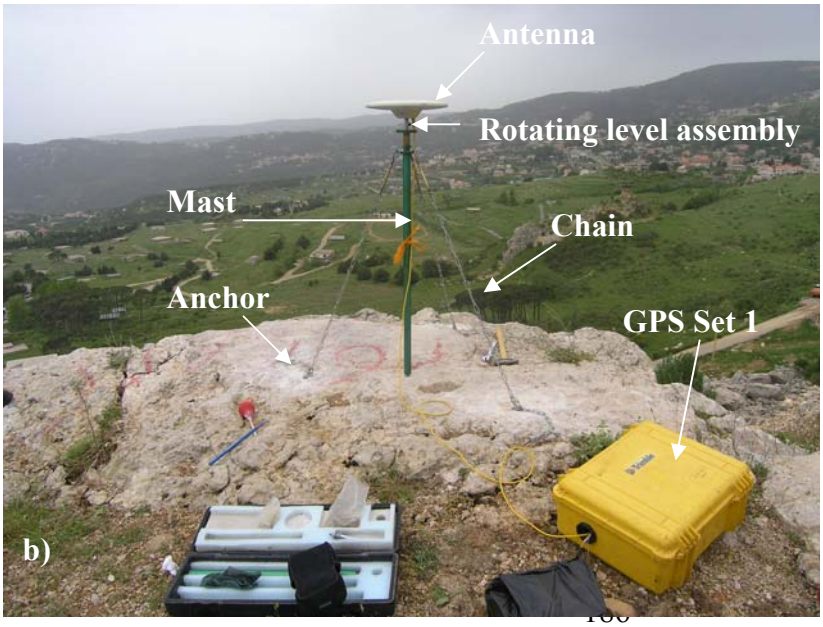

4. Conclusion

This chapter has tackled with different procedures for monitoring mass movement activity. Out of these techniques the radar interferometry and Global Positioning System (GPS) were tested. It is obvious that we are still in the preliminary phase of testing and learning the radar interferometry techniques, especially that the whole work was done in a span of one month during a visit to Missouri University in the United States. There was difficulty to calculate the deformation rate due to MM through InSAR processing due to rugged topography, atmospheric effects and the ERS incident angles. Nevertheless, a DEM of ± 20m altimetric accuracy was produced. Though the IPTA techniques enabled to use additional imageries with large baseline, the interferograms lost coherence overtime span longer than few months. Other manipulating procedures and available imageries in the archive should be tested in the future.

On the other hand, the accumulation of data in the two conducted GPS campaigns in Hammana area did not give a clear image of the movement and its velocity. At least two other campaigns should be raised in order to get results.

GENERAL CONCLUSION

This work is the first of its type in Lebanon on the topic of mass movements at regional scale (1:50,000) using remote sensing and GIS techniques. The adopted approaches can also serve research requirements and management needs in many other Mediterranean countries sharing similar geoenvironmental characteristics, and/or several developing countries worldwide with limited amounts of detailed spatial data and money. They considered the extraction of diverse types of mass movements (MM) from remote sensing data with various resolutions and diverse processing techniques, the establishment of univariate and bivariate relationships between MM occurrence and different terrain parameters (either preconditioning or triggering), mapping of MM susceptibilities/hazard within the studied area, producing quantitative volumetric maps of block falls as well as monitoring of MM activity.

1. Main obtained results

■ Extraction of mass movements (MM) from remote sensing data

The conducted study proves the efficiency and usefulness of applying specific processing treatments on satellite imageries with medium and high spatial resolutions in detecting diverse types of mass movements (MM). By a decreasing order, the following accuracy levels (AL) can be distinguished: **3D anaglyph SPOT4** with AL varying between 64 and 69% for detecting rock/debris falls and landslides, respectively; **SPOT4 image (10 m)** having an AL reaching 62-63% for both MM types; and the **pan-sharpened Landsat TM-IRS (6 m) improved by applying a principal component analysis (PCA)** and showing a quasi-similar accuracy level (60-62%).

Other treatments applied on Landsat TM (with medium spatial resolution - 30 m) like the constitution of false color composites FCC, the merging with satellite imageries of high resolution (IRS – 6 m), and the application of principal component analysis can substantially contribute to the detection of MM with accuracies levels oscillating between 51 and 57%. Even though the minimum visual interpretation error was obtained with 3D anaglyph SPOT4, good results can be attained using Landsat TM images once coupled with specific techniques (pan-sharpen and PCA). These results are of high importance in several countries facing the dangerous risk caused by mass movements due to the low cost of Landsat TM imageries, once compared with high and very high resolution imageries. In addition, remote sensing data can serve mapping mass movements (MM) over extensive areas, especially in the rugged mountainous karstic landscapes frequently distributed in the Mediterranean region.

The errors in interpretation fluctuate not only according to the processing technique, but also due to the difference in MM type. They are minimal once 3D anaglyph SPOT 4 is considered varying between 31% (landslides), 36% (rock and debris falls) and reaching 46% in the case of earth and debris flows. Moreover, 3D anaglyph SPOT4 allows the detection of earth flows which is not possible with all applied treatments described previously. These errors increase to a maximum of 49% if false color composite (FCC) RGB 357 Landsat TM is treated for the detection of landslides, while they attain 52% once rock and debris falls are sensed. These errors are due to very complex terrain characteristics or confusions in visual interpretation process. The latter is complicated and even with well trained experienced investigators, misdetection exists inevitably. This reinforces the necessity of validating the

obtained results by satellite imageries of medium and high resolutions in the field, or using very high resolution imageries such as IKONOS (1 m), Quickbird (0.67 m) or others.

- **Establishing GIS relationships between MM occurrence and terrain parameters**

This study demonstrates also that GIS bivariate and univariate statistical analysis allows exploring dual relationships between MM and the seventeen considered terrain parameters (elevation, slope gradient, slope aspect, slope curvature, lithology, proximity to fault line, karst type, distance to quarries, soil type, distance to drainage line, distance to water sources, rainfall quantity, land cover/use, proximity to roads, seismic events, floods and forest fires), and detecting the most significant ones. In this context, **lithology is the predominant parameter in inducing mass movements, since it shows the highest correlation with other parameters (7 times at 1% level of significance and 3 times at 5%).** The correlation is strong (1% significance level) with proximity to faults, karst type, distance to quarries, soil type, distance to drainage line, distance to water sources (springs), and existence of floods, and is of less strength (5%) if slope curvature, proximity to roads and seismic events are considered.

Other parameters have an influence on activating MM but with diverse degrees of effect. **Among these, two parameters - soil type and distance to water sources (springs) - are correlated 7 times with other parameters (at 1% and 5%).** It was expected that soil type can greatly influence the occurrence of mass movements, and this finding was similarly proved in other studies. However, **the most important fact considered once testing the GIS bivariate correlations between parameters was the integration of distance to water sources (springs) as a reflection of the effect of groundwater in inducing MM**. This effect was not studied in most similar studies conducted at regional scale. It was shown in this work that the outlets of springs may provoke MM under certain conditions. The other considered parameters have certainly an influence on MM occurrence, but this influence was minimal in some cases due to the unavailability of data reflecting more the power of these parameters (e.g., rainfall quantity was used instead of rainfall intensity).

- **Mapping of MM susceptibility/hazard maps**

Depending on the results obtained through detection of MM from remote sensing data and exploration of GIS bivariate and univariate statistical correlations, a newly mathematical decision making method was proposed **– Valuing Analytical Bi-Univariate method (VABU) – that enables mapping (1:50,000 cartographic scale), for the first time, of MM susceptibilities and hazards for (3750 km^2) 36% of the Lebanese total area**.

The used method (VABU) considers two level-weights, allowing a better reflection of the local conditions than other statistical methods – Valuing Accumulation Area (VAA) (depending on one level weight) and Information Value (InfoVal) (requiring detailed measurements of MM areas) methods. **The agreement between MM susceptibility maps produced through these three methods oscillates between 38% and 47.5%, while that linking hazard maps ranges from 36.5% to 44%.** This indicates that the adoption of an appropriate methodology of analysis and modeling is a major basis towards elaborating reliable maps. **These maps were validated in the field, with accuracy levels ranging from 52.5% (VAA method), 67.5% (InfoVal method) and 77.5% (VABU method).**

The high to very high susceptibilities cover 28% of the studied region, whereas 37% is characterized by the medium susceptibility class. This indicates the necessity of immediate action or protecting dangerous areas (high and very high susceptibilities). It is done through implementing specific mitigation measures, and at the same time applying prevention and planning for regional land use construction in the areas under medium susceptibilities, otherwise, these areas can change quickly to a higher more dangerous level. The beneficiaries of such maps are seen as researchers, universities, geotechnical engineers, decision makers, ministries and non-governmental organizations that are involved in land management. Thus, our proposed method can be adopted for predictive mapping of MM susceptibility/hazard in other areas in Lebanon and may be easily extrapolated using the functional capacities of GIS. It can be used also in other Mediterranean countries sharing similar geoenvironmental characteristics. It will be interesting also to test its feasibility in developing countries constrained by availability of money and time.

- **Quantitative mapping of the volume of block falls**

In addition to MM susceptibilities/hazard maps, **decision-tree models were built in the area for mapping the volume of block falls in the frame of GIS**. Such mapping was unavailable not only in Lebanon, but also in many other countries, since emphasis worldwide was put on landslide research rather than other types of mass movements. Moreover, most MM maps are produced with classes of importance level (very high, high, medium, low and very low) either for susceptibility, hazard or risk; and omitting exact values of MM volumes (m^3).

Seven decision-tree models were constructed in the context of this study based on different input terrain parameters and processing techniques (pruned and unpruned). **The most powerful one was the regression unpruned (exploratory) tree-model based on all considered parameters explaining correctly 86% of the variance in the trained data.** Once pruned, this model classifies 50% in block falls volumes by selecting just four parameters (lithology, slope gradient, soil and land cover/use). The unpruned model built using only 4 geological parameters (lithology, soil type, proximity to fault line, and karst type) seems interesting, since it is created using similarly 4 parameters, but it has a higher predictive accuracy (68%).

The produced predictive quantitative block falls' maps at a scale of 1:50,000 can be used to prioritize the choice of specific zones for further measurement and modeling. They are extremely useful fitting management needs and helping in the adoption of measures to reduce the occurrence of harmful block falls, specifically in 18% of the studied area with block falls' volumes exceeding 2000 m^3.

- **MM monitoring using radar interferometry and GPS**

This study has dealt also with monitoring MM activity using radar interferometry and GPS. Two process techniques, i.e. InSAR and permanent scattrers, were utilized to test the displacement in areas that have witnessed major MM. In the first technique, it was difficult to calculate the deformation due to the rugged topography and the ERS incident angles. Nevertheless, this technique allowed the production of DEM with ±20 m altimetric accuracy. In the permanent scattrers techniques, the interferograms lost coherence over time span longer than few months. Other manipulating procedures should be tested in the future in order to detect the deformations.

On the other hand, two GPS campaigns were conducted in the frame of this thesis for monitoring purposes at seasonal basis interval. The accumulation of GPS data readings is requested in order to obtain clear image of the movement if it exists. Therefore, the exposed is only our campaign settings and the distribution of observation monuments.

2. Thesis publications

A certain number of publications have been produced in the context of this work, counting one or more articles for each chapter of the thesis as follows: chapter I [one article submitted], chapter III [2 articles published], chapter IV [one article published], chapter V [2 articles under final stages of preparation], and chapter VI [1 article under final stages of preparation]. Up to date, 3 articles are published in international scientific journals (attached at the end of the thesis), and all published, submitted and prepared articles are summarized as follows:

(1). Abdallah, C., Chorowicz, J., Bou Kheir, R., Khawlie, M., 2005. Detecting major terrain parameters relating to mass movements' occurrence using GIS, remote sensing and statistical correlations, case study Lebanon. ***Remote Sensing of the Environment***, 99, 448-461.

(2). Abdallah, C., Khawlie, M., Bou Kheir, R., 2006. Interprétation visuelle des images satellitaires (Landsat TM, SPOT 4, IRS et IKONOS) et mouvements de masse – cas d'étude au Liban. ***Revue Photo-interprétation***, 1, 3-10.

(3). Abdallah, C., Chorowicz, J., Bou Kheir, R., Dhont, D., 2007. Comparative use of processed satellite images in remote sensing of mass movements: Lebanon as a case study. ***"International Journal for Remote Sensing"***, under press.

(4). Abdallah, C., Chorowicz, J., Bou Kheir, R., Khawlie, M., Dhont, D., 2007. A review of mass movement hazard analysis in the Mediterranean region. ***"Geomorphology"***, submitted.

(5). Abdallah, C., Bou Kheir, R., Chorowicz, J., Khawlie, M., 2007. A GIS decision-tree model for predictive volumetric mapping of block falls', Lebanon. To be submitted in ***"Journal of Soil and Water Conservation***"**.**

(6). Abdallah, C., Chorowicz, J., Bou Kheir, R., Khawlie, M., Dhont, D., 2007. Mass movements' susceptibilities and hazard mapping using a GIS valuing bi-univariate method (VABU), Lebanon. To be submitted in ***"Geology"***.

(7). Abdallah, C., Chorowicz, J., Bou Kheir, R., Khawlie, M., 2007. Comparative evaluation of statistical methods (VABU, VAA and InfoVal) for mapping MM susceptibilities and hazards in Lebanon. To be submitted in ***"Environmental Management".***

In addition to these articles in international scientific journals, oral communications and posters of the thesis work were presented in international conferences. These interventions are summed up as follows:

(a). Abdallah, C., Chorowicz, J., Khawlie, M., 2004. *Assessment of hazard zonation using Remote Sensing and GIS.* The 14th international symposium on remote sensing and development. GORS, Damascus, Syria, 27-30/9/2004 [oral presentation + published abstract].

(b). Abdallah, C., Bou Kheir, R., Chorowicz, J., Dhont, D., 2006. *Comparative satellite image analysis for mass movement detection: Lebanon as a case study*. European General Assembly (EGU), 2-7/4/2006, Vienna, Austria. Geophysical Research Abstracts, European Geosciences Union, vol. 8, 01289, 2006, SRef-ID: EGU06-A-01260, session NH3.03 – Slope movements in weathered materials: recognition, analysis and hazard assessment, p. 346-347 [oral presentation + published abstract].

(c). Abdallah, C., Bou Kheir, R., Khawlie, M., 2007. *Exploratory GIS and RS analysis for the development of statistical correlations between environmental parameters and mass movements' occurrence*. EUGEO: International Conference on the Geographical of Europe. Amsterdam, 20-23/8/2007 [accepted abstract].

This work was presented also in the 10th anniversary of Franco-Lebanese CÈDRE (Coopération pour l'Évaluation et le Développement de la Recherche) **program, held at the prime minister governmental Lebanese palace in 2 June 2006, and received an award for good research and publications**. A poster was also exposed at this event.

3. Perspectives

This work can be further improved in the future, either by ameliorating the modelling approach using other remote sensing/GIS data or other processing techniques, or reducing certain uncertainties in the results. The following improvements and predictions can be envisaged:

(i). Integration of other parameters such as rainfall intensity, vertical and lateral displacement of rocks, dip direction, spacing of discontinuities, roughness, weathering, rock mass strength, etc. that can improve modeling and explain additional variance in the trained data. Future research topic will be based on possibilities of gathering these parameters from satellite imageries like hyperspectral imageries, GIS data and field measurements. This will enhance the establishment of relations between these parameters and MM occurrence, and their incorporating in diverse models for mapping MM susceptibilities and hazards or predicting volumes of block falls.

(ii). Updating and amelioration of existent old data, e.g., geological maps, for a better differentiation between alternate sands and clays shown as one set on these maps characterizing the Neocomian-Barremian formation (C1). This differentiation can allow a better reflection of local conditions, since sands and clays have different behaviour against MM occurrence.

It is interesting, depending on the obtained results, to continue the conducted study and explore several research topics at various axes:

(a). Transfer the modelling approaches adopted in this study to all the country and, therefore, produce maps reflecting dangerous locations of MM occurrence, necessitating immediate interventions.

(b). Test the concept of decision-tree modelling for other mass movement types (e.g. landslides and earth flows) and producing quantitative maps of the volumes of these failures.

(c). Seek finer scales maps (1:5,000 to 1:20,000) of MM susceptibilities and hazards that can be useful for municipalities in Lebanon for managing problems of slope instability and planning infrastructure and development.

(d). Produce risk maps at detailed scales in specific locations of the country (e.g., Hammana) witnessing unstable terrain and dangerous agents. These risk maps will integrate, in addition to the preconditioning and triggering parameters, socio-economic data relevant to the vulnerability of buildings and other properties that can be extracted from remote sensing data (aerial photographs or very high resolution imageries).

(e). Test the capability of other methodologies, like fuzzy logic classification, on predicting the distribution and magnitude of diverse types of mass movements. The results will be also compared with those obtained in this study, for precision and reliability inspection.

(f). Give more significance to role of changing levels of ground water versus impacts on MM. Be it in inducing instability in the overlying surficial sloping mass, or in causing subsidence, or collapse that may trigger different forms of failure.

(g). Work on ameliorating radar interferometry obtained results in this study through an already planned visit to the Missouri University (USA) for postodoctoral research (2008).

(h). Complete at least two other GPS surveys in Hammana area (Mount Lebanon) to get a comprehensive image of the degree of movement. Allocate new GPS monuments in other hazardous areas, like Aaqoura.

References

Abdallah, C., 2001. Lebanon country paper on land resources management. Regional workshop on land resources information systems in the Near East, FAO, Cairo, Egypt, 3-6/9/2001. FAO website: http://www.fao.org/landandwater/swlwpnr/swlwpnr.htm

Abdallah, C., Shaban, A., Khawlie, M., 2002. Utilization of remote sensing and GIS to assign a model for infiltration capacity and water potentiality in Occidental Lebanon. Workshop on mathematical models for sustainable water resources development and their role in decision-making, Rabat, Morocco, 18-20/12/2002.

Abdallah, C., Bou Kheir, R., Khawlie, M., 2006a. Building up an infiltration capacity model using GIS and remote sensing in Occidental Lebanon. Geological Society of America (GSA) annual meeting and exposition, Philadelphia, Pennsylvania, USA, 22-25/10/2006 [poster].

Abdallah, C., Bou Kheir, R., Khawlie, M., Faour, G., 2006b. Comparative analysis of drainage networks extracted from DEMs and conventional approaches in Lebanon. *Lebanese Science Journal*, 7(1), 49-62.

Abbot, B., Bruce, I., Savigny, W., Keegan, T., Oboni, F., 1998. A methodology for the assessment of rock fall hazard and risk along linear transportation corridors. In D. Moore and O. Hungr (eds.), Proceedings of the 8th IAEG Congress. Balkema, Rotterdam, 1195-1200.

Abou Haidar, F., 1997. Quarries, Part 1: The Problem - The Levant, August 20.

Abu El-Ainein, H-S., 1973. Essays on geomorphology of Lebanon, Beirut, 45p.

Ambraseys, N.N., Barazangi, M., 1989. The 1759 earthquakes in the Bekaa valley: Implications for earthquake hazard assessment in the eastern Mediterranean region. *Journal of geophysical research*, 94(B4), 4007-4013.

ACL, 1973. Atlas climatique du Liban. Tome 1. Service météorologique, Ministère des affaires publiques, Beyrouth, Liban, 40p.

ACL, 1982. Atlas climatique du Liban. Tome 1. Service météorologique, Ministère des affaires publiques, Beyrouth, Liban 31p.

Agili, F., Bartolomei, A., Casagli, N., Canuti, P., Catani, F., Ermini, L., Farina, P., Kukavicic, M., Mirannalti, M., Righini, G., 2004. Coupling traditional methods and new technology contributions to landslide risk assessment in the Arno river basin. In W.A. Lacerda, M. Ehrlich, S.A.B. Fontoura, and A.S.F. Sayao (eds.), Landslides: evaluation and stabilization. Balkema, Taylor & Francis Group, London, 151–155.

Aiello, V., Barile, A., Silvestri, F., Pescatore, T.S., Pinto, F., 2004. An application of a GIS based methodology for the seismic zonation of slope stability. In W.A. Lacerda, M. Ehrlich, S.A.B. Fontoura, and A.S.F. Sayao (eds.), Landslides: evaluation and stabilization. Balkema, Taylor & Francis Group, London, 327–335

Aker, N.F., 1980. Landslides in Lebanon. Proceedings of the 1st Arab Symposium on water resources, ACSAD, Damascus, 18-27 November 1978, 59-84.

Alexander, D.E., 1991. Applied geomorphology and the impact of natural hazards on the built environment. *Natural Hazards*, 4(1), 57-80.

Al-Homoud, A.S., Masanat, Y., 1998. A classification system for the assessment of slope stability of terrain along highway routes in Jordan. *Environmental Geology*, 34(1), 59–69.

Almeida-Teixera, M.E., Fantechi, R., Oliveira, R., Gomes-Coelho, A., 1991. Prevention and control of landslides and other mass movements. Commission of the European Communities Report EUR 12918.

Ambraseys, N.N., Barazangi, M., 1989. The 1759 earthquake in the BeKaa valley: implications for earthquake hazard assessment in the eastern Mediterranean region. *Journal of geophysical research*, 94(4), 4007-4013.

Amaral, C., Furtado, A., 2004. Largescale quantitative landslide risk mapping at Favela da Formiga, Rio de Janeiro. In W.A. Lacerda, M. Ehrlich, S.A.B. Fontoura, and A.S.F. Sayao (eds.), Landslides: evaluation and stabilization. Balkema, Taylor & Francis Group, London, 293–296.

Anbalagan, R., 1992. Landslide hazard evaluation and zonation mapping in mountainous terrain. *Engineering geology*, 32, 269-277.

Aniya, M., 1985. Landslide susceptibility mapping in the Amahata river basin, Japan. *Ann Assoc Am Geogr*, 75(1), 102–114.

Antoine, P., 1977. Réflexions sur la cartographie ZERMOS et bilan de expériences en cours. *Bull Bur Rech geol min*, III (1-2), 9–20.

Antoine, P., Pachoud, A., 1976. Enseignements tirés de deux essais de cartographie systématique de glissements de terrain. *Bull. Liaison Labo. P. et Ch.*, n° spécial, 31-39.

Alonso-Sarria, F., Lopez-Bermudez, F., 1994. Rainfall time and space variability during short storms in south-east Spain. Geookodynamik Band XV, 261-278.

Atkinson, P.M., Massari, R., 1998. Generalised linear modelling of susceptibility to landsliding in the Central Alpennines, Italy. *Computers & Geosciences*, 24(1), 373-385.

Arora, M.K., Das Gupta, A.S., Gupta, R.P., 2004. An artificial neural network approach for landslide hazard zonation in the Bhagirathi (Ganga) valley, Himalayas. *International Journal of Remote Sensing*, 22, 559-572.

Ashkenazi, V., Preiss, W.J., Anderson, B., 1980. A geodetic terrestrial and space network. Survey review cumulative index, vol. 1, 117p.

Astaras, T., Kalathas, A., Oikonomidis, D., Lambrinos, N., Soulakellis, N., 1997. Delineation of landslides using GIS and digital image processing techniques on multi-temporal Landsat 5 TM images: a case study from the Pindus mountain, Greece. In A. Spiteri (ed.), Remote Sensing ’96-integrated applications for risk assessment and disaster prevention for the Mediterranean. Balkema, Rotterdam

Atkinson, P.M., Massari, R., 1998. Generalised linear modelling of susceptibility to landsliding in the Central Apennines, Italy. *Computers & Geosciences*, 24(4), 373–385

Augusto, F.O., 2004. Mass movements identification, modelling, analysis and mapping: some experiences in the southern of Brazil, Sao Paulo state. In W.A. Lacerda, M. Ehrlich, S.A.B. Fontoura, and A.S.F. Sayao (eds.), Landslides: evaluation and stabilization. Balkema, Taylor & Francis Group, London, 57-68.

Ayala-Carcedo, F.J., Cubillo-Nielsen, S., Alvarez, A., Domínguez, M.J., Laín, L., Laín, R., Ortíz, G., 2003. Large scales rock fall reach susceptibility maps in La Cabrera Sierra (Madrid) performed with GIS and dynamic analysis at 1:5.000. *Natural Hazards*, 30(3), 341–360.

Ayalew, L., Yamagishi, H., 2005. The application of GIS-based logistic regression for landslide susceptibility mapping in the Kakuda-Yahiko Mountains, Central Japan. *Geomorphology*, 65, 15–31.

Ayalew, L., Yamagishi, H., Ugawa, N., 2004. Landslide susceptibility mapping using GIS-based weighted linear combina-tion, the case in Tsugawa area of Agano river, Niigata Prefecture, Japan. *Landslides*, 1, 73–81.

Ayenew, T., Barbieri, G., 2005. Inventory of landslides and susceptibility mapping in the Dessie area, northern Ethiopia. *Engineering Geology*, 77(1–2), 1–15.

Babu, G.L.S., Mukesh, M.D., 2003. Risk analysis of landslides-a case study. *Geotech Geol Eng*, 21, 113–127.

Baeza, C., 1994. Evaluacion de las condiciones de rotura y de la movilidad de los deslizamientos superficiales mediante el uso de tecnicas de analisis multivariante, Ph.D. thesis, Technical University of Catalonia, Barcelona, Spain.

Baeza, C., Corominas, J., 2001. Assessment of shallow landsliding susceptibility by means of multivariate statistical techniques. *Earth Surface Processes and Landforms*, 26, 1251-1263.

Baillifard, F., Jaboyedov, M., Rouiller, D., Robichaud, G.R., Locat, P., Locat, J., Couture, R., Hamel, G., 2004. Towards a GIS-based rockfall hazard assessment along the Quebec City Promontory, Quebec, Canada. In W.A. Lacerda, M. Ehrlich, S.A.B. Fontoura, and A.S.F. Sayao (eds.), Landslides: evaluation and stabilization. Balkema, Taylor & Francis Group, London, 207–214.

Baldelli, P., Aleotti, P., Polloni, G., 1996. Landslide susceptibility numerical mapping at the Messina Straits crossing site, Italy. In K. Senneset (ed.), Proceedings of the VIth I.S.L., Trondheim, Norway, vol 1. Balkema, Rotterdam, 153–158.

Barbieri, M., Lichtenegger, J., 2005. Data processing in SAR interferometry. In K. Flectcher (ed.), Spaceborne radar applications in Geology: an introduction to imaging radar, and application examples of ERS SAR in geology and geomorphology. European Space Agency (ESA), The Netherlands, 3/1-3/8.

Barredo, J.I., Benavides, A., Hervás, J., van Westen, C.J., 2000. Comparing heuristic landslide hazard assessment techniques using GIS in the Tirajana basin, Gran Canaria Island, Spain. *JAG*, 2(1), 9–23

Basma, A.A., Kallas, N., 2004. Modeling soil collapse by artificial neural networks. *Geotech Geol Eng*, 22, 427–438

Bathurst, J.C., Crosta, G.B., García-Ruiz, J.M., Guzzetti, F., Lenzi, M.A., Aragues, S.R., 2003. DAMOCLES: debris-fall assessment in mountains catchments for local end-users. In D. Rickenman and C. Chen (eds.), Debris-flow hazard mitigation, prediction and assessment. Mill Press Science, Rotterdam, 1073–1083.

Bayes, A.J., Mackey, B.G., 1991. Algorithms for monotonic functions and their application to ecological studies in vegetation science. *Ecological Modeling*, 56, 135-159.

Baynes, F.J., Lee, E.M., 1998. Geomorphology in landslide risk analysis, an interim report. In D. Moore and O. Hungr (eds.), Proceedings of the 8th IAEG Congress, Vancouver. A.A. Balkema, Rotterdam, 1129–1136.

Bell, R., Glade, T., 2004. Quantitative risk analysis for landslides-examples from Bildurdalur, NW Iceland. *Nat Hazards Earth Syst Sci*, 4(1), 117–131.

Benech, C., 1994. Les récentes crues dans les Pyrénées-Orientales, Comparaison à l'aiguat de 1940. In J. Lavabre (éditeur), Les événements hydropluviométriques intenses récemment observés sur le Sud-Est de la France. Actes de la journée scientifique du 2 Juin 1994, Aix-en-Provence, Cemagref, 72-90.

Berardino, P., Costantini, M., Franceschetti, G., Iodice, A., Pietranera, L., Rizzo, V., 2003. Use of differential SAR interferometry in monitoring and modelling large slope instability at Maratea (Basilicata, Italy). *Engineering Geology*, 68(1–2), 31–51.

Berk, R.A., 2003. An introduction to ensemble methods for data analysis. UCLA Department of Statistics Technical Report.

Bernknopf, R.L., Campbell, R.H., Brookshire, D.S., Shapiro, C.D., 1988. A probabilistic approach to landslide hazard mapping in Cincinmati, Ohio, with applications for economic evaluation. *Bulletin of the Association of Engineering Geologists*, 25, 39-56.

Beven, K.J., Kirkby, M.J., 1979. A physically based, variable contributing area model of basin hydrology. *Hydrol Sci Bull*, 24, 43–69.

Beydoun, Z., 1972. A new evaluation of the petroleum prospects of Lebanon with special reference to the Pre-Jurassic. 18th Arab Pet. Cong., Algeria, 80(B-3).

Beydoun, Z., 1976. Observations on geomorphology, transportation and distribution of sediments in western Lebanon and its continental shelf and slope regions. *Marine Geology*, 21, 311-324.

Beydoun, Z., 1977. Petroleum prospects of Lebanon: re-evaluation. *American Association of Petroleum Geologists*, 61, 43-64.

Beydoun, Z., 1988. The Middle East: Regional Geology and Petroleum Resources. Scientific Press Ltd., London, 296p.

Beydoun, Z., 1997. Earthquakes in Lebanon: an overview. *Lebanese Science Bulletin*, 10(1), 43-64.

Bieniawski, Z.T., 1993. Classification of rock masses for engineering: the R.M.R. system and future trends. In Hudson, Brown, Fairhurst, and Hoek (eds.), Comprehensive rock engineering. Pergamon Press, UK.

Binaghi, E., Luzi, L., Madella, P., Pergalani, F., Rampini, A., 1998. Slope instability zonation: a comparison between certainty factor and fuzzy Dempster–Shafer approaches. *Natural Hazards*, 17, 77–97.

Binaghi, E., Boschetti, M., Brivio, P.A., Gallo, I., Pergalani, F., Rampini, A., 2004. Prediction of displacements in unstable areas using a neural model. *Natural Hazards*, 32, 135–154.

Blanc, R.P., Cleveland, G.B., 1968. Natural slope stability as related to geology, San Clemente Area, Orange and San Diego Counties, California. California Division of Mines and Geology Special Report 98, 19p.

Blanchet, G., 1966. Nouveaux aperçus sur le climat du Liban. *Hannon*, 1, 1-18.

Blank, J.P., 1971. The town that disappeared. *Reader's Digest*, 99, 86-90.

Borga, M., Dalla Fontana, G., Da Ros, D., Marchi, L., 1997. Shallow landslide hazard assessment using a physically based model and digital elevation data. *Environmental Geology*, 35(2/3), 81–88.

Borga, M., Dalla Fontana, G., Cazorzi, F., 2002. Analysis of topographic and climatic control on rainfall-triggered shallow landsliding using a quasi-dynamic wetness index. *Journal of Hydrology*, 268, 56–71.

Bou Kheir, R., 2002. Etude des risques d'érosion hydrique des sols par télédétection et SIG : application à une région représentative du Liban. Thèse de doctorat, Institut National Agronomique Paris-Grignon (France), 261p.

Bou Kheir, R., Girard, M-C., Shaban, A., Khawlie, M., Faour, G., Darwish, T., 2001a. Apport de la télédétection pour la modélisation de l'érosion hydrique des sols dans la région côtière du Liban. *Télédétection*, 2(2), 79-90.

Bou Kheir, R., Shaban, A., Girard, M-C., Khawlie, M., 2001b. Impact des activités humaines sur l'érosion hydrique des sols dans la région côtière montagneuse du Liban. *Sécheresse*, 12(3), 157-165.

Bou Kheir, R., Girard, M-C., Khawlie, M., **Abdallah, C.**, 2001c. Erosion hydrique des sols dans les milieux méditerranéens : une revue bibliographique. *Etude et Gestion des Sols*, 8(4), 231-245.

Bou Kheir, R., Shaban, A., Girard, M-C., Khawlie, M., **Abdallah, C.**, 2003. Caractérisation morpho-pédologique des zones karstiques du Liban. Sensibilité des sols à l'érosion hydrique. *Sécheresse*, 14(4), 1-9.

Bou Kheir, R., Cerdan, O., **Abdallah, C.**, 2006. Regional soil erosion risk assessment in Lebanon. *Geomorphology*, 82, 347-359.

Bou Kheir, R., Wilson, J., Deng, Y., 2007a. Use of terrain variables for predictive gully erosion mapping in Lebanon. *Earth Surface Processes and Landforms*, under press.

Bou Kheir, R., Chorowicz, J., **Abdallah, C.**, Damien, D., 2007b. Soil and bedrocks distribution estimated from gully form and frequency: a GIS-based decision-tree model for Lebanon. *Geomorphology*, under press.

Bowman, H.N., 1972. Natural Slope Stability in the City of Greater Woolongong. *N.S.W.Geol Surv Recs*, 14(2), 159–222.

Brabb, E.E., 1984. Innovative approaches to landslide hazard and risk mapping. Proceedings of the IVth ISL, Toronto, vol. 1, 307–324.

Brabb, E.E., Pampeyan, E.H., Bonilla, M.G., 1972. Landslide susceptibility in San Mateo County, California. US Geological Survey Miscellaneous Field Studies, Map MF-360, scale 1:62,500.

Breiman, L., Friedman, J.H., Olshen, R.A., Stone, C.J., 1984. Classification and regression trees. Belmont, CA, Wadsworth.

Breiman, L., 2001. Decision-tree forests. *Machine Learning*, 45(1), 5-32.

Brimicombe, A.J., 1993. Combining positional and attribute uncertainty using fuzzy expectation in a GIS. Proceedings GIS/LIS"93, Minneapolis, 1, 72-81.

Brimicombe, A.J., Bartlett, J.M., 1993. Spatial decision support in flood hazard and flood risk assessment: a Hong Kong case study. Proceedings of the third International Workshop on Geographic Information Systems, Beijing, 2, 93-106.

Browing, J.M., 1973. Catastrophic rock slide, Mount Huascaran, north-central Peru, 31 May 1970, American Association of Petroleum Geologists Buletin, 57, 1335-1441.

Bruckner, E., 1909. Die venezianischen Gletscher. In: A. Penck and E. Bruckner E. (eds.), Die Alpen im Eiszeitalter, Tauchnitz, Lipsia, 3, 954-1042.

Brunsden, D., 1999. Some geomorphological considerations for the future development of landslide models. *Geomorphology*, 30, 13–24.

Buchroithner, M.F., 1995. Problems of mountain hazard mapping using spaceborne remote sensing techniques. *Advanced Space Research*, 15(11), 57-66.

Budetta, P., Calcaterra, D., Santo, A., 1994. Engineering-geological zoning of potentially unstable rock slopes in Sorrentine Peninsula (South Italy). 7th Int. IAEG Cong.. Balkema, Rottecarrrdam, 2119-2126.

Bughi, S., Aleotti, P., Bruschi, R., Andrei, G., Milani, G., Scarpelli, G., 1996. Slow movements of slopes ineterfering with pipelines: modelling vs. monitoring. Proc. 15th Int. Conf. OMAE, Firenze.

Bulmer, M.H., Wilson, J.B., 1999. Comparison of Stellate Volcanoes on Earth's seafloor with Stellate domes on Venus using side scan sonar and Magellan synthetic aperture radar, Earth and Planet. Sci. Lett., 171, 277-287.

Burgmann, R., Rosen, P.A., Fielding, E., J., 2000. Synthetic aperture radar interferometry to measure earth's surface topography and its deformation. *Annu. Rev. Earth Planet Sci*, 28, 169-209.

Burrough, P.A., 1993. Soil variability: a late 20th century view. *Soil and Fertilizers*, 56, 529-562.

Calcaterra, D., de Luca Tupputi Schinosa, F., Fenelli, G.B., 2004. Rockfall hazard assessment at Mt. San Costanzo (Sorrento Peninsula, Italy). In W.A. Lacerda, M. Ehrlich, S.A.B. Fontoura, and A.S.F. Sayao (eds.), Landslides: evaluation and stabilization. Balkema, Taylor & Francis Group, London, 265–272.

Canutti, P., Casagli, N., Catani, F., Fanti, R., 2000. Hydrogeological hazard and risk in archaeological sites: some case studies in Italy. *J Cult Herit*, 1, 117–125.

Capecchi, F., Forcardi, P., 1988. Rainfall and landslides: research into a critical precipitation coefficient in an area of Italy. Proc. 5th Symp. On landslides, Lausanne, Switzerland, 2, 1131-1136.

Cardinali, M., Reichenbach, P., Guzzetti, F., Ardizzone, F., Antonini, G., Galli, M., Cacciano, M., Castellani, M., Salvati, P., 2001. A geomorphological approach to the estimation of landslide hazards and risks in Umbria, Central Italy. *Natural Hazards and Earth System Sciences*, 2, 57-72.

Cardinali, M., Reichenbach, P., Guzzetti, F., Ardizzone, F., Antonini, G., Galli, M., Cacciano, M., Castellani, M., Salvati, P., 2002. A geomorphological approach to the estimation of landslide hazards and risks in Umbria, Central Italy. *Nat Hazards Earth Syst Sci*, 2, 57-72.

Carere, K., Ratto, S., Zanolini, F., 2001. Programme Intereg 2c - Falaises. Prévention des mouvements de versants et des instabilités de falaises, Confrontation des méthodes d'études des éboulements rocheux dans l'arc alpin, 239.

Carnec, C., Massonet, D., King, C., 1996. Two examples of the use of SAR interferometry on displacement fields of small extent. *Geophys. Res. Letts.*, 23(24), 3579-3582.

Carper, W.J., Lillesand, T.M., Kiefer, R.W., 1990. The use of Intensity-Hue-Saturation transformations for merging Spot panchromatic and multispectral image data. *Photogrammetric Engineering and Remote Sensing*, 56(4), 459-467.

Carrara, A., 1983. Multivariate methods for landslide hazard evaluation. *Math Geol*, 15,403-426.

Carrara, A., Guzzetti, F., 1995. Geographical information systems in assessing natural hazards. Kluwer academic publishers, London, 349p.

Carrara, A., Cardinali, M., Detti, R., Guzzetti, F., Pasqui, V., Reichenbach, P., 1991. GIS techniques and statistical models in evaluating landslide hazard. *Earth Surface Processes and Landforms*, 16(5), 427-445.

Carrara, A., Cardinali, M., Guzzetti, F., 1992. Uncertainty in assessing landslide hazard and risk. *ITC journal*, 2, 172-183.

Carrara, A., Cardinali, M., Guzzetti, F., Reichenbach, P., 1995. GIS technology in mapping landslide hazard. In A. Carrara and F. Guzzetti (eds.), Geographical Information Systems in Assessing Natural Hazards, Kluwer Academic Publishers, Dordrecht, The Netherlands, 135-176.

Carrara, A., Guzzetti, F., Cardinali, M., Reichenbach, P., 1999. Use of GIS technology in the Prediction and Monitoring of Landslide Hazard. *Natural Hazards*, 20, 117-135.

Carrara, A., Crosta, G., Frattini, P., 2003. Geomorphological and historical data in assessing landslide hazard. *Earth Surface Processes and Landforms*, 28(10), 1125–1142.

Carro, M., De Amicis, M., Luzi, L., Marzorati, S., 2003. The application of predictive modeling techniques to landslides induced by earthquakes: the case study of the 26 September 1997 Umbria-Marche earthquake (Italy). *Engineering Geology*, 69, 139-159.

Cascale, R., Fantechi, R., Flageollet, J.C., 1994. Temporal occurrence and forecasting of landslides in the European Community. Final Report. European Commission, Science. Research and Development, Report EUR 15805.

Castelli, M., Amatruda, G., Scavia, C., Paro, L., Forlati, E., 2004. The IMIRILAND methodology: a proposal for a multidisciplinary risk assessment procedure wlth respect to large landslide. In W.A. Lacerda, M. Ehrlich, S.A.B. Fontoura, and A.S.F. Sayao (eds.), Landslides: evaluation and stabilization. Balkema, Taylor & Francis Group, London, 229–236.

Catani, F., Farina, P., Moretti, S., Nico, G., Strozzi, T., 2005. On the application of SAR interferometry to geomorphological studies: estimation of landform attributes and mass movements. *Geomorphology*, 66(1–4), 119–131.

Cevik, E., Topal, T., 2003. GIS-based landslide susceptibility mapping for a problematic segment of the natural gas pipeline, Hendek (Turkey). *Environmental Geology*, 44(8), 949–962.

Chacón, J., Irigaray, C., El-Hamdouni, R., Fernández, T., 1996. From the inventory to the risk analysis: improvements to a large scale G.I.S. method. In J. Chacón, C. Irigaray, and T. Fernández (eds.), Landslides. Balkema, Rotterdam, 335–342.

Chau, K.T., Lo. K.H., 2004. Hazard assessment of debris flows for Leung King Estate of Hong Kong incorporating GIS with numerical simulation. *Nat Hazards Earth Syst Sci*, 4(1), 103–116.

Chebbani, R., Djilli, K., Roose, E., 1999. Etude des risques d'érosion dans le bassin versant de l'isser, Algérie. *Bulletin Réseau Erosion*, 19, 85-95.

Childs, S-W., Flint, A-L., 1990. Physical properties of forest soils containing rock fragments. In: S-P. Gessel, D-S.Lacate, G-F. Weetman, and R-F. Powers (eds.), Sustained productivity of forest soils, University of British Columbia, Faculty of Forestry Publ., Vancouver, 95-121.

Chorowicz, J., Scanvic, J-Y., Rouzeau, O., Vargas Cuervo, G., 1998. Observation of recent and active landslides from SAR ERS-1 and JERS-1 imagery using a stereo-simulation approach: example of the Chicamocha valley in Colombia. *International Journal of Remote Sensing*, 19(16), 3187-3196.

Chorowicz, J., Dhont, D. Gündogdu, N., 1999. Neotectonics in the eastern North Anatolian fault region (Turkey) advocates crustal extension: mapping from SAR ERS imagery and Digital Elevation Model. *Journal of Structural Geology*, 21, 511-532.

Chorowicz, J., Deroin, J.P., 2003. La télédétection et la cartographie géomorphologique et géologique. Collection Géosciences (France), 141p.

Choubey, V.D., Litoria, P.K., 1990. Terrain classification and land hazard mapping in Kalsi-Chakrata area (Garhwal Himalaya), India. *ITC Journal*, 1, 65-68.

Chowdhury, R.N., 1996. Aspects of risk assessment for landslides. In K. Senneset (ed.), Proceedings of the VIth I.S.L., Trondheim, Norway. Balkema, Rotterdam, vol. 1, 183–189.

Chowdhury, R., Flentje, P., 1996. Geological and lands instability mapping using G.I.S. package as a building block for the development of a risk assessment procedure. In K. Senneset (ed.), Proceedings of the VIth I.S.L., Trondheim, Norway. Balkema, Rotterdam, vol. 1, 263–269.

Chowdhury, R., Flentje, P., 2003. Role of slope reliability analysis in landslide risk management. *Bull Eng Geol Environ*, 62, 41–46.

Chung, C.F., Fabbri, A.G., van Westen, C.J., 1995. Multivariate regression analysis for landslide hazard zonation. In A. Carrara and F. Guzzetti (eds.), Geographical information systems in assessing natural hazards. Kluwer Academic oublishers, Dodrecht, The Netherlands, 107-142.

Chung, C.F., Fabbri, A.G., 1993. The representation of geoscience information for data integration. *Now renewable Resources*, 2(2), 122-139.

Chung, C.F., Fabbri, A.G., 1998. Three Bayesian prediction models for landslide hazard. In Buscianti (ed.), Proceedings of the International Association of Mathematical Geology, Ischia, Italy, 204–211.

Chung, C.F., Fabbri, A.G., 1999. Probabilistic prediction models for landslide hazard mapping. *Photogrammetric Eng Remote Sensing*, 65(12), 1388–1399.

Chung, C.F., Fabbri, A., Van Westen, C., 1995. Multivariate regression analysis for landslide hazard zonation. In: A. Carrara and F. Guzzetti (eds.), Geographical Information Systems in Assessing Natural Hazards, Kluwer Academic Publishers, Dordrecht, The Netherlands, 107-133.

Clarke, L.A., Pregibon, D., 1992. Tree-based models. In J.M. Chambers, T.J. Hastie (eds.), Statistical models. New York, Chapman and Hall, 377-419.

Clerici, A., Perego, S., Tellini, C., Vescovi, P., 2002. A procedure for landslide susceptibility zonation by the conditional analysis method. *Geomorphology*, 48, 349–364.

Close, N., McComick, E., 1922. Where the mountains walked. *Natl. Geog. Mag.*, 41, 445-464.

Coates, D.R., 1977. Landslides. Geological Society of America. *Review in Engineering Geology*, 3, 1-278.

Codebo, L., Enea, C.R., Del Monaco, G., Margottini, C., 2000. Landslide susceptibility in the Cardoso Slope (Versilla-Italy). Consequences of the flash flood of 19th June 1996. Landslides in research, theory and practice. Thomas Telford, London, 293–298.

Coe, J.A., Godt, J.W., Baum, R.L., Bucknam, R.C., Michael, A., 2004. Landslide susceptibility from topography in Guatemala. In W.A. Lacerda, M. Ehrlich, S.A.B. Fontoura, and A.S.F. Sayao (eds.), Landslides: evaluation and stabilization. Balkema, Taylor & Francis Group, London, 69–78.

Colesanti, C., Ferretti, A., Prati, C., Rocca, F., 2003. Monitoring landslides and tectonic motions with the permanent scatterers technique. *Engineering Geology*, 68(1–2), 3–14.

Connell, L.D., Jayatilaka, C.J., Nathan, R., 2001. Modelling flow and transport irrigation catchments, spatial application of subcatchment model. *Water Resour Res*, 37(4), 965-977.

Conover, W.J., 1980. Practical non-parametric statistics. Second edition. John Wiley and Sons, New York.

Crichton, N.J., 1999. Information point: Spearman's rank correlation. *Journal of clinical nursing*, 8, 763.

Creath, W.B., 1996. Home Buyer's guide to geologic hazards. American Institute of Professional Geologists, Arvada, Colorado, 13-16.

Crosta, G., Frattini, P., Sterlacchini, S., 2001. Valutazione e gestione del rischio da frana, Regione Lombardia, Milano.

Crozier, M.J., 1986. Landslides: causes, consequences and environment. Surry Hills, Croom Helm Pub, London, 192p.

Cruden, D.M., Varnes, D.J., 1996. Landslide types and processes. In: A.K. Turner and R.L. Schuster (eds.), Landslides, Investigation and Mitigation. Transportation Research Board, special report 247, National Research Council, National Academy Press, Washington D.C., 36-75.

Curlander, J.C., McDonough, R.N., 1991. Synthetic aperture radar: systems and signal processing. New York, Wiley, 647p.

Dai, F.C., Lee, C.F., 2001. Frequency–volume relation and prediction of rainfall-induced landslides. *Engineering Geology*, 59(3/4), 253–266.

Dai, F.C., Lee, C.F., 2002. Landslide characteristics and slope instability modelling using GIS, Lantau Island, Hong Kong. *Geomorphology*, 42(3–4), 213–228.

Dai, F.C., Lee, C.F., Li, J., Xu, Z.W., 2000. Assessment of landslide susceptibility on the natural terrain of Lantau Island, Hong Kong. *Environmental Geology*, 40(3), 381–391.

Dai, F.C., Lee, C.F., Ngai, Y.Y., 2002. Landslide risk assessment and management: an overview. *Environmental Geology*, 64(1), 65–87.

Dai, F.C., Lee, C.F., Wang, S.J., 2003. Characterisation of rainfall induced landslides. *International Journal of Remote Sensing*, 24(23), 4817–4834.

Darwish, T., 1988. Particularités régionales de la pédogenèse en Méditerranée orientale. *Lebanese Science Bulletin*, 4(2), 65-74.

Darwish, T., Zurayk, R., 1997. Distribution and nature of Red Mediterranean soils in Lebanon along an altitudinal sequence. *Catena*, 28, 191-202.

Darwish, T., Haddad, T, Faour, G., Awad, M., AbouDaher, M., 1999. Environmental impact due to land use changes in Tripoli area, North Lebanon. 6th International meeting on soils with Mediterranean type of climate, Barcelona, Spain, 748-750.

Davidson, D.A., 1982. The assessment of land use capability: soil, geology and landforms impact on land use planning in developing countries. Proceedings 1st Int. Symp. AGID/AIT, Bangkok, 1982, G2.1-G2.57.

Davies, W.E., 1974. Landslide susceptibility map of part of the Canonsburg 7-1/2 minute quadrangle, Allegheny County and vicinity, Pennsylvania. US Geological Survey Open-File Report 74-276, scale 1:24,000, 8p.

De Araujo, P.C., Riedel, P.S., Santoro, J., Vedovello, R., Tominaga, L.K., Brollo, M.J., Tavares, R., 2004. Analysis of susceptibility to gravitational mass flows based on conditional probability. In W.A. Lacerda, M. Ehrlich, S.A.B. Fontoura, and A.S.F. Sayao (eds.), Landslides: evaluation and stabilization. Balkema, Taylor & Francis Group, London, 251–256.

De la Ville, N., Chumaceiro Diaz, A., Ramirez, D., 2002. Remote sensing and GIS technologies as tools to support sustainable management of areas devastated by landslides. *Environ Dev Sustain*, 4, 221–229.

Del Gaudio, V., Wasowski, J., 2004. Time probabilistic evaluation of seismically induced landslide hazard in Irpinia (Southern Italy). *Soil Dyn Earthquake Eng*, 24, 915–928.

Demmak, A., 1984. Recherche d'une relation empirique entre les apports solides spécifiques et les paramètres physico-climatiques des bassins : cas algérien. *AISH Public*, 144, 403-414.

De Ploey, J., Imeson, A., Oldeman, L-R., 1991. Soil erosion, soil degradation and climatic change. In F-M. Brouwer, A-J. Thomas, and M-J. Chadwick (eds.), Land use changes in Europe. Kluwer Academic Publishers, Dordrecht, 275-292.

DGA, 1963. Topographic maps at a scale 1:20,000 (Hamidieh, Halba, Batroun, Tripoli, Sir El Dannieh, Jbail, Qartaba, Baalbeck, Beirut, Zahle, Rayak, Saida, Jezzine, Rachaya). Republic of Lebanon. Direction of geographic affairs.

Dhont, D., Chorowicz, J., Collet, B., 2005. Evidence of mountain uplift from slope analysis using SAR ERS image, case study Alps. In K. Fletcher (ed.), Space born radar applications in Geology. ESA publications division, The Netherlands, 13.1-13.4.

Dietrich, E.W., Reiss, R., Hsu, M.L., Montgomery, D.R., 1995. A process-based model for colluvial soil depth and shallow landsliding using digital elevation model. *Hydrological processes*, 9, 383-400.

Dikau, R., Brunsden, D., Schrott, L., Ibsen, M.L., 1996. Landslide recognition, identification, movement and causes. Wiley, Chichester.

Donnelly, L.J., McCann, D.M., 2000. The location of abandoned mine workings using thermal techniques. *Engineering Geology*, 57, 39-52.

Dorren, K.A., Heuvelink, G.B., 2004. Effect of support size on the accuracy of a distributed rockfall model. *International Journal of Geographical Information Science*, 18(6), 595-609.

Duan, J., Grant, G., 2000. Shallow landslide delineation for steep forest watersheds based on topographic attributes and probability analysis. In: J. Wilson and J. Gallant (eds.). Terrain analysis: principles and applications. John Wiley and Sons, New York, 311-329.

Duarte, R.M., Marquinez, J., 2002. The influence of environmental and lithologic factors on rockfall at a regional scale: an evaluation using GIS. *Geomorphology*, 43(1-2), 117-136.

Dubertret, L., 1945. Cartes géologiques à l'échelle de 1/50 000 (Hamidieh, Halba, Batroun, Tripoli, Sir El Dannieh, Jbail, Qartaba, Baalbeck, Beirut, Zahle, Rayak, Saida, Jezzine, Rachaya). République Libanaise, Ministère des Travaux publics, Beyrouth, Liban.

Dubertret, L., 1953. Carte géologique au 1/50 000 de la Syrie et du Liban. 21 feuilles avec notice explicative. Ministère des Travaux publics. L'imprimerie Catholique, Damas et Beyrouth.

Dubertret, L., 1955. Carte géologique de la Syrie et du Liban au 1/200 000. 21 feuilles avec notices explicatrices. République Libanaise, Ministère des Travaux publics. L'imprimerie Catholique, Beyrouth, Liban, 47p.

Dubertret, L., 1966. Liban, Syrie et bordure des pays voisins. Première partie. Tableau stratigraphique avec carte géologique au millionième, Not. et Mém., VIII : 251-358.

Eisbacher, G.H., Clague, J.J., 1984. Destructive mass movements in the high mountains: hazard and management. *Geol. Survey Canada*, 84(16), 229p.

Einstein, H.H., 1988. Landslide risk assessment. Proc. 5th symposium on landslides, Lausanne, 1075-1090.

Elachi, C., 1988. Spaceborne radar remote sensing: applications and techniques. New York: IEEE, 255p.

El-Qareh, R., 1967. The submarine springs of Chekka: exploitation of a confined aquifer discharging in the sea. Unpublished M.Sc. Thesis, American University of Beirut, Geology Department, 80p.

Elias, P.B., Bandis, S.C., 2000. Neurofuzzy systems in landslide hazard assessment. Proc. 4th Int. Symp. spatial accuracy assessment in natural resources and environment science, 199-202.

Ercanoglu, M., Gokceoglu, C., 2002. Assessment of landslide susceptibility for a landslide susceptibility for a landslide-prone area (north of Yenice, NW Turkey) by fuzzy approach. *Environmental Geology*, 55, 277-296.

Ercanoglu, M., Gokceoglu, C., Van Asch, T.H., 2004. Landslide susceptibility Zoning North of Yenice (NW Turkey) by multivariate statistical techniques. *Natural Hazards*, 32, 1–23.

Esmali, A., Ahmadi, H., 2003. Using GIS and RS in mass movements hazard zonation. A case study in Germichay watershed, Arbedil, Iran. Map Asia Conference, 2003, 1-10.

Eyers, R., Moore, J., Hervás, J., Liu, J.G., 1998. Integrated use of Landsat TM and SPOT panchromatic imagery for landslide mapping: case histories from southeast Spain. In J.G. Maund and M. Eddleston (eds.), Geohazards in engineering geology, Engineering Geology Special Publication 15. Geological Society, London, 133–140.

FAO, 1983. Garder la terre en vie : L'érosion des sols, ses causes et ses remèdes. *Bulletin pédologique*, 50, 62p.

Faour, G., Bou Kheir, R., Darwish, A., 2006. Méthode globale d'évaluation du risque d'incendies de forêt utilisant la télédétection et les SIG : cas du Liban. *Télédétection*, 5(4), 359-377.

Fard, M.Y., 2001. Slope stability - Study of a real landslide in Tabriz. Proceedings of the 54th Canadian Geotechnical Conference, 2nd Joint IAH and CGS Groundwater Conference, Calgary, Alberta, Canada, 16-19 September 2001, 1, 379-383.

Favre, J.L., Resig, S., Leroi, E., 2000. Conditional landslide hazard mapping. In RE. Melchers and MG. Stewart (eds), Applications of statistics and probability-civil engineering and risk analysis. Balkema, Rotterdam, 55–262.

Fell, R., 1994. Landslide risk assessment and acceptable risk. Canadian Geotechnical Journal, 32(2), 261-272.

Fell, R., Hartford, D., 1997. Landslide risk assessment. In D. Cruden D and R. Fell (eds.), Proceedings of the international workshop on landslide risk assessment, Honolulú. Balkema, Rotterdam, 51–110.

Fernández, T, Irigaray, C, El Hamdouni, R., Chacón, J., 2003. Methodology for landslide susceptibility mapping by means of a GIS: application to the Contraviesa Area (Granada, Spain). *Natural Hazards*, 30(3), 297–308.

Ferreti, A., Prati, C., Rocca, F., 2000. Nonlinear subsidence rate estimation using permanent scatterers in differential SAR interferometry. *IEEE Trans. Geosc. Rem. Sens.*, 38, 2202-2212.

Ferrier, N., Emdad Haque, C., 2003. Hazards risk management methodology for emergency managers: a standardized framework for application. *Natural Hazards*, 28, 271–290.

Filliat, G., 1981. La pratique des sols et des fondations. Mouvements de terrain. Editions du Moniteur, Paris, pp. 555-626.

Fiorillo, F., Guadagno, F.M., Aquino, S., De Blasio, A., 2001. The December 1999 Cervinar Landslide: further debris flow in the pyroclasstic deposits of Campania (Southern Italy). *Bull. Eng. Geol. Environ.*, 60, 171-184.

Flageollet, J.C., 1994. The time dimension in the mapping of earth movements. In R. Casale, R. Fantechi, and J.C. Flageollet (eds.), Temporal occurrence and forecasting of landslides in the European community. Final Report, EUR 15805 EN, Programme EPOCH Contract 90 0025, Brussels, Belgium, vol. 1, 7–70.

Fleury, J., Chorowicz, J., Somma, J., 1999. Discussion on transcurrent fault activity on the Dead Sea Transform in Lebanon and its implications for plate tectonics and seismic hazards. *Journal of the Geological Society*, 154, 757-760.

Fookes, P.G., Dale, S.G., Land, J.M., 1991. Some observations on a comparative aerial photography interpretation of a landslide area. *Quaternary Journal of Engineering Geology*, 24, 249-265.

Foucault, A., Raoult, J.-F., 1992. Dictionnaire de géologie. Masson, Paris, 347p.

Franklin, J., 1998. Predicting the distributions of shrub species in California chaparral and coastal stage communities from climate and terrain-derived variables. *Journal of Vegetation Science*, 9, 733-748.

Friedl, M.A., Brodley, C.E., Strahler, A.H., 1999. Maximizing land cover classification accuracies produced by decision trees at continental to global scales. *IEEE Transactions on Geoscience Remote Sensing*, 37, 969-977.

Fruneau, B., Achache, J., Delacourt, C., 1996. Observations and modelling of the Saint-Etienne-de-Tinee landslide using SAR interferometry. *Tectonophysics*, 265, 181-190.

Gallart, F., Clotet-Perarnau, N., 1988. Some aspects of the geomorphic processes triggered by an extreme rainfall event: the November 1982 flood in the eastern Pyrenees. *Catena*, 13, 79-95.

Garcia-Ruiz, J., White, S.M., Marti, C., Valero, B., Paz Errea, M.P., Gomez Villar, A., 1996. La catastrofe del barranco de Aras (Biescas, Pireneo, Aragones) y su contexto espacio-temporal. Zaragoza, Spain: CSIC Istituto Pirenaico de Ecologia.

Gary, A., Aurora, A., 2006. How does earth work? Physical Geology and the process of science. Pearson, Prentice Hall, New Jersey, 641p.

Gèze, B., 1956. Carte de reconnaissance des sols du Liban à l'échelle de 1/200 000. République libanaise, Ministère de l'Agriculture, Direction de l'Enseignement et la Vulgarisation, Station Agronomique Libano - Française. Notice explicative, 52p.

Ghattas, I., 1975. The geology and hydrology of the western flexure of Mount Lebanon between Dbaiyeh and Jdaide. Unpublished M.Sc. Thesis, American University of Beirut, Geology Department, 99p.

Giafferi, J.L., 1998. L'aléa mouvement de terrain dans les études de dangers des barrages. In D. Moore and O. Hungr (eds.), Proceedings of the 8th IAEG Congress, Vancouver. Balkema, Rotterdam, 1079–1087.

Gibson, A.D., Murphy, W.D., Petley, D.N., 2000. Quantitative landslide analysis using archive airborne Thematic Mapper imagery. ISSMGE and BGS 8th International Symposium on landslides, 26-30 June 2000, 621-626.

Gili, J., Corominas, J., Rius, J., 2000. Using global positioning system techniques in landslide monitoring. *Engineering Geology*, 55, 167-192.

Giordano, A., 1986. A first approximation of soil erosion risk assessment in the southern countries of the European Community. In R.P.C. Morgan and R.J. Rickson (eds.), Erosion assessment and modelling. Commission of the European Communities Report EUR 10860, 3-24.

Girard, M.-C., Girard, C.-M., 1999. Traitement des données de télédétection. Dunod, Paris, 529p.

Girard, M.-C., Girard, C.-M., 2003. Processing of Remote Sensing Data. Balkema, The Netherlands, 487p.

Glade, T., 2004. Linking debris flow hazard assessments with geomorphology. *Geomorphology*, 66, 189-213.

Godefroy, P., Humbert, M., 1983. Cartographie des risques naturels. PER, *Hydrogéologie – géologie de l'ingénieur*, 2, 69-90.

Gokceoglu, C., Aksoy, H., 1996. Landslide susceptibility mapping of the slopes in the residual soils of the Mengen region (Turkey) by deterministic stability analyses and image processing techniques. *Engineering Geology*, 44(1–4), 147–161.

Gordon, S., Lichti, D., Stewart, M., Franke, J., 2003. Structural deformation measurement using terrrestrial laser scanners. Proceedings of the 11th International FIG Sympoisum on deformation measurements, Santorini Island, Greece, 28 May 2003, CD-ROM.

Gomez, F., Meghraoui, M., Darkal, A.N., Sbeinati, R., Darawcheh, R., Tabet, C., Khawlie, M., Charabe, M., Khair, K., Barazangi, M., 2001. Coseismic displacements along the Serhaya fault: an active branch of the Dead Sea Fault System in Syria and Lebanon. *Journal of Geological Society*, 158, 405-408.

Gorsevski, P.V., Gessler, P., Foltz, R.B., 2000. Spatial prediction of landslide hazard using logistic regression and GIS. 4th Int. Conf. on integrating GIS and environmental modelling. Proceedings, Banff, Alberta, Canada, 9p.

Gorsevski, P.V., Gessler, P.E., Jankowski, P., 2003. Integrating a fuzzi k-means classification and a Bayesian approach for spatial prediction of landslide hazard. *J Geograph Syst*, 5, 223–251.

Gostelow, T.P., Naden, P.S., Del Prete, M., Koukis, G., Corominas, J., 1996. Rainfall induced landslides on selected Mediterranean mountainous zones of Italy, Spain and Greece: the application of geographic information systems (GIS) to hazard mapping. In Cascale, R. (ed.), Hydrological and hydrogeological risks. Proceedings of the first review meeting. European Commission EUR 16799, 95-167.

Greenway, D.R., 1987. Vegetation and slope stability. In Anderson and Richards (eds.), Slope stability. John Wiley & Sons, 187-231.

Greenbaum, D., McDonald, A.J.W., Marsh, S.H., 1996. Rapid methods of landslide hazard mapping. Proceedings of the Thematic Conference on Geological Remote Sensing, 11, 1287-1296.

Griffiths, J.S., Mather, A.E., Hart, A.B., 2002. Landslide susceptibility in the Rio Aguas catchment, SE Spain. *Quaternary journal of engineering geology and hydrogeology*, 35(1), 9-17.

Gritzner, M.L., Marcus, W.A., Aspinall, R., Custer, S.G., 2001. Assessing landslide potential using GIS, soil wetness modelling and topographic attributes, Payette River, Idaho. *Geomorphology*, 37(1–2), 149–165.

Groove, A.T., 1996. Physical, biological and human aspects of environmental change. MEDALUS II Report, 39-64.

Guillande, R., Gelugne, P., Bardintzeff, J.M., Brousse, R., Chorowicz, J., Deffontaines, B., Parrot, J-F., 1993. Cartographie automatique de zones à aléas de mouvements de terrain sur l'île de Tahiti à partir de données digitales. *Bull. Geol. Soc. France*, 164(4), 577-583.

Gulla, G., Nicoletti, P.G., Sorriso-Vavo, M., 1988. A portable device for measuring displacements along fractures. Proceedings of the Vth International Synposium on landslides, Lausanne, Balkema, vol. 1, 423-426.

Gupta, R.P., Johsi, B.C., 1989. Landslide hazard zoning using the GIS approach – a case study from the Ramganga catchment, Himalayas. *Engineering Geology*, 28, 119-131.

Gupta, R.P., Saha, A.K., Arora, M.K., Kumar, A., 1999. Landslide hazard zonation in part of the Bhagirathi valley, Garhwal Mimalyas, using integrated remote sensing – GIS, *Himalayan Geology*, 20, 71-85.

Guzzetti, F., 1993. Landslide hazard and risk by GIS-based multivariate models. In P. Reichenbach, F. Guzzetti, and A. Carrara (eds.). International Workshop GIS in assessing natural hazards, 20-22 September 1993, 83-91.

Guzzetti, F., 2000. Landslide fatalities and evaluation of landslide risk in Italy. *Eng. Geol.*, 58, 89-107.

Guzzetti, F., Carrara, A., Cardinali, M., Reichenbach, P., 1999. Landslide hazard evaluation: a review of current techniques and their application in a multi-scale study, Central/Italy. *Geomorphology*, 31, 181-216.

Guzzetti, F., Reichenbach, P., Ghigi, S., 2004. Rockfall hazard and risk assessment along a transportation corridor in the Nera Valley, Central Italy. *Environmental Management*, 34(2), 191–208.

Hakim, B., 1985. Recherches hydrologiques et hydrochimiques sur quelques karsts méditerranéens au Liban, en Syrie et au Maroc. Publications de l'Université Libanaise. Section des études géographiques, tome II, 701p.

Hamblin, K., 1992. Earth's dynamic systems. Macmillan Publishing Company, New York, sixth edition, 750p.

Hansen, A., 1984. Landslide hazard analysis. In D. Brunsden and DB. Prior (eds.). Wiley, Chichester, 523–602.

Hansen, R., 2001. Radar interferometry: data interpretation and error analysis. Kluwer Academic Publishers, Dordrecht, The Netherlands, 308p.

Hansen, A., Brimicombe, A.J., Franks, C., Kirk, P., Tung, F., 1995. Application of GIS to hazard assessment, with particular reference to landslides in Hong Kong. In A. Carrara and F. Guzzetti (eds.), Geographic information systems in assessing natural hazards. Kluwer, The Netherlands, 273-298.

Health, W., Dowling, J.W., 1980. Examples of the use of terrestrial photogrammetry in highway engineering, Transport and road research Lab., Crowthorue, England, 19p.

Heckerman, D., 1986. Probabilistic interpretation of MYCIN's certainty factor. In L.N. Kanal, and JF. Lemmer (eds.), Uncertainty in artificial intelligence. Elsevier, New York, 298–311.

Heinimann, H.R., Hollenstein, K., Kienholz, H., Krummenacher, B., Mani, P., 1998. Methoden zur Analyse und Bewertung von Naturgefarhen. Bundesamt fur Umwelt, Wald und landschaft (BUWAL), Bern.

Hervas, J., Barredo, J.I., Rosin, P.L., Pasuto, A., Mantovani, F., Silvano, S., 2003. Monitoring landslides from optical remotely sensed imagery: the case history of Tessina landslide, Italy. *Geomorphology*, 54, 63-75.

Highland, L.M., 1997. Landslide hazard and risk: current and future directions for the United Stated Geological Survey's landslide Program. In D.M. Cruden and R. Fell (eds.)

Landslide risk assessment. International Workshop Risk Assessment, IUGS Working Group Landslides, Honolulu, Hawaii, USA, 207–213.

Hinojosa, J.A., Leon, C.O., 1978. Unstable soil mapping in Spain. Proceedings of 3rd International Cong. Madrid, section I, 217–227.

Huang, X., Jensen, J.R., 1997. A machine-learning approach to automated knowledge-base building for remote sensing image analysis with GIS data. *Photogrammetric Engineering & Remote Sensing*, 63, 1185-1194.

Hollestein, K., 2005. Reconsidering the risk assessment concept: standardizing the impact description as a building block for vulnerability assessment. *Nat Hazards Earth Syst Sci*, 5, 301–307.

Humbert, M., 1977. La cartographie ZERMOS. Modalités d´établissement des cartes des zones esposes a` des risques lié s aux mouvements du sol et du sous-sol. *Bull Bur Rech Geol Min*, III(1–2), 5–8.

Husein, A.I., Saleh, B., Al-Sheriadeh, M.S., Hamza, M.S., 2000. Mapping of landslide hazard zones in Jordan using remote sensing and GIS. *Journal of Urban Planning and Development ASCE*, 126(1), 1-17.

Huybrechts, E., 1997. L'occupation de la cote libanaise. Observatoire des recherches sur Beyrouth et la Reconstruction. *Lettre d'information*, 10, 19-23.

Irigaray, C., Fernández, T., Chacón, J., 1996. Comparative analysis of methods for landslide susceptibility mapping. In J. Chacón, C. Irigaray, and T. Fernández (eds.), Balkema, Rotterdam, 373–384.

Irigaray, C., Lamas, F., El Hamdouni, R., Fernández, T., Chacón, J., 2000. The importance of precipitation and the susceptibility of the slopes for the triggering of landslides along the roads. *Natural Hazards*, 21(1), 65–81.

Irigaray, C., Fernández, T., Chacón, J., 2003. Preliminary rockslope- susceptibility assessment using GIS and the SMR classification. *Natural Hazards*, 30(3), 309–324.

Jaber, B., 1993. The problem of water in Lebanon. Research and documentation (CSSRD), 150p.

Jager, S., Wieczorek, G.F., 1994. Landslide susceptibility in the Tully Valley Area, Finger Lakes Region, New York. U.S. Geological Survey, Open-File Report, 94-615.

Jibson, R.W., Harp, E.L., Michael, J.A., 1998. A method for producing digital probabilistic seismic landslide hazard maps. Open-file report 98-113. Department of Interior, USGS, USA, 17 pp

Joftic, L., Milliman, J., Sestini, G., 1992. Climate change and the Mediterranean. UNEP-E. Arnold Pub. NY, 20p.

Juang, J.Y., Wang, S.J., Uen, T.M., Gou, Y.S., 1992. Low-field scaling behaviors of global flux pinning in TI-Ba-Ca-Cu-O thin films. *Phys. Rev.*, B46, 1188-1192.

Keefer, D.K., 1993. The susceptibility of rock slopes to earthquake-induced failure. *Association of Engineering Geologists Bulletin*, 30(3), 353-361.

Kehew, A.E., 1995. Geology for engineers and environmental scientists. Englewood cliffs, Second edition, New Jersey, Prentice-Hall, 357-393.

Kelarestaghi, A., 2003. Landslide hazard zonation in shirin rood drainage basin with using Geographical Information System, Sari, Iran. Map Asia 2003, 15-27.

Khawlie, M., 1985. Mass movements: A national plan for their assessment in Lebanon. Proc. GEOCOME II, 22-24 October 1983, Baghdad, Iraq, 141-147.

Khawlie, M., 1986. Land use planning for the redevelopment studies: Typical mountainous area along the eastern Mediterranean coast, Lebanon. *Int. Assoc. Eng. Geol. Bull.*, 38, 95-104.

Khawlie, M., 1992. Shaping the eastern Mediterranean coast by earthquakes: Lebanon. *Geology Today*, 8(2), 58-61.

Khawlie, M., 1994. Hazard mapping: The Abou A'li river flood, Tripoli – Lebanon. In R. Oliveira, L.F. Rodrigues, A.G. Coelho, and A.P. Cunha, (eds.). Proceedings of the Seventh International Congress, Lisbona, Portugal, 5-9 September 1994, 2049-2057.

Khawlie, M., 1995. Environmental constraints and problems of urbanization in Lebanon. Urban Management Program, Lebanese Panel contribution to "City Summit", Istanbul-Habitat II.

Khawlie, M., 1999. Hot spots and sensitive areas: contribution of remote sensing to geoenvironmental mapping in Lebanon. In P. Borrousky (ed.), Geoenvironmental mapping. Balkema publishing, 79-87.

Khawlie, M., 2000. L'environnement du Liban : une ressource perdue (en arabe). Menrikh publisher, 372p.

Khawlie, M., 2003. The impacts of climate change on water resources of Lebanon – Eastern Mediterranean. In C. Giupponi and M. Schecter (eds.), Climate change in the Mediterranean socio-economic perspectives of impacts, vulnerability and adaptation. Edward Edgar pub., United Kingdom, 94-107.

Khawlie, M., Hassanain, H., 1979. A study of some landslides in Lebanon. Proc. Arab Sci. Week, 19th, Damascus, 19p.

Khawlie, M., Hassanain, H., 1984a. Failure phenomena and environmental control of the relatively unstable Hammana area, Lebanon. *Engineering Geology*, 20, 253-264.

Khawlie, M., Hassanain, H., 1984b. Engineering geology of the Hammana landslides, Lebanon. *Quaternary Journal of Engineering Geology*, 17, 137-148.

Khawlie, M., Ghalayini, I., 1985. Geological evaluation of marls in relation to their mass behavior, Achrafieh area, Beirut. The Lebanese Science Bulletin, 1(1), 83-98.

Khawlie, M., A'war, R., 1992. Terrain evaluation for assessment of highways in the mountainous eastern Mediterranean of Lebanon. *Bulletin of the international association of engineering geology*, 46, 71-78.

Khawlie, M., Touma, G., 1993. Determining the behavior of the highly variable basal cretaceous sandstone (Nubian Facies) in Brummana Lebanon. *Lebanese Science Bulletin*, 6(1), 33-45.

Khawlie, M., Shaban, A., **Abdallah, C.**, Darwish, T., Kawass, I., 2005. Watershed characteristics, land use and fabric: The application of remote sensing and geographical information systems. *Lakes & Reservoirs: Research and Management*, 10, 85-92.

Kienholtz, H., 1978. Maps of geomorphology and natural hazard of Grindewald, Switzerland, scale 1:10,000. *Arctic Alpine Res*, 10(2), 169–184.

Kimura, H., Yamaguchi, Y., 2000. Detection of landslide areas using satellite radar interferometry. *Photogrammetric Eng Remote Sensing*, 66(3), 337–344.

Laird, R.T., Perkins, J.B., Bainbridge, D.A., Baker, J.B., Boyd, R.T., Huntsman, D., Staub, P.E., Zucker, M.B., 1979. Quantitative land-capability analysis. US Geological Survey Professional Paper 945. US Department of Interior, Washington, 115p.

Lal, R., 1982. Effects of slope length and terracing on runoff and erosion on a tropical soil. *IAHS Publ.*, 137, 23-31.

Lamouroux, M., 1978. Study of the soils formed on carbonate rocks. Fersialitic pedogenesis in Lebanon. *Dissert. Abstr. International Congress*, 39(1), 51

Lan, H.X., Zhou, C.H., Wang, L.J., Zhang, H.J., Li, R.H., 2004. Landslide hazard spatial analysis and prediction using GIS in the Xiaojiang watershed, Yunnan, China. *Engineering Geology*, 20, 22-30.

Landry, J., 1979. Cartes ZERMOS. Zones exposées à des risques liés aux mouvements du sol et du sous-sol. Région de Longle-Saunier à Oiligny (Jura). Bureau de Recherches Géologiques et Minières, Orléans, 14p.

Larsen, M.C., Parks, J.E., 1997. How wide is a road? the association of roads and mass wasting in a forested mountain environment. *Earth Surface Processes and Landforms*, 22, 835-848.

La Roca Cervignon, N., Calvo-Cases, A., 1988. Slope evolution by mass movements and surface wash (Valls d'Alcoi, Alicante, Spain). *Catena*, 12, 95-102.

Lee, S., 2004. Application of likelihood ratio and logistic regression models to landslide susceptibility mapping using GIS. *Environmental Management*, 34(2), 223–232.

Lees, B.G., Ritman, K., 1991. Decision-tree and rule-induction approach to integration of remotely sensed and GIS data in mapping vegetation in disturbed or hilly environments. *Environmental Management*, 15, 823-831.

Lee, S., Min, K., 2001. Statistical analysis of landslide susceptibility at Yongin, Korea. *Environmental Geology*, 40, 1095–1113.

Lee, S., Talib, J.A., 2005. Probabilistic landslide susceptibility and factor effect analysis. *Environmental Geology*, 47, 982-990.

Lee, S., Choi, J., Min, K., 2002. Landslide susceptibility analysis and verification using the Bayesian probability model. *Environmental Geology*, 43, 120–131.

Lee, S., Choi, J., Chwae, U., Chang, B., 2002. Landslide susceptibility analysis using weight of evidence. IEEE International Geoscience and Remote Sensing Symposium and 24th Canadian Symposium on Remote Sensing: integrating our view of the planet, New York, USA, 2865–2867.

Lee, S., Ryu, J-H., Lee, M-J., Won, J-S., 2003. Use of an artificial neural network for analysis of the susceptibility to landslides at Boun, Korea. *Environmental Geology*, 44, 820–833.

Lee, S., Ryu, J-H., Won, J.S., Park, H.J., 2004a. Determination and application of the weights for landslide susceptibility mapping using an artificial neural network. *Engineering Geology*, 71, 289–302.

Lee, S., Choi, J., Ryu, H., 2004b. Probabilistic landslide hazard mapping using GIS and remote sensing data at Boun, Korea. In W.A. Lacerda, M. Ehrlich, S.A.B. Fontoura, and A.S.F. Sayao (eds.), Landslides: evaluation and stabilization. Balkema, Taylor & Francis Group, London, 85–90.

Leone, F., Favre, J.L., Leroi, E., 1996. Vulnerability assessment of element exposed to mass-movement: working toward a better risk perception. In K. Senneset (ed.), Proceedings of the VIth I.S.L., Trondheim, Norway. Balkema, Rotterdam, 263–269.

Leroi, E., 1996. Landslide hazard-risk maps at different scales: objectives, tools and developments. In: K. Senneset (ed.), Proceedings of the VIth I.S.L., Trondheim, Norway. Balkema, Rotterdam, 35–52.

Leroi, E., 1997. Landslide risk mapping: problems, limitations and developments. In D.M. Cruden and R. Fell (eds.), Landslide risk assessment. Balkema, Rotterdam, 239–250.

Leroueil, S., Locat, J., 1998. Slope movements-geotechnical characterization, risk assessment and mitigation. In D. Moore and O. Hungr (eds.), Proceedings of the 8th IAEG Congress, Vancouver. Balkema, Rotterdam, 933–944.

Leva, D., Nico, G., Tarchi, D., Fortuny-Guasch, J., Sieber, A., 2003. Temporal analysis of a landslide by means of a ground-based SAR Interferometer. *IEEE Trans. Geosci. and Remote Sensing*, 41(4), 45-58.

Liener, S., Kienholz, H., Liniger, M., Krummenacher, B.K., 1996. SLIDISP-a procedure to locate landslide prone areas. In K. Senneset (ed.), Proceedings of the VIth I.S.L., Trondheim, Norway. Balkema, Rotterdam, 279–284.

Lillesand, T.-M., et Kiefer, R.-W. 1994. Remote sensing and image interpretation. 3e éd. John Wiley & Sons Inc. 750 p.

LNCSR-LMoA, 2002. Land cover/use map of Lebanon at a scale of 1:20,000. Lebanese National Council for Scientific Research and Lebanese Ministry of Agriculture.

Lodwick, W.A., Monson, W., Svoboda, L., 1990. Attribute, error and sensitivity analysis of map operations in geographical information systems: suitability and analysis. *International Journal of Geographical Information Systems*, 4, 413-428.

Lopez-Bermudez, F., Romero-Diaz, M-A., 1993. Genesis y consecuencias erosivas de las Iluvias de alta intensidad en la region mediterranean. In I. Cuadernos (ed.), Logrono, Geografica, 7-28.

Luzi, L., Pergalani, F., 1996. Application of statistical and GIS techniques to slope instability zonation (1:50.000 Fabriano geological map sheet). *Soil Dyn Earthquake Eng*, 15(2), 83–94.

Luzi, L., Pergalani, F., 1999. Slope instability in static and dynamic conditions for urban planning: the ‘‘Oltre Po Pavese’’ case history (Regione Lombardia–Italy). *Natural Hazards*, 20, 57–82.

Luzi, L., Pergalani, F., 2000. A correlation between slope failures and accelorometric parameters: the 26 September 1997 earthquake (Umbria-Marche, Italy). *Soil Dyn Earthquake Eng*, 20, 301–313.

Luzi, L., Pergalani, F., Terlien, M.T.J., 2000. Slope vulnerability to earthquakes at subregional scale, using probabilistic techniques and geographic information systems. *Engineering Geology*, 58(3-4), 313–316.

Luzi, G., Macaluso, G., Mecatti, D., Noferini, L., Pieraccini, M., Atzeni, C., 2005. Ground-based radar interferometry: Results of experimental campaigns for landslides monitoring in Italy. New Strategies for European Remote Sensing. Millpress, Rotterdam, ISBN 90 5966 003 X, 567-574.

Maharaj, R.J., 1993. Landslide processes and landslide susceptibility analysis from an upland watershed-a case study from St.Andrew, Jamaica, West Indies. *Engineering Geology*, 34(1–2), 53–79.

Mahr, T., Malgot, J., 1978. Zoning maps for regional and urban development based on slope stability. Proceedings of the IIIrd I.A.E.G. Congress I, Spain, 124–137.

Malczewski, J., 1999. GIS and multi-criteria decision analysis. Wiley, Nueva York.

Manotvani, F., Soeters, R., Westen, C.J., 1996. Remote sensing techniques for landslides studies and hazard zonation in Europe. *Geomorphology*, 15, 213-225.

Mark, R.K., Ellen, S.D., 1995. Statistical and simulation models for mapping debris-flow hazard. In: A. Carrara and F. Guzzetti (eds.). Geographical Information Systems in Assessing Natural Hazards, Kluwer Pub., Dordrecht, the Netherlands, 93-106.

Marquinez, J., Menéndez, R., Farias, P., Jiménez, M., 2003. Predictive GIS-based model of rock fall activity in mountain cliffs. *Natural Hazards*, 30(3), 341–360.

Marshak, S., 2001. Earth: Portrait of a planet. Norton & Company Inc., New Work, 735 p. + appendices.

Massonnet, D., Vadon, H., Rossi, M., 1996. Reduction in the need for phase unwrapping in the radar interferometry. *IEEE Trans. Geosci. Rem. Sens.*, 34(2), 489-497.

Massonnet, D., Feigl, K.L., 1998. Radar interferometry and its application to changes in the Earth’s surface. *Rev. of Geophys.*, 36(4), 441-500.

McDonald, H.C., Grubbs, R.C., 1975. Landsat imagery analysis: an aid for predicting landslide prone areas for highway construction. NASA Earth resource survey symp. Houston, Texas, 9-12 June 1975, vol.1-b, 769-778.

Meijerink, A.M.J., 1988. Data acquisition and data capture through terrain mapping units. *ITC Journal*, 1, 23-44.

Meisina, C., Piccio, A., Tocchio, A., 2001. Some aspects of the landslide susceptibility in the Sorba Valley (western Alps, Italy). In M. Kuhne, H.H. Einstein, E. Krauter, H. Klapperich, and R. Pottler (eds.). International Conference on landslides – Causes,

Impacts and Countermeasures, 17-21 June 2001, Davos, Switzerland, VGE, Essen, 547-556.

Mejía-Navarro, M., Wohl, E.W., Oaks, S.D., 1994. Geological hazards, vulnerability, and risk assessment using GIS: model for Glenwood Springs, Colorado. *Geomorphology*, 10, 331–354.

Méneroud, J.P., 1978. Cartographie des risques dans les Alps-Maritimes (France). Proceedings of the IIIrd I.A.E.G. Congress, II, Chap. 46, 98–107.

Méneroud, J.P., Calvino, A., 1976. Carte ZERMOS. Zones exposées à des risques liés aux mouvements du sol et du sous-sol à 1:25,000 région de la Moyenne Vesubie (Alpes-Maritimes. Bureau de Recherches Géologiques et Minières, Orléans, 11p.

METAP, 1995. Lebanon: assessment of the status of the environment. Final report Med. Envi. Tech. Ass. Program, 90p.

Michaelsen, J., Schimel, D.S., Friedl, M.A., Davis, F.W., Dubayah, R.C., 1994. Regression tree analysis of satellite and terrain data to guide vegetation sampling and surveys. *Journal of Vegetation Science*, 5, 673-686.

Michel-Leiba, M., Baynes, F., Scott, G., Granger, K., 2003. Regional landslide risk to the Cairns Community. *Natural Hazards*, 30, 233–249.

Mikkelsen, P.E., 1996. Field instrumentation. In A.K. Turner and R.L. Schuster (eds.), Landslides investigation and mitigation. TRB special report 247, National Academy Press, Washington, 278-316.

Miles, S.B., Keefer, D.K., Nyerges, T.L., 2000. A case study in GIS based environment model validation using earthquake induced landslide hazard. In G.B.M. Heuvelink and M.J.P. Lemmens (eds.), Accuracy 2000, proceedings. Delft University Press, Delft, 481–492.

Mina, G., 2006. Quarries rehabilitation DSS for prioritization and monitoring system for the rehabilitation process. Report, ELARD company, Beirut, Lebanon.

MoE, 1999. Climate change. Technical annex to Lebanon's first national communication. Final Report, National GHG mitigation strategy – Assessment of Lebanon's vulnerability to climate change. Republic of Lebanon, Ministry of Environment, 67 p + B6-31.

Montgomery, D.R., Dietrich, W.E., 1994. A physically based model for the topographic control of shallow landsliding. *Water Resour. Res.*, 30(4), 1153-1171.

Moon, V., Blackstock, H., 2004. A methodology for assessing landslide hazard using deterministic stability models. *Natural Hazards*, 32, 111–134.

Moore, I.D., Grayson, R.B., Ladson, A.R., 1991. Digital terrain modelling: a review of hydrological, geomorphological, and biological applications. *Hydrological Processes*, 5, 3-30.

Morgan, G.C., Rawlings, G.E., Sobkowicz, J.C., 1992. Evaluating total risk to communities from large debris flows. Proceedings of the 1992 symposium on geohazard. Bi/Tech, Toronto, 225–236.

Morgan, J.N., Sonquist, J.A., 1963. AID-Automatic Interaction Detection, problems in the analysis of survey data and a proposal. *JASA*, 58, 415-434.

Mougin, J.P., 1973. Les mouvements de terrain. Recherche sur les rapports mutuels des études géologiques et de mécanique à l'estimation de la stabilité des pentes. Thèse Docteur-Ingénieur, Université de Grenoble, 160p.

Mulders, M., 2001. Advances in the application of remote sensing and GIS for surveying mountainous land. *JAG*, 3(1), 3-10.

Murphy, P., Patrick, M., Michael, J.P., 1994. Exploring the decision forest: An empirical investigation of Occam's Razor in decision-tree induction. *Journal of Artificial Intelligence Research*, 1, 257-275.

Mutcher, C., Greer, J., 1980. Effect of slope length on erosion from low slopes. *Trans. ASAE*, 23, 866-869.

Mwasi, B., 2001. Land use conflicts resolution in a fragile ecosystem using multi-criteria evaluation (MCE) and a GIS-based decision support system (DSS). Int. Conf. on spatial information for sustainable development, Nairobi, Kenya, International Federation of Surveyors, 11p.

Nagarajan, R., Roy, A., Kumar, R.V., Mukherjee, A., Khire, M.V., 2000. Landslide hazard susceptibility mapping based on terrain and climatic factors for tropical monsoon regions. *Bull Eng Geol Environ*, 58, 275–287.

Nakona, T., 1974. Natural hazards. In G.F. White, and G.F. (ed.). Natural hazards-local, national, global. Oxford Univ. Press, New York, 231-243.

NAP, 2003. National action program to combat desertification. Republic of Lebanon, Ministry of Agriculture, 32p.

Nie, H.F., Diao, S.J., Liu, J.X., Huang, H., 2001. The application of remote sensing technique and AHP-fuzzy method in comprehensive analysis and assessment for regional stability of Chongqing City, China. Proc. Of the 22nd Asian Conf. on remote sensing, vol. 1, Singapore, 660-665.

Nilsen, T.H., Brabb, E.E., 1977. Landslides. In R.D. Borcherdt (ed.), Studies for seismic zonation of the San Francisco Bay Region. US Geological Survey Professional Paper 941-A, 96p.

Ohlmacher, G.C., Davis, J.C., 2003. Using multiple logistic regression and GIS technology to predict landslide hazard in northeast Kansas, USA. *Engineering Geology*, 69(3–4), 331–343.

Okimura, T., Kawatani, T., 1986. Mapping of the potential surface-failure sites on granite mountain slopes. In V. Gardiner, Int. Geomorp Part I. Willey, New York, 121-138.

Ottens, H.F.L., 1992. GIS in Europe. II European Conference on GIS, Brussels, 2-5 April 1991, 1, 1-9.

Ozden, S., Sonmez, K., 1998. Erodibility of some great soil groups in eastern Anatolia. International symposium on arid region soils: share our experiences to conserve the land, Izmir, Turkey, 21-24 September 1998, 154-159.

Pachauri, A.K., Pant, M., 1992. Landslide hazard mapping on geological attributes. *Engineering Geology*, 32, 81-100.

Pachauri, A.K., Gupta, P.V., Chander, R., 1998. Landslide zoning in a part of the Garhwal Himalayas. *Environmental Geology*, 36(3–4), 325–334.

Pack, R.T., Tarboton, D.G., Goodwin, C.N., 1998. The SINMAP approach to terrain stability mapping. In D. Moore and O. Hungr (eds.), Proceedings of the 8th IAEG Congress, Vancouver. Balkema, Rotterdam, pp 1157–1165

Panizza, M., 1973. Glacio pressure implication in the production of landslides in the dolomitic area. *Geol. Appl. Idrogeol.*, 8, 289-297.

Parise, M., 2001. Landslide mapping techniques and their use in the assessment of the landslide hazard. *Phys Chem Earth*, C 26(9), 697–703.

Pellegrini, G.B., Surian, N., 1996. Geomorphological study of the Fadalto landslide, Venetian Prealps, Italy. *Geomorphology*, 15, 337-350.

Petley, D.N., Mantovani, F., Bulmer, M.H., Zannoni, A., 2005. The use of surface monitoring data for the interpretation of landslide movement patterns. *Geomorphology*, 66, 133-147.

Piccio, A., 1988. Slope movements in Scisti del Laghi (Como lake, southern Alps, Italy). In: C. Bonnard (ed.), Landslides, Proceedings of the fifth International Symposium on landslides, vol. 2, Lausanne, Switzerland, 10-15 July 1988, 1349-1352.

Pieraccini, M., Luzi, G., Atzeni, C., 2001. Terrain mapping by ground-based interferometric radar. *IEEE Trans. On Geosci. and Remote Sensing*, 39(10), 2176-2181.

Piloni, G., 1607. Historia della Citta di Belluno. Venezia.

Plassard, J., 1971. Carte pluviométrique du Liban à l'échelle de 1/200 000. République Libanaise. Ministère des travaux publics. Direction Générale de l'Aviation Civile.

Plassard, J., Kogos, S.J., 1981. Séismicité du Liban. Catalogue des séismes ressentis. Collection des annales – Mémoires de l'observatoire de Ksara, Tome IV (Séismologie), Cahier 1, 3eme édition, Conseil National de la Recherche Scientifique, Beyrouth, Liban, 48p.

Poesen, J., 1983. An improved splash transport model. *Zeitshrift fur Geomorphologie*, 29(2), 373-382.

Poesen, J., Lavee, H., 1994. Rock fragments in top soils: significance and processes. *Catena*, 23, 1-28.

Poesen, J., Hooke, J., 1997. Erosion, flooding and channel management in Mediterranean environments of Southern Europe. *Progress in Physical Geography*, 21(2), 157-199.

Pomeroy, J.S., 1974. Landslide susceptibility map of part of the Valencia 7-1/2 minute quadrangle, Allegheny County and vicinity, Pennsylvania. US Geological Survey Open-File Report 74-116, 18p.

Prina, E., Bonnard, Chr., Vulliet, L., 2004. Vulnerability and risk assessment of a mountain road crossing landslides. *Riv Ital Giotec*, 2, 67–79.

Radbruch, D.H., 1970. Map of relative amounts of landslides in California. US Geological Survey Open-File Report 70-1485, 36p.

Radbruch, D.H., Crowther, K.C., 1973. Map showing areas of estimated relative susceptibility to landsliding in California. US Geological Survey Miscellaneous Geologic Investigations Map I-747, scale 1:1,000,000.

Ramlin, M.F., Peltley, D.N., Murphy, W., 2000. The detection of relict landslides using airborne Thematic Mapper Imagery. ISSMGE and BGS 8th Ineternational Symposium on landslides, 26-30 June 2000, 1269-1274.

Rautela, P., Lakhera, R.C., 2000. Landslide risk analysis between Giri and Tons rivers in Himachal Himalaya (India). *IAG*, 2(3/4), 153–160.

Refice, A., Capolongo, D., 2002. Probabilistic modelling of uncertainties in earthquake-induced landslide hazard assessment. *Computers & Geosciences*, 28(6), 735-749.

Refice, A., Bovenga, F., Guerriero, L., Wasowski, J., 2001. InSAR applications to landslide studies. International Geoscience and Remote Sensing Symposium (IGARSS), 1,144–146.

Reifenberg, A., 1935. Soil formation in the Mediterranean. Transact. 3rd Intern. Congr. Soil Sci., Paris 1, 306-309.

Reifenberg, A., 1952. The soils of Syria and Lebanon. *Soil Science*, 3(1), 68-88.

Remondo, J., González-Díez, A., Dííaz de Terán, J.R., Cendrero, A., Fabbri, A., Chung, C.J.F., 2003. Validation of landslide susceptibility maps examples and applications from a case study in Northern Spain. *Natural Hazards*, 30(3), 437–449.

Remondo, J., Bonachea, J., Cendrero, A., 2004. Probabilistic landslide hazard and risk mapping on the basis of occurrence and damages in the recent past. In W.A. Lacerda, M. Ehrlich, S.A.B. Fontoura, and A.S.F. Sayao (eds.), Landslides: evaluation and stabilization. Balkema, Taylor & Francis Group, London, 125–130.

Rezig, S., Favre, J.L., Leroi, E., 1996. The probabilistic evaluation of landslide risk. In: K. Senneset (ed.), Proceedings of the VIth I.S.L., Trondheim, Norway. Balkema, Rotterdam, 351–355.

Rickenmann, D., Zimmermann, M., 1993. The 1987 debris flows in Switzerland: documentation and analysis. *Geomorphology*, 8, 175-189.

Rizzo, V., 2002. GPS monitoring and new data on slope movements in the Maratea Valley(potenza, Basilicata). *Phys Chem Earth*, 27, 1535–1544.

Rizzo, V., Tesauro, M., 2000. SAR interferometry and field data of Randazzo landslide (Eastern Sicily, Italy). *Phys Chem Earth*, 25(9), 771–780.

Rocha, G.C., 2004. Landslide risk mapping methodology applied to medium size urbanities in Brazil: case study of Juiz de Fora town, Minas Gerais state. In W.A. Lacerda, M. Ehrlich, S.A.B. Fontoura, and A.S.F. Sayao (eds.), Landslides: evaluation and stabilization. Balkema, Taylor & Francis Group, London, 297–302.

Rodríguez Ortiz, J.M., Prieto, C., Hinojosa, J.A., 1978. Regional studies on mass movements in Spain. Proceedings of the IIIrd I.A.E.G. Congress I, 1(29), 267–278.

Romana, M., 1985. New adjustment ratings for application of Bieniawski's classification to slopes. International symposium on the role of rock mechanics, ISRM, Zacatecas, 49–53.

Romeo, R., 2000. Seismically induced landslide displacements: a predictive model. *Engineering Geology*, 58, 337-351.

Roose, E., 1994. Introduction à la GCES. *Bulletin pédologique FAO*, 70, 420p.

Roose, E., Arabi, M., Brahamia, K., Chebbani, R., Mazour, M., Morsli, B., 1993. Erosion en nappe et ruissellement en montagne méditerranéenne algérienne. Réduction des risques érosifs et intensification sur la production agricole par la GCES : synthèse des campagnes 1984-1995 sur un réseau de 50 parcelles d'érosion. *Cahiers Orstom, série Pédologie*, 28(2), 289-308.

Rott, H., Scheuchl, B., Siegel, A., Grasemann, B., 1999. Monitoring very slow slope movements by means of SAR interferometry: a case study from a mass waste above a reservoir in the Otztal Alps, Austria. Geophyscal Res. Letters, 26, 1629-1632.

Rumsey, H.C., Morris, G.A., Green, R.R., Goldstein, R.M., 1974. A radar brightness and altitude image of a portion of Venus. *Icarus*, 23, 1-7.

Saaty, T.L., 1980. The analytical hierarchical process. McGraw Hill, New York, 350p.

Saaty, L.T., 1988. The analytical hierarchy process: planning, priority setting, resource allocation. RWS publications, Pittsburgh, 287 p.

Sabagh, G.N., 1966. Géologie des gisements ferrifères du Liban. Thèse Doctorat d'Université, Grenoble, 153p.

Safi, S., 1999. Assessing climate change impacts and adaptation on marine ecosystems. Lebanon's National Program for climate change (L-NPCC). UNDP, Ministry of Environment, Beirut.

Saha, A.K., Gupta, R.P., Arora, M.K., 2002. GIS-based landslide hazard zonation in the Bhagirathi (Ganga) valley, Himalayas. *International Journal of Remote Sensing*, 23 (2), 357-369.

Saha, A.K., Gupta, R.P., Sarkar, I., Arora, M.K., Csaplovics, E., 2005. An approach for GIS-based statitistical landslide susceptibility zonation-witj a case study in the Himalayas. *Landslides*, 1, 61-2005.

Sanlaville, P., 1977. Etude géomorphologique de la région littorale du Liban. Publications de l'Université Libanaise. Section des études géographiques, Beyrouth, tome I, 405p.

Santacana, N., Baeza, B., Corominas, J., De Paz, A., Marturia, J., 2003. A GIS-based multivariate statistical analysis for shallow landslide susceptibility mapping in La Pobla de Lillet Area (Eastern Pyrenees, Spain). *Natural Hazards*, 30, 281-295.

Sauchyn, D.J., Trench, N.R., 1978. Landsat applied to landslide mapping. *PE & RS*, 44(6), 735-741.

Saaty, L.T., Vargas, L.G., 2001. Models, methods, concepts, and applications of the analytical hierarchy process. Kluwer Academic, Boston, 333 p.

Sayegh, A-H., Saliba, A-T., 1969. Some physical and chemical properties of soils in the Beqaa's plain, Lebanon. *Soil Science*, 20, 168-175.
Schiavon, G., Del Frate, F., D'Ottavio, D., Stramondo, S., 2003. Landslide identification by SAR interferometry: the Sarno case. International Geoscience and Remote Sensing Symposium (IGARSS), 4, 2428–2429.
Schindler, C., Gyger, M., 1988. The landslide of Zug seen 100 years after the analysis of Albert Hiem. Proceedings of the fifth international symposium on landslide, Lausanne, 2, 1371-1380.
Schmidt, R.H., MacCannel, J., 1955. Basic problems, techniques and theory of isopleth mapping. *J Am Stat Assoc*, 50(269), 220–239.
Schmoll, H.R., 1974. Slope-stability map of Anchorage and vicinity. Alaska US GeolSurv Misc Inv Map I–787–E.
Scott, G.R., 1972. Map showing landslides and areas susceptible to landslides in the Morrison Quadrangle, Jefferson County, Colorado. US Geological Survey. Map I-790-B, USA.
Schuster, R.L., Fleming, R.W., 1986. Economic losses and fatalities due to landslides. *Association of Engineering Geologists Bulletin*, 23(1), 11-28.
Searle, T.R., 1972. The geotechnical properties of cretaceous clay-shales in Lebanon. Thesis, University of Salford, 247p.
Sefidgari, R., 2002. Evaluating of landslide hazard zonation methods of Damavand drainage basin. M.Sc. Thesis, Tehran University, Iran.
Selby, M.J., 1980. A rock mas strength classification for geomorphic purposes: with tests from Antarctica and New Zealand. *Zeitschrift fur Geomorphology*, 24, 31-51.
Seshgiri, D.N., Lakshmi Kanathan, C.B., Upendran, R., Subramanian, K., 1982. Landslide zonation in Nilgiri Plateau, Tamilnadu, India. Proceedings, Fourth Congress of IAEG, New Delhi, 1, 379-390.
Shorn, J., 1902. Die Erden von Tirol und Voralberg. Innsburck, 186p.
Shortliffe, E.H., Buchanan, G.G., 1975. A model of inexact reasoning in medicine. *Math Biosci*, 23, 351–379.
Shou, K.J., Wang, C.F., 2003. Analysis of the Chiufengershan landslide triggered by the 1999 Chi-Chi earthquake in Taiwan. Engineering Geology, 68, 237-250.
Siddle, R.C., Dakhal, A.S., 2003. Recent advances in the spatial and temporal modeling of shallow landslides. International Congress on Modelling and Simulation. University of Wales, Nedlands, 602–607.
Simons, D.B., Li, R.M., Ward, T.J., 1978. Mapping of potential landslide areas in terms ofslope stability. Fort Collins, Colorado. Civil Engineering Dept., Colorado State University, 75p.
Singhroy, V., 1995. SAR integrated techniques for geohazard assessment. *Advanced Space Research*, 15(11), 67-78.
Singhroy, V., Molch, K., 2004. Characterizing and monitoring rockslides from SAR techniques. *Adv Space Res*, 33(3), 290–295.
Soeters, R., van Westen, C.J., 1996. Slope instability recognition, analysis and zonation. In A.K. Turner and R.L. Schuster (eds.), Landslides investigation and mitigation. Transportation Research Board, Special Report 247. National Academy Press, Washington, 129–177.
Sorriso-Valvo, M., 2002. Landslides: from inventory to risk. In R. Rybá and S. Wagner (eds.), Proceedings of the 1st European conference on landslides, Prague. Balkema, Rotterdam, 59–79.
Spieker, E.C., Gori, P.L., 2000. National landslide hazards mitigation strategy: a framework for loss reduction. Open-file report 00-450, Department of Interior, U.S.G.S., USA, 49p.

Spieker, E.C., Gori, P.L., 2003a. Partnerships for reducing landslide risk: assessment of the national landslide hazards mitigation strategy. The National Academy of Sciences Press, Washington, DC.

Spieker, E.C., Gori, P.L., 2003b. National landslide hazards mitigation strategy: a framework for loss reduction. USGS Circular 1244. US Department of Interior, U.S.G.S. Reston, Virginia, 56p.

Spizzichino, D., Falconi, L., Delmonaco, G., Margottini, C., Puglisi, V., 2004. Integrated approach for landslide risk assessment of Craco village (Italy). In W.A. Lacerda, M. Ehrlich, S.A.B. Fontoura, A.S.F. Sayao (eds.), Landslides: evaluation and stabilization. Balkema, Taylor & Francis Group, London, 237–242.

STADL, 2002. Schéma directeur d'aménagement du territoire libanais. Rapport final, Dar El Handassah (Liban) et IAURIF (France), 239p.

Stephens, P.R., 1988. Use of satellite data to map landslides. 9th Asian Conf. on remote sensing, Bangkok, Thailand, 23-29 November 1988, J11.1-J11.7.

Talhouk, S.N., Zurayk, R., Khuri, S., 2001. Conservation of the coniferous forests of Lebanon: past, present and future prospects. *Oryx*, 35(3), 206-215.

Tarchi, D., Casagli, N., Fanti, R., Leva, D.D., Luzi, G., Pasuto, A., Pieraccini, M., Silvano, S., 2003. Landslide monitoring by using ground-based SAR interferometry: an example of application to the Tessina landslide in Italy. *Engineering Geology*, 68(1– 2), 15–30.

Tarzi, J., Paeth, R., 1975. Genesis of a Mediterranean red and a white rendzina soil from Lebanon. *Soil Science*, 120(4), 272-277.

Tavitian, C., 1974. Clay mineralogy and geotechnical properties of cretaceous clay-shales in Lebanon. Ph.D. thesis, University of Salford, 247p.

Tayara, Z., 1998. Etude hydro-pluviométrique comparative des basins versants de la région côtière intermédiaire du Liban (le Damour, l'Awali-Bisri, le Sainiq et le Zahrani). Publications de l'Université Libanaise, Section des études géographiques, 1, 225p.

Terlian, M.T.J., Van Asch, T.W.J., van Westen, C.J., 1995. Deterministic modelling in GIS-based landslide hazard assessment. In A. Carrara, and F. Guzzetti (eds.), Geographical information system in assessing natural hazards. Kluwer Academic Publishers, Dordrecht, The Netherlands, 57-77.

Thornes, J-B., 1995. Mediterranean desertification and the vegetation cover. In: R. Fantechi, D. Peter, P. Balabanis and J-L. Rubio (eds.), Desertification in a European context: physical and socioeconomic aspects. European Commission Report EUR 15415, 169-194.

Tuglaman, K., 1975. The stratigraphy, structure and hydrogeology of Naher El-Kaleb-Ma'ameltien coastal area. Unpublished M.Sc. Thesis, American University of Beirut, Geology Department, 79p.

Turner, A.K., Schuster, R.L., 1996. Landslides, Investigation and Mitigation. Transportation Research Board, special report 247, National Research Council, National Academy Press, Washington D.C., 673p.

Turrini, M.C., Visintainer, P., 1998. Proposal of a method to define areas of landslide hazard and application to an area of the Dolomites, Italy. *Engineering Geology*, 50, 255–265.

Uromeihy, A., Mahdavifar, M.R., 2000. Landslide hazard zonation of the Khorshrostam area, Iran. *Bull Eng Geol Environ*, 58, 207–213.

USGS, 1967. Earth Science information in land use planning. US Geological Survey, Circular no. 721.

van Westen, C.J., 1993. Application of geographic information system to landslide hazard zonation. *ITC publication*, 15, ITC Enschede, 245p.

van Westen, C.J., 1997. Statistical landslide hazard analysis. Aplication guide, ILWIS, 2.1 for windows. *ITC*, Enschede, The Netherlands, 73-84.

van Westen, C.J., 2000. The modelling of landslide hazards using GIS. *Surveys in Geophysics*, 21(2-3), 241-255.
van Westen, C.J., 2004. Geoinformation tools for landslide risk assessment: an overview of recent developments. In W.A. Lacerda, M. Ehrlich, S.A.B. Fontoura, A.S.F. Sayao (eds.), Landslides: evaluation and stabilization. Balkema, Taylor & Francis Group, London, 39–56.
Varnes, D.J., 1978. Landslide types and processes. In E.B. Eckel (ed.), Landslides and engineering practice, special report n° 29, Highway Research Board, pp.20-47.
Varnes, D.J., 1984. Landslide hazard zonation: a review of principles and practice. UNESCO Press, Paris, 63p.
Vaunat, J., Leroueil, S., 2002. Analysis of post-failure slope movements within the framework of hazard and risk analysis. *Natural Hazards*, 26, 83–109.
Vecchia, O., 1978. A simple terrain index for the stability of hillsides or scarps. In J.D. Geddes (ed.), Large ground movements and structures. Wiley, New York Toronto, 449-461.
Verheye, W., Osman, A., 1974. Observations sur la lithologie du Liban Sud et son influence sur le développement des sols et le façonnement du paysage. Institut des Recherches Agronomiques Liban. Publication no. 55, série scientifique, Septembre 1974, 38p.
Venables, W.M., Ripley, B.D., 1994. Modern applied statistics with S-Plus. New-York: Springer.
Verstappen, H.T., 1995. Aerospace technology and natural disaster reduction. *Advanced Space Research*, 15(11), 3-15.
Vietmeier, J., Wagner, W., Dikau, R., 2000. Monitoring moderate slope movements (landslides) in the Southern French Alps using differential SAR interferometry. European Space Agency (special publication) ESA SP, 478, 559–563.
Wainwright, J., 1996. Hillslope response to extreme storm events: the example of the Vaison-La-Romaine event. In M-C. Anderson and S-M. Brooks (eds.), Advances in hillslope processes. Chichester, Wiley, 997-1026.
Walley, C.D., 1998. Some outstanding issues in the geology of Lebanon and their importance in the tectonic evolution of the Levantine region. In A.H.F. Robertson and M.C. Comas (eds.), Collision-related processes in the Mediterranean region. *Tectonophysics*, 298, 37-62.
Wang, S.Q., Unwin, D.J., 1992. Modeling landslide distribution on loess soils in China: an investigation. *International Journal of Geographical Information Systems*, 6, 391-405.
Wang, X., Jiang, Y., Zhao, Y., Pan, L., 2002. Study and application on the visualization of geological information system in landslideYanshilixue Yu Gongcheng Xuebao/Chinese. *J Rock Mech Eng*, 21, 2511–2514.
Way, D.S., 1978. Terrain Analysis. McGraw-Hill Inc., New York. 438p.
Wegmuller, U., Strozzi, T., 1998. Characterization of differential interferometry approaches. EUSAR'98, 25-27 May 1998, Friedrichshafen, Germany, VDE-Verlag, ISBN 3-8007-2359-X, 237-240.
Werner, C., Wiesmann, W.A., Strozzi, T., 2003. Interferometric point target analysis with JERS-1 L-Band SAR data. IGARSS'03, Toulouse, France, 21025 July 2003, 6p.
Wetzel, H.U., Roessner, S., Sarnagoev, A., 2000. Remote sensing and GIS based geological mapping for assessment of landslide hazard in Southern Kyrgyztan (Central Asia). In C.A. Brebbia and P. Pascolo (eds.), Management information systems 2000-GIS and remote sensing. Management information systems, vol 1. WIT Press, Ashurst, 355–366.
Wieczorek, G.F., Gori, P.L., Jager, S., Kappel, W.M., Negussey, D., 1996. Assessment and management of landslide hazards near Tully valley landslide, Syracuse, New York,

USA. Proc. 7th Int. Symposium on landslides, Trondheim, Balkema, Rotterdam, 411-416.
Wilkerson, F.D., Schmid, G.L., 2003. Debris flow in Glacier National Park, Montana: geomorphology and hazards. *Geomorphology*, 55, 317-328.
Wu, W., Sidle, R.C., 1995. A distributed slope stability model for steep forested basins. *Water resources research*, 31, 2097-2110.
Wu, S.R., Shi, L., Wang, R.J., Tan, C.X., Hu, D.G., Mei, Y.T., Xu, R.C., 2001. Zonation of the landslide hazards in the fore reservoir region of the three Gorges project on the Yangtze river. *Engineering Geology*, 59, 51-58.
Xie, Q.M., Xia, Y.Y., 2004. Systems theory for risk evaluation of landslide hazard. *Int J Rock Mech Min Sci*, 41(3), CD-ROM, Elsevier, Netherlands.
Yadav, R.R., Kulieshius, P., 1992. Dating of earthquakes: Tree ring responses to the catastrophic earthquake of 1887 in Alma-Ata, Kazakhstan. *The Geographical Journal*, 158(3), 295-299.
Yan, T.Z., 1988. Advances on quantitative prediction of landslide researches. *Hydrogeological Engineering Geology*, 6, 8-14.
Yatsut, E., 1967. Some problems on mass movements. *Geografiska Annaler Series A*, 49a(2-4), 396-401.
Yin, K.L., Yan, T.Z., 1988. Statistical prediction model for slope instability of metamorphosed rocks. *Landslides*, 2, 1269-1272.
Yuan, D., Lucas, J.R., Holland, D.E., 1998. A Landsat MSS time series model and its application in geological mapping. *ISPRS Journal of Photogrammetry & Remote Sensing*, 53, 39-53.
Zaruba, Q., Mencl, V., 1982. Landslides and their control. 2nd ed., Amesterdam, Elsevier.
Zaruba, Q., Mencl, V., 1969. Landlides and their control. Elsevier, Amesterdam, 205p.
Zemp, M., 2002. GIS-basierte Modellierung der glazialen Sedimentbilanz. Diploma thesis, Department of Geography, University of Zurich, Zurich.
Zerger, A., 2002. Examining GIS decision utility for natural hazard risk modelling. *Environ Modell Softw*, 17, 287–294.
Zhang, H., Burton, S., 1999. Recursive Partitioning in the Health Sciences. Springer, New York, 226p.
Zhou, G., Li, R., 2000. Accuracy evaluation of ground points from IKONOS high-resolution satellite imagery. *Photogrammetric Engineering and Remote Sensing*, 66(9), 1103-1112.
Zhou, C.H., Yue, Z.Q., Lee, C.F., Zhu, B.Q., Wang, Z.H., 2001. Satellite image analysis of a huge landslide at Yi Gong, Tibet, China. *Quarterly Journal of Engineering Geology and Hydrogeology*, 34, 325-332.
Zhou, G., Esaki, T., Mitani, Y., Xie, M., Mori, J., 2003. Spatial probabilistic modeling of slope failure using an integrated GIS Monte Carlo simulation approach. *Engineering Geology*, 68(3–4), 373–386.
Zisk, S.H., 1972. Lunar topography: first radar-interferometer measurements of the Alphonsus-Ptolemaeus-Arzachel region. *Science*, 178, 977-980.

Annex 1
ISP commands description

a)

Create Symbolic Links to the SLC's:

ln -s /rif/data/ers/slc/078/2925/e1/e1_20607/20607.slc e120607.slc
ln -s /rif/data/ers/slc/078/2925/e2/e2_00934/00934.slc e200934.slc

Create the parameter files:(to know the SLC geometry)

par_MSP /progs/gamma/MSP/sensors/ERS1_ESA.par
/rif/data/ers/slc/078/2925/e1/e1_20607/p20607.slc.par e120607.par
par_MSP /progs/gamma/MSP/sensors/ERS2_ESA.par
/rif/data/ers/slc/078/2925/e2/e2_00934/p00934.slc.par e200934.par

---

b)

Offset Estimation;
create_offset e120607.par e200934.par e120607_e200934.off

image intensity:
init_offset e120607.slc e200934.slc e120607.par e200934.par e120607_e200934.off 2 10

init_offset e120607.slc e200934.slc e120607.par e200934.par e120607_e200934.off 1 1

Coarse Registration;
offset_pwr e120607.slc e200934.slc e120607.par e200934.par e120607_e200934.off e120607_e200934.offs e120607_e200934.snr 150 150 e120607_e200934.offsets 1 50 50 6.5

c)

Fine Registration;
offset_fit e120607_e200934.offs e120607_e200934.snr e120607_e200934.off e120607_e200934.coffs e120607_e200934.coffsets 6.5 4 1
(get std deviation in range shud be about 0.1 or one-tenth of a pixel resoltion for ERS is 20m by 5m..ie. 20m in range and 5m in azimuth)

---

d)

Interpolate slave in master geometry using offset polynomial(estimated in offset_fit step):
resampling step

SLC_interp e200934.slc e120607.par e200934.par e120607_e200934.off e200934.rslc e200934.rpar

Interferogram Generation:(Complex Multiplication)
Both the slc's have been resampled to the geometry of e212958, so use *.rslc and *.rpar files:

ln -s
ln -s

SLC_intf e120607.rslc e200934.rslc e120607.rpar e200934.rpar e120607_e200934.off e120607_e200934.int 2 10
rasmph e120607_e200934.int 2456
gimp e120607_e200934.int.ras

Generate a multi-look image(mli) for each SLC:

multi_look e120607.rslc e120607.rpar e120607.rmli e120607.rmli.par 2 10
multi_look e200934.rslc e200934.rpar e200934.rmli e200934.rmli.par 2 10

#create symbolic links for power images
ln -s e120607.mli e120607_e200934.pwr1
ln -s e200934.rmli e120607_e200934.pwr2

raspwr is to generate a raster file from power image(or amplitude image)
2456 is the width of the interferogram.
gimp is a visualization tool that comes with Linux (not GAMMA)
raspwr e120607_e200934.pwr1 2456
gimp e120607_e200934.pwr1.ras

==========

e)

Initial baseline estimate
base_init e120607.par e200934.rpar - - e120607_e200934.base 0

Flatten the Interferomgram (remove curved earth phase)----> Usually used for preview
rasmph is to generate a raster file from wrapped phase.

```
ph_slope_base e120607_e200934.int e120607.par e120607_e200934.off
e120607_e200934.base e120607_e200934.flt
rasmph e120607_e200934.flt 2456
gimp e120607_e200934.flt.ras

================================================
```

f)

```
# With that done, proceed with phase simulation and differential InSAR ...

ln -s ../GEO/078.hgt_map

# Topographic Phase simulation step --> to calculate the phase contributrion due to
topography(from DEM);
# 078.hgt_map comes out of the geocoding step:

phase_sim e120607.par e120607_e200934.off e120607_e200934.base 078.hgt_map
e120607_e200934.sim_unw 0 0
rasrmg e120607_e200934.sim_unw 2456
gimp e120607_e200934.sim_unw.ras


# Subtract the topographic phase from the wrapped interferogram.
# The result is a wrapped phase without topography.


sub_phase e120607_e200934.int e120607_e200934.sim_unw
../GEO/e120607_e200934.geo_par  1 0
rasmph e120607_e200934.int_notopo 2456
```

g)

```
ITERATIVE FILTERING ----to reduce phase noise
Run filter on the wrapped interferogram without topography to reduce phase noise.
adf e120607_e200934.int_notopo e120607_e200934.128.sm_notopo
e120607_e200934.smcc 2456 .5 128 - - - - .15
rasmph e120607_e200934.128.sm_notopo 2456
gimp e120607_e200934.128.sm_notopo.ras


# Mask points with low coherence (here below 0.25)---> helps proper unwrapping.

rascc_mask e120607_e200934.smcc e120607_e200934.pwr1 2456 - - - - - .25 - - - - -
e120607_e200934.smcc_25_mask.ras
gimp e120607_e200934.smcc_25_mask.ras

# Phase Unwrapping Step;
# Unrwapped phase without topography:
```

```
mcf e120607_e200934.128c.sm_notopo e120607_e200934.smcc
e120607_e200934.smcc_15_mask.ras e120607_e200934.128c.unw25 2456 0 - - - - 1
1 - - - 1
rasrmg e120607_e200934.128c.unw25 e120607_e200934.pwr1 2456 - - - - - 1
gimp e120607_e200934.128c.unw25.ras

# Add topographic phase back to generate a complete unwrapped interferogram:(with
topogrphay, deformation, and curved Earth)...effectively, it is the same as running an
mcf unwrapping step on the wrapped interferogram (*.int)
#Essentially done to improve baseline estimate.

sub_phase e120607_e200934.128c.unw25 e120607_e200934.sim_unw
../GEO/e120607_e200934.geo_par e120607_e200934.128c.unw_noflat 0 1
==============================================
```

h)

```
# Extract GCPs to improve baseline estimate


extract_gcp 078.hgt_map e120607_e200934.off 078.gcp 25 25
e120607_e200934.smcc_70_mask.ras
gcp_phase e120607_e200934.128c.unw_noflat e120607_e200934.off 078.gcp
e120607_e200934.gcp_data
base_ls e120607.par e120607_e200934.off e120607_e200934.gcp_data
e120607_e200934.base 0

# Precise baseline calculation
base_perp e120607_e200934.base e120607.par e120607_e200934.off

# Use precise baseline to estimate topographic phase contribution accurately
phase_sim e120607.par e120607_e200934.off e120607_e200934.base 078.hgt_map
e120607_e200934.128c.sim_unw2 0 1

# Use the accurate topographic phase estimate and subtract from the complete
unwrapped interferogram
# The output is a differential interferogram showing only phase due to deformation.

sub_phase e120607_e200934.128c.unw_noflat e120607_e200934.128c.sim_unw2
../GEO/e120607_e200934.geo_par e120607_e200934.128c.unw_dif 0 0

rasrmg e120607_e200934.128c.unw_dif e120607_e200934.pwr1 2456 - - - - - 1
rasrmg e120607_e200934.128c.unw_dif - 2456 - - - - - 1 - - - -
e120607_e200934.128c.unw_dif_nopwr.ras
```

Annex 2
IPTA preparation

Link original SLCs
cd rslc0

```
ln -s ../../resample/e104732.rslc
ln -s ../../resample/e105233.rslc
ln -s ../../resample/e106235.rslc
ln -s ../../resample/e111245.rslc
ln -s ../../resample/e111746.rslc
ln -s ../../resample/e120607.rslc
ln -s ../../resample/e121609.rslc
ln -s ../../resample/e122110.rslc
ln -s ../../resample/e125116.rslc
ln -s ../../resample/e132631.rslc
ln -s ../../resample/e200934.rslc
ln -s ../../resample/e201936.rslc
ln -s ../../resample/e202437.rslc
ln -s ../../resample/e205443.rslc
ln -s ../../resample/e206445.rslc
ln -s ../../resample/e215964.rslc
ln -s ../../resample/e221976.rslc
ln -s ../../resample/e226986.rslc
ln -s ../../resample/e242016.rslc
ln -s ../../resample/e242517.rslc
ln -s ../../resample/e212958.slc e212958.rslc

# copy the rpar files

cp ../../resample/*.rpar *.rpar

cp ../../resample/e104732.rpar e104732.rpar
cp ../../resample/e105233.rpar e105233.rpar
cp ../../resample/e106235.rpar e106235.rpar
cp ../../resample/e111245.rpar e111245.rpar
cp ../../resample/e111746.rpar e111746.rpar
cp ../../resample/e120607.rpar e120607.rpar
cp ../../resample/e121609.rpar e121609.rpar
cp ../../resample/e122110.rpar e122110.rpar
cp ../../resample/e125116.rpar e125116.rpar
cp ../../resample/e132631.rpar e132631.rpar
cp ../../resample/e200934.rpar e200934.rpar
cp ../../resample/e201936.rpar e201936.rpar
cp ../../resample/e202437.rpar e202437.rpar
cp ../../resample/e205443.rpar e205443.rpar
cp ../../resample/e206445.rpar e206445.rpar
cp ../../resample/e215964.rpar e215964.rpar
cp ../../resample/e221976.rpar e221976.rpar
cp ../../resample/e226986.rpar e226986.rpar
```

Annex 2 *(continue)*

cp ../../resample/e242016.rpar e242016.rpar
cp ../../resample/e242517.rpar e242517.rpar
cp ../../resample/e212958.par e212958.rpar

Cut subset of SLCs

cd rslc

SLC_copy <SLC_in> <SLC_par_in> <SLC_out> <SLC_par_out> [fcase] [sc] [roff] [nr] [loff] [nl] [swap] [header_lines]

SLC_copy ../rslc0/e104732.rslc ../rslc0/e104732.rpar e104732.rslc e104732.rpar 2 - 812 500 13250 2500
SLC_copy ../rslc0/e105233.rslc ../rslc0/e105233.rpar e105233.rslc e105233.rpar 2 - 812 500 13250 2500
SLC_copy ../rslc0/e106235.rslc ../rslc0/e106235.rpar e106235.rslc e106235.rpar 2 - 812 500 13250 2500
SLC_copy ../rslc0/e111245.rslc ../rslc0/e111245.rpar e111245.rslc e111245.rpar 2 - 812 500 13250 2500
SLC_copy ../rslc0/e111746.rslc ../rslc0/e111746.rpar e111746.rslc e111746.rpar 2 - 812 500 13250 2500
SLC_copy ../rslc0/e120607.rslc ../rslc0/e120607.rpar e120607.rslc e120607.rpar 2 - 812 500 13250 2500
SLC_copy ../rslc0/e121609.rslc ../rslc0/e121609.rpar e121609.rslc e121609.rpar 2 - 812 500 13250 2500
SLC_copy ../rslc0/e122110.rslc ../rslc0/e122110.rpar e122110.rslc e122110.rpar 2 - 812 500 13250 2500
SLC_copy ../rslc0/e125116.rslc ../rslc0/e125116.rpar e125116.rslc e125116.rpar 2 - 812 500 13250 2500
SLC_copy ../rslc0/e132631.rslc ../rslc0/e132631.rpar e132631.rslc e132631.rpar 2 - 812 500 13250 2500
SLC_copy ../rslc0/e200934.rslc ../rslc0/e200934.rpar e200934.rslc e200934.rpar 2 - 812 500 13250 2500
SLC_copy ../rslc0/e201936.rslc ../rslc0/e201936.rpar e201936.rslc e201936.rpar 2 - 812 500 13250 2500
SLC_copy ../rslc0/e202437.rslc ../rslc0/e202437.rpar e202437.rslc e202437.rpar 2 - 812 500 13250 2500
SLC_copy ../rslc0/e205443.rslc ../rslc0/e205443.rpar e205443.rslc e205443.rpar 2 - 812 500 13250 2500
SLC_copy ../rslc0/e206445.rslc ../rslc0/e206445.rpar e206445.rslc e206445.rpar 2 - 812 500 13250 2500
SLC_copy ../rslc0/e215964.rslc ../rslc0/e215964.rpar e215964.rslc e215964.rpar 2 - 812 500 13250 2500
SLC_copy ../rslc0/e221976.rslc ../rslc0/e221976.rpar e221976.rslc e221976.rpar 2 - 812 500 13250 2500
SLC_copy ../rslc0/e226986.rslc ../rslc0/e226986.rpar e226986.rslc e226986.rpar 2 - 812 500 13250 2500

Annex 2 *(continue)*

SLC_copy ../rslc0/e242016.rslc ../rslc0/e242016.rpar e242016.rslc e242016.rpar 2 - 812 500 13250 2500
SLC_copy ../rslc0/e242517.rslc ../rslc0/e242517.rpar e242517.rslc e242517.rpar 2 - 812 500 13250 2500
SLC_copy ../rslc0/e212958.rslc ../rslc0/e212958.rpar e212958.rslc e212958.rpar 2 - 812 500 13250 2500

create RSLC_tab file

these file is to Keep track of all the SLCs and its parametric files

Make MLI images of all SLCs

cd ..
<SLC_tab> <MLI_dir> <rlks> <azlks> [sflag] [scale] [exp]

mk_mli_all RSLC_tab rmli 1 5

#extract point values, generate pSLC_par

<SLC_tab> <plist> <pmask> <pSLC_par> <pSLC> <SLC_rec_num>

SLC2pt RSLC_tab pt - pSLC_par pSLC -

PREPARE AND IMPORT DEM DATA

multi_look <SLC> <SLC_par> <MLI> <MLI_par> <rlks> <azlks> [loff] [nlines] [scale] [image_format]

multi_look rslc/e212958.rslc rslc/e212958.rpar bloudan.11.mli bloudan.11.mli.par 1 1

Start importing the DEM

ln -s geo/bloudan.hgt

data2pt <f_in> <par_in> <plist> <SLC_par> <pdata> <rec_num> <type>

data2pt bloudan.hgt bloudan.11.mli.par pt rslc/e212958.rpar phgt0 1 2

To make an image of the DEM,

mk_2d_im <plist> <pmask> <itab> <SLC_par> <pdata> <srec> <nrec> <par_out> <type> <imode> <radius> <np_min> <out_dir> <ref_im> <cycle> <sflag> [start] [nlines]

mk_2d_im pt - itab rslc/e212958.rpar phgt0 1 1 rmli/e212958.rmli.par 2 3 1.2 1 . rmli/rmli_1_5.ave 200.0 1

Annex 3
ITAB table

A	B	C	D
1	4	1	1
1	5	2	1
1	8	3	1
1	10	4	1
1	15	5	1
1	16	6	1
1	17	7	1
4	5	8	1
4	8	9	1
4	10	10	1
4	15	11	1
4	16	12	1
4	17	13	1
5	8	14	1
5	10	15	1
5	15	16	1
5	16	17	1
5	17	18	1
8	10	19	1
8	15	20	1
8	16	21	1
8	17	22	1
10	15	23	1
10	16	24	1
10	17	25	1
15	16	26	1
15	17	27	1
16	17	28	1
2	3	29	1
2	7	30	1
2	12	31	1
2	18	32	1
2	19	33	1
3	7	34	1
3	12	35	1
3	18	36	1
3	19	37	1
7	12	38	1
7	18	39	1
7	19	40	1
12	18	41	1
12	19	42	1
18	19	43	1
4	9	44	1
4	13	45	1
4	14	46	1
9	13	47	1
9	14	48	1
13	14	49	1

A) Reference SLC record
B) Second SLC record
C) The interferogram point data stack record
D) A validity flag (1 = valid, 0 = not valid)

Annex 4
IPTA Commands

a)

mk_msr_pt <SLC_tab> <SLC_par> <MLI_par> <MLI_ras> <MSR_dir> [PWR_min] [mode] [MSR_cal] [PWR_cal] [min_MSR] [num_MSR] [delta_MSR]

mk_msr_pt RSLC_tab rslc/e212958.rpar rmli/e212958.rmli.par rmli/rmli_1_5.ave.ras msr .5 2 1.5 1 1.2 8 .1

==========

b)

evaluate spectral correlation function in the sp directory

mk_sp_all <SLC_tab> <sp_dir> [rlks] [azlks] [PWR_min] [CC_min] [MSR_min]

mk_sp_all RSLC_tab sp 4 4 .5 .4 1.2

#select points from spectral diversity result

thres_im_pt <f_in> <width> <plist> <t_min> <t_max> <rlks> <azlks>

thres_im_pt sp/ave.sp_cc 500 sp/pt_cc_33 .33 - 1 1

create image

ras_pt <plist> <pmask> <ras_in> <ras_out> [rlks] [azlks] [r] [g] [b] [xs] [zflg] [mflg]

ras_pt sp/pt_cc_33 - rmli/rmli_1_5.ave.ras sp/pt_cc_33.ras 1 5

#merge point lists

merge_pt <plist_tab> <plist_out> <N_min> <r_tol> <az_tol>

merge_pt plist_tab pt 1 0 0

ras_pt pt - rmli/rmli_1_5.ave.ras pt.ras 1 5

==========

c)

make point interferograms

mk_int_all <plist> <pmask> <pSLC_par> <itab> <pSLC> <pbase> <pint> [log]
mk_int_all pt - pSLC_par itab pSLC pbase pint pint.log

#make differential interferograms

mk_diff_all <plist> <pmask> <pSLC_par> <itab> <pbase> <bflag> <pint> <int_type> <phgt> <pdef> <patm> <psim_unw> <pdiff> [log]
mk_diff_all pt - pSLC_par itab pbase 0 pint 1 phgt0 - - psim_unw0 pdiff0

mk_2d_im <plist> <pmask> <itab> <SLC_par> <pdata> <srec> <nrec> <par_out> <type> <imode> <radius> <np_min> <out_dir> <ref_im> <cycle> <sflag> [start] [nlines]
mk_2d_im pt - itab rslc/e212958.rpar pdiff0 1 - rmli/e212958.rmli.par 0 - 4 3 diff0 rmli/rmli_1_5.ave - 0

==========

d)

Quality Control: qc_pt using threshhold of 1.0

qc_pt <plist> <pmask_in> <pmask_out> <pSLC_par> <itab> <pbase> <base_flag> <pdiff> <type> [sigma_max] [psigma] [dh_max] [def_max] [model] [bmax] [dtmax] [radius]
qc_pt pt - pmsk0a pSLC_par itab pbase 0 pdiff0 1 1.0 psigma0a

ras_pt pt - rmli/rmli_1_5.ave.ras pt.ras 1 5
ras_pt pt pmsk0a rmli/rmli_1_5.ave.ras pt_msk0a.ras 1 5

dis_ipta pt pmsk0a pSLC_par - itab pbase 0 pdiff0 1 pt_msk0a.ras 60. .02 2

==========

e)

run multi_def_pt to get first estimate of height corrections and deformation rate

multi_def_pt <plist> <pmask_in> <pSLC_par> <ppos> <itab> <pbase> <bflag> <pdiff> <pdiff_type> <np_ref> <pres> <pdh> <pdef> <punw> <psigma> <pmask_out> [dh_max] [def_max] [rpatch] [sigma_max] [sigma_max2] [model] [noise_min] [bmax] [dtmax]

to display with ga grph we run the following command
dis_ipta pt pmsk0a pSLC_par - itab pbase 0 pdiff0 1 pt_msk0a.ras 10. .005 2

Annex 4 ***(continue)***

multi_def_pt pt pmsk0a pSLC_par - itab pbase 0 pdiff0 1 16210 pres0 pdh0 - - psigma0 pmsk0 60 .01 25 2.5 1 2 - 300 750| tee def0.out

try to enhance by raising the patch size 100

multi_def_pt pt pmsk0a pSLC_par - itab pbase 0 pdiff0 1 16210 pres0 pdh0 - - psigma0 pmsk0 60 .01 100 1.2 .8 2 - 300 750 | tee def0.out

def_mod_pt <plist> <pmask_in> <pSLC_par> <ppos> <itab> <pbase> <bflag> <pdiff> <pdiff_type> <np_ref> <pres> <pdh> <pdef> <punw> <psigma> <pmask_out> [dh_max] [def_max] [sigma_max] [model] [pdh_err] [pdef_err] [ppc_err] [bmax] [dtmax]

def_mod_pt pt pmsk0a pSLC_par - itab pbase 0 pdiff0 1 23471 pres0 pdh0 - punw0 psigma0 pmsk0 60 .03 1.5 2 - - - 300 2800 | tee def0.out

==========

f)

adding height corrections;
lin_comb_pt pt pmsk0 phgt0 - pdh0 - phgt1 - 0 1 1 2
pdisdt_pwr24 pt pmsk0 rslc/e212958.rpar pdh0 - rmli/e212958.rmli.par rmli/rmli_1_5.ave 200 2

pdisdt_pwr24 pt pmsk0 rslc/e212958.rpar pdh0 - rmli/e212958.rmli.par rmli/rmli_1_5.ave 200 2

==========

g)

Height Iteration #1

making differential interferograms;(pdiff1 is wrapped differential)
mk_diff_all pt pmsk0 pSLC_par itab pbase 0 pint 1 phgt1 - - psim_unw1 pdiff1

ras_pt pt pmsk0 rmli/rmli_1_5.ave.ras pt_msk0.ras 1 5
dis_ipta pt pmsk0 pSLC_par - itab pbase 0 pdiff1 1 pt_msk0.ras 60. .02 2

def_mod_pt pt pmsk0 pSLC_par - itab pbase 0 pdiff1 1 23471 pres1 pdh1 pdef1 punw1 psigma1 pmsk1 30 .03 1.3 2 - - - 500 2800 | tee def1.out

Annex 4 ***(continue)***

lin_comb_pt pt pmsk0 phgt1 - pdh1 - phgt2 - 0 1 1 2
pdisdt_pwr24 pt pmsk0 rslc/e212958.rpar pdh1 - rmli/e212958.rmli.par
rmli/rmli_1_5.ave 200 2

Height Iteration #2

mk_diff_all pt pmsk0 pSLC_par itab pbase 0 pint 1 phgt2 - - psim_unw2 pdiff2

dis_ipta pt pmsk0 pSLC_par - itab pbase 0 pdiff2 1 pt_msk0.ras 60. .02 2

def_mod_pt pt pmsk0 pSLC_par - itab pbase 0 pdiff2 1 23471 pres2 pdh2 pdef2 punw2
psigma2 pmsk2 30 .03 1.3 2 - - - 500 2800| tee def2.out

lin_comb_pt pt pmsk0 phgt2 - pdh2 - phgt3 - 0 1 1 2
pdisdt_pwr24 pt pmsk2 rslc/e212958.rpar pdh2 - rmli/e212958.rmli.par
rmli/rmli_1_5.ave 200 2
ssh
pdisdt_pwr24 pt pmsk2 rslc/e212958.rpar pdef2 - rmli/e212958.rmli.par
rmli/rmli_1_5.ave 0.05 2

#Now use the deformation estimates in the last iteration to make differential interferograms so that it accounts for both topo and deformation;

==========

h)

Iteration #3

mk_diff_all pt pmsk0 pSLC_par itab pbase 0 pint 1 phgt3 pdef2 - psim_unw3 pdiff3

dis_ipta pt pmsk0 pSLC_par - itab pbase 0 punw3 1 pt_msk0.ras 60. .02 2

def_mod_pt pt pmsk0 pSLC_par - itab pbase 0 pdiff3 1 23471 pres3 pdh3 pdef3 punw3
psigma3 pmsk3 1 .005 1.1 2 - - - 500 2800| tee def3b.out

pdisdt_pwr24 pt pmsk3 rslc/e212958.rpar pdef3 - rmli/e212958.rmli.par
rmli/rmli_1_5.ave 0.01 2

pdisdt_pwr24 pt pmsk2 rslc/e212958.rpar punw3 - rmli/e212958.rmli.par
rmli/rmli_1_5.ave 6.28 2

Use the resdual to estimate atmosphere etc...
Spatial filtering;
spf_pt pt pmsk3 rslc/e212958.rpar pres3 pres3_spf - 2 30 1

Temporal filtering;
tpf_pt pt pmsk3 pSLC_par itab pres3_spf pres3_tpf 2 600 1 5

lin_comb_pt pt pmsk0b pres3_spf - pres3_tpf - patm3 - 0 1 -1 2 1

spf_pt pt pmsk3 rslc/e212958.rpar patm3 patm3_spf - 2 30 1

pdisdt_pwr24 pt pmsk3 rslc/e212958.rpar patm3 - rmli/e212958.rmli.par
rmli/rmli_1_5.ave 6.28 2

(Make sure you add the new estimates of atmosphere and deformation and height(if any) at the end of each iteration)

lin_comb_pt pt pmsk3 phgt3 - pdh3 - phgt4 - 0 1 1 2
lin_comb_pt pt pmsk3 pdef2 - pdef3 - pdef4 - 0 1 1 2

==========

i)

Iteration #4

New Iteration:(accounting for atmospheric phase while generating differential intfgms)

mk_diff_all pt pmsk0 pSLC_par itab pbase 0 pint 1 phgt4 pdef4 patm3_spf psim_unw4 pdiff4

pdisdt_pwr24 pt pmsk0 rslc/e212958.rpar pdiff4 - rmli/e212958.rmli.par
rmli/rmli_1_5.ave 6.28 2
dis_ipta pt pmsk0 pSLC_par - itab pbase 0 pdiff4 1 pt_msk0.ras 60. .02 2

def_mod_pt pt pmsk0 pSLC_par - itab pbase 0 pdiff4 1 23471 pres5 pdh5 pdef5 punw5 psigma5 pmsk5 60 .01 1.5 2 - - - 300 1200

Compare punw4 and punw5;
dis_ipta pt pmsk0 pSLC_par - itab pbase 0 punw3 0 pt.ras
dis_ipta pt pmsk0 pSLC_par - itab pbase 0 punw5 0 pt.ras

Use the resdual to estimate atmosphere etc...
Spatial filtering;

Annex 4 *(continue)*

spf_pt pt pmsk0 rslc/e212958.rpar pres5 pres5_spf - 2 30 1

Temporal filtering;
tpf_pt pt pmsk0 pSLC_par itab pres5_spf pres5_tpf 2 600 1 5

lin_comb_pt pt pmsk0 pres5_spf - pres5_tpf - patm4 - 0 1 -1 2 1

spf_pt pt pmsk3 rslc/e212958.rpar patm4 patm4_spf - 2 30 1

pdisdt_pwr24 pt pmsk3 rslc/e212958.rpar patm3 - rmli/e212958.rmli.par
rmli/rmli_1_5.ave 6.28 2

==========
lin_comb_pt pt pmsk0 phgt4 - pdh5 - phgt5 - 0 1 1 2
lin_comb_pt pt pmsk0 pdef4 - pdef5 - pdef6 - 0 1 1 2

Iteration #5

mk_diff_all pt pmsk0 pSLC_par itab pbase 0 pint 1 phgt5 pdef6 patm4_spf psim_unw5 pdiff5

def_mod_pt pt pmsk0 pSLC_par - itab pbase 0 pdiff5 1 23471 pres6 pdh6 pdef7 punw6 psigma6 pmsk6 60 .01 1.5 2 - - - 300 1200

dis_ipta pt pmsk0 pSLC_par - itab pbase 0 pdiff5 1 pt_msk0.ras 60. .02 2

dis_ipta pt pmsk3 pSLC_par - itab pbase 0 pdiff4 1 pt.ras